

# Modelling quartz luminescence signal dynamics relevant for dating and dosimetry

Towards a generalised understanding of radiofluorescence signal dynamics

DISSERTATION

zur Erlangung des Grades

Doktor der Naturwissenschaften

(Dr. rer. nat.)

an der Fakultät für Biologie, Chemie und Geowissenschaften

der Universität Bayreuth

vorgelegt von

JOHANNES FRIEDRICH

geboren in Pegnitz

Bayreuth, 2018



Die vorliegende Arbeit wurde in der Zeit von Oktober 2015 bis Juni 2018 in Bayreuth am Lehrstuhl Geomorphologie unter Betreuung von Herrn Dr. Christoph Schmidt angefertigt.

Vollständiger Abdruck der von der Fakultät für Biologie, Chemie und Geowissenschaften der Universität Bayreuth genehmigten Dissertation zur Erlangung des akademischen Grades eines Doktors der Naturwissenschaften (Dr. rer. nat.).

Dissertation eingereicht am :	27.06.2018
Zulassung durch die Promotionskommission:	04.07.2018
Wissenschaftliches Kolloquium:	14.12.2018

Amtierender Dekan:	Prof. Dr. Stefan Peiffer
--------------------	--------------------------

Prüfungsausschuss:

Dr. Christoph Schmidt	(Gutachter)
Prof. Dr. Markus Fuchs	(Gutachter)
Prof. Dr. Michael Hauhs	(Vorsitz)
Prof. Dr. Andrea Carminati	
(Weitere Gutachterin: Prof. Dr. Regina DeWitt)	

**Für meine Familie**

# Contents

<b>Zusammenfassung</b>	<b>XI</b>
<b>Summary</b>	<b>XIII</b>
<b>List of Tables</b>	<b>XV</b>
<b>List of Figures</b>	<b>XIX</b>
<b>List of Abbreviations</b>	<b>XXIX</b>
<b>1 Synopsis</b>	<b>1</b>
1.1 Introduction . . . . .	1
1.1.1 Numerical models in luminescence . . . . .	1
1.1.2 Aims of this thesis . . . . .	2
1.1.3 Outline of this thesis . . . . .	3
1.2 Energy levels in solids . . . . .	4
1.2.1 Energy levels in a perfect crystal . . . . .	4
1.2.2 Energy levels in real crystals . . . . .	7
1.3 Defects in quartz . . . . .	9
1.4 Describing luminescence phenomena . . . . .	12
1.4.1 Mathematical description of luminescence . . . . .	13
1.4.2 Alternative luminescence descriptions . . . . .	19
1.5 Quartz radiofluorescence . . . . .	20
1.5.1 Definition . . . . .	20
1.5.2 Process of luminescence production . . . . .	20
1.5.3 RF emissions of quartz . . . . .	22
1.6 The Bailey (2001) model . . . . .	24
1.6.1 Description of the model . . . . .	24
1.6.2 Simulating the geological sample history . . . . .	25
1.6.3 The impact of the Bailey (2001) model . . . . .	26
1.6.4 Problems with current luminescence models simulating RF . . . . .	27
1.7 Results . . . . .	28
1.7.1 Improving numerical quartz models . . . . .	28
1.7.2 Technical investigations and developments . . . . .	29
1.7.3 Methodological investigations . . . . .	31

1.7.4	Awards . . . . .	32
1.8	Research outlook . . . . .	33
1.8.1	Numerical simulations . . . . .	33
1.8.2	Methods . . . . .	33
1.9	Discussion and conclusion . . . . .	34
1.9.1	Quartz RF measurements . . . . .	34
1.9.2	Quartz RF simulations . . . . .	35
	References . . . . .	38
<b>2</b>	<b>Solving Ordinary Differential Equations to Understand Luminescence: 'RLum-Model', an Advanced Research Tool for Simulating Luminescence in Quartz Using R</b>	<b>47</b>
2.1	Introduction . . . . .	48
2.2	Methods . . . . .	50
2.2.1	Description of implemented luminescence models . . . . .	50
2.2.2	Software and integration . . . . .	53
2.3	Creating data with 'RLumModel' . . . . .	54
2.3.1	Selecting a quartz luminescence model in 'RLumModel' . . . . .	56
2.3.2	Creating sequences in 'RLumModel' . . . . .	56
2.3.3	Deep control of sample history . . . . .	58
2.4	Working examples . . . . .	59
2.4.1	Simulating general TL/OSL/RF phenomena . . . . .	59
2.4.1.1	Simulating a TL curve and shift of TL peak with varying heating rate . . . . .	59
2.4.1.2	Simulating thermal activation characteristics (TACs) . . . . .	61
2.4.1.3	Simulating dependency of the OSL signal on the illumination power density . . . . .	61
2.4.1.4	Temperature dependence of the OSL signal . . . . .	63
2.4.1.5	Simulating quartz radiofluorescence (RF) . . . . .	63
2.4.2	Simulating and analysing SAR measurements . . . . .	64
2.5	Discussion and conclusions . . . . .	68
	References . . . . .	71
<b>3</b>	<b>Quartz radiofluorescence: a modelling approach</b>	<b>75</b>
3.1	Introduction . . . . .	76
3.2	Material and methods . . . . .	77
3.2.1	Quartz samples . . . . .	77
3.2.2	Measurement conditions . . . . .	77
3.2.3	Data analysis . . . . .	77
3.3	Quartz UV-RF measurements . . . . .	78
3.3.1	Preheat experiments . . . . .	78

3.3.2	Signal stability tests . . . . .	80
3.4	Quartz UV-RF simulations . . . . .	81
3.4.1	Defining the model . . . . .	81
3.4.2	Matching experimental results and simulations . . . . .	84
3.4.3	Further simulation results . . . . .	86
3.5	Discussion . . . . .	89
3.6	Conclusions . . . . .	90
3.7	Acknowledgements . . . . .	91
	References . . . . .	92
<b>4</b>	<b>The basic principles of quartz radiofluorescence dynamics in the UV - analytical, numerical and experimental results</b>	<b>95</b>
4.1	Introduction . . . . .	96
4.2	Description of the model . . . . .	96
4.3	Derivation of the analytical expressions . . . . .	98
4.4	Comparison of analytical expressions and numerical results . . . . .	99
4.4.1	Case I: empty R-centre ( $m_1 = 0$ ) . . . . .	100
4.4.2	Case II: empty R-centre and empty electron trap ( $m_{10} = 0, n_0 = 0$ ) . . . . .	101
4.4.3	Case III: Random distribution of holes . . . . .	103
4.5	Comparison with experimental results . . . . .	105
4.5.1	Materials and methods . . . . .	105
4.5.2	Measurements in the UV . . . . .	106
4.5.3	Interpretation . . . . .	107
4.6	Discussion . . . . .	109
4.7	Conclusion . . . . .	111
4.8	Acknowledgements . . . . .	111
4.A	Appendix . . . . .	112
4.A.1	Derivation of the coefficient $C_2$ . . . . .	112
4.A.2	Derivation of the concentration of holes in the R- and L-centre (for $m_{10} = 0$ ) . . . . .	113
4.A.2.1	Concentration of holes in the L-centre . . . . .	113
4.A.2.2	Concentration of holes in the R-centre . . . . .	114
4.A.2.3	Concentration of electrons in the deep trap . . . . .	114
	References . . . . .	115
<b>5</b>	<b>On the dose rate dependence of radiofluorescence signals of natural quartz</b>	<b>117</b>
5.1	Introduction . . . . .	118
5.2	Materials and methods . . . . .	119
5.2.1	Quartz samples . . . . .	119
5.2.2	Measurement conditions . . . . .	119
5.2.3	Data analysis . . . . .	119

5.3	Results . . . . .	119
5.3.1	Effect of different dose rates on the C band (3.42 eV) . . . . .	120
5.3.2	Analysis . . . . .	122
5.3.2.1	Initial signal . . . . .	122
5.3.2.2	Signal dynamics . . . . .	122
5.4	Simulations . . . . .	125
5.4.1	Defining the model . . . . .	125
5.4.2	Matching experimental results and simulations . . . . .	127
5.5	Discussion . . . . .	130
5.5.1	Curve fitting . . . . .	130
5.5.2	Expanded numerical model . . . . .	131
5.5.3	Potential for an application? . . . . .	131
5.6	Conclusion . . . . .	134
5.7	Acknowledgements . . . . .	135
	References . . . . .	136
<b>6</b>	<b>Radiofluorescence as a Detection Tool for Quartz Luminescence Quenching Processes</b>	<b>139</b>
6.1	Introduction . . . . .	140
6.2	Materials and methods . . . . .	141
6.2.1	Quartz samples . . . . .	141
6.2.2	Measurement conditions . . . . .	142
6.2.2.1	Setup for thermal quenching measurements . . . . .	142
6.2.2.2	Setup for dose quenching measurements . . . . .	142
6.2.3	Data analysis . . . . .	142
6.3	Measurements . . . . .	143
6.3.1	Thermal quenching . . . . .	143
6.3.2	Dose quenching . . . . .	145
6.4	Simulations . . . . .	148
6.4.1	Defining the model . . . . .	148
6.4.2	Matching experimental results and simulations . . . . .	148
6.4.2.1	Thermal quenching . . . . .	148
6.4.2.2	Dose quenching . . . . .	148
6.5	Discussion . . . . .	151
6.5.1	Thermal quenching . . . . .	151
6.5.2	Dose quenching . . . . .	152
6.5.3	Limitation of our study . . . . .	152
6.6	Conclusions . . . . .	153
6.7	Acknowledgements . . . . .	154
	References . . . . .	155

---

<b>7</b>	<b>Making the Invisible Visible: Observing the UV-reversal Effect in Quartz using Radiofluorescence</b>	<b>159</b>
7.1	Introduction . . . . .	160
7.2	Material and methods . . . . .	161
7.2.1	Quartz samples . . . . .	161
7.2.2	Measurement conditions . . . . .	162
7.2.3	Data analysis . . . . .	162
7.3	Quartz UV-RF measurements . . . . .	163
7.3.1	Varying UV-bleaching times . . . . .	163
7.3.2	Detecting the UV-reversal effect . . . . .	166
7.4	Quartz UV-RF simulations . . . . .	168
7.4.1	Defining the model . . . . .	168
7.4.2	Matching experimental results and simulations . . . . .	169
7.4.3	Simulations with a more comprehensive model . . . . .	170
7.5	Discussion . . . . .	174
7.6	Conclusions . . . . .	175
7.7	Acknowledgements . . . . .	175
	References . . . . .	176
<b>8</b>	<b>Further results</b>	<b>179</b>
8.1	Recuperation of the UV-RF signal after storing at RT . . . . .	179
8.2	Determining absorbed doses with UV-RF . . . . .	182
8.2.1	Measurement protocol . . . . .	182
8.2.2	Dose recovery tests . . . . .	185
8.3	Inverse modelling . . . . .	188
8.3.1	Sensitivity analysis of quartz luminescence simulations . . . . .	188
8.3.1.1	Global sensitivity analysis . . . . .	188
8.3.1.2	Local sensitivity analysis . . . . .	189
8.3.2	Finding appropriate model parameters . . . . .	191
8.3.3	Software and integration . . . . .	193
8.3.4	Conclusion . . . . .	194
8.4	Monte-Carlo simulations of RF . . . . .	195
8.4.1	Basics of Monte-Carlo simulations . . . . .	195
8.4.2	Performing Monte-Carlo simulations . . . . .	198
8.4.3	Comparison with other numerical methods . . . . .	199
8.4.4	Discussion . . . . .	201
	References . . . . .	203
	<b>Appendices</b>	<b>207</b>

<b>A</b>	<b>Supplementary material of publications</b>	<b>207</b>
A.1	Chapter 2 . . . . .	207
A.2	Chapter 3 . . . . .	216
A.3	Chapter 4 . . . . .	225
A.4	Chapter 5 . . . . .	232
<b>B</b>	<b>Contribution to the manuscripts</b>	<b>245</b>
B.1	Publication I - Chapter 2 . . . . .	245
B.2	Publication II - Chapter 3 . . . . .	246
B.3	Publication III - Chapter 4 . . . . .	247
B.4	Publication IV - Chapter 5 . . . . .	248
B.5	Publication V - Chapter 6 . . . . .	249
B.6	Publication VI - Chapter 7 . . . . .	250
<b>C</b>	<b>List of publications and presentations</b>	<b>251</b>
C.1	Peer reviewed journals . . . . .	251
C.1.1	accepted/published . . . . .	251
C.2	Conference posters and presentations . . . . .	252
C.3	Invited talks . . . . .	253
	<b>Acknowledgements</b>	<b>255</b>
	<b>(Eidesstattliche) Versicherungen und Erklärungen</b>	<b>257</b>

# Zusammenfassung

Die Methoden der Thermolumineszenz (TL) und der optisch stimulierten Lumineszenz (OSL) sind mittlerweile etablierte, geowissenschaftliche Werkzeuge und ermöglichen beispielsweise Datierungen archäologischer Artefakte oder quartärer Sedimente. Besonders Quarz eignet sich für diese Anwendungen, da es das zweithäufigste Mineral in der Erdkruste ist. Um das komplexe System der Ladungsträgerbewegungen im Quarzkristall zu verstehen, helfen numerische Simulationen, insbesondere gekoppelte Differentialgleichungen, deren Lösungen die zeitlichen Verläufe von Ladungsträgerkonzentrationen im Kristall beschreiben. Im Jahr 2001 wurde ein umfassendes Modell veröffentlicht, das viele Effekte und Phänomene der Quarzlumineszenz im UV (Ultraviolett) gut beschreibt und Grundlage für viele weitere Veröffentlichungen ist. Nichtsdestotrotz konnte insbesondere das Phänomen der UV-Radiofluoreszenz (UV-RF), der Emission von Photonen im UV während der Wechselwirkung mit ionisierender Strahlung, nicht hinreichend simuliert werden. Die Methode der Radiofluoreszenz bietet jedoch einige Vorteile gegenüber anderen Lumineszenzsignalen, z.B. die Möglichkeit zur direkten Beobachtung temperaturabhängiger Lumineszenzeffekte.

Die vorliegende Arbeit zeigt zum einen grundlegende, experimentelle Untersuchungen zur Quarz UV-RF und zum anderen die qualitative Simulation von UV-RF und möglichst vieler anderer Lumineszenzphänomene. Hierzu wurden bereits publizierte Quarzmodelle und ihre zugehörigen Parameter im Open-Source Softwarepaket *RLumModel* zusammengefasst. Die Handhabung wurde möglichst einfach gehalten, sodass eine Benutzung ohne fortgeschrittene Programmierkenntnisse und physikalisches Hintergrundwissen möglich ist. Das grundlegende Verhalten der UV-RF nach unterschiedlichen Vorheiztemperaturen wurde systematisch untersucht und dabei festgestellt, dass die maximale Signalintensität nach Vorheizen auf  $\sim 550^\circ\text{C}$  eintritt. Nach Anpassung der Ladungsträgerkonzentrationen in den Modellparametern konnten die experimentellen Ergebnisse erfolgreich simuliert werden. Weitere Untersuchungen zur Abhängigkeit des UV-RF Signals von der Dosisleistung der Strahlungsquelle erfüllten die theoretisch hergeleiteten Erwartungen, dass die Signalintensität linear mit der Dosisleistung und der Abfall der Signalintensität in den ersten Sekunden linear mit dem Quadrat der Dosisleistung steigt. Dieses Verhalten konnte ebenfalls nach Modifikationen der Modellparameter mit hoher Genauigkeit numerisch abgebildet werden.

In allen numerischen Untersuchungen wurde diagnostiziert, dass die Haupteigenschaften der durchgeführten Experimente mit einem vereinfachten Modell aus drei verschiedenen Energiestufen simuliert werden können. Auf Grundlage dieses Modells konnten analytische

Lösungen für die UV-RF Signaldynamik berechnet werden und es wurde dabei festgestellt, dass diese aus der Summe einer exponentiell abklingenden und exponentiell zunehmenden Funktion zusammengesetzt sind. Dieses grundlegende Verhalten lässt sich auch auf andere Emissionsbänder übertragen und ist nicht auf den UV Bereich beschränkt.

Weitere anwendungsbezogene Ergebnisse liefern die Untersuchungen zu Quenchingmechanismen in Quarz. Radiofluoreszenz bietet die Möglichkeit *thermal-quenching* in Rekombinationszentren zu beobachten und daraus notwendige Parameter zu berechnen, die wiederum als Grundlage für Simulationen dienen. Ebenso ist es möglich das Phänomen des *dose-quenching* direkter als bisher zu analysieren. Vergleiche mit etablierten Messmethoden für thermal- und dose-quenching zeigen, dass UV-RF Möglichkeiten zum besseren Verständnis von Lumineszenzeffekten in Quarz bietet. Simulationen zu beiden Effekten konnten erfolgreich umgesetzt werden. Darüber hinaus wurden Beobachtungen wie der *UV-reversal* Effekt mit UV-RF direkter als jemals zuvor untersucht und bekräftigten die Modellvorstellung, dass Vorheizen und UV-Bestrahlung gegensätzliche Ladungsträgerverschiebungen verursachen. Eine Anwendung zur Bestimmung absorbiertes ionisierender Strahlung in Quarz mit Hilfe der UV-RF konnte zunächst theoretisch und anschließend auch experimentell gezeigt werden. Mit Hilfe der entwickelten Messmethode wurden absorbierte Dosen von bis zu  $\sim 300$  Gy mit einer Genauigkeit von  $\pm 10\%$  erfolgreich bestimmt. Die Anwendungen der Methode können von der Quellenkalibrierung, bis hin zur Datierung von zuvor ausgeheizten Materialien, wie z.B. Keramiken, reichen.

Um aus Simulationen Vorhersagen zu generieren (*forward modelling*), müssen zunächst passende Parameter gefunden werden. Dazu wurden an den bereits vorhandenen Parametersets Sensitivitätsanalysen durchgeführt, um die für das jeweilige Signal einflussreichsten Parameter zu extrahieren. Anschließend wurden diese Parameter so angepasst, dass sie gemessene Lumineszenzsignale möglichst genau abbilden (*inverse modelling*). Diese Technik wurde auf TL und OSL Signale angewandt. Sensitivitätsanalysen und inverse modelling sind ebenfalls im Softwarepaket *RLumModel* implementiert. Dies hilft z.B. möglicherweise zeitaufwändige Messungen zunächst zu simulieren. Als methodologische Weiterentwicklung werden darüber hinaus erste Überlegungen und Ergebnisse von Monte-Carlo Simulationen für Quarz RF vorgestellt und mit bisher etablierten Methoden verglichen.

Diese Arbeit zeigt, dass das Zusammenspiel von experimentellen Untersuchungen und numerischen Simulationen ein umfassenderes Verständnis von Lumineszenz bietet. Darüber hinaus besitzt Radiofluoreszenz an Quarzen ein breites Anwendungsgebiet und liefert wichtige Erkenntnisse über Ladungsträgerbewegungen im Quarzkristall. So sind verschiedene Radiofluoreszenzphänomene mit Hilfe des Bändermodell erklärbar und lassen sich nach einigen Parameteranpassungen nahtlos in bereits vorhandene Modelle integrieren.

# Summary

Thermoluminescence (TL) and optically stimulated luminescence (OSL) are well-established methods in geoscience, e.g., used to date archaeological sites or quaternary sediments. Quartz is well suited for that purpose because it is the second most abundant mineral in Earth's continental crust. Numerical simulations, especially coupled differential equations, can help to understand the complex system of charge carrier transport in the quartz crystal because the solutions of these differential equations describe the charge carrier movement by time. In 2001 a comprehensive quartz model was published which was able to describe many known effects and phenomena concerning quartz luminescence in the UV spectrum (ultra-violet). This publication is the foundation of many more published models in recent years. Nevertheless, the luminescence emitted while irradiating quartz with ionising radiation, known as radiofluorescence (RF), was not well implemented in the model, because even basic observations are not reproducible. Radiofluorescence offers some key advantages, e.g., direct and real-time observation of temperature-driven effects on luminescence production.

This thesis presents fundamental experimental UV-RF investigations and the qualitatively successful simulation of RF and other luminescence signals and phenomena. Published quartz models and parameters had been gathered in an open-source software package called *RLumModel*. The software has been designed for simplicity to allow use without deep knowledge of programming or physical understanding of the model. Fundamental behaviour of UV-RF signals was tested by annealing to different temperatures before UV-RF measurement. The maximum signal intensity was measured after annealing to  $\sim 550^\circ\text{C}$ . Numerical simulations are able to reproduce this characteristic after some modifications of charge carrier concentrations in the model parameters. Further investigations on the dose rate dependence of the UV-RF signal fulfil theoretical findings that the signal intensity is linearly-dependent on the dose rate and the slope of the initial UV-RF signal is linearly-dependent on the squared dose rate. Again, after some parameter modifications the numerical simulations are able to mimic this behaviour. It was remarkable that in all numerical investigations a simple three-energy-level model was able to simulate the main characteristics of the observed effects. Due to this, analytical solutions for the UV-RF signal dynamic were derived. The finding from these analytical solutions is a fitting function for UV-RF signals which is a composite of two exponential functions: an increasing and a decreasing exponential. This behaviour is not restricted to the UV band and can also be transferred to other emission bands.

Investigating quenching mechanisms in quartz yield the power of RF for further applications because RF offers the possibility to measure, e.g., *thermal-quenching* more directly. With these measurements it is possible to directly calculate thermal quenching parameters which can be implemented in the numerical model. Another phenomenon, called *dose-quenching*, can also be measured more directly. Comparisons with other methods measuring quenching effects show the possibilities of RF as analysis tool in quartz luminescence. Both quenching effects were also simulated and are again in accordance with experimental results. In addition to that, long-known effects such as the *UV-reversal* were also analysed more directly via UV-RF and confirm the idea of reversibility of annealing and UV illumination. Another application is the determination of absorbed doses with UV-RF, which was first found by numerical simulations. Further experimental data confirm that the new developed measurement protocol is able to recover doses up to  $\sim 300$  Gy with a accuracy of  $\pm 10\%$  with UV-RF. Possible applications of this method range from source calibration to dating of annealed material, e.g., ceramics.

Generating predictions from simulations (*forward modelling*) needs appropriate parameters. To get these parameters, sensitivity analysis of the used parameter sets was applied to extract parameters influencing the outcome of the simulations most. Subsequently these parameters were adjusted by fitting them to luminescence signals (*inverse modelling*). This method was applied to TL and OSL signals. Sensitivity analysis and inverse modelling are also included in the software package *RLumModel*. This will help saving measurement time because users can first simulate their sequences. To develop further methods to calculate RF signals from models, the first ideas and results from Monte-Carlo simulations for quartz RF are presented and compared to established numerical methods.

This thesis shows that the interaction of experiments and simulations offers a comprehensive understanding of luminescence. Furthermore, it has been shown that radiofluorescence of quartz has a wide range of applications and provides important insights into charge carrier distributions in quartz crystals. Different radiofluorescence phenomena can be explained with the energy-band-model and can be implemented seamlessly in existing models by adjusting model parameters.

# List of Tables

1.1	Luminescence emission bands in quartz and related defects. Modified after Götze (2012a) and Krbetschek et al. (1997). . . . .	12
1.2	Spectral parameters of the emission bands resulting from Gaussian deconvolution of RF spectra. The nomenclature is adopted from Fasoli & Martini (2016). . . . .	23
1.3	Comparison of two different sample histories from Bailey (2001) and Bailey (2002). . . . .	26
1.4	Summary of all investigated quartz samples in the thesis. Chapters 3 to 7 are published/submitted manuscripts, Ch. 8 contains unpublished results. . .	32
2.1	Summary of quartz luminescence traps/centres (levels) in different luminescence models and their numbering. If there is a change in numbering of levels between 'RLumModel' and the particular publication, the original level number is given in italics. The dashed line shows the border between electron traps and hole centres. . . . .	51
2.2	Description of the abbreviations used in the differential equations. . . . .	52
2.3	Differences in implemented quartz luminescence models. 'PEC' means photoeviction constant and 'OCS' optical cross section, see main text. . . . .	53
2.4	Keywords for creating a sequence in 'RLumModel'. Note that 100% optical power equals to $20 \text{ mW cm}^{-2}$ (Bailey 2001). Values $> 100\%$ are allowed. . .	57
2.5	Keywords for creating a SAR sequence with 'RLumModel'. The keyword <code>Irr_2recover</code> is only necessary for creating a DRT sequence. Note that 100% optical power equals to $20 \text{ mW cm}^{-2}$ (Bailey 2001). Values $> 100\%$ are allowed. . . . .	58
2.6	Summary of sample histories for models implemented in 'RLumModel'. . . .	59
3.1	Description of the abbreviations used in the differential equations. . . . .	83
3.2	The Qtz- $A_1$ parameters of Bailey (2001) are shown together with their modified values used in the simulations presented in this study (bold values). . .	83
3.3	The simulation steps for the UV-RF simulation. For each new preheat temperature a new (simulated) aliquot was used. The line after step 8 indicates the end of the sample history. Steps 9 and 10 represent the simulated measurements in the laboratory. . . . .	83

4.1	Used parameters for the comparison between analytical and numerical solutions.	100
5.1	Spectral parameters of the emission bands resulting from Gaussian deconvolution of the spectra. . . . .	120
5.2	Description of the abbreviations used in the differential equations (5.1) – (5.4).	126
5.3	Simulation parameters . . . . .	126
5.4	Single steps for the simulations. Steps 7 and 8 represent the simulated measurements in the laboratory. . . . .	127
5.5	Model parameters used for simulating the data shown in Fig. 5.9. The parameters for the deep electron trap, R <sub>1</sub> -centre and L-centre are identical to the ones presented in Table 5.3. . . . .	131
5.6	Protocol for dose recovery with UV-RF. . . . .	134
6.1	Summary of arithmetic average of $W$ , $K$ and $T_{1/2}$ derived from fitting of Eq. (6.1) and (6.2) to the experimentally obtained RF curves. The given uncertainty range ( $1\sigma$ standard deviation) reflects the variety of different aliquots. . . . .	144
7.1	Measurement protocol for varying bleaching times. All annealing steps were performed with $5\text{ K s}^{-1}$ . For detailed information, see text. . . . .	163
7.2	Estimation of fitted parameters in Fig. 7.4 with std. error from fitting procedure.	165
7.3	Measurement protocol detecting the UV-reversal effect. . . . .	166
7.4	Used parameters for the comparison between analytical and numerical solutions. No heating steps were included in this simulation. . . . .	170
7.5	Model parameters used for simulating the data shown in Figs. 7.9 and 7.10. The parameters for the deep electron trap, R- and L-centre are identical to the ones presented in Table 7.4. . . . .	172
7.6	The simulation steps for the UV-RF simulation with the comprehensive model. Steps 9 to 12 represent the simulated measurements in the laboratory and are comparable with steps 1 to 4 in Table 7.1. . . . .	172
8.1	Protocol for dose recovery with UV-RF. . . . .	183
8.2	Change of parameter values before and after inverse modelling for TL and OSL simulations. The corresponding TL and OSL curves are given in Figs. 8.11 and 8.12. *: The <i>tgcd</i> package is able to calculate glow curve parameters from TL, but not from OSL curves. . . . .	192
8.3	Used parameters for the Monte-Carlo simulation of quartz UV-RF. . . . .	198
8.4	Used parameters for the Monte-Carlo simulation of feldspar IR-RF. In contrast to Table 8.3 the new parameter $\bar{A}_{m_n}$ describes the probability of a hole transport into the IR-RF trap. . . . .	202

B.1	Individual contributions to Publication I - Chapter 2. *: No measurements were conducted in the publication. . . . .	245
B.2	Individual contributions to Publication II - Chapter 3. . . . .	246
B.3	Individual contributions to Publication III - Chapter 4. . . . .	247
B.4	Individual contributions to Publication IV - Chapter 5. . . . .	248
B.5	Individual contributions to Publication V - Chapter 6. . . . .	249
B.6	Individual contributions to Publication VI - Chapter 7. . . . .	250



# List of Figures

1.1	Right-hand side of Eq. (1.3) plotted against $k_0a$ for $P = 3\pi/2$ . The marked regions are regions of $k_0a$ for which $k$ can be calculated. So this is called an <i>allowed</i> region. Note that the forbidden regions become narrower as the value of $k_0a$ becomes larger. . . . .	6
1.2	Electron density of states for the Kronig-Penney model. Note the values of 0 for $D(E)$ . The used input values are: $V = 5$ eV, $a = 1.5$ E-10 m, $b = 5$ E-10 m and $m = 9.1$ E-31 kg. . . . .	7
1.3	Subfigure(a) shows the energy band of an ideal semiconductor for $T = 0$ K. All electrons occupy the valence band with energy $E_V$ . The band gap between $E_V$ and $E_C$ (energy of the conduction band) divides the valence from the conduction band. Increasing the temperature leads to a redistribution of electrons according to the Fermi-Dirac distribution and some electrons are able to reach the conduction band. Figures modified and redrawn after Enderlein & Horing (1997). . . . .	8
1.4	Schematic energy band model for a crystal lattice with impurities. $E_V$ is the energy of the valence band, $E_C$ the energy of the conduction band, $E_D$ the energy of the donors and $E_A$ the energy of the acceptors. . . . .	9
1.5	Schema of most common point defects (from Götze (2012b)). . . . .	11
1.6	Schematic energy band model with demarcation levels and definition of electron trap, hole trap and recombination centre. Filled dots illustrate electrons and open dots holes. . . . .	14
1.7	Schematic energy band of the OTOR model with one electron trap and one recombination centre. The corresponding values for recombination centre and electron trap are given as well as the allowed transitions (arrows). . . .	15
1.8	Comparison of different kinetic orders for the analytical solution in the case of TL. Used parameters: $N = n_0 = 1$ E+17 cm <sup>-3</sup> , $s = 1$ E+13 s <sup>-1</sup> , $\beta = 1$ K s <sup>-1</sup> and $E = 1$ eV. For the general-order kinetics, $b = 1.5$ was used. . . . .	17
1.9	Configurational coordinate diagram with radiative and non-radiative transitions. Explanation see text in Ch. 1.5.2. Modified from Nasdala et al. (2004). . . . .	22
1.10	Deconvolution into Gaussian components of the RF emission spectra for quartz sample BT586 after annealing to 500 °C for 10 min. . . . .	24
1.11	Schematic energy band model by Bailey (2001). . . . .	26

1.12	The effect of different preheat temperatures on the RF signal simulated with model parameter suggested by Bailey (2001), Friedrich et al. (2017a), and Pagonis et al. (2007a, 2008a), respectively. . . . .	28
1.13	RF simulations for different values of the concentration of the $R_1$ centre. The reference data set was the one presented in Ch. 5. . . . .	37
1.14	Numerical simulations with different values of the concentration of the $R_1$ centre for (a) TL and (b) OSL. No differences in the signal dynamics are visible in the normalised signal. . . . .	37
2.1	Comprehensive energy-band-model for quartz, for details see Table 2.1. . . . .	50
2.2	Flow chart of exemplary data processing in 'RLumModel'. . . . .	55
2.3	TL curve simulation after 'Bailey2001'. . . . .	61
2.4	Shift of TL peaks with varying heating rates using parameters from 'Bailey2001'. . . . .	61
2.5	Change of electron concentration in the 110 °C TL trap while simulating TL after 'Bailey2001'. . . . .	62
2.6	Simulated thermal activation characteristics (TAC) of the 110 °C TL signal for the model and parameter set by 'Pagonis2007'. . . . .	62
2.7	Dependency of the OSL signal on the illumination power density for the parameter set 'Bailey2004'. The inset shows the linearity of the initial 0.1 s of the OSL signal with increasing illumination power density. . . . .	62
2.8	Temperature dependence of the OSL signal as simulated with the 'Bailey2001' model for different measurement temperatures. The inset plots the integrated OSL (0 – 60 s) against measurement temperature. . . . .	63
2.9	RF simulation and concentration of holes in the reservoir centre $R_1$ (inset) as resulting from the 'Bailey2001' model (Bailey 2001: Fig. 12). . . . .	64
2.10	Resetting of the natural signal with the model 'Pagonis2008' in the DRT sequence. . . . .	65
2.11	DRT results for the model 'Pagonis2008'. Every data point is the result of a $D_e$ estimation with a specific preheat temperature, see main text. The errors of the $D_e$ values are so small, that they do not appear in this plot. . . . .	67
2.12	Results of a simulated SAR sequence using the model 'Pagonis2008' with a burial dose of 200 Gy and a simulated dose rate during irradiation of 1 Gy s <sup>-1</sup> . The plot was created with function <code>Luminescence::analyse_SAR.CWOSL()</code> . . . . .	70

3.1	(a) UV-RF signal for sample BT586 for different preheat temperatures (hold for 120 s) prior to the RF measurements. For each temperature a new aliquot was used. The values are normalized to the last data point of each measurement and the total absorbed dose is 600 Gy during each RF measurement. For the sake of clarity the UV-RF curves for preheat temperatures from 100 °C to 250 °C were removed, because no change was observed. (b) The same data as (a) but with absolute values and a logarithmic x-axis. . . . .	79
3.2	(a) UV-RF signal for sample BT1195 for different preheat temperatures (holding for 120 s). The values are normalized to the last data point of each measurement. The total absorbed dose was 600 Gy during each RF measurement. For the sake of clarity the UV-RF curves for preheat temperatures from 100 °C to 250 °C were removed, because no change was observed. (b) The same data as (a) but with absolute values and a logarithmic x-axis. . . . .	79
3.3	Initial UV-RF signal for different preheat temperatures (holding for 120 s) for samples BT586 and BT1195 normalized to the initial signal at 550 °C. . . . .	80
3.4	(a) UV-RF signals for sample BT586 for 11 cycles for a preheat at 500 °C for 120 s between each cycle. The total absorbed dose was 600 Gy for each RF cycle. The curves are normalized to the last data point. (b) The same data as (a) but with absolute values and a logarithmic x-axis. . . . .	81
3.5	Schematic diagram of the comprehensive Bailey (2001) model for quartz. . . . .	84
3.6	(a) Simulation of the sequence presented in Table 3.3 with the parameters from Table 3.2. The RF signal is normalized to the last signal value at 10,000 s. Subfigure (b) shows the simulated initial RF signal from the main figure. The values on the y-axis are normalized to the highest value of all initial signals. . . . .	85
3.7	Simulation of the experimental results from Fig 3.4. Following the sample history, a preheat to 500 °C and a subsequent RF step were simulated, see steps 9 and 10 in Table 3.3. . . . .	86
3.8	(a) Same simulation as for Figs. 3.6 and 3.7 (b) but using the simplified model with energy levels 5, 6, and 8 only (see Table 3.2). . . . .	87
3.9	The concentration of electrons in the deep trap and holes in the R-centre and the L-centre after the preheat step (step 9 in Table 3.3) for the simplified three-energy-level model. The values are normalized to the total amount of electrons. . . . .	88
3.10	Simulations for different burial doses for step 7 in the sample history (see step 7 in Table 3.3). (a) shows initial RF signals for different preheat temperatures and for 6 different burial doses. (b) is a detailed view on the initial RF signal at 450 °C. The initial signal was plotted against the simulated burial dose. . . . .	89

4.1	Energy-band-scheme of the three-level model employed to simulate RF at room temperature. The arrows indicate the allowed transitions of electrons/holes during RF. All indices with <i>1</i> indicate the parameters belonging to the R-centre and <i>2</i> those belonging to the L-centre. A detailed description of the parameters is given in table 4.1. . . . .	97
4.2	Different UV-RF curves when solving Eqs. (4.1) – (4.5) numerically. Eleven different starting concentrations of the L-centre were calculated. Note that the initial RF signal and the slope are further analysed in Figs. 4.3 and 4.4.	101
4.3	The analytically and numerically derived solutions for the initial RF signal for different degrees of filling of the L-centre. . . . .	102
4.4	Slope of the RF signal against the filling of the L-centre. . . . .	102
4.5	3D plot of the initial RF signal for an arbitrary distribution of holes in the L- and R-centre. 100,000 different combinations of L- and R-centre concentrations were calculated. . . . .	104
4.6	3D plot of the initial RF signal slope for an arbitrary distribution of holes in the L- and R-centre. 100,000 different combinations of L- and R-centre concentrations were calculated. . . . .	104
4.7	Histogram of the slope of the initial RF signal from -0.1 to the maximum value. About 14 % of all combinations lead to a positive slope signal. . . . .	105
4.8	(a), (c), and (e) show the UV-RF signal dynamics in the C band for untreated quartz samples. (b), (d), and (f) show the UV-RF signal dynamics in the C band for preheated quartz samples (500 °C). All signals from preheated samples as well as the signal from untreated sample BT586 were fitted with Eq. (4.21). Data displayed in Subfig. (c) and (e) were fitted using Eq. (4.18), where parameter <i>B</i> is negative. . . . .	108
4.9	Comparison of the model by Bailey (2001) and Zimmerman (1971) for a simulated UV-RF signal. The starting condition was $m_{1_0} = n_0 = M_1$ , see case I in Sec. 4.4.1. . . . .	110
4.10	Comparison between the model by Bailey (2001) and Zimmerman (1971) for the concentration of holes in the R-centre for the same simulation as shown in Fig. 4.9. The starting condition was $m_{1_0} = n_0 = M_1$ , see case I in Sec. 4.4.1.	110
5.1	RF intensity versus time for the C band (3.37 – 3.47 eV) for different dose rates. Subfigure (a) shows the results for BT586 and (b) for FB. . . . .	121
5.2	Same data as in Fig. 5.1 normalised to the first data point. Subfigure (a) shows the results for BT586 and (b) for FB. . . . .	123
5.3	Translation of the data from Fig. 5.2 (b) to a dose-axis. The measurement time was $\sim 23$ min, so doses from 13.6 – 680 Gy were applied. . . . .	124
5.4	First data point of Fig. 5.1 versus dose rate for quartz samples BT586 and FB. The grey shaded area is the 95 % confidence level interval. . . . .	124

5.5	Initial slope (second data point minus first data point) of the UV-RF signal plotted against the square of dose rate for quartz samples BT586 ( $R^2 = 0.997$ ) and FB ( $R^2 = 0.999$ ). The grey shaded area is the 95 % confidence level interval. . . . .	125
5.6	Simulation of the experimental results from Figs. 5.1 and 5.2. The simulation parameters were adjusted to fit the results of sample FB. Subfigure (a) shows the absolute values of the simulation and (b) is normalised to the first data point. . . . .	128
5.7	Simulation of the experimental results from Fig. 5.5. Subfigure (a) shows the change of the initial signal with dose rate and subfig. (b) the change of the initial slope with the squared dose rate. The grey shaded area is the 95 % confidence level interval. . . . .	129
5.8	Analysis of the UV-RF signals of sample BT586 using Eq. (5.5). Subfigure (a) shows the experimental data (dots) and fits to Eq. (5.5) (lines). Subfigure (b) shows the plot of the fitting parameter $C^{-1}$ (decay rate) against the dose rate for both used samples. The grey shaded area is the 95 % confidence level interval. . . . .	132
5.9	Simulation of the experimental results from Fig 5.5 with model parameters presented in Table 5.5. The results are similar to the ones obtained with the three-energy-level model given in Table 5.3 and Fig. 5.6. . . . .	133
5.10	Simulations of the protocol given in Table 5.6. Curve $RF_{lab}$ is shifted along the x-axis until congruence with the regenerated curve $RF_{reg}$ is reached. In that way, the dose given in $RF_{dose}$ can be determined. Note that $RF_{dose}$ and $RF_{reg}$ are on top of each other because after step 1 in Table 5.6 no sensitivity changes are expected. . . . .	134
6.1	Normalised UV-RF curve during cooling from 500 °C to RT with 1 K s <sup>-1</sup> for sample BT1195. Also included is the fit to Eq. (6.1) (green). . . . .	144
6.2	(a) UV-RF curves (b) UV-TL curves from quartz sample FB2A. For graphical reasons only nine out of 100 measured curves are shown. The sequence with which these results were obtained, is described in detail in Sec. 6.3.2 . . . .	145
6.3	(a) UV-RF curves (b) OSL curves from quartz sample BT1195. For graphical reasons only nine out of 100 measured curves are shown. . . . .	145
6.4	Combined signals for quartz sample (a) BT1195 and (b) FB2A for dose quenching measurements with the 110 °C TL peak as quenching indicator. In each graph, the second RF channel, the integrated ( $\pm 5$ channels from maximum) TL signal and the RF reference signal are plotted against dose. .	147

6.5	Combined signals for quartz (a) BT1195 and (b) FB2A for dose quenching measurements with the initial OSL signal as quenching indicator. In each graph, the second RF channel, the integrated (first second) OSL signal and the RF reference signal are plotted against dose. . . . .	147
6.6	Simulated UV-RF curve during cooling from 400 °C to RT with 1 K s <sup>-1</sup> . The used parameter set is the same as that presented in (Friedrich et al. 2017a). Used parameters for $W$ and $K$ were 0.64 eV and 2.8 E+07, respectively. The fit returns values in the same range as the inserted parameter values ( $W = 0.67$ eV, $K = 5.82$ E+07). . . . .	149
6.7	Simulated dose quenching experiment with the 110 °C TL peak as indicator. Subfigure (a) shows the simulated RF curves, (b) the simulated 110 °C TL peak and (c) the combined signals including a reference RF signal, as described in Sec. 6.3.2. . . . .	149
6.8	Simulated dose quenching experiment with OSL as indicator. Subfigure (a) shows the simulated RF curves, (b) the simulated OSL decay curve and (c) the combined signals including a reference RF signal, as described in Sec. 6.3.2.	150
6.9	Charge concentrations in different energy levels normalised to the highest value of each concentration. Beyond $\sim 150$ Gy, the hole concentration in the L-centre begins to increase what is the reason for the increasing luminescence signals. . . . .	150
7.1	Radiofluorescence spectra measurements for two quartz samples. Different line types indicate different times/doses during the measurement (solid line: $\sim 7$ Gy, dotted: $\sim 143$ Gy, dashed: $\sim 279$ Gy). A decreasing C band (peak maximum at $\sim 3.42$ eV) is apparent in the two investigated samples. Vertical dotted lines mark the detection window, limited by the used filter, see Sec. 7.2.2.	162
7.2	Typical results of different UV bleaching times for all measured quartz samples. Subfigure (a) BT1248 after 10 min UV bleaching, (b) BT586 after 40 min and (c) FB1A after 120 min. The vertical line indicates the bleaching event and different line types indicate different measured aliquots. . . . .	164
7.3	Normalised (to the last data point) UV-RF curves of sample BT1248 after different UV bleaching times ranging from 2 min to 120 min. Different line types indicate different measured aliquots. . . . .	165
7.4	RF ratio of the last channel before UV bleaching and first channel after UV bleaching for all measured samples. The dots represent the mean value and the error bars the std. error for all measured aliquots. The lines indicate a fit according to Eq. (7.1). . . . .	165

7.5	Experimental results for sample FB1A before (red lines) and after (blue lines) UV bleach and annealing to (a) 300 °C and (b) 500 °C. This corresponds to step 2 (red lines) and 5 (blue lines) in Table 7.3. Different line types indicate different measured aliquots. Horizontal lines mark the initial signal intensity of step 2 and indicate if an annealing temperature is capable of fully recovering this intensity. . . . .	167
7.6	Recuperation of the primary RF signal (before UV bleaching) after UV bleaching and annealing to different temperatures. The line indicates the mean of the two measured aliquots (filled dots). Crosses are average values of the all measured aliquots. . . . .	168
7.7	Simulation of different UV bleaching times ranging from 2 min to 120 min. The vertical line at 2,000 s marks the bleaching event. . . . .	171
7.8	RF ratio calculated from Fig. 7.7. See Fig. 7.4 for the experimental analysis.	171
7.9	Results of the numerical simulations with the comprehensive quartz model.	173
7.10	Results of the simulation of different values of parameter $P$ , the power density of the UV light against the calculated decay parameter $B$ . The line indicates an linear fit through all points and suggests a direct linearity. . . . .	174
8.1	Result for sample FB1A for 30 d waiting with normalised y-axis and just one aliquot. The black line indicates the fit for the RF curve before storage but extended to the complete x-axis. . . . .	180
8.2	Result for sample FB1A for 10 min (a) and 30 d (b) waiting, respectively. The vertical line indicates the waiting event and different line types indicate different measured aliquots. . . . .	181
8.3	All measured storage times of sample BT1248 and FB1A against the recuperated UV-RF signal. The grey shaded area is the 95 % confidence level interval. . . . .	182
8.4	Example of the used dose determination technique. For explanations see text.	184
8.5	Procedure of curve shifting of $RF_{lab}$ onto the $RF_{reg}$ signal. The given dose of 1 ks was underestimated because the best fit results in $930 \pm 2$ s. . . . .	184
8.6	Boxplot of a dose-recovery-test with UV-RF for quartz sample (a) BT586, (b) FB1A, (c) BT1248, and (d) Hyaline. For every measurement 5 aliquots were used. Different colours identify different used channel ranges to calculate the equivalent dose $D_e$ . . . . .	187
8.7	Global sensitivity analysis of a TL signal for $E$ in the range between $\pm 0.1$ eV around its nominal value of 0.97 eV. Marked are the TL curves belonging to the smallest and highest value of $E$ (green: 0.87 eV; red: 1.07 eV). . . . .	189
8.8	Explanation of a TL sensitivity analysis. Two simulated TL peaks with values of 0.970 and 0.975 eV for $E$ , respectively. . . . .	190

8.9	Sensitivity analysis of a TL simulation with parameters by Bailey (2001) for the 110 °C TL peak. The higher the absolute value at the y-axis, the higher the influence to the model output. . . . .	190
8.10	Sensitivity analysis of a OSL simulation with parameters by Bailey (2001) for the optical active traps level 3 and 4 and the corresponding parameters for thermal assistance energy $E_{th}$ and photoionisation cross-section $\sigma$ , see Ch. 1.4 and 1.6. . . . .	191
8.11	Result of the inverse modelling method for the 110 °C TL peak. Three different signals are shown: (I) The experimental data (red), (II) the simulation with the new calculated parameters for $E$ and $s$ (green, see Table 8.2), and (III) the simulation with the original parameters by Bailey (2001) (blue). . . . .	192
8.12	Result of the inverse modelling method for a natural OSL curve. Three different signals are shown: (I) The experimental data (red), (II) the simulation with the new calculated parameters for $E$ and $s$ (green, see Table 8.2), and (III) the simulation with the original parameters by Bailey (2001) (blue). . . . .	193
8.13	Example state of a cluster in the Monte-Carlo simulation of RF. . . . .	197
8.14	Results of Monte-Carlo simulations for different numbers of clusters. Subfigure a) shows the behaviour for a different number of clusters. The total number of simulated electron-hole creations was the same for all calculations. Subfigure b) shows the total number of RF signal as sum of all clusters. . . . .	199
8.15	Average signal of 100 clusters with parameters from Table 8.3 and four different pair-production rates. . . . .	200
8.16	Same data as in Fig. 8.15 but normalised to the first data point. The black lines indicate the solutions solving the system of ODEs numerically, see Ch. 8.4.3. . . . .	200
8.17	Results of the simulation of IR-RF with the model suggested by Trautmann et al. (1999) for different initial fillings of the IR-RF trap. The black lines indicate the ODE solutions which are in agreement with the Monte-Carlo results. . . . .	201





# List of Abbreviations

$A_i$	Conduction band to electron trap transition probability
$A_j$	Valence band to hole centre transition probability
$B_j$	Conduction band to hole centre transition probability
$E_A$	Energy of the acceptor level
$E_C$	Energy of the conduction band
$E_{D_n}$	Demarcation energy for electrons
$E_{D_p}$	Demarcation energy for holes
$E_D$	Energy of the donor level
$E_F$	Fermi level
$E_G$	Energy of the band gap, defined as $E_C - E_V$
$E_V$	Energy of the valence band
$E_i$	Electron trap depth below the conduction band
$E_j$	Hole centre depth above the valence band
$E_{th_i}$	Thermal assistance energy
$N_i$	Concentration of electron traps
$N_j$	Concentration of hole centres
$P$	Stimulation photon flux
$R$	Ionisation rate (pair production rate)
$T$	Absolute temperature
$V$	Potential energy
$W$	Activation energy for thermal quenching
$\Psi$	Wave function of the quantum system
$\epsilon_F$	Fermi energy, not to be mixed up with $E_F$
$\sigma_{0i}$	Photo eviction constant or photoionisation cross section for electron traps
$\sigma_{m_2}$	Photo eviction constant of L-centre
$k_B$	Boltzmann constant
$n_c$	Concentration of electrons in the conduction band
$n_i$	Concentration of trapped electrons
$n_j$	Concentration of trapped holes in centres
$n_v$	Concentration of holes in the valence band
$s_i$	Frequency factor for electron traps

## *List of Abbreviations*

---

$s_j$	Frequency factor for hole centres
$t$	Time
<b>R</b>	Programming language
CB	Conduction band
$D_e$	Equivalent dose
DRT	Dose-recovery-test
FWHM	Full width at half maximum
GOT	General-one-trap model
$i$	Imaginary unit
ICP-MS	Inductively coupled plasma mass spectrometry
IR-RF	Infra-Red Radiofluorescence
$k$	Crystal wave vector
L-centre	Luminescence centre
LM-OSL	Linearly modulated optically stimulated luminescence
MAAD	Multi-aliquot additive-dose protocol
ODE	Ordinary Differential Equation
OSL	Optically stimulated luminescence
OTOR	One-trap-one-recombination-centre model
PHPT	Preheat-plateau-test
R-centre	Reservoir centre
RF	Radiofluorescence, synonym to Radioluminescence (RL)
RL	Radioluminescence
RT	Room temperature
SAR	Single-aliquot regenerative-dose protocol
SEM	Scanning electron microscope
TAC	Thermal activation characteristics
TL	Thermoluminescence
TSL	Thermally stimulated luminescence
UV	Ultra violet
VB	Valence band

XXX

# 1 Synopsis

## 1.1 Introduction

### 1.1.1 Numerical models in luminescence

The purpose of computing is insight,  
not numbers.

---

*Hamming (1962)*

To gain insight into the nature of unknown effects is as old as mankind itself. In 1663 Sir Robert Boyle reported to the Royal Society of London an experiment where he held a piece of diamond “near the Flame of a Candle, till it was qualify’d to shine pretty well in the Dark” (Boyle 1664). Nowadays this phenomenon is known as thermoluminescence but it was already described in the seventeenth century. Nevertheless, the term *luminescence* was first introduced by Wiedemann (1889) two centuries later. The physics behind luminescence phenomena (e.g., phosphorescence or fluorescence) was unclear because a complete understanding of these phenomena requires basic concepts of quantum mechanics, which was not established until the early years of the twentieth century (Marfunin & Schiffer 1979; Yukihiro & McKeever 2011). The findings of quantum mechanics changed the understanding of atoms and subatomic particles completely and gave explanations of observations done in the centuries before. This represented an enormous progress in very different contexts and applications. Subsequently the development of different devices was a direct consequence of the findings from quantum mechanics, e.g., lasers, transistors, and so the microchip, to name a few examples. Electronic devices revolutionised science and measurements had been performed with an accuracy and complexity such as never before. One of these inventions was the photomultiplier which played an important role in the application of luminescence phenomena because it offers the possibility to detect light very sensitively (Aitken 1985; Hine & Brownell 2013). An application related to this technical development was the use of the luminescence phenomenon as age determination tool for archaeology and geology. For that purpose many measurement protocols were developed in order to find the accumulated dose stored in a mineral to finally calculate an age (e.g., for pottery or the last deposit of sediments (Aitken 1985, 1998)).

With a mathematical description of the processes taking place in luminescence phenomena another field came into play: numerical methods. Due to the complex interaction in quantum mechanical systems the solutions of even simple models can not be solved analytically and

numerical solutions are needed. The development of more precise and faster numerical algorithms for more complex systems goes hand in hand with the increase of computation power in the twentieth century (Gear & Skeel 1987). Starting by Randall & Wilkins (1945) with one differential equation to Halperin & Braner (1960), who developed a system of three differential equations describing the TL process, and with even more allowed transitions of charge carriers (Bräunlich & Scharmann 1966) the development of theoretical luminescence models is visible. First these equations were solved analytically by making assumptions but in the 1970s and 80s the first numerical solutions appeared by Bull et al. (1986), Chen et al. (1981, 1984), Kelly et al. (1971), and McKeever et al. (1985a).

Much more detailed insights into the behaviour of the complex luminescence process was gained by numerical solutions in the last few decades. With increasing number of publications concerning luminescence measurements or new developments as new dating protocols (e.g., the SAR protocol (Murray & Wintle 2000) or the IR-RF technique (Krbetschek & Trautmann 2000; Trautmann et al. 1998, 1999)) the need for numerical solutions is unbroken to further explain luminescence behaviour.

### 1.1.2 Aims of this thesis

The development of the energy band model in quantum mechanics was a breakthrough and the foundation of many explanations concerning luminescence. The system of equations to solve for explaining charge carrier transport in crystals is long known and the phenomena explained range from TL (Randall & Wilkins (1945)) to complex OSL processes, e.g., TT-OSL (thermally-transferred OSL (Pagonis et al. 2008a)). During the past decades many different parameter sets for many different quartz luminescence effects were published until Bailey (2001) published a comprehensive quartz model which is able to simulate many known measurement protocols and quartz phenomena, especially TL and OSL. Bailey (2001) also showed that the suggested model is able to simulate luminescence during irradiation with ionizing particles (radioluminescence (RL) or radiofluorescence (RF)) but no comparison to real measurement data has been given. In 2002, Bailey published a new measurement protocol including RF as correction for sensitivity changes in the most commonly used dating protocol, the single-aliquot regenerative-dose (SAR) protocol (Murray & Wintle 2000). Nevertheless, an experimental proof as well as comparisons between numerical solutions of RF and experimental data are still missing.

The objective of this thesis is to close the gap between missing quartz RF experiments and the integration of the results of these experiments into existing quartz models. This thesis is part of the DFG project SCHM 3051/4-1 “*Modelling quartz luminescence signal dynamics relevant for dating and dosimetry - Towards a generalised understanding of radiofluorescence signal dynamics*”. One problem of comparing RF experiments and simulations was the fact that only custom-built instruments were able to record luminescence during irradiation with ionising radiation. Since the progress in radiofluorescence dating of feldspar (IR-RF), two manufacturers (*Risø* and *Freiberg Instruments*) offer RF attachments for their measurement

devices. Since then a huge variety of RF experiments can be carried out, so it appears overdue to fathom the potentials of quartz RF and to integrate it into a model concept. The late development of common luminescence measurement equipment for RF is one of the reasons investigating fundamental RF behaviour and compare it to model predictions in this thesis. The main questions to be solved here are:

1. How could existing models be re-evaluated and modified to be at least able to reproduce results from RF experiments?
2. How are different modifications and types of quartz ( $\alpha$ -,  $\beta$ -quartz, quartz from different geological and geographical origin) represented in the model?
3. Is there a way to vary input parameters of the model to be able to easily reproduce luminescence behaviour of various quartz samples?
4. Can an open source software package be developed to enable model predictions for a wide range of the luminescence community?
5. Can RF be used to obtain a higher accuracy of luminescence dating (through elimination of systematic errors in the dating procedure) and, hence, progress in Quaternary geochronology?

### 1.1.3 Outline of this thesis

In the following the relationship between the chapters in this thesis is given.

**Chapter 1** gives an overview of the development of models for luminescence production, especially the development of the energy band model used in quartz luminescence simulations. Subsection 1.7 also summarises the main results of the thesis.

**Chapter 2** builds the base for the modelling work within this project. With the developed **R**-package *RLumModel* it is possible to simulate quartz luminescence in an elaborated framework. Within this study many examples of known quartz luminescence phenomena are given. Different already published numerical models are included and facilitate the usage.

**Chapter 3** shows the first successful simulations of experimentally obtained UV-RF results. Basic behaviour of different quartz samples after different preheat temperatures were analysed. An explanation for the strong decrease of the initial UV-RF signal after 550 °C was given by numerically investigating the concentration of charge carriers in different energy levels. Furthermore, the interrelationship of the initial signal in quartz UV-RF signals on the burial dose was investigated.

In order to better understand the signal dynamics in quartz UV-RF, **Chapter 4** describes the derivation of analytical solutions for a simple three-energy-level model. These results are compared with numerical solutions of the problem. With these findings a fitting function for quartz UV-RF was developed and compared with experimental data. Furthermore, the behaviour of the initial signal and the slope of the UV-RF curve were analytically derived for different degrees of filled energy levels.

In **Chapter 5** further analysis of basic behaviour of quartz RF was conducted by irradiating quartz samples with different dose rates and recording RF spectra. The theoretical findings of Chapter 4 are proved experimentally and numerical simulations are used to simulate the dose rate effects. In addition, a first concept of using UV-RF for a dosimetric application is given.

Further applications of quartz RF are given in **Chapter 6**: Two known quenching processes in quartz were investigated with UV-RF. A simple measurement protocol determining important thermal quenching parameters is given and compared with values from literature. A comparison between UV-OSL/TL with UV-RF signals is executed to better understand the phenomena of dose quenching.

**Chapter 7** investigates the effect of illuminating quartz with far UV light. Radiofluorescence offers a more direct view to hole transfers in the electronic system of quartz and the known effect of UV-reversal is investigated more directly than before. The interplay between annealing and UV illumination is shown by analysing the UV-RF signal of quartz.

Further results of the project are given in Chapter 8. **Subsection 8.1** describes the recuperation of the UV-RF signal after different storage times. These results are important for **subsec. 8.2**, which describes the possibility for using UV-RF as dosimetric application. These investigations are explained in detail, summarised, and finally the results of dose recovery tests for different applied doses are presented.

Additional findings regarding the development of numerical luminescence models are presented in **subsec. 8.3**. Here a technique called *inverse modelling* is introduced in luminescence modelling. This method makes it possible to fit model parameters with experimentally obtained data. Further analysis tools like local and global sensitivity analyses are presented and tested. The technique is applied on TL and OSL curves and the results from the simulations with fitted parameters are in accordance with experimental data. **Subsection 8.4** introduces another method to calculate RF signals numerically. The idea is to use clusters of electron-hole pairs and calculate the RF signal statistically with *Monte-Carlo* methods instead of solving sets of ODEs numerically. The results from this new method are compared with the classical approach.

## 1.2 Energy levels in solids

### 1.2.1 Energy levels in a perfect crystal

Ionic crystals were the first solids analysed for crystal form and elastic properties. Born (1926) executed experiments with X-rays and, assuming the crystal to be built up of positively and negatively charged ions, gave first values of their lattice energies and elastic properties (Mott & Gurney 1940). The smallest unit of a crystal is a *primitive cell* and identical primitive cells form the periodicity of the crystal lattice when joining them together. As a consequence, an *ideal crystal* is an object of infinite length (Madelung 2012). Schrödinger (1926) developed, after lots of preliminary studies, a schema to handle the

electron system in crystalline materials, the *Schrödinger equation*. The time-independent Schrödinger equation (1.1) describes the movement of a single particle in an electric field.

$$\left[ \frac{\hbar^2}{2m} \nabla^2 + V(\mathbf{r}) \right] \Psi(\mathbf{r}) = E\Psi(\mathbf{r}) \quad (1.1)$$

$\hbar$  is the reduced Planck constant ( $\hbar = \frac{h}{2\pi}$ ),  $m$  is the particle's reduced mass,  $\nabla^2$  is the Laplacian,  $V$  is the potential energy,  $\Psi$  is the wave function of the quantum system,  $\mathbf{r}$  is the position vector and  $E$  is a constant equal to the total energy of the system. Based on Eq. (1.1), Bloch (1929) developed the theorem that the wave function solution from Eq. (1.1) in a periodic crystal lattice is given by:

$$\Psi_{\mathbf{k}}(\mathbf{r}) = u_{\mathbf{k}}(\mathbf{r}) \cdot \exp(i\mathbf{k} \cdot \mathbf{r}) \quad (1.2)$$

Here  $u_{\mathbf{k}}(\mathbf{r})$  is the Bloch function with the same spatial periodicity as the crystal.  $\mathbf{k}$  is the crystal wave vector and  $i$  the imaginary unit. Summing up, Eq. (1.2) says that multiplying a plane wave with a periodic function results in a Bloch wave (Kittel 2005; Madelung 2012).

Assuming the simplest case, a one-dimensional periodic lattice with ions distance  $a$ , mass of the particle  $m$  and length of the potential  $b$  results directly in the existence of band gaps. This model is called *Kronig-Penney model* (Kronig & Penney 1931) and the solution for that model are given in the following. The model can even be more simpler if the potential  $V$  is zero except at atomic sites, where it is infinity, or in other words: the peaks in the potential are delta functions. Kronig & Penney (1931) found a solution using a Bloch function with the side condition that Eq. (1.3) is true.

$$\cos(ka) = \cos(k_0a) + \frac{P}{k_0a} \cdot \sin(k_0a) \quad (1.3)$$

In Eq. (1.3)  $P = \frac{mVba}{\hbar^2}$  and  $k_0^2 = \frac{2m|E|}{\hbar^2}$ . Note that in Eq. (1.3) not every value for  $k_0a$  gives a solution to the left-hand side of the equation. The expression  $\cos(ka)$  has to be in the range of -1 and 1. Figure 1.1 shows the right-hand side of Eq. (1.3) for a fixed value of  $P = 3\pi/2$ , as suggested in the original publication by Kronig & Penney (1931). The coloured regions show the parts in which the right-hand side of Eq. (1.3) lies between -1 and 1. These regions are called the *allowed* region because a real solution exists. From Fig. 1.1 it can be concluded that the forbidden regions become narrower as the value of  $k_0a$  becomes larger. Another fact is that if  $P$  vanishes (which in turn means that the potential  $V$  is zero) the forbidden zones disappear and a continuous spectrum of all energies from 0 to  $\infty$  is allowed. This is the case for free electrons. The other extreme is that  $P$  approaches infinity. This corresponds to an isolated atom with infinity distance to the next neighbour (Hummel 2011).

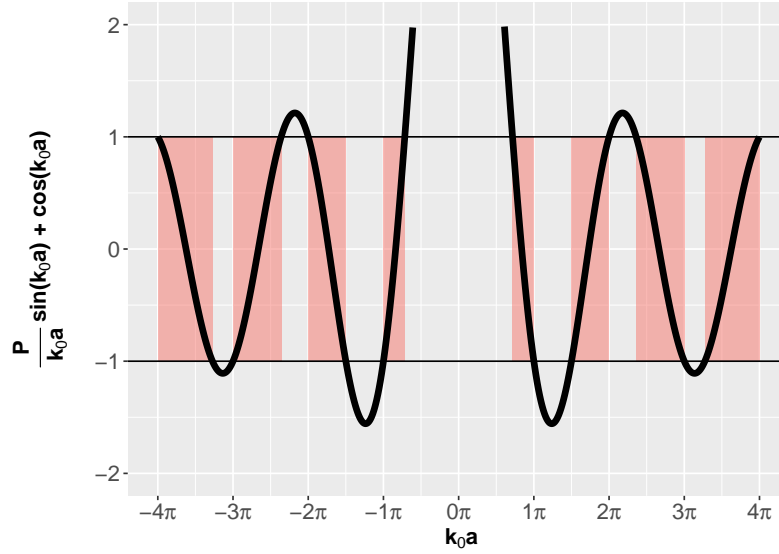


**Figure 1.1:** Right-hand side of Eq. (1.3) plotted against  $k_0 a$  for  $P = 3\pi/2$ . The marked regions are regions of  $k_0 a$  for which  $k$  can be calculated. So this is called an *allowed* region. Note that the forbidden regions become narrower as the value of  $k_0 a$  becomes larger.

Note that in Eq. (1.3) the relationship between  $E$  and  $k$  is given because on the right-hand side of Eq. (1.3)  $k_0$  is related to  $E$  via  $k_0^2 = \frac{2m|E|}{\hbar^2}$ . Solving this relation and plotting the electron density of states (Fig. 1.2) shows the existence of forbidden zones, where the density for electron states is 0. The zones between are called *bands*. When filling up the allowed states, according to Pauli's exclusion principle, until all available electrons are accommodated, the Fermi energy  $\epsilon_F$  defines the energy of the topmost filled level in the ground state ( $T = 0$  K) of the system (Kittel 2005). The valence band is defined as the closest band which is filled with electrons at  $T = 0$  K. In contrast to that the conduction band is the lowest energy level with no electrons. The band gap is the difference between the lowest point of the conduction band (conduction band edge) and the highest point of the valence band (valence band edge, see Fig. 1.3). When the temperature increases it is possible that electrons from the valence band are excited to the conduction band and the material is electrically conductive (Kittel 2005). The probability that an energy state will be occupied in thermal equilibrium is given by the Fermi-Dirac distribution. It is worth noting that when an energy gap between the valence and conduction band exists, the Fermi level must be exactly in the middle of the gap when  $T = 0$  K (Swendsen 2012). With this definition a distinction between different electrical properties is possible (Enderlein & Horing 1997):

1. **Insulator:** In terms of the above written context, an insulator is a material with a large high band gap ( $> 3.5$  eV) and the Fermi level lies in the band gap.
2. **Semiconductor:** The Fermi level also lies in the band gap but is near enough to the valence and conduction band to get thermally populated by electrons.
3. **Conductor:** The Fermi level lies within the conduction band.

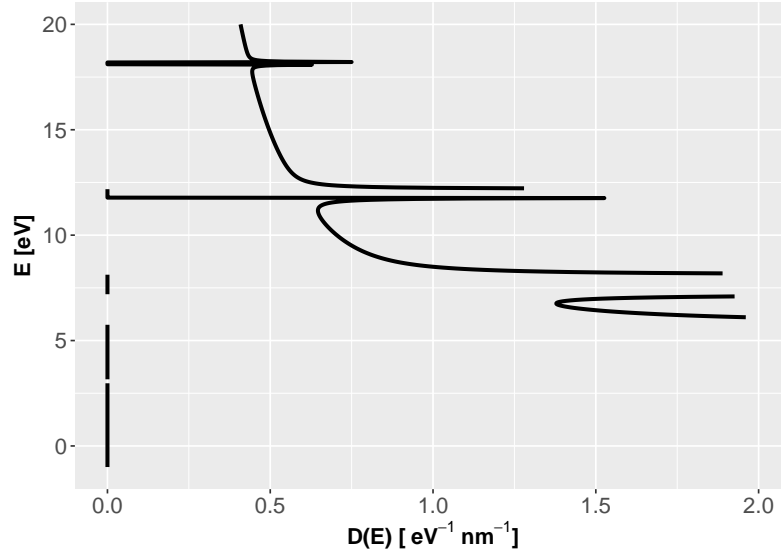


**Figure 1.2:** Electron density of states for the Kronig-Penney model. Note the values of 0 for  $D(E)$ . The used input values are:  $V = 5 \text{ eV}$ ,  $a = 1.5 \text{ E-10 m}$ ,  $b = 5 \text{ E-10 m}$  and  $m = 9.1 \text{ E-31 kg}$ .

When an electron gets excited into the conduction band it is leaving behind an unoccupied state. Instead of dealing with electrons in the valence band, it is easier dealing with missing electrons in an almost full valence band. These missing electrons are called *holes* and are quasi particles. Holes in the valence band behave like freely mobile positive charge carriers (Enderlein & Horing 1997). This concept will be important when describing different effects in semiconductors or insulators.

Since we are dealing with a natural material, the perfect crystal lattice is just an oversimplification of the real crystal lattice. Figure 1.3 summarises the findings from the ideal crystal: For  $T = 0 \text{ K}$  (subfig. (a)) all electrons are in the valence band with the maximum energy  $E_V$ . The next band is the conduction band with energy  $E_C$ .  $E_F$  is the Fermi level and exactly in the middle of  $E_V$  and  $E_C$ . The difference  $E_G = E_C - E_V$  is the band gap energy. If the temperature is higher than  $0 \text{ K}$ , some electrons are able to reach the conduction band and they leave behind a hole in the valence band (subfig. (b)). Note that thermally overcoming  $E_G$  is not possible for insulators. The example describes a semiconductor, e.g., Si or Ge.

### 1.2.2 Energy levels in real crystals

In an ideal crystal an electron in the conduction band can move freely throughout the whole crystal because every positive ion offers a position of exactly equal energy. The same is true for a hole in the valence band. But any irregularity in the lattice (see Ch. 1.3) will lead to a modification of the perfect crystal lattice (Mott & Gurney 1940). The effect of impurities in a crystal lattice can be enormous: 1 boron atom to  $10^5$  silicon atoms increases the conductivity of pure silicon at room temperature by a factor of  $10^3$  (Kittel 2005).

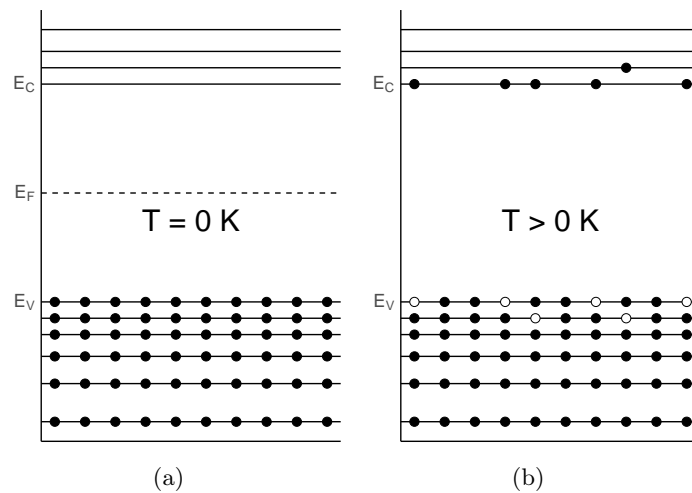


**Figure 1.3:** Subfigure(a) shows the energy band of an ideal semiconductor for  $T = 0 \text{ K}$ . All electrons occupy the valence band with energy  $E_V$ . The band gap between  $E_V$  and  $E_C$  (energy of the conduction band) divides the valence from the conduction band. Increasing the temperature leads to a redistribution of electrons according to the Fermi-Dirac distribution and some electrons are able to reach the conduction band. Figures modified and redrawn after Enderlein & Horing (1997).

Introducing impurities in a crystal lattice can be followed by the appearance of local levels in the band gap (doping). The reason is a change in the potential energy given in Eq. (1.1). The potential energy  $V(\mathbf{r})$  changes to  $V(\mathbf{r}) + V'(\mathbf{r})$ . The second term differs from zero in a particular volume close to the defect. Nevertheless, this again is an oversimplification because impurities are distributed chaotically in space in natural materials (Gribkovskii 1998).

Depended on the impurity, new energy levels above or below the Fermi level will be created. Continuing the example from the beginning of the section, doping silicon with boron (group III element) will lead to a new energy level in the forbidden zone just above the valence band. Due to the fact that boron has three valence electrons, the boron in the silicon lattice can catch an additional electron. This in turn means that a hole is migrating in the valence band because the holes move in the opposite direction of the electrons. This kind of dopants is called *acceptors*.

Bringing a group V element into the silicon crystal lattice will lead to the opposite effect: Four outer electrons of, e.g. phosphorus, combine with the silicon atoms and the remaining electron can move throughout the crystal lattice. This kind of dopants is called *donors* and they give rise to new energy bands near the conduction band (Bräunlich et al. 1979; Enderlein & Horing 1997; Kittel 2005). Figure 1.4 summarises these concepts. In contrast to the ideal crystal from Fig. 1.3 now energy levels in the forbidden zone appear and act as traps for electrons and/or holes. These traps can hold electrons and holes for a fairly long time, even geological times. This is very important for geological applications and will be discussed later. The causes for lattice defects are manifold and will be explained in detail

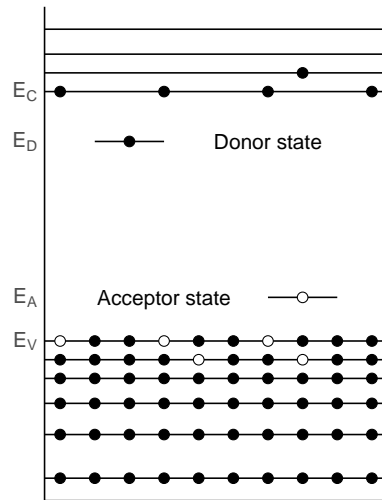


**Figure 1.4:** Schematic energy band model for a crystal lattice with impurities.  $E_V$  is the energy of the valence band,  $E_C$  the energy of the conduction band,  $E_D$  the energy of the donors and  $E_A$  the energy of the acceptors.

for quartz in Sec. 1.3.

### 1.3 Defects in quartz

Silica ( $\text{SiO}_2$ ) in crystalline and non-crystalline (amorphous) form makes up 12.6 wt% of the Earth's crust and hence is the second-most abundant mineral after feldspar (Götze 2012b; Preusser et al. 2009). Quartz is the most prominent phase of  $\text{SiO}_2$  and exists in two different forms:  $\alpha$ - (low temperature) and  $\beta$ - (high temperature) quartz. Under surface conditions ( $\sim 20^\circ\text{C}$  and 105 kPa)  $\alpha$ -quartz is the stable form. When heating above  $573^\circ\text{C}$   $\alpha$ -quartz transforms to  $\beta$ -quartz.

The basic structure of  $\alpha$ -quartz is built from  $\text{SiO}_4$  tetrahedra which are linked by sharing each of their corners (Preusser et al. 2009).  $\alpha$ -quartz has no centre of symmetry and together with its anisotropy it gives rise to the piezoelectric effect. Anisotropy is just one cause which can destroy the perfect crystal lattice. When the extension of the defect is limited to a few interatomic distances, it is treated as zero-dimensional defect and is called *point defect* (Benz & Neumann 2014). Further the distinction between *intrinsic* and *extrinsic* is used. Extrinsic defects are incorporations of foreign ions in the lattice and interstitial positions. Intrinsic defects are displaced atoms, and/or defects associated with silicon or oxygen vacancies (Götze 2012b). In summary more than 20 different types of point defects have been detected in quartz during the last few decades (Götze 2012a). Figure 1.5 gives an overview about the most common point defects in quartz. The  $[\text{AlO}_4]^0$  centre is the most common trace-element related defect centre in quartz. This centre is the result of the substitution of  $\text{Si}^{4+}$  by  $\text{Al}^{3+}$  and an electron hole is created. Other types of defects in quartz are small interstitial ions (Li, Na, H) that can move along the c-axis channels, e.g.,

$\text{Li}^+$  in Fig. 1.5 (Preusser et al. 2009). These interstitial ions form the diamagnetic centre  $[\text{AlO}_4/\text{M}^+]^0$ .  $M$  is a placeholder for different interstitials, e.g.,  $\text{Li}^+$ ,  $\text{Na}^+$ ,  $\text{H}^+$ .

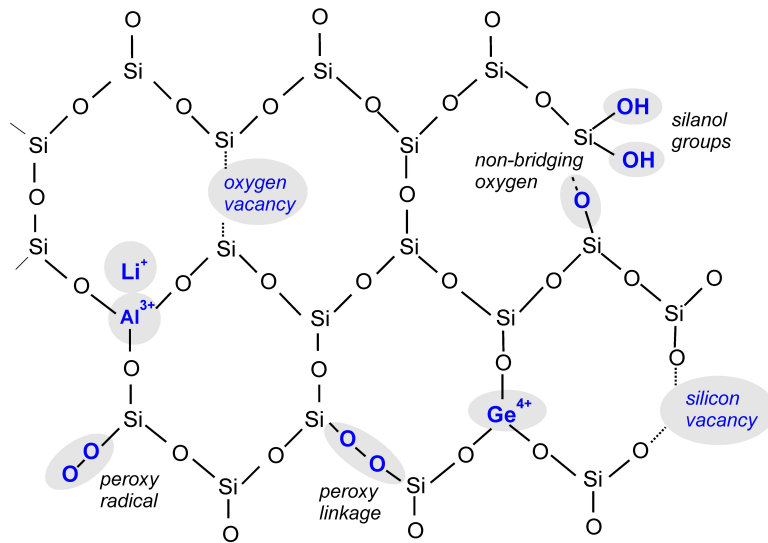


**Figure 1.5:** Schema of most common point defects (from Götze (2012b)).

It was shown that gamma- or X-ray irradiation can cause the transformation from  $[\text{AlO}_4/\text{M}^+]^0$  to  $[\text{AlO}_4]^0$  and forms smoky quartz (Götze 2012b). Other types of defects are connected to vacancies either of oxygen or silicon. Many more defects are known but will be not described here in detail. As mentioned in Sec. 1.2.2, every defect causes a disturbance of the potential energy of a perfect crystal lattice and local levels in the band gap are formed. Different defects are connected to specific energy levels in the band gap which can emit light during excitation with a stimulus (see Sec. 1.4). Table 1.1 gives an overview of luminescence emissions bands in quartz and the related defects. Several defects can be attributed to oxygen and silicon vacancies, e.g., the so-called *neutral O vacancy*, which is the removal of an O atom. At this defect a hole can be trapped and an  $E'$  centre arises. In Sec. 1.5.3 the specific emission during radiofluorescence are described in more detail.

A detailed overview of quartz defects can be found in the works by Götze (2009, 2012a,b), Krbetschek et al. (1997), Marfunin & Schiffer (1979), and Preusser et al. (2009), and references therein.

EMISSION [nm]	EMISSION [eV]	SUGGESTED ACTIVATOR
175	7.3	Intrinsic emission of pure SiO <sub>2</sub>
290	4.28	Oxygen vacancy (E' centre)
330 – 340	3.75 – 3.6	Oxygen vacancy (E' centre) [AlO <sub>4</sub> /Li <sup>+</sup> ] centre [TiO <sub>4</sub> /Li <sup>+</sup> ] centre
380 – 390	3.2 – 3.1	[AlO <sub>4</sub> /M <sup>+</sup> ] centre (M <sup>+</sup> = Li <sup>+</sup> , Na <sup>+</sup> , H <sup>+</sup> ) [H <sub>3</sub> O <sub>4</sub> ] <sup>0</sup> hole centre
450	2.8	E' centre with self-trapped exciton
500	2.45	Extrinsic emission Interstitial impurity cations (Li <sup>+</sup> , Na <sup>+</sup> , H <sup>+</sup> ) [AlO <sub>4</sub> ] <sup>0</sup> , [GeO <sub>4</sub> /M <sup>+</sup> ] <sup>0</sup> centre
580	2.1	Oxygen vacancy (E' centre)
620 – 650	1.97 – 1.91	Non-bridging oxygen hole centres with several precursors
705	1.7	Substitutional Fe <sup>3+</sup>
1280	0.97	Interstitial molecular O

**Table 1.1:** Luminescence emission bands in quartz and related defects. Modified after Götze (2012a) and Krbetschek et al. (1997).

## 1.4 Describing luminescence phenomena

Chen & McKeever (1997) give a definition of luminescence:

Luminescence is the emission of light from a material following the initial absorption of energy from an external source.

The initial excitation can occur by a variety of sources and so different names for different luminescence phenomena exist (Chen & McKeever 1997; McKeever 1988; Nasdala et al. 2004; Sunta 2014), e.g.,

- Photoluminescence: Excited by the absorption of light
- Cathodoluminescence: Excited by the absorption of energy from an electron beam
- Radioluminescence: Excited by the absorption of nuclear energy ( $\alpha$ -,  $\beta$ -,  $\gamma$ - or X-rays)
- Electroluminescence: Excited by the absorption of electrical energy
- Chemiluminescence: Excited by the absorption of chemical energy
- Bioluminescence: Excited by the absorption of biochemical energy
- Triboluminescence: Excited by the absorption of mechanical energy
- Sonoluminescence: Excited by the absorption of sound waves

The perhaps most famous luminescence phenomenon is *thermoluminescence* (TL) but heating is not the main energy source of the emitted light. The initial excitation is typically given by irradiation with ionising radiation. Therefore, the term *thermally stimulated luminescence* (TSL) would be more appropriate but for historical reasons the term TL is more popular (Chen & McKeever 1997). For OSL (optically stimulated luminescence) the term is more appropriate because here the initial excitation is also the irradiation

with ionising radiation. Due to the historical development of the quantitative description of luminescence, the following section introduces the development of the mathematical description of luminescence for TL. This is done by showing the development of luminescence models in general. In Sec. 1.5 a detailed look at RF is given.

### 1.4.1 Mathematical description of luminescence

In this section equations for describing the thermoluminescence phenomena mathematically will be presented. Therefore the findings from Sec. 1.2 are continued and further simplified to describe them mathematically.

One helpful definition is the differentiation between *electron trap*, *hole trap* and *recombination centre*. For that reason an important definition is given by Bräunlich et al. (1979): demarcation levels. Demarcation level  $E_{D_n}$  is the energy for electrons at which the electron has equal probability of being thermally released into the conduction band or recombining with a free hole. The same concept can be used for holes and  $E_{D_p}$  can be defined as the energy level at which the thermal release of a hole is equal to the recombination with an electron. All energy levels between  $E_{D_n}$  and  $E_C$  are called electron traps. Hole traps are defined as the energy states between  $E_{D_p}$  and  $E_V$ . All states between  $E_{D_n}$  and  $E_{D_p}$  are recombination centres for electrons and holes (see Fig. 1.6). This does not imply that no electrons can transit into a hole trap, or a hole into an electron trap because this nomenclature is just based on probabilities. It can be summarised that the energy levels for recombination centres are located in the middle of the forbidden zone. It is further pointed out, that a recombination centre at low temperatures can become a trapping centre at higher temperatures (Yukihara & McKeever 2011). Further assumptions and simplifications are (following Chen & McKeever (1997)):

- All transitions into or out of localized states are going via the valence (for holes) or conduction band (for electrons). So no direct transfer (tunnelling) of charge between electron trap and recombination centre is allowed.
- All transitions of electrons from the conduction band into electron traps are non-radiative, emitting phonons. The same is true for holes from the valence band to hole traps.
- Transitions of free electrons from the conduction band to trapped holes in recombination centres or from free holes to trapped electrons in electron traps are radiative and hence emitting photons.
- A freed charge can not distinguish between its primary trap and all other traps of the same type.

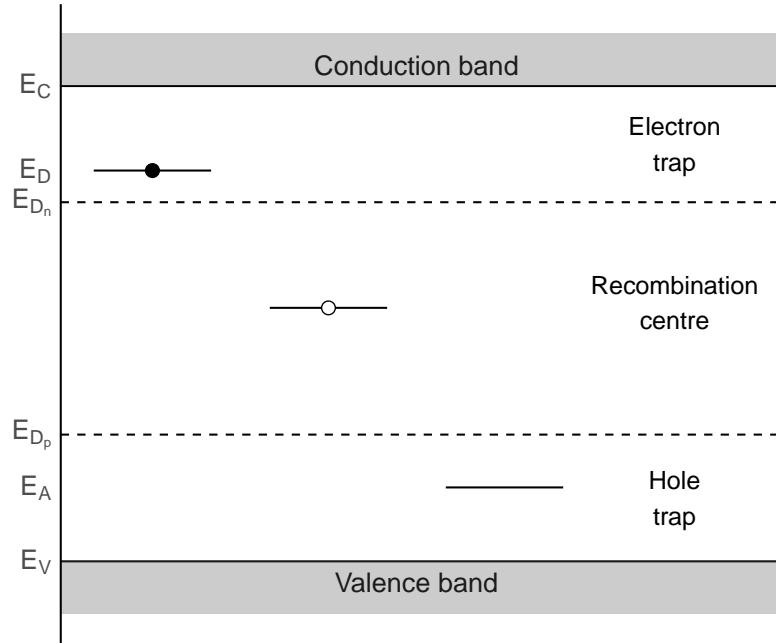


**Figure 1.6:** Schematic energy band model with demarcation levels and definition of electron trap, hole trap and recombination centre. Filled dots illustrate electrons and open dots holes.

Following the historical development of luminescence models, starting with a very simple *one-trap-one-recombination-centre* (OTOR, also called *general one trap* (GOT)) model (see Fig. 1.7; arrows indicate allowed transitions), will lead to ordinary first-order coupled differential equations (1.4) to (1.7).

$$\frac{dn_c}{dt} = p \cdot n - n_c \cdot (N - n) \cdot A_n - n_c \cdot m \cdot B \quad (1.4)$$

$$\frac{dn_v}{dt} = 0 \quad (1.5)$$

$$\frac{dn}{dt} = -p \cdot n + n_c \cdot (N - n) \cdot A_n \quad (1.6)$$

$$\frac{dm}{dt} = -n_c \cdot B \cdot m \quad (1.7)$$

The intensity of the simulated signal is equal to  $-\frac{dm}{dt}$ .  $N$  is the total concentration of traps and  $n(t)$  the concentration of filled traps at time  $t$ .  $n_c(t)$  ( $n_v(t)$ ) is the concentration of electrons (holes) in the conduction (valence) band. Parameter  $A_n$  is the probability of an

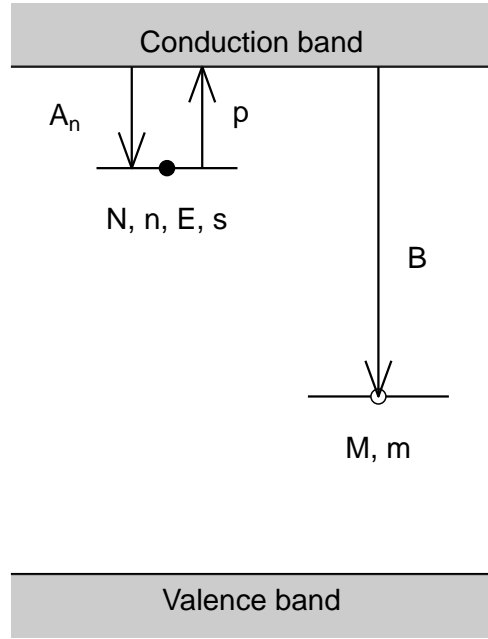


**Figure 1.7:** Schematic energy band of the OTOR model with one electron trap and one recombination centre. The corresponding values for recombination centre and electron trap are given as well as the allowed transitions (arrows).

electron in the conduction band captured by an electron trap and  $A_m$  for being captured by a trapped hole in the recombination centre. Parameter  $m(t)$  describes the concentration of filled traps at time  $t$  and  $B$  is the probability of an electron in the conduction band captured by a hole centre. The probability of being thermally or optically freed is summarised in the parameter  $p$  and has to be specified by the stimulation type.

Due to the fact that TL was the phenomenon analysed in depth in the last decades, the next passage will follow the historical development of the solution of Eqs. (1.4) to (1.7). One major assumption made to derive an analytical solution is the so called *quasi-equilibrium* approach. This assumption ensures that all excited charge carriers (electrons or holes) relax instantly into their traps or recombination centres. The mathematical expression is given in Eq. (1.8). More details can be found in Chen & McKeever (1997) and Sunta (2014).

$$\frac{dn_c}{dt} \ll \frac{dn}{dt} \quad \text{and} \quad n_c \ll n \quad (1.8)$$

Randall & Wilkins (1945) were the first publishing an analytical solution of the OTOR model with the assumptions made before and with the restriction of no retrapping ( $A_n = 0$ , *first-order kinetics*). In case of TL  $p$  can be replaced with  $s \cdot \exp\left(-\frac{E}{k_B T}\right)$  and one yields Eq. (1.9).

$$I_{TL} = n \cdot s \cdot \exp\left(\frac{-E}{k_B T}\right) \quad (1.9)$$

$E$  is the thermal trap depth of the electron trap,  $s$  the frequency factor (a constant describing the attempts to escape per second; usually in the range  $10^9$  to  $10^{16} \text{ s}^{-1}$ ),  $k_B$  is Boltzmann's constant and  $T$  the absolute temperature. Temperature  $T$  is connected to time  $t$  via the heating rate  $\beta = \frac{dT}{dt}$ . Solving Eq. (1.4) to (1.7) with the above mentioned approximations leads to the well-known *Randall-Wilkins* first-order expression for  $I_{TL}$ :

$$I_{TL} = n_0 s \exp\left(\frac{-E}{k_B T}\right) \exp\left\{\frac{-s}{\beta} \int_{T_0}^T \exp\left(\frac{-E}{k_B \Theta}\right) d\Theta\right\} \quad (1.10)$$

, where  $n_0$  is the initial value of  $n$  at  $t = 0$  and  $\Theta$  is a dummy variable representing the temperature.  $T_0$  is the temperature at the beginning of the heating run, and  $T = T_0 + \beta \cdot t$  (Chen & McKeever 1997; Randall & Wilkins 1945; Sunta 2014). With Eq. (1.10) it was possible to describe several phenomena of the TL glow curve. Due to the fact that TL glow curves are not the main focus of this thesis, the reader is referred to literature given in this section.

In 1948 Garlick & Gibson presented solutions for the case of allowed retrapping,  $A_n/B = 1$ . Analysing this expression, along with  $N \gg n$  and  $n = m$ , yields:

$$I_{TL} = \frac{n_0^2}{N} s \exp\left(\frac{-E}{k_B T}\right) \left[1 + \frac{n_0 s}{\beta N} \int_{T_0}^T \exp\left(\frac{-E}{k_B \Theta}\right) d\Theta\right]^{-2} \quad (1.11)$$

Due to  $I_{TL} \propto n_0^2$  this kinetics is called *second-order kinetics*. Nevertheless, for both cases, first-order or second-order kinetics, special combinations of parameters have to be considered. May & Partridge (1964) published a solution of Eqs. (1.4) to (1.7) with no restrictions for the trapping to retrapping ratio, called *general-order kinetics*. This solution can be written as shown in Eq. (1.12). Note that this solution is just valid for  $b \neq 1$  and Eq. (1.11) (second-order kinetics) can be derived with  $b = 2$ . Figure 1.8 shows the solutions of Eqs. (1.10), (1.11), and (1.12) with the same parameters:  $N = n_0 = 1 \text{ E}+17 \text{ cm}^{-3}$ ,  $s = 1 \text{ E}+13 \text{ s}^{-1}$ ,  $\beta = 1 \text{ K s}^{-1}$  and  $E = 1 \text{ eV}$ . For the general-order kinetics,  $b = 1.5$  was used.

$$I_{TL} = n_0^b N^{1-b} s \exp\left(\frac{-E}{k_B T}\right) \left[1 + \frac{s(b-1)(n_0/N)^{b-1}}{\beta} \int_{T_0}^T \exp\left(\frac{-E}{k_B \Theta}\right) d\Theta\right]^{-\frac{b}{b-1}} \quad (1.12)$$

With the increase in computational power in the 70's it was possible to solve the coupled ODEs (1.4) to (1.7) numerically. Kelly et al. (1971) concluded from their numerical solutions, that the quasi-equilibrium condition (Eq. (1.8)) is valid for only a part of all physically meaningful parameters. They calculated an exact solution and obtained a wide range of possible TL peaks shapes and intensities.

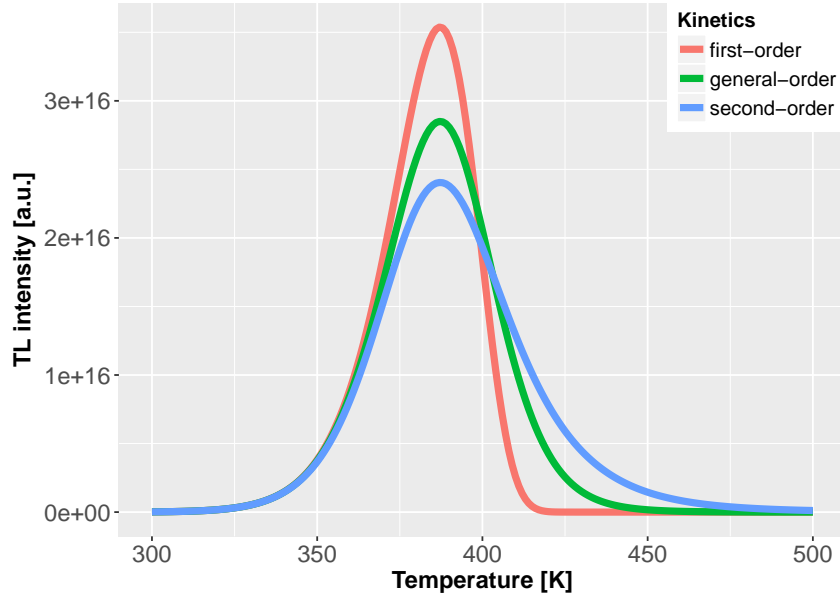


**Figure 1.8:** Comparison of different kinetic orders for the analytical solution in the case of TL. Used parameters:  $N = n_0 = 1 \text{ E}+17 \text{ cm}^{-3}$ ,  $s = 1 \text{ E}+13 \text{ s}^{-1}$ ,  $\beta = 1 \text{ K s}^{-1}$  and  $E = 1 \text{ eV}$ . For the general-order kinetics,  $b = 1.5$  was used.

Note that until now all given references used  $\frac{dn_v}{dt} = 0$ , which means that no hole transition is allowed. Furthermore, just one electron trap and one hole trap were included in the models. It is also possible to free electrons from the electron traps by optical stimulation and so parameter  $p$  in Eq. (1.6) is defined as  $p = \sigma \cdot \Phi$ , where  $\sigma$  is the photoionisation cross-section and  $\Phi$  the incident photon flux (Yukihara & McKeever 2011). Simulating irradiation processes (creation of electron-hole pairs), another parameter  $R$  is necessary, which describes the number of created electrons and holes per  $\text{cm}^3$  per s. Combining all these points will lead to a system of coupled differential equations with  $q$  electron traps and  $r$  centres (hole- and recombination centres), see Eqs. (1.13) to (1.16). Counting index  $i$  corresponds to electron traps and index  $j$  to hole centres. Examples can be found in Fig. 2.1 (ten electron traps, four centres) or Fig. 4.1 (one electron trap, two centres).

$$\frac{dn_i}{dt} = n_c \cdot (N_i - n_i) \cdot A_i - n_i \cdot \sigma \cdot \Phi - n_i \cdot s_i \cdot \exp\left(\frac{-E_i}{k_B \cdot T}\right) \quad (1.13)$$

$$\frac{dn_j}{dt} = n_v \cdot (N_j - n_j) \cdot A_j - n_j \cdot s_j \cdot \exp\left(\frac{-E_j}{k_B \cdot T}\right) - n_c \cdot n_j \cdot B_j \quad (1.14)$$

$$\frac{dn_c}{dt} = R - \sum_{i=1}^q \left(\frac{dn_i}{dt}\right) - \sum_{j=q+1}^{q+r} (n_c \cdot n_j \cdot B_j) \quad (1.15)$$

$$\frac{dn_v}{dt} = R - \sum_{j=q+1}^{q+r} \left( \frac{dn_j}{dt} \right) - \sum_{j=q+1}^{q+r} (n_c \cdot n_j \cdot B_j) \quad (1.16)$$

Note that Eqs. (1.13) to (1.16) are in principle the same equations as Eqs. (1.4) to (1.7) but with an arbitrary number of electron and hole traps and simultaneous optical and thermal stimulated release of electrons. In contrast to models with no allowed hole transitions, the luminescence signal can no longer be described by the change of concentration of holes in time. The signal intensity is now defined as  $n_c \cdot n_j \cdot B_j$ , where index  $j$  corresponds to a luminescence centre (see Sec. 1.6).

Nevertheless, not all recombined electron-hole pairs in luminescence centres give raise to the luminescence signal. There are radiative and non-radiative transitions with probabilities  $\Gamma_R$  and  $\Gamma_{NR}$ , respectively. This leads to the definition of an efficiency factor  $\eta$  (Yukihara & McKeever 2011):

$$\eta = \frac{\Gamma_R}{\Gamma_R + \Gamma_{NR}} \quad (1.17)$$

A strong temperature dependency was found affecting the luminescence signal, called *thermal quenching* (Gurney & Mott 1939; Wintle 1975). And so Eq. (1.17) modifies to:

$$\eta(T) = \left( 1 + K \cdot \exp\left(\frac{-W}{k_B \cdot T}\right) \right)^{-1} \quad (1.18)$$

$K$  is a dimensionless constant and  $W$  is the activation energy and both values depend on the measured luminescence centre and hence the emission band. In Sec. 1.5 a more detailed derivation of Eq. (1.18) is given. Finally, the efficiency corrected signal can be calculated via Eq. (1.19).

$$L = \eta(T) \cdot n_c \cdot n_j \cdot B_j \quad (1.19)$$

Not all parameters mentioned in Eqs. (1.13) to (1.16) are necessary in every single simulation step, because the excitation is different. The following list gives an overview of different excitation stimuli and their corresponding parameter values:

- Irradiation:  $R \neq 0$
- Illumination:  $\Phi \neq 0$
- Thermal stimulation:  $\beta = \frac{dT}{dt} \neq 0$

In principle it is possible to simulate different excitation stimuli simultaneously, e.g., illumination and heating or irradiation and heating.

Solving coupled ordinary differential equations led to an enormous knowledge explaining several phenomena, e.g., (list not exhaustive):

- TL phenomena: Bailey (2001), Chen & Fogel (1993), Chen et al. (2011, 2012), Chen & Pagonis (2013), and Pagonis et al. (2009b, 2011)
- OSL phenomena: Bailey (2001), Chen et al. (2009), Chruścińska (2009), Chruścińska & Przegiętka (2011), Chruścińska et al. (2017), Jain et al. (2015), Kijek & Chruścińska (2017), and Pagonis et al. (2007b, 2009b)
- Sensitivity changes: Adamiec et al. (2004), Bailey (2001), Chen et al. (1994), Chen & Leung (1999), Chen & Pagonis (2015), Kitis et al. (2006), Pagonis & Carty (2004), Pagonis et al. (2008b), and Subedi et al. (2010)
- Radioluminescence: Bailey (2001, 2002), Pagonis et al. (2009a), and Trautmann (2000)

A detailed overview presenting different luminescence simulations in great detail can be found in Chen & Pagonis (2011). Describing luminescence effects with the energy band model has been quite successful over the last few decades, especially since Bailey presented his comprehensive luminescence model for quartz in 2001. The parameters were very successful in describing a huge variety of effects and several cited publications used the parameters from Bailey (2001) or slightly modifications. Nevertheless, a problem with the energy band model is the large number of free parameters because no unique solution exists (Yukihara & McKeever 2011). An acceptable fit of different measurement data (e.g., thermal activation, OSL behaviour, high dose experiments) with numerical simulations can lead to the conclusion that the theory is consistent with experiments. “But this should not be mistaken as proof” (Bräunlich et al. 1979).

### 1.4.2 Alternative luminescence descriptions

There exist other approaches than the energy band model to describe luminescence production. One of them is the *defect pair model*, proposed by Itoh et al. (2001, 2002). As already mentioned in Sec. 1.3, natural quartz inherits impurities. Different studies have shown that distinct impurities give rise to distinct TL peaks or OSL (Guzzo et al. (2009, 2017), Martini et al. (2009, 2012b), McKeever et al. (1985b), Petrov & Bailiff (1995), and Vaccaro et al. (2017)). Itoh et al. (2001) combined these findings from literature and created a new description of luminescence. The most striking difference to the energy band model is the use of defect pairs rather than trapped electrons and holes. They successfully described the 110 °C and 325 °C peak and the OSL in quartz and they also explained the shift in wavelength of luminescence emissions between room temperature and 325 °C. A recent publication by Williams & Spooner (2018) also included the 160 °C and 220 °C TL peak and extended the existing model. Nevertheless, as already mentioned by Chen & McKeever (1997), this model can just explain first order behaviour, which is true for the 110 °C and 325 °C TL peak in quartz, but not found for the 375 °C TL peak (Preusser et al. 2009). A detailed overview of TL and OSL behaviour linked to specific defects and a detailed description of the defect pair model is given in Preusser et al. (2009).

Another alternative approach is the use of *Monte-Carlo* simulations instead of solving ODEs numerically. Some authors mentioned that the energy band model is not able to simulate spatial correlations between traps and recombination centres (Mandowski & Świątek 1992, 1994). In the approach by Kulkarni (1994) and Mandowski & Świątek (1992) just one of the three allowed transitions (I) freeing an electron to the conduction band, (II) trapping of an electron or (III) recombination are allowed in a specific time step. Monte-Carlo simulations are performed with the total population of carriers simultaneously and the goal is to find the transition with the lowest time. This is the only transition which is executed in this time step (Pagonis et al. 2014). The advantage of the Monte-Carlo approach is that even small cluster sizes can be calculated, where the traditional energy band model fails. Monte-Carlo simulations consider clusters of traps as separate systems and then the continuous differential equations are not valid. Pagonis et al. (2014) gave examples of the difference between Monte-Carlo and ODE solutions in TL and OSL simulations.

## 1.5 Quartz radiofluorescence

### 1.5.1 Definition

The emission of light after stimulation has a characteristic lifetime  $\tau_C$ . When  $\tau_C$  is  $< 10^{-8}$  s the process is called *fluorescence*, otherwise *phosphorescence* (McKeever 1988). It is worth noting that even the fast emission of light with  $\tau_C < 10^{-8}$  s is orders of magnitude greater than the lattice vibration ( $\sim 10^{-15} - 10^{-14}$  s, Nasdala et al. (2004)). In literature there is no clear distinction between *radioluminescence* (RL) and *radiofluorescence* (RF). Nasdala et al. (2004) pointed out that “radioluminescence is the generic term for the generation of luminescence light upon excitation with corpuscular radiation”. Recent literature uses the term *radioluminescence* mostly describing a bombardment with X-rays (Boggs & Krinsley 2006; Rendell & Clarke 1997). Lehman (1963) used the term radiofluorescence as one of the first authors and explicitly pointed to the fact that this term describes luminescence emitted during irradiation. The term *radiofluorescence* is widely used in feldspar dating in the infrared (IR-RF; Buylaert et al. (2012), Erfurt & Krbetschek (2003a), Frouin et al. (2015), and Kreutzer et al. (2017)) but was also named IR radioluminescence (IR-RL) at the beginning of the development of this technique (Erfurt & Krbetschek 2003b; Krbetschek & Trautmann 2000; Trautmann et al. 1999). In the following the term radiofluorescence is used as synonym for radioluminescence.

### 1.5.2 Process of luminescence production

Section 1.4.1 described the mathematical basics for luminescence but did not explain the emission and absorption spectra or thermal quenching (Eq. (1.18)). For this purpose the *configurational coordinate diagram* was introduced, see Fig. 1.9. It shows the potential energy curves (parabola) of the luminescence centre as a function of the relative distance  $r$  of the

nucleus to the equilibrium position. The equilibrium position is the electron in the ground state.  $r_0$  is the equilibrium position of the centre ground state and  $r_1$  the position of the centre in the excited state. Horizontal lines ( $n, m = 0, 1, 2$ ) represent the vibrational states of the harmonic oscillator (Yukihara & McKeever 2011). Transitions between ground and excited state are indicated by vertical arrows  $E_a$  and  $E_e$  because the electronic transition is much faster than the crystal relaxation (Franck-Condon principle, Mott & Gurney (1940)). Note also that the parabola in Fig 1.9 intersect. This will be important explaining thermal quenching.

In the configurational coordinate diagram an electron from the conduction band is trapped in an excited state of the recombination centre, e.g.,  $m = 2$ . The electron transits non-radiative into the ground state  $m = 0$  of the excited state by emitting phonons. Due to the fact that energy loss via phonon absorption is not possible any more, the electron undergoes a radiative transition to an excited state of the ground state  $n = 2$  with energy  $E_e$ . From there, again a non-radiative (phonon emitting) transition is possible until the energy state  $n = 0$  is reached. Absorbing energy  $E_a$  can excite the electron back to a vibrational state of the excited state and the process described can start again. The difference between the absorption energy  $E_a$  and the emission energy  $E_e$  is called *Stokes shift* (Krbetschek et al. 1997; Nasdala et al. 2004; Yukihara & McKeever 2011).

Within this framework the explanation for thermal quenching (Sec. 1.4.1) is the following: With increasing temperature the probability that an electron reaches higher vibrational states  $m$  increases. When the electron gains sufficient energy to reach the crossing point of the parabola, the system can relax to the ground state of by non-radiative transition via phonon emission along the parabola (Yukihara & McKeever 2011). Assuming the probability of non-radiative transition given by  $\Gamma_{NR} = \Gamma_0 \cdot \exp\left(\frac{-W}{k_B T}\right)$ , where  $W$  is related to the energy required for the system to reach the crossing point in Fig. 1.9, Eq. (1.17) from Sec. 1.4 changes to the same equation as given in Eq. (1.18):

$$\eta(T) = \frac{\Gamma_R}{\Gamma_R + \Gamma_0 \cdot \exp\left(\frac{-W}{k_B T}\right)} = \frac{1}{1 + K \cdot \exp\left(\frac{-W}{k_B T}\right)} \quad (1.20)$$

The nomenclature is the same as given in Sec. 1.4 but now with an explanation for  $W$  and  $K = \Gamma_0/\Gamma_R$ .

It is also possible that an electron in the excited state will gain further energy by photon absorption and escapes to the conduction band. This phenomenon is called *thermally assisted excitation* (Nasdala et al. 2004) and is considered in numerical simulations by modifying  $\sigma$  (photoionisation cross-section, see Sec. 1.4.1):

$$\sigma = \sigma_0 \exp\left(\frac{-E^{th}}{k_B T}\right) \quad (1.21)$$

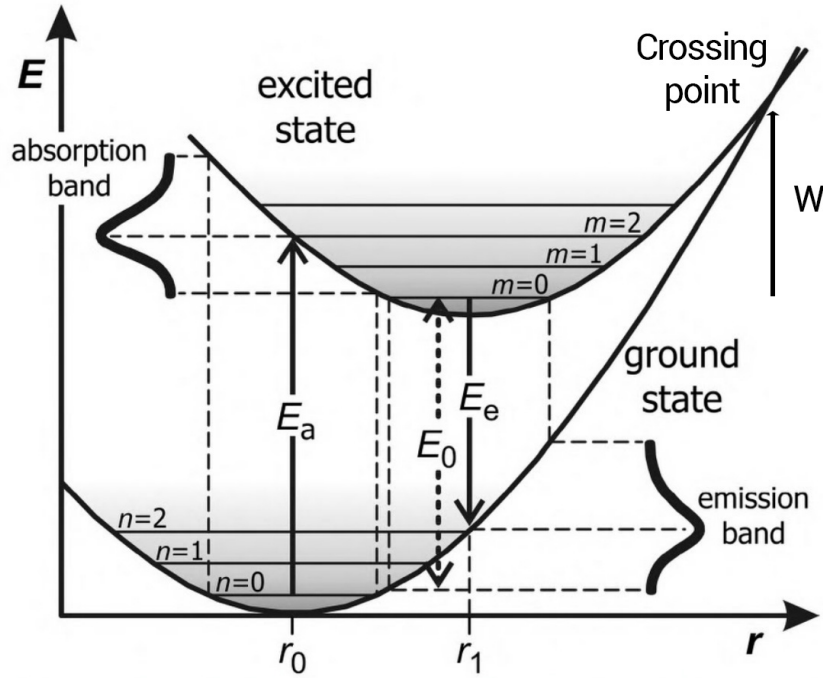


**Figure 1.9:** Configurational coordinate diagram with radiative and non-radiative transitions. Explanation see text in Ch. 1.5.2. Modified from Nasdala et al. (2004).

$\sigma_0$  is the photo-ejection constant at  $T = \infty$  and  $E^{th}$  is the *thermal assistance energy* [eV] (Bailey 2001). A more detailed explanation of the configurational coordinate diagram be found in Gaft et al. (2015).

### 1.5.3 RF emissions of quartz

The previous sections showed that the energy (and thus the wavelength) of the emitted photon is strongly connected to luminescence centres. Radiofluorescence spectra of quartz were investigated quite extensive in the past. A comprehensive overview of studies, sample types and excitation emissions is given in Schmidt et al. (2015: Tab. 1). The main emissions of RF will be explained briefly in the following.

Three main emissions are known to be present in quartz: TL, OSL, and RF have common emissions in the red ( $\sim 620$  nm), in the blue ( $\sim 470$  nm), and in the UV ( $\sim 340 - 380$  nm). With RF it is possible to excite nearly all luminescence centres and with this technique it was possible to detect that the UV and blue emissions are composite (Martini et al. 2012b). The blue emission splits into an emission at 490 nm (A band) and 440 nm (B band) and the UV emission in 360 nm (C band) and 330 nm (D band). In a more recent study by Fasoli & Martini (2016) another emission band at 315 nm (M band) in quartz annealed at 1,000 °C for 10 min was detected. The X band was found just in RF spectra but not in TL spectra and the interpretation is that the X band is not participating at all in the TL recombination of the 110 °C TL peak (Fasoli & Martini 2016). Table 1.2 summarises all these observed bands with their peak energy  $E$  [eV], corresponding wavelength  $\lambda_{max}$  [nm]

and the full width at half maximum (FWHM) [eV].

Band	E [eV]	$\sim \lambda_{\max}$ [nm]	FWHM [eV]
O	1.92	635	0.39
A	2.51	490	0.46
B	2.79	440	0.46
X	3.06	395	0.89
C	3.42	360	0.58
M	3.73	330	0.45
D	3.93	315	0.49

**Table 1.2:** Spectral parameters of the emission bands resulting from Gaussian deconvolution of RF spectra. The nomenclature is adopted from Fasoli & Martini (2016).

The behaviour of the A band (2.51 eV) is dominated by an increase during prolonged irradiation and dominates the RF as well as the TL emission. Heating quartz to 500 °C induced a strong UV emission in the C band. The effect is even more intense applying a dose of a few hundred Gray before annealing, very similar to the *pre-dose effect* (Fasoli & Martini 2016; Zimmerman 1971). The C band (3.42 eV) is the most important band in the simulations presented in this thesis because the parameters presented in Bailey (2001) are adjusted to this emission but for TL and OSL. The other reason why the C band is so important for simulations is the fact that many publications suppose the recombination centre responsible for this emission is the same for TL and OSL (Chen & Li 2000; Franklin et al. 1995; Krbetschek et al. 1997; Martini et al. 2009, 2012a; Schilles et al. 2001; Shimizu et al. 2006; Stoneham & Stokes 1991). The M band (3.73 eV) appears when the quartz sample was annealed to 1,000 °C and is not relevant for most of the natural quartzes. This emission band could be an explanation for the shift of the UV peak with temperature (Rendell et al. 1994).

Figure 1.10 shows an example of a deconvolved spectrum of sample BT586, which was annealed to 500 °C for 10 min and measured afterwards (more details see Ch. 5). The figure shows the first measurement after the thermal treatment and the C band is the dominant emission band in the spectra.

Fasoli & Martini (2016) connected the C band to the element Aluminium (*Al*) because the investigated smoky quartz is known to contain more *Al* than synthetic quartzes and the smoky quartz shows a much more enhanced C band than the synthetic one. This matches with the findings of other authors, see Table 1.1. Nevertheless, also following Fasoli & Martini (2016) it is not possible to find a straightforward correlation between a specific emission band and an extrinsic impurity concentration.

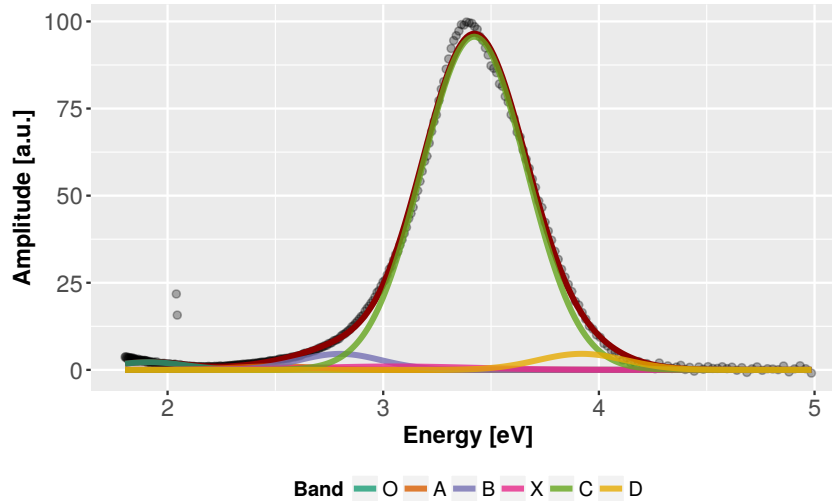


**Figure 1.10:** Deconvolution into Gaussian components of the RF emission spectra for quartz sample BT586 after annealing to 500 °C for 10 min.

## 1.6 The Bailey (2001) model

In 2001 Bailey published a comprehensive quartz model which summarised the findings from decades of quartz luminescence modelling. Furthermore, Bailey (2001) also conducted measurements to identify further model parameters and included these results in the model, e.g., the optical activation following dose quenching. The presented model parameters are able to reproduce a wide variety of quartz luminescence phenomena and measurement protocols.

### 1.6.1 Description of the model

The main components of the Bailey (2001) model will be described here. The model was developed representing the major elements of the electronic system of natural (sedimentary) quartz. One of the main restrictions of the model is the significance just for the 380 nm emission band, which is the main emission band of quartz TL/OSL. Although the model was not developed for RF, Bailey showed some simulated RF signals but did not compare them with experimental data (Bailey 2001: Sec. 3.4.4).

Five electron traps were included in the Bailey (2001) model and all of the traps are thermally connected to the conduction band. In contrast to that, not all implemented electron traps allow photo-excitation. The first electron trap, *level 1*, is responsible for the 110 °C TL peak. This TL peak can be found ubiquitously in sedimentary quartz samples and a recent publication by Vaccaro et al. (2017) clearly connected this electron trap to the element Germanium *Ge*. Some publications also connected this trap to photo-stimulated luminescence and so the trap is also optically sensitive ( $\sigma \neq 0$ , see Sec. 1.4.1). Level 2 is an electron trap connected to the 230 °C TL peak and is a medium-stable trap. It is included because different number of peaks are known in the temperature range from 100 – 300 °C

TL. Since no photo-ejection is known from this trap,  $\sigma = 0$  is suggested. Levels 3 and 4 are implemented to mimic the OSL medium and fast component of quartz (Bailey et al. 1997). Many models suggest a deep electron trap responsible for many luminescence phenomena, e.g., TL peak shapes or supralinear growth. Although this kind of trap is often called *thermally disconnected*, it has a finite value for parameter  $E$  and  $s$  (see Sec. 1.4.1).

The model suggested by Bailey (2001) possesses four different recombination centres. As defined in Sec. 1.4.1 and Fig. 1.6. This model just included recombination centres and no hole traps as defined in the previous sections. Luminescence models with hole traps can be found by, e.g., Chen & Pagonis (2004), Figel & Goedicke (1999), Oniya (2015), and Pagonis et al. (2003). Two so called *R-centres* (reservoir centre, levels 6 and 7) play an important role by explaining dose quenching (see Sec. 6) and the well-known pre-dose effect (see Sec. 3) because these levels are thermally unstable. In contrast to that, level 8 and 9 are thermally very stable and called *L-centre* (luminescence centre) and *K-centre* (killer centre), respectively. Level 8 is called luminescence centre because it is responsible for the simulated luminescence signal which appears due to the recombination of an electron from the conduction band with a trapped hole in this centre. This mechanism tries to mimic the behaviour of the main OSL and TL emission around 380 nm. Level 9, the *killer centre*, represents all recombination centres other than R-centres that are either non-radiative or outside the UV region. So the model is theoretically able to simulate the behaviour of the C band (see Sec. 1.5.3). All recombination centres are thermally connected to the valence band but a photo-excitation of holes out of the centres is not implemented in the original model of Bailey (2001). Figure 1.11 shows the schematic energy band diagram for the model by Bailey (2001).

## 1.6.2 Simulating the geological sample history

In order to simulate the geological history of a quartz sample several different approaches exist. It is impossible to simulate geological time, irradiation periods, and daylight exposure exactly fitting to a measured sample. Therefore, simplifications are unavoidable. In the earliest version of the Bailey (2001) model geological dose rates of  $1 \text{ Gy s}^{-1}$  were used, which are far away from realistic dose rates in nature. Thus, Bailey (2001) used raised temperature irradiation as a simplification of lower dose rates. With increasing computational power it was possible in 2004 to simulate much more realistic natural dose rates of  $1 \text{ Gy ka}^{-1}$ . Nevertheless, many authors use different sample histories fitting best to the expected results. Table 1.3 shows two different sample histories from Bailey (2001) and Bailey (2002). A comprehensive comparison of more published approaches is given in Ch. 2, Table 2.6.

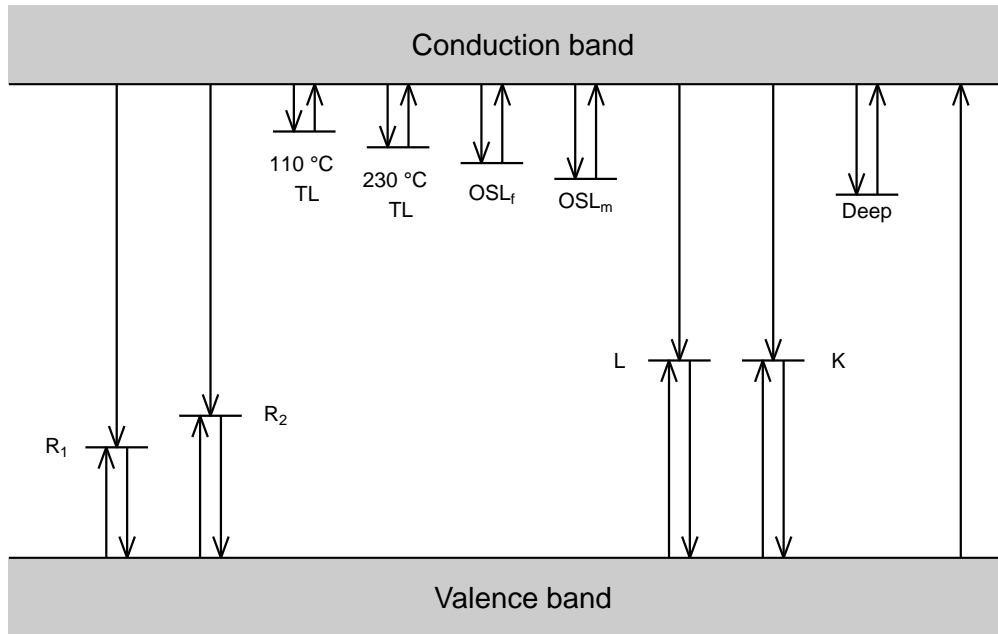


**Figure 1.11:** Schematic energy band model by Bailey (2001).

MODEL	SAMPLE HISTORY
Bailey 2001	crystallisation $\rightarrow$ 1 kGy using $1 \text{ Gy s}^{-1}$ at $20^\circ\text{C}$ (geological dose) $\rightarrow$ heat to $350^\circ\text{C}$ (geological time) $\rightarrow$ illuminate at $200^\circ\text{C}$ for 100 s (repeated daylight exposure) $\rightarrow$ 20 Gy using $0.01 \text{ Gy s}^{-1}$ at $220^\circ\text{C}$ (burial dose)
Bailey 2002	crystallisation $\rightarrow$ 2 kGy using $200 \text{ Gy s}^{-1}$ at $250^\circ\text{C}$ (geological dose) $\rightarrow$ illuminate at $250^\circ\text{C}$ for 5 ks (repeated daylight exposure) $\rightarrow$ 10 Gy using $0.01 \text{ Gy s}^{-1}$ at $220^\circ\text{C}$ (burial dose)

**Table 1.3:** Comparison of two different sample histories from Bailey (2001) and Bailey (2002).

### 1.6.3 The impact of the Bailey (2001) model

Since the publication of the Bailey (2001) model many authors used these parameters (or ones with small modifications) to describe further luminescence phenomena, e.g., Adamiec et al. (2004, 2006), Bailey (2002, 2004), Chen & Pagonis (2011), Chruścińska (2010), Friedrich et al. (2016, 2017a,c, 2018a,b), Kijek & Chruścińska (2016, 2017), Kitis et al. (2006), and Pagonis et al. (2007a,b, 2008a,b, 2009b, 2010).

Most of the authors mentioned changed the values of different parameters, but some others also changed the number of electron traps or recombination centres. In the following some examples of modifications of the original model proposed by Bailey (2001) are given:

- Bailey (2004) himself added three optical active electron traps to describe the slow component of the OSL signal more precise than in the initial model in 2001.
- Adamiec et al. (2004, 2006), and Adamiec (2005) added a third R-centre to describe the high temperature sensitivity increase in thermal activation characteristics (TAC).
- Pagonis et al. (2008a, 2009b, 2011) added two additional electron traps to successfully simulate TT-OSL (thermally transferred OSL) and BT-OSL (basic transfer OSL).
- In this thesis it is shown that the suggestion already made by Bailey (2001) to implement also the photo-excitation of recombination centres was realised successfully (Ch. 7).

#### 1.6.4 Problems with current luminescence models simulating RF

Although the model parameters presented by Bailey (2001) are able to simulate a lot of known luminescence phenomena, there are problems concerning RF simulations. Worthwhile emphasising is that RF simulations were also presented in the origin publication in 2001 but not compared to experimental results. In Bailey (2002) the author presented a RL-SAR (radioluminescence corrected SAR) method where the RL signal is used as sensitivity correction. Within the presented model the simulations show consistent results but an experimental proof has been missing. One of the reasons for that can be the non availability of luminescence readers able to detect RF and OSL sequentially during that time. Meanwhile there exist luminescence readers as the Freiberg Instruments Lexsyg research (Richter et al. 2013) or an attachment for Risø machines (Lapp et al. 2012) which fulfil these requirements. Nevertheless, the proposed correction method by Bailey (2002) was never used as a standard procedure and measurements did not confirm the theoretical findings (pers. communication with Sebastian Kreutzer).

One of the main criticism towards the publication by Bailey (2001, 2002) is the missing comparison to experimental RF data, e.g., given by Krbetschek et al. (1997), Krbetschek & Trautmann (2000), and McKeever et al. (1983). An example is the measurement of RF signals after different preheat temperatures, as shown in McKeever et al. (1983). Therein an enhancement of the initial RF signal is expected for temperatures around 400 °C. Figure 1.12 shows the attempt to simulate this phenomenon with different parameters provided by Bailey (2001), Friedrich et al. (2017a), and Pagonis et al. (2007a, 2008a). The expected result can not be reproduced using the models by Bailey (2001) and Pagonis et al. (2007a). A better performance is reached with Pagonis et al. (2008a) and more realistic results are obtained by model parameters developed through this thesis, see Ch. 3. Ch. 2 to Ch. 7 show the way of conducting fundamental RF experiments and implementing models and new parameter sets describing the experiments as precise as possible.

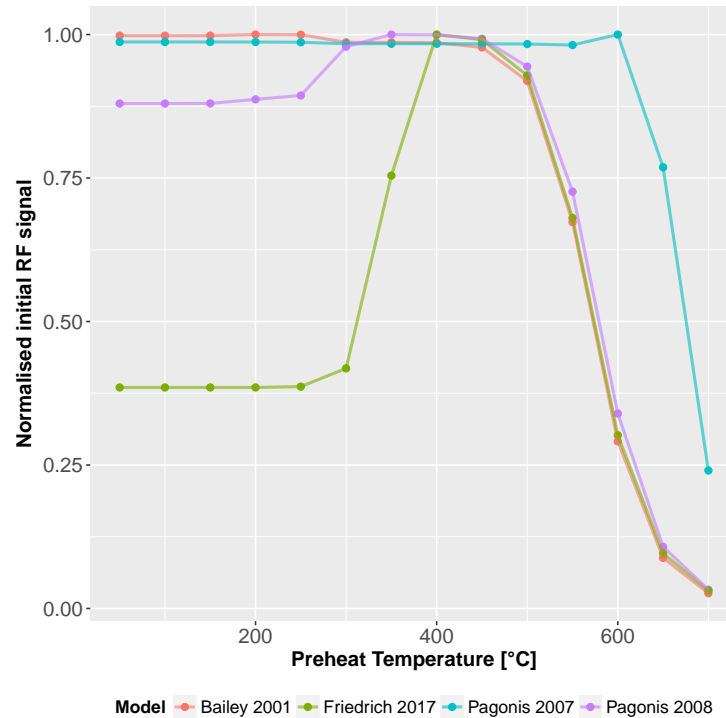


**Figure 1.12:** The effect of different preheat temperatures on the RF signal simulated with model parameter suggested by Bailey (2001), Friedrich et al. (2017a), and Pagonis et al. (2007a, 2008a), respectively.

## 1.7 Results

### 1.7.1 Improving numerical quartz models

The publications presented in Ch. 2 to Ch. 7 extend the existing numerical quartz models by a crucial step: simulating the luminescence signal during irradiation processes. This step is important, because the simulation of the sample history over millions of years under these conditions is crucial for the simulation. Comparing the signal during irradiation (radiofluorescence, see Sec. 1.5) with the outcome of the numerical simulations gives an approximation if the suggested parameters are able to fit the experimental data. In the past numerical models were tested to fit OSL and TL signals and sometimes to hypothetical RF signals (Bailey 2001, 2002), see Sec. 1.6.4. All presented parameter sets in this thesis were tested for different quartz signals and known quartz luminescence phenomena, e.g., thermal-activation curves, preheat-plateau tests, OSL behaviour and for the first time with experimentally-obtained RF signals. So the presented models and parameters represent more comprehensive values for numerical quartz models than given in the past.

The key to achieve this accordance between experiments and simulations was to enhance the concentration of the reservoir centres (R-centres). The effects on the OSL and TL signals are minimal because the electron traps are not affected by this modification. The idea behind this modification was the strong connection to the pre-dose phenomena (see

Ch. 2 and further investigations in Sec. 5.5). Some very fundamental effects known from quartz UV-RF were successfully modelled and explained within the energy band model, e.g., sensitivity changes during the irradiation-preheating cycles (Ch. 3) or competition between energy levels (Ch. 4). Furthermore, more complex simulations are executable with improved numerical quartz models. As shown in Ch. 6 the first numerical solutions of irradiating and heating/cooling the crystal simultaneously were possible and mimic real experiments in a good manner. Also the effect of different dose rates was modelled successfully and confirm the suggested luminescence mechanism even for dose rates varying one order of magnitude (Ch. 5). In addition to that, long known quartz phenomena as the UV-reversal effect (Ch. 7) were simulated successfully by adding a time rate of eviction of holes from the L-centre. All improvements on numerical models go hand in hand with experimental results.

Important to note is that all published quartz parameters are just changed minimally to obtain maximal accordance with other experiments. This is important because other successfully modelled TL and/or OSL phenomena are just minimally affected by these changes because the changes are mostly related to recombination centres. To quantify the impact of changes of different model parameters, the method of *sensitivity analysis* was introduced in luminescence modelling. With this method the impact of small changes to one parameter on the outcome of the simulations can be expressed numerically. Hence, it is possible to compare different parameter impacts. The results can be summarised as follows: For TL simulations, the critical parameters are the trap depth  $E$ , and the frequency factor  $s$ , see Sec. 1.4.1. The method can be applied to several luminescence signals, e.g., OSL, LM-OSL, and RF and is fully implemented in the software package presented in Sec. 1.7.2. The benefit from this kind of analysis is the knowledge of parameters worth using for *inverse modelling*. This technique was used to fit model parameters to real experiments. For that purpose it is necessary to know parameters which influence the simulated signal most. These parameters are fitted to experimental data and the results for inverse modelling of luminescence signals are given in Sec. 8.3. Using model predictions and explanations is just meaningful when the model is able to reproduce as much as possible known phenomena. So fitting the model parameters to these results is very important to gain more precise predictions.

Summing up, the published quartz parameter sets are able to mimic a wide range of known quartz luminescence signals and phenomena and mark a progress in quartz luminescence simulations. The consistency between simulated and empirical data is strong but this does not indicate that the model is correct. It just means that the model is self-consistent.

### 1.7.2 Technical investigations and developments

One of the main investigations of this thesis is the development of the freely-available, open-source software package *RLumModel* written in **R** (Friedrich et al. 2016, 2017b; R Core Team 2017). The first study presented in Ch. 2 describes in detail the usage of the software package. The software has been designed for simplicity to guarantee an

ease-of-use without deep knowledge of programming or mathematical understanding of ODE solving. Usually just one function with two arguments is needed. The function is named `model_LuminescenceSignals()`. The argument `model` sets automatically the parameters from different important quartz models given in literature, e.g., `model = "Bailey2001"` loads the parameters given in Bailey (2001). The second argument is `sequence` and a list of commands can be created by (a) the *Risø Sequence Editor*, (b) a built-in SAR sequence generator or (c) self-explanatory keywords. The core of the package is the system of ODEs (see Sec. 1.4.1) and the algorithms to solve this system for different initial conditions and parameters. The user of the package does not have to know anything about this system or the solving algorithms, all is automatically calculated in the back-end of the package via C++ to guarantee a fast computation even for huge parameters or for simulated geological times. To visualise the findings, the infrastructure of the **R**-package *Luminescence* is used (Kreutzer et al. 2012, 2018). The following code shows a typical example of the usage:

```
1 sequence <- list(  
2   IRR = c(temp = 20, dose = 10, dose_rate = 1),  
3   TL = c(temp_begin = 20, temp_end = 400, heating_rate = 5))  
4  
5 model.output <- model_LuminescenceSignals(  
6   model = "Bailey2001",  
7   sequence = sequence)
```

This code can be read as follows: At a temperature of 20 °C a dose of 10 Gy is applied with a dose rate of 1 Gy s<sup>-1</sup> followed by a TL measurement from 20 °C to 400 °C with a heating rate of 5 °C s<sup>-1</sup>. This results in a TL curve like the one published in Bailey (2001: Figure 1). It is also possible to plot the change over time for the concentration of charge carriers. This is one of the big advantages of simulations and they offer a deep look in the behaviour of energy levels. For an overview of the possibilities of the **R**-package see the vignettes (a long-form guide for a specific package) in the software itself. The possibility to use custom defined parameter sets is another advantage because it offers the user freedom to investigate their own parameter sets or even use the software package to simulate other materials connected to the energy band model, e.g., Al<sub>2</sub>O<sub>3</sub>. This is also shown in many examples in the vignettes.

The software package is the base for the published numerical solutions in Ch. 3, 5, 6, and 7. The package is published on *CRAN* (Comprehensive R Archive Network<sup>1</sup>) and was downloaded more than 10,000 times since February 2016. The package is maintained continuously and examples are given in the manual, the vignettes, the homepage<sup>2</sup> and in the appendices of published manuscripts (see App. A).

With the **R**-package *RLumModel* it is also possible to create sensitivity analyses to find the parameters with the highest impact on the outcome of the simulations. This is the base

---

<sup>1</sup><https://cran.r-project.org/package=RLumModel>

<sup>2</sup><http://r-lum.github.io/RLumModel>

of the inverse modelling approach where it is possible to calculate model parameters from real measurement data.

During the project also other software applications were developed: *rxylib* and *rxylib Shiny*. *rxylib* is able to read different x-y data formats from scientific measurement devices, e.g., powder diffraction or spectroscopy data. The browser application *rxylib Shiny* is able to read these data within a browser and further analyse the data, e.g., fit them to different functions. It is also possible to save the results as high-resolution images on the hard disk. The programs are free software and the source code and can be found on [github.com](https://github.com)<sup>3</sup>.

### 1.7.3 Methodological investigations

Due to the fact that little methodological data about quartz RF had been published at the begin of the project, the first studies included fundamental investigations. So the results presented in Ch. 3 show the behaviour of the UV-RF signal for different annealing temperatures ranging from 50 to 700 °C. Two different quartz samples show similar behaviour concerning the initial signal intensity and signal dynamics. Both samples show a strong increase in UV-RF intensity after 350 °C and have the highest UV-RF intensity after a 550 °C annealing treatment. At even higher temperatures the initial intensity is decreasing very fast.

After these first results, further investigations towards the strong increase after preheating were carried out. In Ch. 4 the behaviour of the UV-RF signal (C band at 3.42 eV) after a 10 min preheat to 500 °C for three different quartz samples was investigated. The C band shows a variety of signal dynamics without any pretreatment. Two quartz samples show an increasing signal during UV-RF measurement, while one sample has a decreasing intensity. Nevertheless, after a preheat to 500 °C for 10 min all samples show a strong decreasing signal during measurement. From a three-energy-level model analytical solutions for the RF signal versus time (or dose) were derived. These functions fit both conditions (no treatment and thermal treatment) for all samples in a good manner. Qualitatively, the two component fitting function can be seen as a superposition of two processes: (I) filling of the luminescence centre with holes (building up the signal) and (II) recombination of electrons with these holes (decaying function). The results from this study are not restricted to the C band and can also be transferred to other emission bands (see Sec. 1.8).

The publication in Ch. 5 investigated the effect of different dose rates on two different quartzes from different geological origin after a preheat to 500 °C for 10 min. The main observations for the C band are summarised as follows:

- The higher the dose rate, the higher the signal intensity,
- the higher the dose rate, the higher the intensity difference between the first and the last measurement,
- the decay time of the C band during irradiation is sample dependent.

<sup>3</sup><https://github.com/R-Lum/rxylib> and <https://github.com/JohannesFriedrich/rxylibShiny>

Again, the results from the previous study (Ch. 4) were used to fit the signals for different dose rates and a good agreement was obtained. Another result of these study was that the UV-RF signal of quartz can be used determine absorbed doses. The reason is the independency of RF signal characteristics on the dose rate. To establish this method more experimental evidence is needed but the main idea is given in this study. Further experimental results can be found in Sec. 8.2.

The study presented in Ch. 6 investigates thermal- and dose quenching effects on three different quartz samples and provides a simple method to determine quenching parameters: After preventing sensitivity changes by cycles of irradiation and heating, the sample will be heated up to 500 °C and cooled down while irradiating with ionising radiation (measure the RF signal). Fitting the temperature against intensity curve will directly give the quenching parameters.

Furthermore, the effect of far UV illumination on the UV-RF signal was investigated in Ch. 7 on three quartz samples. The results show that the UV light reduces the intensity of the UV-RF signal as expected. By applying different times of UV illumination a time rate of optical excitation of holes from the L-centre can be calculated. In addition to that, the pre-dose and the UV-reversal effect can be observed more directly because an obligatory test dose response for the 110 °C TL peak is void by using RF.

Table 1.4 shows a summary of used quartz samples in different chapters in this thesis. Further information about the samples, geological background and their preparation procedure are given in the particular chapters.

SAMPLE	CHAPTER					
	3	4	5	6	7	8
BT586	✓	✓	✓	✓	✓	✓
BT1195	✓			✓		
Hyaline		✓				✓
Smoky quartz		✓				
FB			✓	✓	✓	✓
BT1248					✓	✓

**Table 1.4:** Summary of all investigated quartz samples in the thesis. Chapters 3 to 7 are published/submitted manuscripts, Ch. 8 contains unpublished results.

#### 1.7.4 Awards

During the project two major student awards were won. In 2016 the award for the best student poster at the *UK LED* meeting in Liverpool was won. The title of the poster was “Finding appropriate model parameters for luminescence simulations: inverse modelling and model fitting with Markov-Chain Monte-Carlo methods in RLumModel”. The findings and results of the poster and further developments since the presentation are summarised in

Sec. 8.3.

With the talk about “Radiofluorescence as detection tool for quenching processes in quartz luminescence” the best oral presentation for fundamentals (Martin Aitken Prize) was gained at the *International Conference on Luminescence and Electron Spin Resonance Dating* in September 2017. The publication to this talk can be found in Ch. 6.

## 1.8 Research outlook

The results obtained in this thesis show the possibility to use quartz RF and luminescence simulations in a wide range of topics. The following sections will present possible further ways of developing both numerical simulations and methods concerning RF.

### 1.8.1 Numerical simulations

The presented inverse modelling approach (Sec. 8.3) can be used to create sample dependent parameters useful for further simulations and predictions for specific quartz samples. Therefore a pre-defined measurement sequence covering as many as possible luminescence signals (TL, OSL, LM-OSL, and RF) could be executed and then inversely fitted to existing quartz models. This approach can save measurement time because time-consuming or complex measurements can first be simulated and analysed virtually. Furthermore, the inverse modelling technique can be extracted to other fields than luminescence because many free available software packages exist which help users to create customised inverse modelling approaches.

Until now no spatial relationship between electron traps, hole centres, and recombination centres is included in the most common used Bailey (2001) model. Nevertheless, the development of Monte-Carlo methods for luminescence tries to take spatial relationship as well as localised transitions into account. The models developed by Mandowski & Świątek (1992, 1994, 1996, 1998, 2000) and Mandowski (2002, 2005, 2006) show the effects of using small clusters with less charge carriers, e.g., peaks that could not be attributed to any real trap level in a solid (Mandowski & Świątek 1997). A model which combines both (localised and non-localised) transitions could explain more luminescence phenomena.

### 1.8.2 Methods

The findings from Ch. 4 encourage using the fitting function found for the C band also for other bands. This is possible because the function can be applied to conditions where two competitive processes with exponential characteristics are involved. Own tests confirmed this idea but due to the interest on the C band no other bands were investigated in detail in the publications.

Due to the strong annealing dependency of the UV-RF signal, investigated in Ch. 3, the signal could be used as indicator for thermal treatment of quartz in the past (without

irradiating subsequent to the thermal treatment. Otherwise the C band will decrease during irradiation (Fasoli & Martini 2016; Friedrich et al. 2016) and no prediction of former heating can be made). When an annealed and an un-annealed sample of a batch is available, with the systematic pre-heating experiments presented in Ch. 3 a first limitation of the annealing temperature could be made by comparing the C band intensity of the annealed sample with the constructed C band intensity vs. annealing temperature curve, see Fig. 3.3.

Chapter 7 showed that is possible (in the framework of the energy band model) to transfer holes from L-centres to R-centres by illuminating quartz with far UV light. The effect can be reversed by annealing the quartz sample after illumination. Thus, the thesis showed different ways to manipulate the distribution of holes. These methods can be used to bring quartz samples in specific conditions to further analyse the electronic system in quartz. RF offers the possibility to investigate already known phenomena in more detail, as shown in Ch. 6 and 7. Another long known effect in quartz is thermal quenching. The investigations in Ch. 6 showed the first comprehensive analysis of thermal quenching parameters measured directly with UV-RF. The approach used can be extended to spectrometric measurements with subsequent deconvolution of the spectra into Gaussian components. So different emission bands at once can be analysed. The advantage of using spectrometric measurements is the more precise detection of single bands because in our approach it is not possible to distinguish different emissions within the detected wavelength region.

Concerning a dating application the initial findings from Ch. 5 and the experimental proofs in Sec. 8.2 give evidence that quartz UV-RF is capable to recover absorbed doses. The major drawback is that used quartz samples had to be heated up to  $\sim 500^\circ\text{C}$  before dose application. Hence, determining natural absorbed doses is limited to a small fraction of materials, e.g., ceramics. Nevertheless, this method can be used for, e.g., calibrating radiating sources. Before irradiating with a calibrated source, the samples had to be annealed to  $\sim 500^\circ\text{C}$  to guarantee a decreasing C band in the UV-RF signal. When the UV-RF signal is detected with a photomultiplier, as executed in Sec. 8.2, acceptable results are obtained. Further investigations are needed to establish the presented UV-RF dose determination.

## 1.9 Discussion and conclusion

### 1.9.1 Quartz RF measurements

The experimental investigations in this thesis are of fundamental nature and cover the behaviour after different annealing temperatures, signal stability tests (Ch. 3). Furthermore, dose rate effects (Ch. 5), observations of quenching (Ch. 6), and UV-reversal effects (Ch. 7) were systematically analysed. In addition to that a fitting function for RF signal dynamics was derived and successfully applied in several studies (Ch. 4, Ch. 5). All studies, except the ones presented in Ch. 4 and Ch. 5, were executed with a Freiberg Instruments *lexsyg research* reader (Richter et al. 2013). The experimental results from studies in Ch. 4 and Ch. 5 were recorded with a home-made apparatus in Milan, Italy, at the *Dipartimento*

*di Scienza dei Materiali* at the University of Milano-Bicocca. The advantage of spectra measurements are that single bands can be deconvolved into Gaussian components and hypothesis can be tested more precisely than using a photomultiplier. In a photomultiplier the distinction between single emission bands in the recorded wavelength range is almost impossible. Nevertheless, due to the strong C band enhancement after annealing to  $\sim 500^\circ\text{C}$  it will be ensured that the main component recorded with a photomultiplier is indeed the C band. For this thesis it is important that the C band is recorded because the model parameter presented are optimised for that emission band. It is important to bear in mind that investigating other RF emission bands can be more difficult.

In all studies different quartz samples with different pre treatment (e.g., annealed to  $700^\circ\text{C}$ , bleached in the solar light simulator) were used to obtain possible differences in the UV-RF signal. Nevertheless, no significant differences between these samples during the studies were obtained. Just minimal changes in the decay of the C band or the level of intensity after long irradiation had been observed. So the differences between quartz samples can be modelled by changing the parameters in the simulation, see Sec. 1.1.2 and 1.9.2.

By applying an analysis technique used for feldspar dating to UV-RF a new way of using quartz UV-RF for dosimetric applications was found. Due to the huge amount of available data points and the high signal intensity a high accuracy is reached (Sec. 8.2). If the impact of different factors in the measurement protocol (Table 8.1, e.g., preheat temperature, length of preheat, length of measuring the natural signal) are investigated in more detail, more precise results as presented until now could be reached (achievement 5 in Sec. 1.1.2).

### 1.9.2 Quartz RF simulations

In this thesis systematic comparisons between RF measurements and simulations are presented and showed that RF phenomena are reproducible within the energy band model. The main modification was the adjustment of the concentration of the thermal unstable reservoir centres (R-centre, see Sec. 1.6). The idea came up because the experimental results from Ch. 3 are very similar to the known pre-dose effect (Bailiff 1994). In the first publications presented on Ch. 3 the concentration of the  $R_1$  centre was enhanced by a factor 10 to reach concordance with experimental results. Again, in Ch. 5 the concentration of the  $R_1$  centre was enhanced by a factor of  $\sim 33$  compared to the original value by Bailey (2001). Note that in both chapters the signals to match were obtained by different quartz samples.

Nevertheless, the concentration of the R-centres seem to have huge impact on the RF signal in the numerical simulations. Figure 1.13 illustrates these findings by taking the models presented in Ch. 5 and change the concentration of the  $R_1$  centre systematically by 5 orders of magnitude. The simulated sequence was the same for all parameter sets and the effect on the simulated RF signal is enormous. Note the huge doses on the x-axis. The

signal dynamic is completely changing for different values of the  $R_1$  concentration. For high values (factor  $1 \text{ E}+01$  and  $1 \text{ E}+02$ , or in absolute values:  $1 \text{ E}+11$  and  $1 \text{ E}+12 \text{ cm}^{-3}$ , respectively) the RF signals show nearly the same results and do not change their signal dynamic towards higher intensities for very long irradiation times. Furthermore, the TL and OSL signal were also investigated with the same parameters as the RF signals in Fig. 1.13. Figure 1.14 shows these (normalised) signals and no obvious differences in both signals are detected. The signal intensities changed but normalising the results show no difference in the signal dynamics, except small changes above  $300 \text{ }^\circ\text{C}$ .

These findings confirm the idea that the RF signal dynamic is very sensitive to concentration changes in the recombination centres while TL and OSL are not affected that much. This is also the reason why any other phenomena ( $110 \text{ }^\circ\text{C}$  TL peak change with different heating rates, OSL with varying reading temperature, etc.), investigated in Ch. A, do not change.

Furthermore, the thesis shows in Sec. 8.4 that not just the energy band model is able to give meaningful results for RF simulations but also the Monte-Carlo method. Until now the results are in accordance with ODE solutions which indicate that the concept of performing these kind of simulations seems to be acceptable. Nevertheless, the simulations performed with Monte-Carlo methods for TL and OSL on a very small number of charge carriers (Pagonis & Chen 2015) were not realised until now. This needs further investigations and other concepts then presented here.

In summary, it can be concluded that the energy band model is able to describe many experimentally obtained RF results well. Therefore some modifications on already published data sets are needed, especially on the concentration of reservoir centres. It has been shown that a change in the reservoir centres concentration has a huge impact on RF, but not on TL or OSL signals. With these results the aim reproducing RF results with existing models was reached (Sec. 1.1.2). Furthermore, the thesis presents an advanced method of calculating proper model parameters by using the inverse modelling approach, see Sec. 8.3. Hence, the aim from Sec. 1.1.2 of finding a way to vary input parameters to easily reproduce luminescence behaviour of different quartz samples was reached as well. The users of the software package *RLumModel* can use the complete benefit of these technique to automatically calculate proper model parameters fitting their measured samples. Besides this feature the actual intention of creating this kind of open-source software was to enable a wide range of people the opportunity of using luminescence modelling without background knowledge of solving ODEs or the physical processes behind it (aim 4 in Sec. 1.1.2).

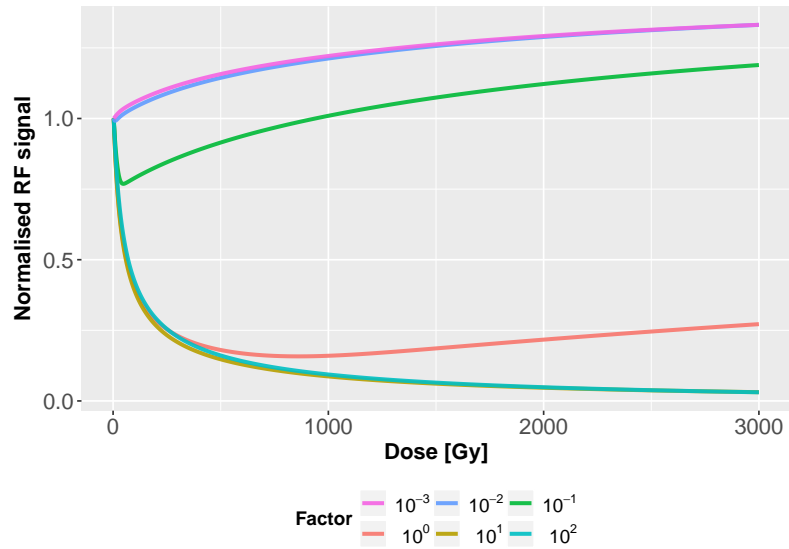


**Figure 1.13:** RF simulations for different values of the concentration of the  $R_1$  centre. The reference data set was the one presented in Ch. 5.

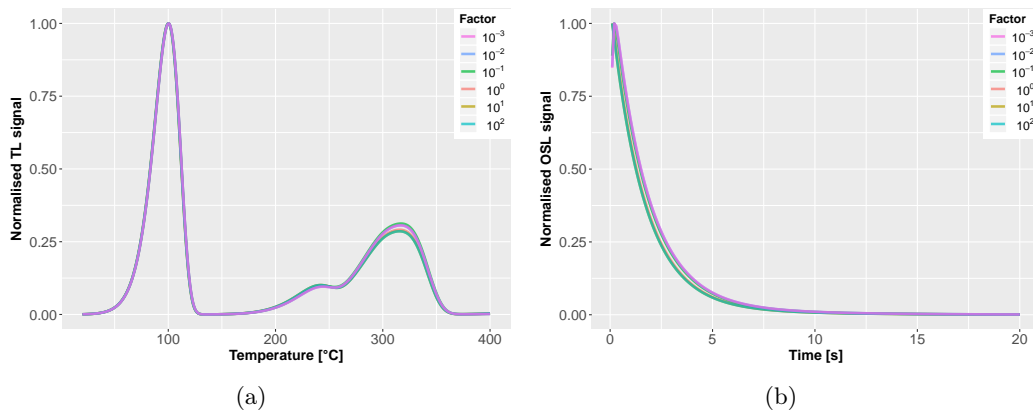


**Figure 1.14:** Numerical simulations with different values of the concentration of the  $R_1$  centre for (a) TL and (b) OSL. No differences in the signal dynamics are visible in the normalised signal.

## References

- Adamiec, G., Garcia-Talavera, M., Bailey, R. M., La Torre, P. I. de, 2004. Application of a genetic algorithm to finding parameter values for numerical simulation of quartz luminescence. *Geochronometria* 23, 9–14.
- Adamiec, G., 2005. Investigation of a numerical model of the pre-dose mechanism in quartz. *Radiation Measurements* 39(2), 175–189.
- Adamiec, G., Bluszcz, A., Bailey, R. M., Garcia-Talavera, M., 2006. Finding model parameters: Genetic algorithms and the numerical modelling of quartz luminescence. *Radiation Measurements* 41(7), 897–902.
- Aitken, M. J., 1985. *Thermoluminescence dating*. Academic press.
- Aitken, M. J., 1998. *An introduction to optical dating: the dating of Quaternary sediments by the use of photon-stimulated luminescence*. Oxford University Press.
- Bailey, R. M., Smith, B. W., Rhodes, E. J., 1997. Partial bleaching and the decay form characteristics of quartz OSL. *Radiation Measurements* 27(2), 123–136.
- Bailey, R. M., 2001. Towards a general kinetic model for optically and thermally stimulated luminescence of quartz. *Radiation Measurements* 33(1), 17–45.
- Bailey, R. M., 2002. Simulations of variability in the luminescence characteristics of natural quartz and its implications for estimates of absorbed dose. *Radiation Protection Dosimetry* 100, 33–38.
- Bailey, R. M., 2004. Paper I - Simulation of dose absorption in quartz over geological timescales and its implications for the precision and accuracy of optical dating. *Radiation Measurements* 38(3), 299–310.
- Bailiff, I., 1994. The pre-dose technique. *Radiation Measurements* 23(2), 471–479.
- Benz, K.-W., Neumann, W., 2014. *Introduction to crystal growth and characterization*. John Wiley & Sons.
- Bloch, F., 1929. Über die Quantenmechanik der Elektronen in Kristallgittern. *Zeitschrift für Physik* 52(7-8), 555–600.
- Boggs, S., Krinsley, D., 2006. *Application of cathodoluminescence imaging to the study of sedimentary rocks*. Cambridge University Press.
- Born, M., 1926. Atomtheorie des festen Zustandes (Dynamik der Kristallgitter). In: Sommerfeld, A. (Ed.), *Encyklopädie der Mathematischen Wissenschaften mit Einschluss ihrer Anwendungen: Fünfter Band: Physik*. Vieweg+Teubner Verlag, 527–781.
- Boyle, R., 1664. *Experiments and considerations touching colours*.
- Bräunlich, P., Scharmann, A., 1966. Approximate Solution of Schön's Balance Equations for the Thermoluminescence and the Thermally Stimulated Conductivity of Inorganic Photoconducting Crystals. *physica status solidi (b)* 18(1), 307–316.
- Bräunlich, P., Kelly, P., Fillard, J.-P., 1979. Thermally stimulated luminescence and conductivity. In: *Thermally stimulated relaxation in solids*. Springer, 35–92.

- Bull, R., McKeever, S., Chen, R., Mathur, V., Rhodes, J. F., Brown, M., 1986. Thermoluminescence kinetics for multipeak glow curves produced by the release of electrons and holes. *Journal of Physics D: Applied Physics* 19(7), 1321–1334.
- Buylaert, J.-P., Jain, M., Murray, A., Thomsen, K., Lapp, T., 2012. IR-RF dating of sand-sized K-feldspar extracts: A test of accuracy. *Radiation Measurements* 47(9), 759–765.
- Chen, G., Li, S., 2000. Studies of quartz 110 °C thermoluminescence peak sensitivity change and its relevance to optically stimulated luminescence dating. *Journal of Physics D: Applied Physics* 33(4), 437–443.
- Chen, R., McKeever, S. W., Durrani, S., 1981. Solution of the kinetic equations governing trap filling. Consequences concerning dose dependence and dose-rate effects. *Physical Review B* 24(9), 4931–4994.
- Chen, R., Mathur, V., Rhodes, J. F., Brown, M., McKeever, S., Bull, R., 1984. Thermoluminescence governed by simultaneous thermal stimulation of electrons and holes. *physica status solidi (b)* 126(1), 361–369.
- Chen, R., Fogel, G., 1993. Supralinearity in Thermoluminescence Revisited. *Radiation Protection Dosimetry* 47(1-4), 23–26.
- Chen, R., Fogel, G., Kristianpoller, N., 1994. Theoretical account of the sensitization and de-sensitization in quartz. *Radiation Measurements* 23(2), 277–279.
- Chen, R., McKeever, S. W. S., 1997. *Theory of Thermoluminescence and Related Phenomena*. World Scientific, Singapore.
- Chen, R., Leung, P., 1999. Modeling the pre-dose effect in thermoluminescence. *Radiation Protection Dosimetry* 84(1-4), 43–46.
- Chen, R., Pagonis, V., 2004. Modelling thermal activation characteristics of the sensitization of thermoluminescence in quartz. *Journal of Physics D: Applied Physics* 37, 159–164.
- Chen, R., Pagonis, V., Lawless, J., 2009. A new look at the linear-modulated optically stimulated luminescence (LM-OSL) as a tool for dating and dosimetry. *Radiation Measurements* 44, 344–350.
- Chen, R., Lawless, J., Pagonis, V., 2011. A model for explaining the concentration quenching of thermoluminescence. *Radiation Measurements* 46, 1380–1384.
- Chen, R., Pagonis, V., 2011. *Thermally and Optically Stimulated Luminescence: A Simulation Approach*. John Wiley & Sons, Chichester.
- Chen, R., Lawless, J., Pagonis, V., 2012. Two-stage thermal stimulation of thermoluminescence. *Radiation Measurements* 47(9), 809–813.
- Chen, R., Pagonis, V., 2013. Modeling TL-like thermally assisted optically stimulated luminescence (TA-OSL). *Radiation Measurements* 56, 6–12.
- Chen, R., Pagonis, V., 2015. Study of the stability of the TL and OSL signals. *Radiation Measurements* 81, 192–197.
- Chruścińska, A., 2009. Modelling the thermal bleaching of OSL signal in the case of a competition between recombination centres. *Radiation Measurements* 44, 329–337.

- Chruścińska, A., 2010. On some fundamental features of optically stimulated luminescence measurements. *Radiation Measurements* 45, 991–999.
- Chruścińska, A., Przegiętka, K. R., 2011. Analysis of OSL intensity increase with temperature and its consequences for dating applications. *Radiation Measurements* 46(12), 1514–1517.
- Chruścińska, A., Kijek, N., Topolewski, S., 2017. Recent development in the optical stimulation of luminescence. *Radiation Measurements* 106, 13–19.
- Enderlein, R., Horing, N. J., 1997. *Fundamentals of Semiconductor Physics and Devices*. World Scientific.
- Erfurt, G., Krbetschek, M., 2003a. IRSAR—A single-aliquot regenerative-dose dating protocol applied to the infrared radiofluorescence (IR-RF) of coarse-grain K feldspar. *Ancient TL* 21(1), 35–42.
- Erfurt, G., Krbetschek, M., 2003b. Studies on the physics of the infrared radioluminescence of potassium feldspar and on the methodology of its application to sediment dating. *Radiation Measurements* 37(4), 505–510.
- Fasoli, M., Martini, M., 2016. The composite nature of the thermoluminescence UV emission of quartz. *Journal of Luminescence* 173, 120–126.
- Figel, M., Goedicke, C., 1999. Simulation of the Pre-Dose Effect of the 110 °C TL Peak in Quartz. *Radiation Protection Dosimetry* 84(1-4), 433–438.
- Franklin, A., Prescott, J. R., Scholefield, R., 1995. The mechanism of thermoluminescence in an Australian sedimentary quartz. *Journal of Luminescence* 63(5-6), 317–326.
- Friedrich, J., Kreutzer, S., Schmidt, C., 2016. Solving ordinary differential equations to understand luminescence: 'RLumModel', an advanced research tool for simulating luminescence in quartz using R. *Quaternary Geochronology* 35, 88–100.
- Friedrich, J., Pagonis, V., Chen, R., Kreutzer, S., Schmidt, C., 2017a. Quartz radiofluorescence: a modelling approach. *Journal of Luminescence* 186, 318–325.
- Friedrich, J., Kreutzer, S., Schmidt, C., 2017b. *RLumModel: Solving Ordinary Differential Equations to Understand Luminescence*. (R package version 0.2.3). CRAN. <https://CRAN.R-project.org/package=RLumModel>,
- Friedrich, J., Fasoli, M., Kreutzer, S., Schmidt, C., 2017c. The basic principles of quartz radiofluorescence dynamics in the UV - analytical, numerical and experimental results. *Journal of Luminescence* 192, 940–948.
- Friedrich, J., Fasoli, M., Kreutzer, S., Schmidt, C., 2018a. On the dose rate dependence of radiofluorescence signals of natural quartz. *Radiation Measurements* 111, 19–26.
- Friedrich, J., Kreutzer, S., Schmidt, C., 2018b. Radiofluorescence as a detection tool for quartz luminescence quenching processes. *Radiation Measurements*.
- Frouin, M., Huot, S., Mercier, N., Lahaye, C., Lamothe, M., 2015. The issue of laboratory bleaching in the infrared-radiofluorescence dating method. *Radiation Measurements* 81, 212–217.
- Gaft, M., Reisfeld, R., Panczer, G., 2015. *Modern luminescence spectroscopy of minerals and materials*. Springer.

- Garlick, G., Gibson, A., 1948. The electron trap mechanism of luminescence in sulphide and silicate phosphors. *Proceedings of the Physical Society* 60, 574–590.
- Gear, C., Skeel, R., 1987. The Development of ODE Methods: A Symbiosis between Hardware and Numerical Analysis. *Proceedings of the ACM conference on History of scientific and numeric computation*, ACM, 105–115.
- Götze, J., 2009. Chemistry, textures and physical properties of quartz—geological interpretation and technical application. *Mineralogical Magazine* 73(4), 645–671.
- Götze, J., 2012a. Application of cathodoluminescence microscopy and spectroscopy in geosciences. *Microscopy and Microanalysis* 18(6), 1270–1284.
- Götze, J., 2012b. Classification, Mineralogy and Industrial Potential of SiO<sub>2</sub> Minerals and Rocks. In: Götze, J., Möckel, R. (Eds.), *Quartz: Deposits, Mineralogy and Analytics*. Springer, 1–27.
- Gribkovskii, V., 1998. Theory of Luminescence. In: Vij, D. (Ed.), *Luminescence of Solids*. Springer, 1–43.
- Gurney, R., Mott, N., 1939. Luminescence in solids. *Transactions of the Faraday Society* 35, 69–73.
- Guzzo, P. L., Khoury, H. J., Miranda, M. R., Barreto, S. B., Shinohara, A. H., 2009. Point defects and pre-dose requirements for sensitization of the 300 °C TL peak in natural quartz. *Physics and Chemistry of Minerals* 36(2), 75–85.
- Guzzo, P. L., Souza, L. B. F. de, Barros, V. S., Khoury, H. J., 2017. Spectroscopic account of the point defects related to the sensitization of TL peaks beyond 220 °C in natural quartz. *Journal of Luminescence* 188, 118–128.
- Halperin, A., Braner, A., 1960. Evaluation of thermal activation energies from glow curves. *Physical Review* 117, 408–415.
- Hamming, R., 1962. *Numerical Methods for Scientists and Engineers*. McGraw-Hill.
- Hine, G. J., Brownell, G. L., 2013. *Radiation dosimetry*. Elsevier.
- Hummel, R. E., 2011. *Electronic Properties of Materials*. Springer Science & Business Media.
- Itoh, N., Stoneham, D., Stoneham, A. M., 2001. The predose effect in thermoluminescent dosimetry. *Journal of Physics: Condensed Matter* 13(10), 2201–2209.
- Itoh, N., Stoneham, D., Stoneham, A., 2002. Ionic and electronic processes in quartz: mechanisms of thermoluminescence and optically stimulated luminescence. *Journal of Applied Physics* 92(9), 5036–5044.
- Jain, M., Sohbaty, R., Guralnik, B., Murray, A., Kook, M., Lapp, T., Prasad, A., Thomsen, K., Buylaert, J., 2015. Kinetics of infrared stimulated luminescence from feldspars. *Radiation Measurements* 81, 242–250.
- Kelly, P., Laubitz, M. J., Bräunlich, P., 1971. Exact Solutions of the Kinetic Equations Governing Thermally Stimulated Luminescence and Conductivity. *Physical Review B* 4(6), 1960–1968.

- Kijek, N., Chruścińska, A., 2016. Natural and laboratory OSL growth curve - Verification of the basic assumption of luminescence dating. *Radiation Measurements* 90, 233–237.
- Kijek, N., Chruścińska, A., 2017. On the equivalence of natural and laboratory growth curves in luminescence dating - The effect of deep traps and luminescence centres. *Radiation Measurements* 106, 477–482.
- Kitis, G., Pagonis, V., Chen, R., 2006. Comparison of experimental and modelled quartz thermal-activation curves obtained using multiple-and single-aliquot procedures. *Radiation Measurements* 41, 910–916.
- Kittel, C., 2005. *Introduction to Solid State Physics*. John Wiley & Sons.
- Krbetschek, M., Götze, J., Dietrich, A., Trautmann, T., 1997. Spectral information from minerals relevant for luminescence dating. *Radiation Measurements* 27(5-6), 695–748.
- Krbetschek, M., Trautmann, T., 2000. A spectral radioluminescence study for dating and dosimetry. *Radiation Measurements* 32(5), 853–857.
- Kreutzer, S., Schmidt, C., Fuchs, M. C., Dietze, M., Fischer, M., Fuchs, M., 2012. Introducing an R package for luminescence dating analysis. *Ancient TL* 30(1), 1–8.
- Kreutzer, S., Murari, M. K., Frouin, M., Fuchs, M., Mercier, N., 2017. Always remain suspicious: a case study on tracking down a technical artefact while measuring IR-RF. *Ancient TL* 35(1), 20–30.
- Kreutzer, S., Burow, C., Dietze, M., Fuchs, M. C., Schmidt, C., Fischer, M., Friedrich, J., 2018. *Luminescence: Comprehensive Luminescence Dating Data Analysis*. (R package version 0.8.4). <https://CRAN.R-project.org/package=Luminescence>,
- Kronig, R. d. L., Penney, W., 1931. Quantum mechanics of electrons in crystal lattices. *Proceedings of the Royal Society A: Mathematical, Physical and Engineering Sciences* 130(814), 499–513.
- Kulkarni, R., 1994. The development of the Monte Carlo method for the calculation of the thermoluminescence intensity and the thermally stimulated conductivity. *Radiation Protection Dosimetry* 51(2), 95–105.
- Lapp, T., Jain, M., Thomsen, K. J., Murray, A. S., Buylaert, J.-P., 2012. New luminescence measurement facilities in retrospective dosimetry. *Radiation Measurements* 47(9), 803–808.
- Lehman, R. L., 1963. Crystalline luminescence of cell-nuclear chemicals under ionizing radiation. PhD thesis at the University of California, Lawrence Radiation Laboratory Berkeley, California.
- Madelung, O., 2012. *Introduction to Solid-State Theory*. Vol. 2. Springer Science & Business Media.
- Mandowski, A., Świątek, J., 1992. Monte Carlo simulation of thermally stimulated relaxation kinetics of carrier trapping in microcrystalline and two-dimensional solids. *Philosophical Magazine B* 65, 729–732.

- Mandowski, A., Świątek, J., 1994. Monte Carlo simulation of TSC and TL in spatially correlated systems. Proceedings of 8th International Symposium on Electrets (ISE 8), IEEE, 461–466.
- Mandowski, A., Świątek, J., 1996. On the influence of spatial correlation on the kinetic order of TL. Radiation Protection Dosimetry 65, 25–28.
- Mandowski, A., Świątek, J., 1997. Trapping and recombination properties due to trap clustering. Journal de Physique III 7(12), 2275–2280.
- Mandowski, A., Świątek, J., 1998. Thermoluminescence and trap assemblies - results of Monte Carlo calculations. Radiation Measurements 29, 415–419.
- Mandowski, A., Świątek, J., 2000. The kinetics of trapping and recombination in low dimensional structures. Synthetic Metals 109, 203–206.
- Mandowski, A., 2002. The theory of thermoluminescence with an arbitrary spatial distribution of traps. Radiation Protection Dosimetry 100, 115–118.
- Mandowski, A., 2005. Semi-localized transitions model for thermoluminescence. Journal of Physics D: Applied Physics 38, 17–21.
- Mandowski, A., 2006. Calculation and properties of trap structural functions for various spatially correlated systems. Radiation Protection Dosimetry 119, 85–88.
- Marfunin, A. S., Schiffer, V., 1979. Spectroscopy, luminescence and radiation centers in minerals. Springer Berlin.
- Martini, M., Fasoli, M., Galli, A., 2009. Quartz OSL emission spectra and the role of  $[\text{AlO}_4]^\circ$  recombination centres. Radiation Measurements 44(5), 458–461.
- Martini, M., Fasoli, M., Villa, I., Guibert, P., 2012a. Radioluminescence of synthetic and natural quartz. Radiation Measurements 47(9), 846–850.
- Martini, M., Fasoli, M., Galli, A., Villa, I., Guibert, P., 2012b. Radioluminescence of synthetic quartz related to alkali ions. Journal of Luminescence 132(4), 1030–1036.
- May, C., Partridge, J., 1964. Thermoluminescent kinetics of alpha-irradiated alkali halides. The Journal of Chemical Physics 40(5), 1401–1409.
- McKeever, S. W. S., Strain, J., Townsend, P., Uvdal, P., 1983. Effects of thermal cycling on the TL and radioluminescence of quartz. Specialist seminar on TL and ESR dating. 3, 123–132.
- McKeever, S. W. S., Rhodes, J. F., Mathur, V., Chen, R., Brown, M., Bull, R., 1985a. Numerical solutions to the rate equations governing the simultaneous release of electrons and holes during thermoluminescence and isothermal decay. Physical Review B 32(6), 3835–3843.
- McKeever, S. W. S., Chen, C., Halliburton, L., 1985b. Point defects and the pre-dose effect in natural quartz. Nuclear Tracks and Radiation Measurements (1982) 10(4-6), 489–495.
- McKeever, S. W. S., 1988. Thermoluminescence of solids. Vol. 3. Cambridge University Press.
- Mott, N. F., Gurney, R. W., 1940. Electronic processes in ionic crystals. Clarendon Press.

- Murray, A. S., Wintle, A. G., 2000. Luminescence dating of quartz using an improved single-aliquot regenerative-dose protocol. *Radiation Measurements* 32(1), 57–73.
- Nasdala, L., Götze, J., Hanchar, J. M., Gaft, M., Krbetschek, M. R., Beran, A., Libowitzky, E., 2004. Luminescence techniques in Earth sciences. *Spectroscopic methods in mineralogy* 6, 43–91.
- Oniya, E. O., 2015. Dependence of heating rates of thermal activation on thermal activation characteristics of 110 °C TL peak of quartz: A simulation approach. *Radiation Physics and Chemistry* 115, 171–178.
- Pagonis, V., Kitis, G., Chen, R., 2003. Applicability of the Zimmerman predose model in the thermoluminescence of predosed and annealed synthetic quartz samples. *Radiation Measurements* 37(3), 267–274.
- Pagonis, V., Carty, H., 2004. Simulation of the experimental pre-dose technique for retrospective dosimetry in quartz. *Radiation Protection Dosimetry* 109(3), 225–234.
- Pagonis, V., Chen, R., Wintle, A., 2007a. Modelling thermal transfer in optically stimulated luminescence of quartz. *Journal of Physics D: Applied Physics* 40(4), 998–1006.
- Pagonis, V., Wintle, A., Chen, R., 2007b. Simulations of the effect of pulse annealing on optically-stimulated luminescence of quartz. *Radiation Measurements* 42(10), 1587–1599.
- Pagonis, V., Wintle, A. G., Chen, R., Wang, X. L., 2008a. A theoretical model for a new dating protocol for quartz based on thermally transferred OSL (TT-OSL). *Radiation Measurements* 43, 704–708.
- Pagonis, V., Balsamo, E., Barnold, C., Duling, K., McCole, S., 2008b. Simulations of the predose technique for retrospective dosimetry and authenticity testing. *Radiation Measurements* 43(8), 1343–1353.
- Pagonis, V., Lawless, J. L., Chen, R., Andersen, C., 2009a. Radioluminescence in  $\text{Al}_2\text{O}_3\text{:C}$  - analytical and numerical simulation results. *Journal of Physics D: Applied Physics* 42(17), 175107.
- Pagonis, V., Wintle, A. G., Chen, R., Wang, X. L., 2009b. Simulations of thermally transferred OSL experiments and of the ReSAR dating protocol for quartz. *Radiation Measurements* 44(5), 634–638.
- Pagonis, V., Ankjærsgaard, C., Murray, A., Jain, M., Chen, R., Lawless, J., Greilich, S., 2010. Modelling the thermal quenching mechanism in quartz based on time-resolved optically stimulated luminescence. *Journal of Luminescence* 130(5), 902–909.
- Pagonis, V., Adamiec, G., Athanassas, C., Chen, R., Baker, A., Larsen, M., Thompson, Z., 2011. Simulations of thermally transferred OSL signals in quartz: Accuracy and precision of the protocols for equivalent dose evaluation. *Nuclear instruments and methods in physics research section B: Beam interactions with materials and atoms* 269(12), 1431–1443.
- Pagonis, V., Gochnour, E., Hennessey, M., Knowler, C., 2014. Monte Carlo simulations of luminescence processes under quasi-equilibrium (QE) conditions. *Radiation Measurements* 67, 67–76.

- Pagonis, V., Chen, R., 2015. Monte Carlo simulations of TL and OSL in nanodosimetric materials and feldspars. *Radiation Measurements* 81, 262–269.
- Petrov, S., Bailiff, I., 1995. The 110 °C TL peak in synthetic quartz. *Radiation Measurements* 24(4), 519–523.
- Preusser, F., Chithambo, M. L., Götte, T., Martini, M., Ramseyer, K., Sendezera, E. J., Susino, G. J., Wintle, A. G., 2009. Quartz as a natural luminescence dosimeter. *Earth-Science Reviews* 97(1), 184–214.
- R Core Team, 2017. *R: A Language and Environment for Statistical Computing*. R Foundation for Statistical Computing. Vienna, Austria. <https://www.R-project.org/>,
- Randall, J., Wilkins, M., 1945. Phosphorescence and electron traps. I. The study of trap distributions. *Proceedings of the Royal Society of London A: Mathematical, Physical and Engineering Sciences* 184(999), 366–389.
- Rendell, H., Townsend, P., Wood, R., Luff, B., 1994. Thermal treatments and emission spectra of TL from quartz. *Radiation Measurements* 23(2-3), 441–449.
- Rendell, H., Clarke, M., 1997. Thermoluminescence, radioluminescence and cathodoluminescence spectra of alkali feldspars. *Radiation Measurements* 27(2), 263–272.
- Richter, D., Richter, A., Dornich, K., 2013. Lexsyg - A new system for luminescence research. *Geochronometria* 40(4), 220–228.
- Schilles, T., Poolton, N., Bulur, E., Bötter-Jensen, L., Murray, A., Smith, G., Riedi, P., Wagner, G., 2001. A multi-spectroscopic study of luminescence sensitivity changes in natural quartz induced by high-temperature annealing. *Journal of Physics D: Applied Physics* 34(5), 722–731.
- Schmidt, C., Kreutzer, S., DeWitt, R., Fuchs, M., 2015. Radiofluorescence of quartz: A review. *Quaternary Geochronology* 27, 66–77.
- Schrödinger, E., 1926. Quantisierung als Eigenwertproblem. *Annalen der Physik* 385(13), 437–490.
- Shimizu, N., Mitamura, N., Takeuchi, A., Hashimoto, T., 2006. Dependence of radioluminescence on TL-properties in natural quartz. *Radiation Measurements* 41(7), 831–835.
- Stoneham, D., Stokes, S., 1991. An investigation of the relationship between the 110 °C TL peak and optically stimulated luminescence in sedimentary quartz. *International Journal of Radiation Applications and Instrumentation. Part D. Nuclear Tracks and Radiation Measurements* 18(1-2), 119–123.
- Subedi, B., Kitis, G., Pagonis, V., 2010. Simulation of the influence of thermal quenching on thermoluminescence glow-peaks. *physica status solidi (a)* 207(5), 1216–1226.
- Sunta, C., 2014. *Unraveling Thermoluminescence*. Springer.
- Swendsen, R. H., 2012. *An Introduction to Statistical Mechanics and Thermodynamics*. Oxford University Press.

- Trautmann, T., Krbetschek, M., Dietrich, A., Stolz, W., 1998. Investigations of feldspar radioluminescence: potential for a new dating technique. *Radiation Measurements* 29(3-4), 421–425.
- Trautmann, T., Krbetschek, M., Dietrich, A., Stolz, W., 1999. Feldspar radioluminescence: a new dating method and its physical background. *Journal of Luminescence* 85(1), 45–58.
- Trautmann, T., 2000. A study of radioluminescence kinetics of natural feldspar dosimeters: experiments and simulations. *Journal of Physics D: Applied Physics* 33(18), 2304–2310.
- Vaccaro, G., Panzeri, L., Paleari, S., Martini, M., Fasoli, M., 2017. EPR investigation of the role of germanium centers in the production of the 110 °C thermoluminescence peak in quartz. *Quaternary Geochronology* 39, 99–104.
- Wiedemann, E., 1889. Zur Mechanik des Leuchtens. *Annalen der Physik* 273(6), 177–248.
- Williams, O. M., Spooner, N. A., 2018. Defect pair mechanism for quartz intermediate temperature thermoluminescence bands. *Radiation Measurements* 108, 41–44.
- Wintle, A., 1975. Thermal Quenching of Thermoluminescence in Quartz. *Geophysical Journal International* 41(1), 107–113.
- Yukihara, E. G., McKeever, S. W., 2011. *Optically stimulated luminescence: fundamentals and applications*. John Wiley & Sons.
- Zimmerman, J., 1971. The radiation-induced increase of the 100 °C thermoluminescence sensitivity of fired quartz. *Journal of Physics C: Solid State Physics* 4(18), 3265–3276.

# 2 Solving Ordinary Differential Equations to Understand Luminescence: 'RLumModel', an Advanced Research Tool for Simulating Luminescence in Quartz Using R

Johannes Friedrich<sup>1</sup>, Sebastian Kreutzer<sup>2</sup>, Christoph Schmidt<sup>1</sup>

<sup>1</sup> Chair of Geomorphology & BayCEER, University of Bayreuth, 95440 Bayreuth, Germany

<sup>2</sup> IRAMAT-CRP2A, Université Bordeaux Montaigne, Maison de l'Archéologie, Esplanade des Antilles, 33607 Pessac Cedex, France

*Quaternary Geochronology* 35, 88 – 100, 2016

<https://doi.org/10.1016/j.quageo.2016.05.004>

## Abstract

Kinetic models of quartz luminescence have gained an important role for predicting experimental results and for understanding charge transfers in (natural) quartz.

Here we present and discuss the new **R**-package 'RLumModel', offering an easy-to-use tool for simulating quartz luminescence signals (TL, OSL, LM-OSL and RF) based on five integrated and published parameter sets. Simulation commands can be created (a) using the *Risø Sequence Editor*, (b) a built-in SAR sequence generator or (c) self-explanatory keywords for customised sequences. Results can be analysed seamlessly using the **R**-package 'Luminescence' along with a visualisation of concentrations of electrons and holes in every trap/centre as well as in the valence and conduction band during all stages of the simulation. Examples of simulated luminescence phenomena and dating protocols are given, and the presented code snippets are available in the supplementary material. Package and source code are provided under the General Public License (GPL-3) conditions.

## 2.1 Introduction

Combining theoretical concepts with numerical modelling is an important way in elucidating so far unexplained luminescence behaviour. On the basis of discovered causal mechanisms and model predictions, systematic experimental errors while developing new methods may be avoided. Revealing the mechanisms of charge flow in quartz thus contributes to higher accuracy and precision of luminescence-based dosimetry. More generally, robust model predictions pave the way for hypothesis-driven and directed research, instead of conducting blindly a vast number of non-directed experiments. While experimental results are important to verify or falsify a model's validity, the model itself helps in finding appropriate experiments with its predictions. It is thus an interconnected process between experimental validation and theoretical guidance that puts forward the understanding of luminescence production in quartz.

A proper understanding of luminescence production and its mathematical approximation is a challenge since the early 1930s (e.g., Urbach 1930). It was not until 1945 that Randall & Wilkins (1945) assumed first-order kinetics and used a differential equation to describe the thermoluminescence (TL) process. Three years later, Garlick & Gibson (1948) presented a differential equation for TL assuming second-order kinetics and studied the properties of its solution.

Accounting for the transition between trapped state, conduction band and recombination centre, Halperin & Braner (1960) were the first who suggested a single TL peak based on three coupled first-order differential equations. These equations could not be solved analytically, and simplifying assumptions were needed to solve the equations for certain conditions. However, numerical solutions are required to solve these equations for more complicated cases, which can be done nowadays with affordable computation power. More recently, the theory of TL has been extensively studied and mathematically described by e.g., Chen & McKeever (1997) and McKeever et al. (1997) (cf. for a more detailed summary of the historical development of luminescence models in Chen & Pagonis 2011: Ch. 1.3).

Consequently, during last the 15 years, a vast number of simulations for TL and OSL phenomena based on solving differential equations numerically was published by Adamiec et al. (2004), Adamiec (2005), Chen & Pagonis (2004), Chen et al. (2009, 2011), Chen & Pagonis (2013, 2014), Chruścińska (2009, 2010), Kitis et al. (2006), and Pagonis et al. (2003, 2007, 2008a, 2010, 2011) .

In 2001, Bailey published a comprehensive quartz model, which is able to reproduce a variety of known luminescence phenomena of quartz. In the following years, more specific problems (e.g., TT-OSL by Pagonis et al. (2008a)) were analysed by applying this model with modified parameters (Bailey 2002, 2004; Pagonis et al. 2007, 2008a). In an ideal case, these specific adjustments should at the same time not restrict the model's general applicability (McKeever & Chen 1997), which appears to be partly not the case for all models (see discussion in Section 2.4.2).

Modern computers easily solve coupled differential equations (see next section for details), but the user usually has to adapt a specific programming language. Writing code for efficiently solving a set of differential equations and implementing all model parameters requires enormous effort and is time-consuming. Furthermore, code used for modelling was often written in only commercially available programming frameworks, e.g., *Mathematica*<sup>TM</sup> (Chen & Pagonis 2011; Pagonis et al. 2006) or *MATLAB*<sup>TM</sup> (Chruścińska 2013).

The statistical programming language **R** offers an alternative, open source and free software environment for statistical computing and graphics with the possibility to install add-ons (called 'packages') for different purposes and problems (R Development Core Team 2016).

Here we present an easy-to-use approach for modelling luminescence signals bundled in a new **R**-package called 'RLumModel'. Few commands are sufficient to simulate TL/OSL/RF curves and adapt these simulations to own needs. This contribution is based on unpublished work (Friedrich 2014) and the original code was translated from *MATLAB*<sup>TM</sup> (Friedrich 2014) to **R** and extended to account for more recent developments.

The package 'RLumModel' uses the **R**-package 'deSolve' (Soetaert et al. 2012) for solving differential equations in **R** and further refers to the analysis tools in the **R**-package 'Luminescence' (Dietze et al. 2013; Fuchs et al. 2015; Kreutzer et al. 2012). In contrast to the recently presented work by Peng & Pagonis (2016), no special programming skills are needed to create own simulations and to produce graphical output, and the full integration as **R**-package offers all benefits of this statistical environment (e.g., documentation, complex modification of objects, straightforward graphical output, automatic code validation).

The focus of the presented work lies on the direct transfer of known luminescence scenarios in nature and in the laboratory to the here presented tool, e.g., easy implementation of a SAR sequence as generated by the *Risø Sequence Editor*. The user does neither require a deep understanding of **R** coding nor of solving ordinary differential equations (ODEs). Choosing a sequence and running it with one of the implemented luminescence models directly results in a graphical output.

Further details of the implementation in the package 'RLumModel' are presented below (Sec. 2.4), and a variety of quartz luminescence phenomena is simulated using simple code lines. Additional working scripts as well as all here presented **R** code are given with the supplementary material. Note: Throughout this manuscript, **R** code snippets are typed in monospace letters. To further distinguish between functions originating from other packages than 'RLumModel', these functions are indicated by the package name followed by a doubled double dot (::), e.g., `Luminescence::plot_RLum()` refers to a function called `plot_RLum()` from the **R**-package 'Luminescence'.

## 2.2 Methods

### 2.2.1 Description of implemented luminescence models

All models presented here are based on the energy-band-model for quartz (see Fig. 2.1), which is popular for quartz luminescence simulations. Bailey (2001) published a comprehensive quartz model, which is able to reproduce several TL/OSL phenomena. The original model underwent a lot of modifications since its first publication and the summary of all models implemented in 'RLumModel' is given in Figure 2.1. Note that not every model contains all energy levels shown there and that all models are restricted to the UV emission of quartz. As this contribution is not a review of the individual models, the reader is referred to primary literature (Bailey 2001, 2002, 2004; Pagonis et al. 2007, 2008a) for more detailed information. Table 2.1 shows the implemented electron traps/hole centres for every model by name and level-number in 'RLumModel'. If there is a change between numbering the levels in 'RLumModel' and the particular publication, the original level number is given in italics.

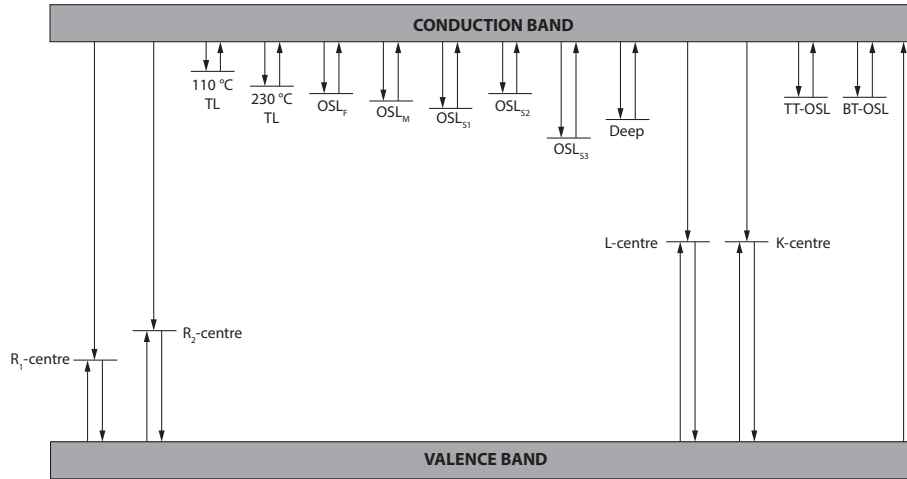


**Figure 2.1:** Comprehensive energy-band-model for quartz, for details see Table 2.1.

All these models are based upon a system of coupled differential equations describing charge transitions within the system. The number of differential equations that needs to be solved depends on the number of electron traps ( $q$ ) and hole centres ( $r$ ). The following differential equations (2.1)-(2.4) are to be solved in a quartz luminescence simulation. A description of the used abbreviations is given in Table 2.2.

$$\frac{dn_i}{dt} = n_c \cdot (N_i - n_i) \cdot A_i - n_i \cdot P \cdot \sigma_{0i} \cdot e^{-E_{th_i}/(k_B \cdot T)} - n_i \cdot s_i \cdot e^{-E_i/(k_B \cdot T)} \quad (2.1)$$

$$\frac{dn_j}{dt} = n_v \cdot (N_j - n_j) \cdot A_j - n_j \cdot s_j \cdot e^{-E_j/(k_B \cdot T)} - n_c \cdot n_j \cdot B_j \quad (2.2)$$

LEVEL	Bailey 2001	Bailey 2002	Bailey 2004	Pagonis et al. 2007	Pagonis et al. 2008b
110 °C TL	1	1	1	1	1
230 °C TL	2	2	2	2	2
OSL <sub>F</sub>	3	3	3	3	3
OSL <sub>M</sub>	4	4	4	4	4
OSL <sub>S1</sub>		5	5		
OSL <sub>S2</sub>		6	6		
OSL <sub>S3</sub>		7	7		
Deep	5	8	8	5	5
TT-OSL					6
BT-OSL					7
R <sub>1</sub> -centre	6	9	<i>11</i>	9	<i>12</i>
R <sub>2</sub> -centre	7	10	<i>12</i>	10	<i>11</i>
K-centre	8	9	<i>11</i>	11	<i>10</i>
L-centre	9	8	<i>12</i>	9	<i>9</i>
NAME IN RLumModel	'Bailey2001'	'Bailey2002'	'Bailey2004'	'Pagonis2007'	'Pagonis2008'

**Table 2.1:** Summary of quartz luminescence traps/centres (levels) in different luminescence models and their numbering. If there is a change in numbering of levels between 'RLumModel' and the particular publication, the original level number is given in italics. The dashed line shows the border between electron traps and hole centres.

$$\frac{dn_c}{dt} = R - \sum_{i=1}^q \left( \frac{dn_i}{dt} \right) - \sum_{j=q+1}^{q+r} (n_c \cdot n_j \cdot B_j) \quad (2.3)$$

$$\frac{dn_v}{dt} = R - \sum_{j=q+1}^{q+r} \left( \frac{dn_j}{dt} \right) - \sum_{j=q+1}^{q+r} (n_c \cdot n_j \cdot B_j) \quad (2.4)$$

Note that Bailey (2001, 2002, 2004) published a different equation for the change in population of holes with time for the valence band, which is not correct in terms of charge neutrality, see Eq. (2.5), which is equal to Eq. (2.4).

$$\begin{aligned} \frac{dn_v}{dt} &= \frac{dn_c}{dt} + \sum_{i=1}^q \left( \frac{dn_i}{dt} \right) - \sum_{j=q+1}^{q+r} \left( \frac{dn_j}{dt} \right) \\ &= R - \sum_{j=q+1}^{q+r} \left( \frac{dn_j}{dt} \right) - \sum_{j=q+1}^{q+r} (n_c \cdot n_j \cdot B_j) \end{aligned} \quad (2.5)$$

Equation (2.4) is taken from Pagonis et al. (2007, 2008a) and also applied for simulations using the models by Bailey (2001, 2002, 2004). The main differences between models are the number and concentration of electron traps ( $q$  and  $N_i$ ), the used pair-production rate  $R$ , the values for the photoionisation cross section  $\sigma$  and the photon flux  $P$ , respectively (see Table 2.3).

2 Solving Ordinary Differential Equations to Understand Luminescence: 'RLumModel', an Advanced Research Tool for Simulating Luminescence in Quartz Using **R**

ABBREVIATION	DESCRIPTION	UNIT
$n_c$	Concentration of electrons in the conduction band	$\text{cm}^{-3}$
$n_v$	Concentration of holes in the valence band	$\text{cm}^{-3}$
$N_i$	Concentration of electron traps	$\text{cm}^{-3}$
$n_i$	Concentration of trapped electrons	$\text{cm}^{-3}$
$s_i$	Frequency factor	$\text{s}^{-1}$
$E_i$	Electron trap depth below the conduction band	eV
$N_j$	Concentration of hole centres	$\text{cm}^{-3}$
$n_j$	Concentration of trapped holes in centres	$\text{cm}^{-3}$
$s_j$	Frequency factor for hole centres	$\text{s}^{-1}$
$E_j$	Hole depth above the valence band	eV
$A_i$	Conduction band to electron trap transition probability	$\text{cm}^3 \text{s}^{-1}$
$A_j$	Valence band to hole centre transition probability	$\text{cm}^3 \text{s}^{-1}$
$B_j$	Conduction band to hole centre transition probability	$\text{cm}^3 \text{s}^{-1}$
$P$	Stimulation photon flux	see discussion below
$\sigma_{0i}$	Photo eviction constant or photoionisation cross section, respectively	see discussion below
$E_{th_i}$	Thermal assistance energy	eV
$k_B$	Boltzmann constant	$\text{eV K}^{-1}$
$T$	Absolute temperature	K
$R$	Ionisation rate (pair production rate)	$\text{cm}^{-3} \text{s}^{-1}$
$t$	Time	s

**Table 2.2:** Description of the abbreviations used in the differential equations.

Bailey (2002, 2004) used absolute photon flux values in units of  $(\text{cm}^2 \cdot \text{s})^{-1}$  for parameter  $P$  and photoionisation cross section values in units of  $\text{cm}^2$  for parameter  $\sigma_{0i}$ . It must be considered that  $\sigma$  itself depends on the wavelength  $\lambda$  of the stimulation light, so that  $\sigma = \sigma(\lambda)$  (Singarayer & Bailey 2004) and that

$$P = \frac{Pd}{h \cdot c} \cdot \lambda,$$

where  $h$  is Planck's constant,  $c$  the speed of light,  $Pd$  is the power density and  $\lambda$  the wavelength of the stimulation light.

All other models (Bailey 2001; Pagonis et al. 2007, 2008a) use the rate of optical excitation of electrons from OSL traps to conduction band ( $\text{s}^{-1}$ ), also called 'photo-eviction constant' (Pagonis et al. 2007), which is the product of the  $P$  and  $\sigma$ . Therefore  $P$  is dimensionless in these models.  $R$  (not to be mixed up with **R**, the name of the programming language) describes the number of produced electron-hole pairs per second and per  $\text{cm}^3$  and is arbitrary (see footnote 4 in Bailey 2001), but the given values in Table 2.3 describe an effective dose rate equivalent to  $1 \text{ Gy s}^{-1}$ .

	Model by author				
	'Bailey2001'	'Bailey2002'	'Bailey2004'	'Pagonis2007'	'Pagonis2008'
Number of electron traps	5	8	8	5	7
Number of hole centres	4	4	4	4	4
Use of $\sigma$	PEC	OCS	OCS	PEC	PEC
$R$ value	5 E+07	3 E+10	2.5 E+10	5 E+07	5 E+07

**Table 2.3:** Differences in implemented quartz luminescence models. 'PEC' means photo eviction constant and 'OCS' optical cross section, see main text.

Luminescence results from recombination of conduction band electrons with trapped holes in luminescence centres (L-centre) and hence the luminescence signal  $L$  is defined as:

$$L = n_c \cdot n_{L\text{-centre}} \cdot B_{L\text{-centre}} \cdot \eta(T) \quad (2.6)$$

$n_{L\text{-centre}}$  is the concentration of hole-populated luminescence centres without specific level numbering in the energy-band-model, because in this work the number of the luminescence centres is different depending on the individual model (see Table 2.1). The same applies to  $B_{L\text{-centre}}$ . In Eq. (2.6),  $\eta(T)$  is the luminescence efficiency factor (Bailey 2001; Wintle 1975), as known from thermal quenching, and can be calculated via

$$\eta(T) = \frac{1}{1 + K \cdot e^{-\frac{W}{k_B \cdot T}}} \quad (2.7)$$

$K$  is a dimensionless constant with the value 2.8 E+7 and  $W$  is the activation energy with 0.64 eV. These values are only valid for the UV-emission in quartz. For further information, the reader is referred to Wintle (1975) and Bailey (2001: footnote 5).

### 2.2.2 Software and integration

All presented quartz models were re-coded from the literature using the statistical programming language **R** (R Development Core Team 2016) and bundled in an own **R**-package 'RLumModel' available under general public licence conditions (GPL-3) on CRAN<sup>1</sup>. The package itself depends on the **R**-package 'Luminescence' (Dietze et al. 2013, 2016; Fuchs et al. 2015; Kreutzer et al. 2012; R Luminescence Development Team 2016), from which it inherits the infrastructure, object structure and functionality. On the opposite, the **R**-package 'Luminescence' (upcoming versions  $\geq 0.6.0$ ) contains the **R**-package 'RLumModel' and comprises a function termed `model_LuminescenceSignals()`, which is identical in grammar and functionality to the function of the same name in the 'RLumModel' package. This structure was chosen to account for two requirements: (1) maximum coding flexibility and (2) seamless and straightforward integration of modelling in the **R**-package

<sup>1</sup><https://cran.r-project.org/package=RLumModel>

'Luminescence'. Therefore, the package 'RLumModel' is of much lighter weight, easy to maintain and can have independent release and development cycles. On the other hand, for users familiar with the existing R-package 'Luminescence' the here presented work will appear as an additional feature that can be directly accessed. By definition, both packages are fully compatible, i.e., objects produced by 'RLumModel' can be directly processed in the R-package 'Luminescence' for further analysis. This is possible because the output value from 'RLumModel' is of class `RLum.Analysis` and thus directly usable by functions from the R-package 'Luminescence'. This functionality will be demonstrated in the examples given below.

All presented simulations were carried out on a standard PC with *Intel i7<sup>TM</sup>* and 16 GB memory on *Windows 7<sup>TM</sup>*. For solving the coupled differential equations, 'RLumModel' uses the ODE solver `lsoda` (part of the R-package 'deSolve', Soetaert et al. (2012)), because it processes initial value problems for stiff or non-stiff systems of first-order ordinary differential equations very fast by switching automatically between stiff and non-stiff problems. A comparison between two different ODE solvers from the package 'deSolve' (`lsoda` and `ode`) results in a computation time of 7.7s for `ode` and 5.7s for `lsoda` on the used system when simulating a TL curve including sample history with identical output (not shown here). Furthermore, as parameter values - relating to the number of electron and hole centres - vary among models, a different configuration also requires a new system of differential equations to be implemented in the code (Peng & Pagonis 2016). With 'RLumModel', the number of coupled differential equations will automatically be adjusted, because of an identifying feature for electron traps and hole centres: An algorithm identifies if  $B_j = 0$  (electron trap, see Section 2.2.1) or  $B_j \neq 0$  (hole trap). For users, it is thus possible to change the available sets or construct own parameter sets with arbitrary numbers of electron traps and hole centres without the need to take care about coding the right syntax of the ODEs, without changing the complete code and without advanced knowledge of R coding.

Additionally, the R-package 'RLumModel' includes software tests to increase the stability of the package. These tests were written using the R-package 'testthat' (Wickham 2011) and are automatically run when building the package before publishing it on CRAN. This ensures a high reliability of the provided R code.

## 2.3 Creating data with 'RLumModel'

The main function for simulating luminescence signals is called `model_LuminescenceSignals()` and requires information on the parameter set to choose, a sequence to be run and further optional parameters to adjust the model output. Figure 2.2 shows the general workflow. The single processes to obtain results from 'RLumModel' and the arguments of the `model_LuminescenceSignals()` function will be described in detail in this section.

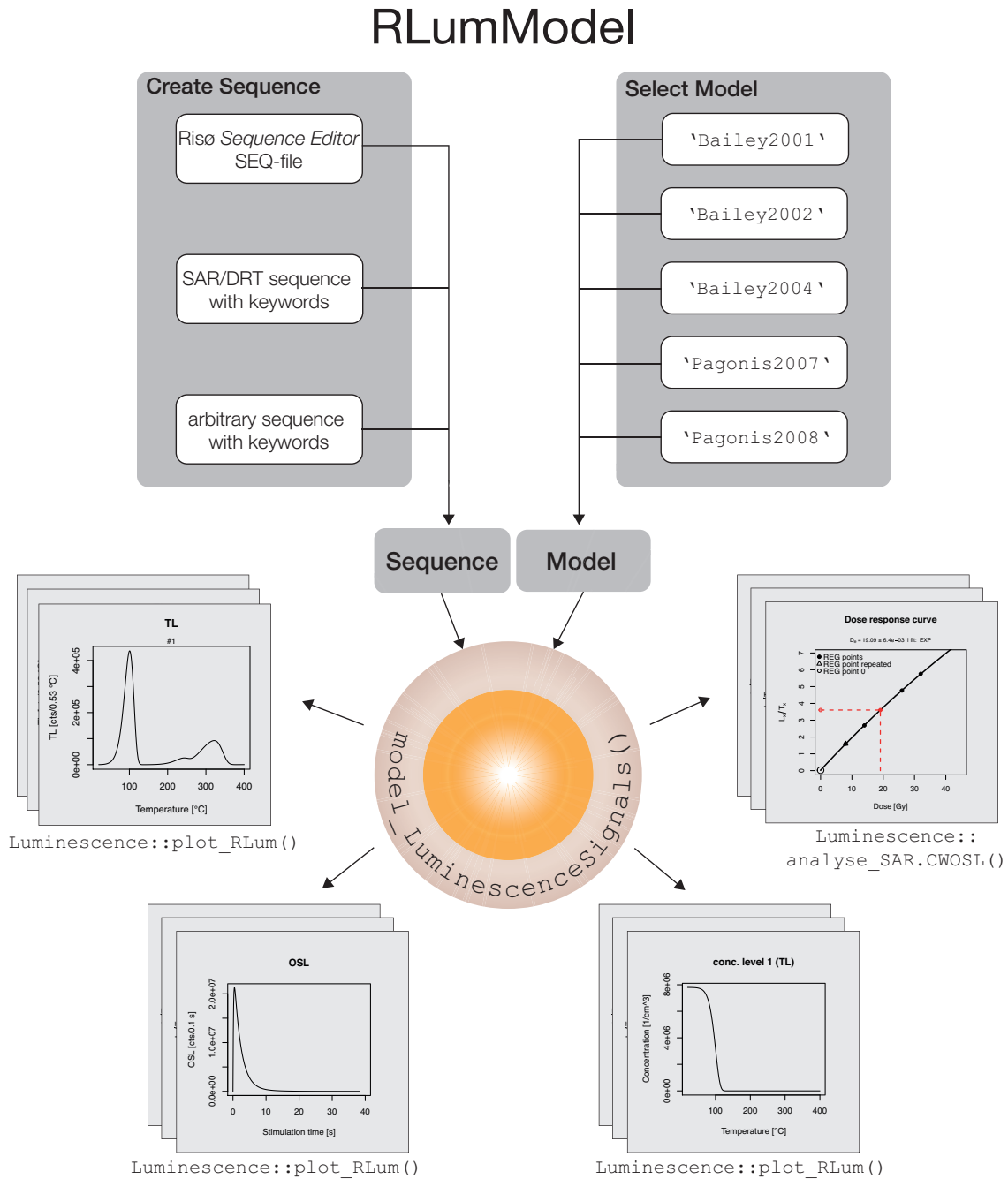


**Figure 2.2:** Flow chart of exemplary data processing in 'RLumModel'.

### 2.3.1 Selecting a quartz luminescence model in 'RLumModel'

The first argument required for the function `model_LuminescenceSignals()` is the name of a quartz luminescence model to be used, respectively the used parameter set in this quartz luminescence model. All currently implemented quartz luminescence models were described in Sec. 2.2.1. The command to select a set of parameters from a specific model in 'RLumModel' is a character string with the name of the author and the year (cf. Table 2.1), e.g.,

```
1 model <- "Bailey2004"
```

The corresponding parameter set will be loaded automatically with the function call.

### 2.3.2 Creating sequences in 'RLumModel'

The second argument in the `model_LuminescenceSignals()` function is the sequence to be simulated. There are three different ways of creating a sequence. The first one is to use the popular and freely available *Risø Sequence Editor version 4.36*<sup>2</sup> to build a personal sequence and to save it as a SEQ-file (\*.seq). Files created by the *Sequence Editor* can be imported directly using the path of the SEQ-file. The package comes along with an example SEQ-file in the package folder in 'extdata'. Thus, a potential sequence is created with

```
1 sequence <- system.file(  
2   "extdata",  
3   "example_SAR_cycle.SEQ",  
4   package = "RLumModel")
```

or wherever the SEQ-file is stored. While in the *Sequence Editor* irradiation is commonly defined in seconds, performing the simulation requires a dose transformation to gray. Therefore, the function `model_LuminescenceSignals()` offers a special argument called `lab.dose_rate`, representing the dose rate of the irradiation unit in the laboratory. By default, this dose rate is  $1 \text{ Gy s}^{-1}$ , but can be modified, e.g.,

```
1 lab.dose_rate <- 0.105
```

The second way of creating a sequence is by referring to a list with keywords and a certain order of code numbers or named values, which are given in Table 2.4. With these keywords, it is possible to create quickly an R object of type `list`, which can be read by the `model_LuminescenceSignals()` function. Example:

```
1 sequence <- list(  
2   IRR = c(temp = 20, dose = 10, dose_rate = 1),  
3   TL = c(temp_begin = 20, temp_end = 400, heating_rate = 5))
```

---

<sup>2</sup>[http://www.nutech.dtu.dk/english/Products-and-Services/Dosimetry/Radiation-Measurement-Instruments/TL\\_OSL\\_reader/Software;2016-04-11](http://www.nutech.dtu.dk/english/Products-and-Services/Dosimetry/Radiation-Measurement-Instruments/TL_OSL_reader/Software;2016-04-11)

This sequence describes an irradiation simulation at 20 °C with a dose of 10 Gy and a dose rate of 1 Gy s<sup>-1</sup>, which is followed by a TL simulation from 20 °C to 400 °C with a heating rate of 5 °C s<sup>-1</sup>. Note that it is important that for each sequence keyword like 'IRR' or 'TL' either the vector has to be named or the correct order of arguments is requested, see 'sub-arguments' in Table 2.4. Henceforth only the ordered way of typing arguments is used. Thus the above mentioned code is equivalent to the following one:

```
1 sequence <- list(
2   IRR = c(20, 10, 1),
3   TL = c(20, 400, 5))
```

ARGUMENTS	DESCRIPTION	SUB-ARGUMENTS
TL	Thermally stimulated luminescence	'temp_begin', 'temp_end', 'heating_rate'
OSL	Optically stimulated luminescence	'temp', 'duration', 'optical_power'
ILL	Illumination	'temp', 'duration', 'optical_power'
LM_OSL	Linear modulated OSL	'temp', 'duration', optional: 'start_power', 'end_power'
RF	Radiofluorescence	'temp', 'dose', 'dose_rate'
IRR	Irradiation	'temp', 'dose', 'dose_rate'
CH	Cutheat	'temp', optional: 'duration', 'heating_rate'
PH	Preheat	'temp', 'duration', optional: 'heating_rate'
PAUSE	Pause	'temp', 'duration'

**Table 2.4:** Keywords for creating a sequence in 'RLumModel'. Note that 100 % optical power equals to 20 mW cm<sup>-2</sup> (Bailey 2001). Values > 100 % are allowed.

However, creating a SAR or dose-recovery-test (DRT) sequence with the *Risø Sequence Editor* or with keywords is time-consuming, because it contains a lot of individual sequence steps (preheat, optical stimulation, irradiation, ...). Therefore, a third way was implemented in 'RLumModel' to create a SAR sequence after Murray & Wintle (2000) applying the (required) keywords `RegDose`, `TestDose`, `PH`, `CH` and `OSL_temp`. In addition to these keywords, the user is able to set more detailed parameters for the SAR sequence, see Table 2.5:

```
1 sequence <- list(
2   RegDose = c(0, 10, 20, 50, 90, 0, 10),
3   TestDose = 5,
4   PH = 240,
5   CH = 200,
6   OSL_temp = 125)
```

To simulate a DRT, the user has to add the keyword `Irr_2recover` and a value in the list of instructions. This will create a sequence for a DRT with the value of `Irr_2recover` as the dose to recover (given dose). When choosing this kind of sequence generation, an illumination at 125 °C for 70s is simulated to reset the 'natural' signal defined by the sample history (see Sec. 2.3.3). Here the period of 70s was chosen to sufficiently deplete the natural signals; with regard to the implemented models, after 70s < 1 % of initial intensity remains. An example is given in Sec. 2.4.2.

ABBREVIATION	DESCRIPTION	EXAMPLE ARGUMENTS
RegDose	Dose points of the regenerative cycles [Gy]	c(0, 80, 140, 260, 320, 0, 80)
TestDose	Test dose for the SAR cycles [Gy]	50
PH	Temperature of the preheat [ $^{\circ}$ C]	240
CH	Temperature of the cutheat [ $^{\circ}$ C]	200
OSL_temp	Temperature of OSL read out [ $^{\circ}$ C]	125
OSL_duration	Duration of OSL read out [s]	default: 40
Irr_temp	Temperature of irradiation [ $^{\circ}$ C]	default: 20
PH_duration	Duration of the preheat [s]	default: 10
dose_rate	Dose rate of the laboratory irradiation source [ $\text{Gy s}^{-1}$ ]	default: 1
optical_power	Percentage of the full illumination power [%]	default: 90
Irr_2recover	Dose to be recovered in a dose-recovery-test [Gy]	20

**Table 2.5:** Keywords for creating a SAR sequence with 'RLumModel'. The keyword `Irr_2recover` is only necessary for creating a DRT sequence. Note that 100% optical power equals to  $20 \text{ mW cm}^{-2}$  (Bailey 2001). Values  $> 100\%$  are allowed.

For all sequences, temperature differences between sequence steps are automatically simulated with a heating or cooling step in between. Also, after irradiating the sample, it is automatically kept at irradiation temperature for further 5 s to allow the system to relax prior to the next step (Bailey 2001).

### 2.3.3 Deep control of sample history

All models apply different so-called 'sample histories' to simulate the geological past of natural sedimentary quartz grains, starting with crystallisation, meaning that all traps are empty. Usually, simplified sequences consisting of irradiation, bleaching and heating aim at mimicking sedimentary cycles in geological timescales, and due to increased computation power in the last decade it was possible to simulate very small irradiation dose rates over geological timescales with acceptable computation times (Bailey 2004). In contrast to the usage of very low natural dose rates, Bailey (2001) suggested the simulation of irradiation at higher temperatures, because high dose rate irradiation at  $220^{\circ}\text{C}$  was found to adequately mimic the observation of low/zero populations in both shallow electron and hole trapping centres. Measurements of natural quartz samples appear to confirm this assumption (Bailey 2001). Nevertheless, each model uses a unique sample history simulation. Table 2.6 summarises published sample histories (Bailey 2001, 2002, 2004; Pagonis et al. 2007, 2008a).

Using a luminescence model to simulate measurements in the laboratory asks for an already completed sample history. The user of the `model_LuminescenceSignals()` function has the choice of simulating a sample history within the created sequence or not. All sample histories of the five luminescence models were run and the results are stored within the package. When choosing the function argument `simulate_sample_history = FALSE` (the default) the stored results of  $n_i, n_j, n_c, n_v$  at the end of the sample history are recalled for further calculations. Thus, the written sequence is directly used for simulating a measurement in the laboratory of a sample with mimicked geological history. In contrast to

MODEL	SAMPLE HISTORY
Bailey 2001	crystallisation → 1000 Gy using 1 Gy s <sup>-1</sup> at 20 °C (geological dose) → heat to 350 °C (geological time) → illuminate at 200 °C for 100 s (repeated daylight exposure) → 20 Gy using 0.01 Gy s <sup>-1</sup> at 220 °C (burial dose)
Bailey 2002	crystallisation → 2 kGy using 200 Gy s <sup>-1</sup> at 250 °C (geological dose) → illuminate at 250 °C for 5 ks (repeated daylight exposure) → 10 Gy using 0.01 Gy s <sup>-1</sup> at 220 °C (burial dose)
Bailey 2004	crystallisation → 50 Ma using 1 Gy ka <sup>-1</sup> at 20 °C (geological dose) → 10 cycles of 10 ka irradiation using 1 Gy ka <sup>-1</sup> at 20 °C + 6000 s illumination → 'palaeodose' using 1 Gy ka <sup>-1</sup> at 20 °C (burial dose)
Pagonis 2007	same as Bailey 2001
Pagonis 2008	crystallisation → 1000 Gy using 1 Gy s <sup>-1</sup> at 20 °C (geological dose) → heat to 350 °C (geological time) → illuminate at 200 °C for 100 s (repeated daylight exposure) → 200 Gy using 0.01 Gy s <sup>-1</sup> at 220 °C (burial dose)

**Table 2.6:** Summary of sample histories for models implemented in 'RLumModel'.

that, the user can choose `simulate_sample_history = TRUE` and create a customised sample history by writing a new sequence. Note that in Bailey (2004) the palaeodose was variable, but is set to 20 Gy in the `model_LuminescenceSignals()` function. If another palaeodose is desired, the user is invited to write an adjusted sample history sequence, as described in Sec. 2.3.2 and `simulate_sample_history = TRUE`.

## 2.4 Working examples

In this section, detailed examples for simulating quartz luminescence signals with different stimulation modes (TL, OSL, and RF) are presented. All code lines can be easily modified by the user to obtain customised results.

### 2.4.1 Simulating general TL/OSL/RF phenomena

#### 2.4.1.1 Simulating a TL curve and shift of TL peak with varying heating rate

First of all, a sequence is needed, which produces a TL signal after the sample has received a dose:

```
1 sequence <- list(
2   IRR = c(20, 10, 1),
3   TL = c(20, 400, 5))
```

Here, at a temperature of 20 °C a dose of 10 Gy was applied with a dose rate of 1 Gy s<sup>-1</sup> followed by a TL measurement from 20 °C to 400 °C with a heating rate of 5 °C s<sup>-1</sup>.

Running this sequence with the `model_LuminescenceSignals()` function produces a model output:

```
1 model.output <- model_LuminescenceSignals(  
2   model = "Bailey2001",  
3   sequence = sequence)
```

This results in a TL curve like the one published in Bailey (2001: Fig. 1), see Fig. 2.3. In a further step, known TL phenomena like the shift of the TL peak with varying heating rate are simulated (Fig. 2.4). For this purpose, a loop over a TL simulation changes the heating rate in each run. The code for this simulation is shown in the supplementary material (Sec. A.1), code example 2.4.1.1. With the modelling tool 'RLumModel' it is also possible to plot the temporal evolution of electron and hole concentrations in traps/centres and the delocalised bands ( $n_i, n_j, n_c, n_v$ ) in the course of TL, CW-OSL, LM-OSL, and RF simulations. Therefore, the model output of `model_LuminescenceSignals()` is directly transferred to the function `Luminescence::plot_RLum()` as argument `object`. The argument `subset` can be used to limit the object to be analysed.

The following code returns  $n_i, n_j, n_c$  and  $n_v$  as a function of  $T$ , as resulting from a TL simulation. Note the brackets "(TL)", which ensure that the concentrations and not the TL curve will be plotted here:

```
1 plot_RLum(  
2   object = model.output,  
3   subset = list(  
4     recordType = "(TL)"))
```

The function `Luminescence::plot_RLum()` fully supports all common **R** plot arguments, e.g., `col` or `type` (R Development Core Team 2016) and special 'Luminescence' arguments like `norm = TRUE` to normalise to the highest value (R Luminescence Development Team 2016). An overview of all records can be obtained with the function `Luminescence::structure_RLum()`. To obtain the electron concentration in the 110 °C TL trap, addressing this level is possible with the following code:

```
1 plot_RLum(  
2   object = model.output,  
3   subset = list(  
4     recordType = "conc. level 1 (TL)"))
```

The resulting plot is shown in Fig. 2.5 and, as expected, the concentration of electrons decreases abruptly at a temperature of  $\sim 100$  °C. A further example of this function is given in Sec. 2.4.1.5.

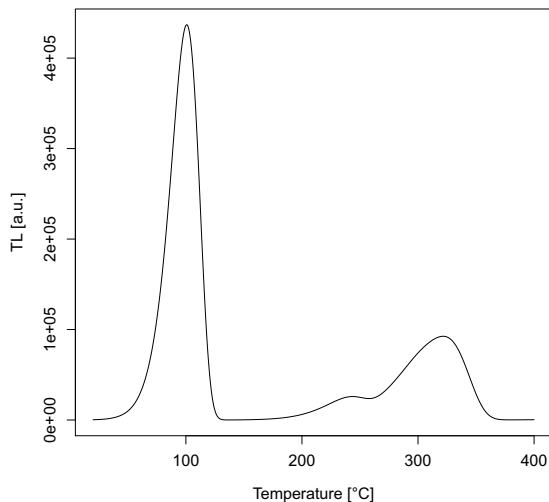


**Figure 2.3:** TL curve simulation after 'Bailey2001'.

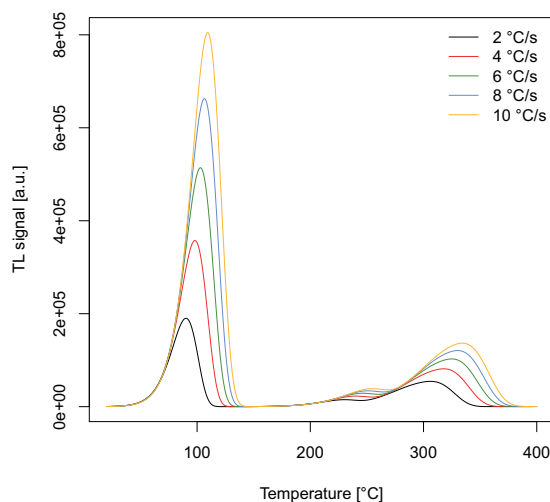


**Figure 2.4:** Shift of TL peaks with varying heating rates using parameters from 'Bailey2001'.

#### 2.4.1.2 Simulating thermal activation characteristics (TACs)

Another frequently simulated phenomenon is the sensitisation of quartz TL by  $\beta$ - or  $\gamma$ -irradiation followed by activation at high temperatures (annealing; Adamiec et al. 2004; Pagonis et al. 2003, 2008b; Zimmerman 1971), termed as thermal activation characteristics (TACs). For a simulation sequence, the reader is referred to Pagonis et al. (2008b: Table 1). To simulate this phenomenon with the `model_LuminescenceSignals()` function, a loop causing a stepwise increase of the activation temperature is needed. The resulting intensity of the 110°C TL peak can be plotted against the activation temperature, see Fig. 2.6, which shows TAC for the model parameters of 'Pagonis2007'. TACs can be created from every other model presented here by changing the name of the model in the `model_LuminescenceSignals()` function. The complete running example is given in the supplementary material (Sec. A.1), code example 2.4.1.2.

#### 2.4.1.3 Simulating dependency of the OSL signal on the illumination power density

The function `model_LuminescenceSignals()` is also capable of simulating OSL phenomena. Figure 2.7 shows the dependency of the OSL signal on the power density of illumination ( $P$ , see Table 2.2) for the model 'Bailey2004'. Here, a loop over different power densities was used, as to see in the code example 2.4.1.3 in the supplementary material (Sec. A.1). The inset in Fig. 2.7 demonstrates the linear relationship between normalised OSL (normalised to unity at the count-rate measured using the maximum power) and illumination power density in the range 0 – 200 mW cm<sup>-2</sup>. This simulation followed Bailey (2001: Fig. 14), but with the parameter set from 'Bailey2004'.

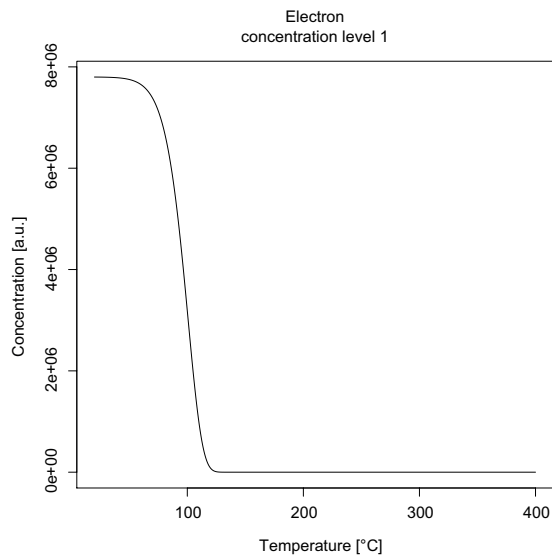


**Figure 2.5:** Change of electron concentration in the 110 °C TL trap while simulating TL after 'Bailey2001'.

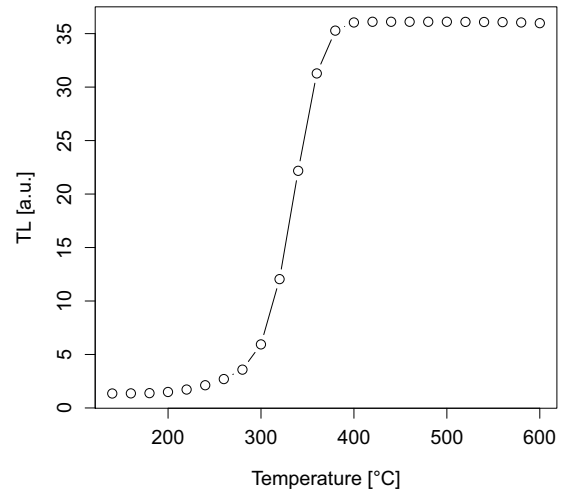


**Figure 2.6:** Simulated thermal activation characteristics (TAC) of the 110 °C TL signal for the model and parameter set by 'Pagonis2007'.

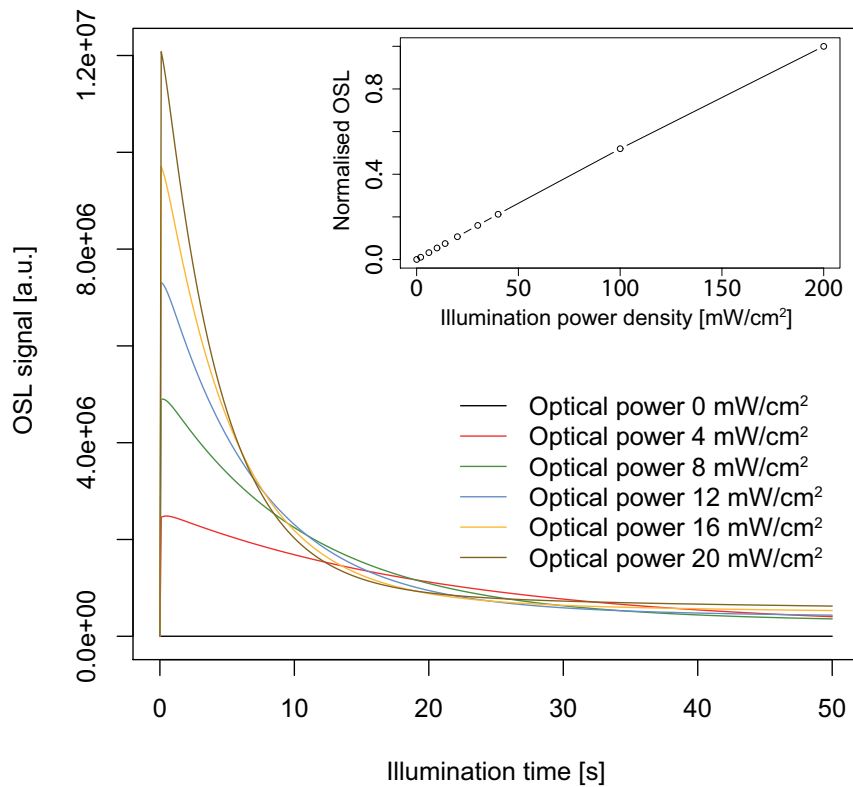


**Figure 2.7:** Dependency of the OSL signal on the illumination power density for the parameter set 'Bailey2004'. The inset shows the linearity of the initial 0.1 s of the OSL signal with increasing illumination power density.

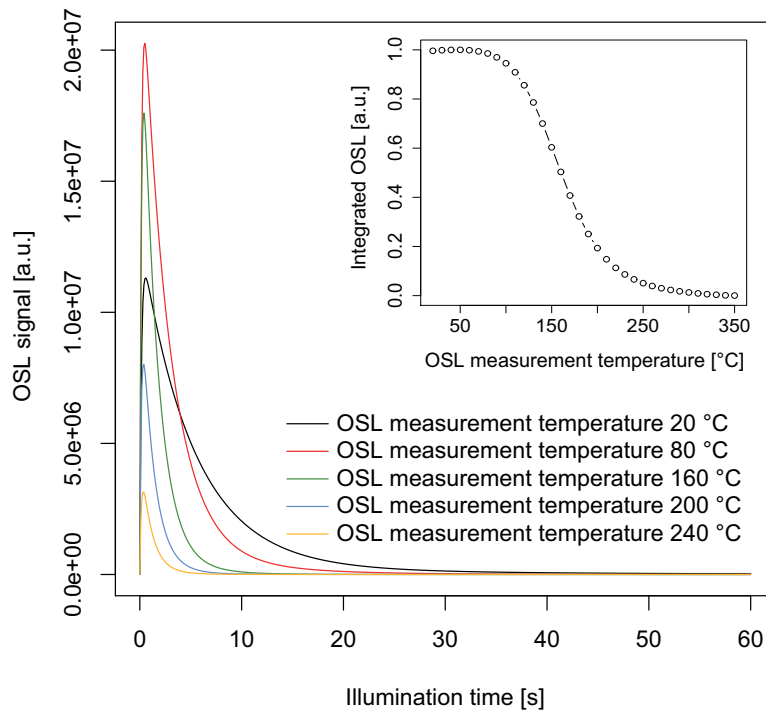


**Figure 2.8:** Temperature dependence of the OSL signal as simulated with the 'Bailey2001' model for different measurement temperatures. The inset plots the integrated OSL (0 – 60 s) against measurement temperature.

#### 2.4.1.4 Temperature dependence of the OSL signal

Another known OSL observation is the thermal dependency of the quartz OSL signal shape and intensity and the associated phenomena of thermal quenching and thermally assisted detrapping (McKeever et al. 1997; Spooner 1994). The simulation by Bailey (2001) can be reproduced (see Sec. A.1, code example 2.4.1.4) and the results are shown in Fig. 2.8 and are in good accordance with experimental results (McKeever et al. 1997). Flexible data handling allows, for instance, plotting the integrated OSL signal against OSL stimulation temperature (inset of Fig. 2.8). This phenomenon is known as 'thermal quenching' and is typical for quartz (Huntley et al. 1996; Spooner 1994; Wintle 1975).

#### 2.4.1.5 Simulating quartz radiofluorescence (RF)

Radiofluorescence occurs while ionizing radiation due to the recombination of conduction band electrons with trapped holes (Schmidt et al. 2015). Hence Eqs. (2.1) – (2.4) describe theoretically the mechanism of radiofluorescence. Bailey (2001: Sec. 3.4.4) published a simulation of radiofluorescence of quartz and he suggested that the form of the RF curve is strongly linked to the population of one of the reservoir centres. He showed this by plotting the hole concentration of the reservoir centre  $R_1$  along with the shape of the RF curve (Bailey 2001: Fig. 12). With the package 'RLumModel', it is easy to reproduce the results with the following code:

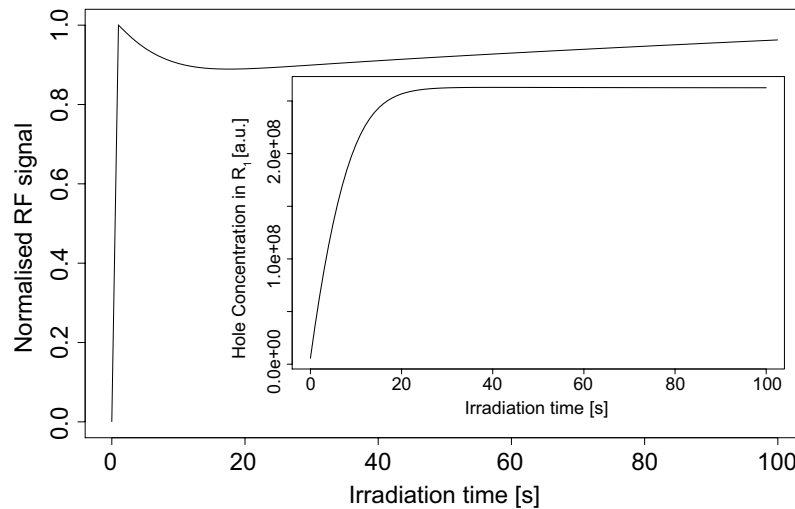


**Figure 2.9:** RF simulation and concentration of holes in the reservoir centre  $R_1$  (inset) as resulting from the 'Bailey2001' model (Bailey 2001: Fig. 12).

```

1 sequence = list(RF = c(20, 100, 1))
2
3 model.output <- model_LuminescenceSignals(
4   model = "Bailey2001",
5   sequence = sequence,
6   norm = TRUE)

```

This code describes an RF simulation at 20 °C with a dose of 100 Gy and a dose rate of 1 Gy s<sup>-1</sup>. The extra argument `norm = TRUE` normalises the data to the highest value. The function `plot_RLum` yields the hole concentration in the reservoir centre  $R_1$  (level 6, see Table 2.1) as a function of dose. These few lines of code result in Fig. 2.9:

```

1 plot_RLum(
2   object = model.output,
3   subset = list(recordType = "conc. level 6 (RF)"))

```

## 2.4.2 Simulating and analysing SAR measurements

The focus of this work is the simulation of luminescence signals used for retrospective dosimetry, especially in the course of SAR measurements. The SAR protocol according to Murray & Wintle (2000) aims at determining the radiation dose received by a sample since its last sunlight exposure or heating above 350 °C, known as equivalent dose  $D_e$ . How to write a sequence for a SAR/DRT simulation was mentioned in Sec. 2.3.2. This section gives some detailed examples and shows the implementation in the **R**-package 'Luminescence'. In the following, a complete SAR measurement is simulated, including a preheat-plateau-test (PHPT) and a DRT. The combined PHPT and DRT will yield the appropriate preheat temperature at which a certain dose is best reproducible. For the whole simulation in this section, the model 'Pagonis2008' is chosen, implying a burial dose of 200 Gy (Table 2.6).

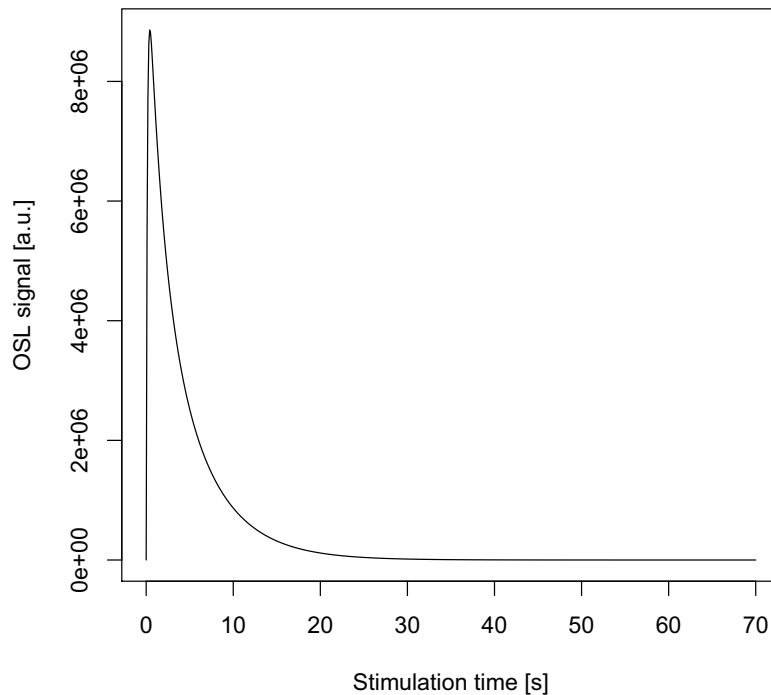


**Figure 2.10:** Resetting of the natural signal with the model 'Pagonis2008' in the DRT sequence.

For simulating a DRT, it is necessary to define a sequence with the keyword `Irr_2recover`, as mentioned in Sec. 2.3.2. As can be seen in Fig. 2.10, the natural OSL signal is completely erased with this sequence.

It should be mentioned that a simulation of a combined PHPT and DRT may be very time-consuming, because for every preheat temperature a complete SAR cycle has to be run. A typical DRT sequence featuring various PH temperatures in 'RLumModel' is listed below. Note that in such a DRT simulation a loop over different preheat temperatures has to be written, utilising characteristic parameters from the literature. The test dose is set to 10% and the regeneration dose points to 40%, 70%, 130%, 160%, 0% and 40% of the recovery dose. The data created by 'RLumModel' can be directly passed to the functions `Luminescence::analyse_SAR.CWOSL()` and `Luminescence::plot_DRTResults()` for routine analyses and plotting.

```

1  ##set PH temperatures
2  PH_temp <- seq(from = 160, to = 300, by = 20)
3
4  ##set regeneration doses
5  RegDose = c(0, 80, 140, 260, 320, 0, 80)
6
7  ##loop over PH temperatures
8  DRT.output <- lapply(1:length(PH_temp), function(x) {
9
10   sequence <- list(

```

## 2 Solving Ordinary Differential Equations to Understand Luminescence: 'RLumModel', an Advanced Research Tool for Simulating Luminescence in Quartz Using R

---

```
11     RegDose = RegDose,
12     TestDose = 20,
13     PH = PH_temp[x],
14     CH = PH_temp[x],
15     OSL_temp = 125,
16     Irr_2recover = 200)
17
18 model.output <- model_LuminescenceSignals(
19     sequence = sequence,
20     model = "Pagonis2008",
21     plot = FALSE,
22     verbose = FALSE)
23
24 results <- analyse_SAR.CWOSL(
25     object = model.output,
26     signal.integral.min = 1,
27     signal.integral.max = 7,
28     background.integral.min = 301,
29     background.integral.max = 401,
30     fit.method = "EXP",
31     dose.points = RegDose,
32     plot = FALSE)
33
34 temp <- get_RLum(results)
35 out <- data.frame(
36     De = temp$De,
37     De.error = temp$De.Error)
38
39 return(out)
40 })
41
42 ##output as data.frame for plot_DRTResults
43 DRT.result <- as.data.frame(do.call(rbind,DRT.output))
44
45 ##plot DRT.results
46 plot_DRTResults(
47     DRT.result,
48     preheat = PH_temp,
49     given.dose = 200)
```

In the code above in line 32, `plot = FALSE` was chosen, because a single OSL plot is not necessary to analyse a SAR sequence. To calculate a  $D_e$  from the produced `RLum.Analysis` object `model.output`, the function `Luminescence::analyse_SAR.CWOSL()` is suitable. After specifying a number of evaluation parameters (signal and background integration interval, dose points and fit function for the dose response curve) and the analysis process, the reduced data are stored in an `RLum.Results` object, here termed `results`. A background integration interval from 301 to 401 translates to the signal from 30 s to 40 s, because a channel has the default width of 0.1 s. Accordingly, the signal integral ranges from

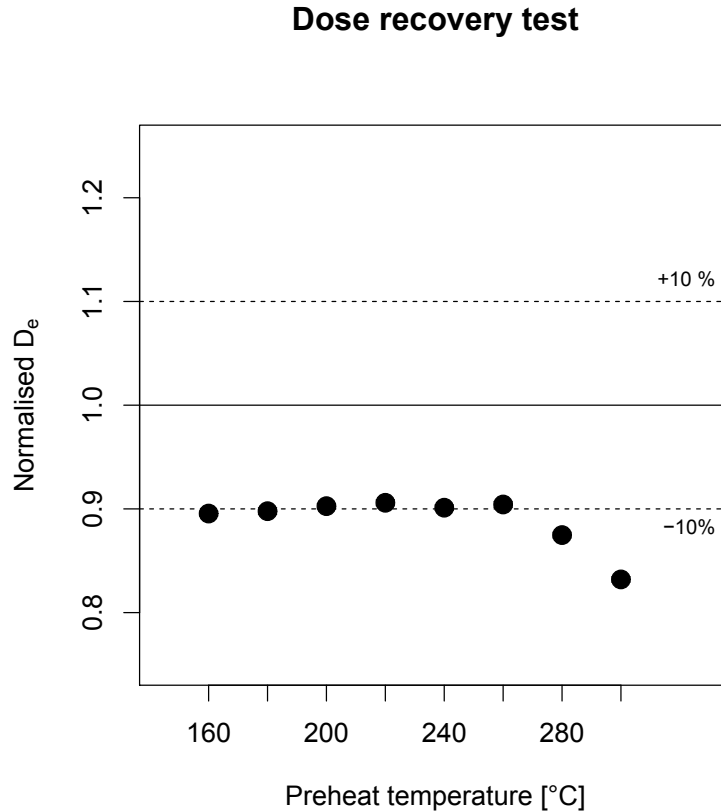


**Figure 2.11:** DRT results for the model 'Pagonis2008'. Every data point is the result of a  $D_e$  estimation with a specific preheat temperature, see main text. The errors of the  $D_e$  values are so small, that they do not appear in this plot.

0.1 s to 0.7 s. This results in a plot with three parts. Part one includes all OSL and - if the preheat was a TL measurement - all TL curves, giving an optical summary of the simulated data and the chosen integral limits (not shown here). Part two shows the dose response curve and the calculated  $D_e$ , the  $D_e$  distribution following a Monte-Carlo simulation for estimating the standard error, and the evolution of the test dose response throughout the SAR sequence (Fig. 2.12). Part three illustrates the rejection criteria (recycling ratio, recuperation and standard error of the  $D_e$ , not shown here). The performance of the DRT for a given dose of 200 Gy with the above mentioned parameters is shown in Fig. 2.11. The given dose of 200 Gy is always underestimated but the limits of 10 % deviation from the recovery dose, a preheat and cutheat temperature of 220 °C was adopted for the SAR measurement.

For determining a  $D_e$  from 'natural' signals, generally the same code as described here applies (just without `Irr_2recover`). An executable example of a SAR cycle is given in the supplementary material (Sec. A.1), code example 2.4.2b. Figure 2.12 shows the dose response curve for the 'Pagonis2008' model with a burial dose of 200 Gy (see Table 2.6). The model 'Pagonis2008' returns a  $D_e$  of  $122.7 \pm 0.31$  Gy for a burial dose of 200 Gy after

simulating the SAR protocol. This implies a significant dose underestimation of this SAR sequence, although the most appropriate preheat temperature was chosen. Higher test doses yielded a better DRT but do not result in a proper  $D_e$  estimation. It is striking that the sensitivity changes as indicated by the test dose response for every SAR cycle are substantial (Fig. 2.12). It implies that this model is successful in simulating TT-OSL, but not in accurately measuring a burial dose with the SAR protocol for the pre-defined sample history.

To show the reproducibility of a burial dose from one of the implemented models with 'RLumModel', the model 'Bailey2001' was chosen. Here, a DRT was simulated in the same way as in the example mentioned above. Applying a preheat temperature of 240 °C, a cutheat temperature of 200 °C and a test dose of 2 Gy, a SAR sequence was simulated, giving a  $D_e$  of  $18.72 \pm 9 \times 10^{-3}$  Gy. The accuracy of this model to reproduce a burial dose of 20 Gy using the SAR protocol is thus better than 10 %. Sensitivity changes as deduced from the test dose response are much lower than for the 'Pagonis2008' model.

A cross-check of the results of the SAR protocol for different models with different burial doses was simulated. Therefore the sample history of model 'Bailey2001' was changed to a burial dose of 200 Gy and then a combined PHPT and DRT and subsequently a SAR protocol are simulated. The DRT results in very good behaviour in terms of dose recovery, but the SAR protocol shows a  $D_e$  of  $57.02 \text{ Gy} \pm 0.02 \text{ Gy}$ . In contrast to that, the 'Pagonis2008' model, simulated with a burial dose of 20 Gy and the best preheat temperature according to the PHPT, shows a  $D_e$  of  $18.52 \pm 0.02 \text{ Gy}$  and thus an acceptable result in terms of obtaining the correct burial dose (data not shown here).

## 2.5 Discussion and conclusions

The new **R**-package 'RLumModel' was presented, enabling an efficient and user-friendly simulation of quartz luminescence signals based on the energy-band-model. To date, the package includes five models reported in the literature to simulate specific quartz luminescence phenomena (Bailey 2001, 2002, 2004; Pagonis et al. 2007, 2008a). Several options are provided to create a sequence to be simulated: (I) with the *Risø Sequence Editor* (version 4.36) and direct use of the \*.SEQ file as function input, (II) with a list of keywords for the step to be simulated (e.g., IRR, TL, ...) and a named or sorted vector, (III) with SAR and DRT templates. Once a model is chosen and a sequence created, only one function call is necessary to obtain simulation results. 'RLumModel' automatically loads the **R**-package 'Luminescence' to evaluate the model output.

It was shown that several TL, OSL, and RF phenomena from published literature can be easily reproduced, demonstrating the suitability of this new model tool. The function `Luminescence::plot_RLum()` allows tracing the charge population of each trapping site and the delocalised bands throughout all stages of the simulation as well as plotting TL, OSL, and RF curves from the simulations. The quartz luminescence models implemented

in 'RLumModel' are adopted without any quality test for their validity. With 'RLumModel' it is now possible to compare different luminescence models and show their strengths and weaknesses for different research questions. The calculations of the simulations may be not as fast as in other publications like 'KMS' (Peng & Pagonis 2016) but 'RLumModel' offers maximum flexibility, e.g., in creating own parameter sets without deep **R**-coding and in analysing the results with existing routines like the **R**-package 'Luminescence' (R Luminescence Development Team 2016).

It should be noted that in addition to the modelling approach making use of differential equations derived from the energy-band-model, there exist other, so far less popular, concepts of quartz luminescence. Itoh et al. (2002) presented a model based on defect pairs rather than trapped electrons and holes, which can, e.g., explain the 110 °C and 325 °C TL peak in quartz. By contrast, Mandowski & Świątek (1992, 1998, 2000) published a luminescence model for TL based on Monte-Carlo calculations, which are common in statistical physics. According to that, Pagonis et al. (2014) presented a simplified Monte-Carlo method for TL and LM-OSL simulations.

The here presented work cannot replace own experimental work that may lead to a better understanding of quartz luminescence phenomena. However, simulations are capable of supporting a proper experimental design, making them more efficient and potentially less time-consuming. Therefore, hypotheses driven experimental work can be more clearly defined and tested.

## Acknowledgements

We thank Vasilis Pagonis for his support via e-mail. The initial work for this contribution in summer 2014 was gratefully supported by two complementary projects entitled "*Radiofluorescence of quartz: Challenges towards a dating application*" (DFG, SCHM 3051/2-1 und FU 417/16-1 and DAAD-PPP USA, Prof. Dr. Markus Fuchs, id: 56022859). The work of JF is now supported by the DFG (project "*Modelling quartz luminescence signal dynamics relevant for dating and dosimetry*", SCHM 3051/4-1). The work of SK would not have been possible without support by the LaScArBx. LaScArBx is a research programme supported by the ANR (ANR-10-LABX-52). The authors acknowledge invaluable support by the **R**-'Luminescence' team.

## Nota bene

In the course of the preparation of this contribution in October 2015, the authors had been in e-mail contact with Vasilis Pagonis and Peng Jun. Thanks to the open communication, the authors gained knowledge of parallel work on a translation of existing quartz luminescence models originally implemented in *Mathematica*<sup>TM</sup> to **R** (KMS: Kinetic Model Simulations, <https://github.com/pengjunUCAS/KMS>, Peng & Pagonis 2016). Due to the very

different development stages, the type and focus of the integration, it was decided to proceed separately. Herewith we state that our R coding was carried out independently, mostly in summer 2015. None of the R code published on *GitHub*<sup>TM</sup> for the 'KMS' was used.

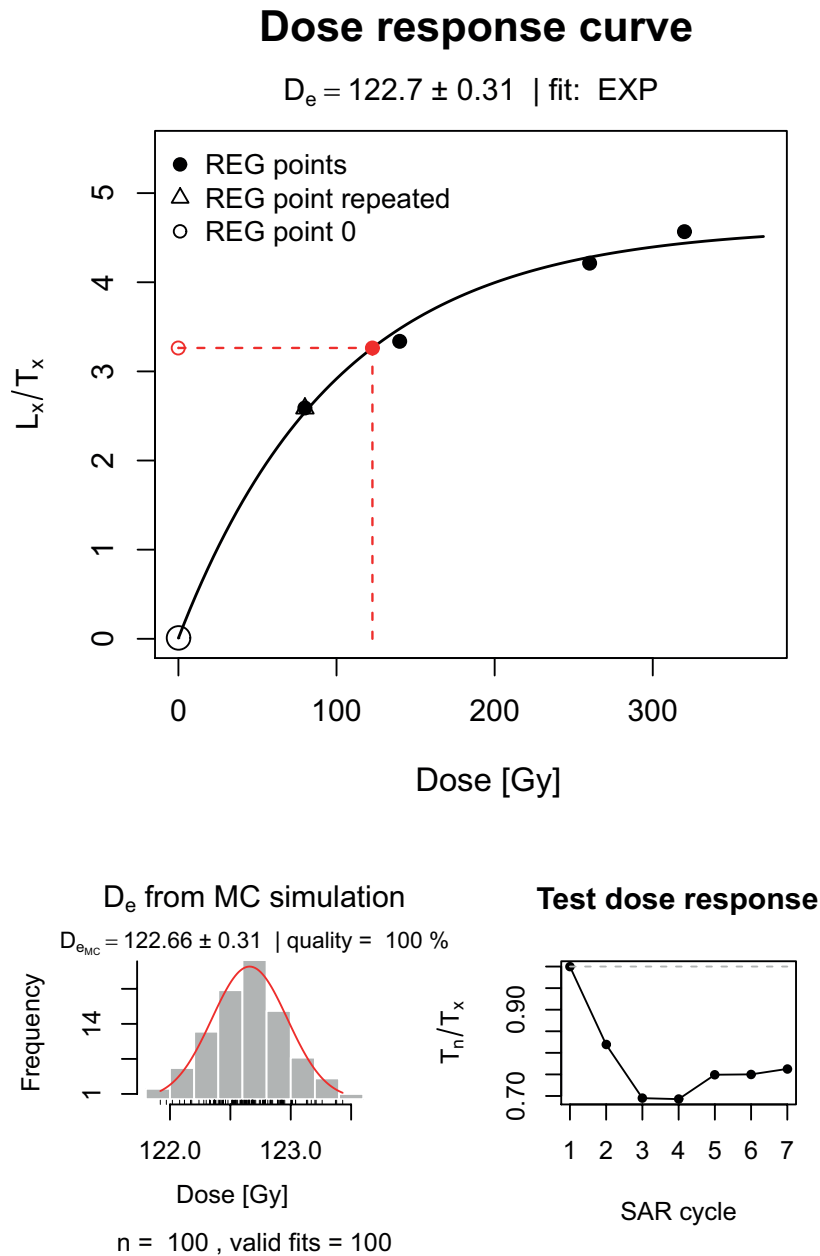


**Figure 2.12:** Results of a simulated SAR sequence using the model 'Pagonis2008' with a burial dose of 200 Gy and a simulated dose rate during irradiation of  $1 \text{ Gy s}^{-1}$ . The plot was created with function `Luminescence::analyse_SAR.CWOSL()`.

## References

- Adamiec, G., Garcia-Talavera, M., Bailey, R. M., La Torre, P. I. de, 2004. Application of a genetic algorithm to finding parameter values for numerical simulation of quartz luminescence. *Geochronometria* 23, 9–14.
- Adamiec, G., 2005. Investigation of a numerical model of the pre-dose mechanism in quartz. *Radiation Measurements* 39(2), 175–189.
- Bailey, R. M., 2001. Towards a general kinetic model for optically and thermally stimulated luminescence of quartz. *Radiation Measurements* 33(1), 17–45.
- Bailey, R. M., 2002. Simulations of variability in the luminescence characteristics of natural quartz and its implications for estimates of absorbed dose. *Radiation Protection Dosimetry* 100, 33–38.
- Bailey, R. M., 2004. Paper I - Simulation of dose absorption in quartz over geological timescales and its implications for the precision and accuracy of optical dating. *Radiation Measurements* 38(3), 299–310.
- Chen, R., McKeever, S. W. S., 1997. *Theory of Thermoluminescence and Related Phenomena*. World Scientific, Singapore.
- Chen, R., Pagonis, V., 2004. Modelling thermal activation characteristics of the sensitization of thermoluminescence in quartz. *Journal of Physics D: Applied Physics* 37, 159–164.
- Chen, R., Pagonis, V., Lawless, J., 2009. A new look at the linear-modulated optically stimulated luminescence (LM-OSL) as a tool for dating and dosimetry. *Radiation Measurements* 44, 344–350.
- Chen, R., Lawless, J., Pagonis, V., 2011. A model for explaining the concentration quenching of thermoluminescence. *Radiation Measurements* 46, 1380–1384.
- Chen, R., Pagonis, V., 2011. *Thermally and Optically Stimulated Luminescence: A Simulation Approach*. John Wiley & Sons, Chichester.
- Chen, R., Pagonis, V., 2013. Modeling TL-like thermally assisted optically stimulated luminescence (TA-OSL). *Radiation Measurements* 56, 6–12.
- Chen, R., Pagonis, V., 2014. The Role of Simulations in the Study of Thermoluminescence (TL). *Radiation Measurements* 71, 8–14.
- Chruścińska, A., 2009. Modelling the thermal bleaching of OSL signal in the case of a competition between recombination centres. *Radiation Measurements* 44, 329–337.
- Chruścińska, A., 2010. On some fundamental features of optically stimulated luminescence measurements. *Radiation Measurements* 45, 991–999.
- Chruścińska, A., 2013. Influence of spectral width of stimulation band on the shape of OSL curve. *Radiation Measurements* 56, 18–22.
- Dietze, M., Kreutzer, S., Fuchs, M. C., Burow, C., Fischer, M., Schmidt, C., 2013. A practical guide to the R package Luminescence. *Ancient TL* 31(1), 11–18.

- Dietze, M., Kreutzer, S., Burow, C., Fuchs, M. C., Fischer, M., Schmidt, C., 2016. The abanico plot: Visualising chronometric data with individual standard errors. *Quaternary Geochronology* 31, 12–18.
- Friedrich, J., 2014. Auswirkungen des Erhitzens und Belichtens auf das Radiofluoreszenzsignal von Quarz: Experimentelle Messungen und numerische Simulation. MA thesis, University of Bayreuth.
- Fuchs, M. C., Kreutzer, S., Burow, C., Dietze, M., Fischer, M., Schmidt, C., Fuchs, M., 2015. Data processing in luminescence dating analysis: An exemplary workflow using the R package 'Luminescence'. *Quaternary International* 362, 8–13.
- Garlick, G., Gibson, A., 1948. The electron trap mechanism of luminescence in sulphide and silicate phosphors. *Proceedings of the Physical Society* 60, 574–590.
- Halperin, A., Braner, A., 1960. Evaluation of thermal activation energies from glow curves. *Physical Review* 117, 408–415.
- Huntley, D., Short, M., Dunphy, K., 1996. Deep traps in quartz and their use for optical dating. *Canadian Journal of Physics* 74, 81–91.
- Itoh, N., Stoneham, D., Stoneham, A., 2002. Ionic and electronic processes in quartz: mechanisms of thermoluminescence and optically stimulated luminescence. *Journal of Applied Physics* 92(9), 5036–5044.
- Kitis, G., Pagonis, V., Chen, R., 2006. Comparison of experimental and modelled quartz thermal-activation curves obtained using multiple-and single-aliquot procedures. *Radiation Measurements* 41, 910–916.
- Kreutzer, S., Schmidt, C., Fuchs, M. C., Dietze, M., Fischer, M., Fuchs, M., 2012. Introducing an R package for luminescence dating analysis. *Ancient TL* 30(1), 1–8.
- Mandowski, A., Świątek, J., 1992. Monte Carlo simulation of thermally stimulated relaxation kinetics of carrier trapping in microcrystalline and two-dimensional solids. *Philosophical Magazine B* 65, 729–732.
- Mandowski, A., Świątek, J., 1998. Thermoluminescence and trap assemblies - results of Monte Carlo calculations. *Radiation Measurements* 29, 415–419.
- Mandowski, A., Świątek, J., 2000. The kinetics of trapping and recombination in low dimensional structures. *Synthetic Metals* 109, 203–206.
- McKeever, S. W. S., Chen, R., 1997. Luminescence models. *Radiation Measurements* 27(5), 625–661.
- McKeever, S. W. S., Bøtter-Jensen, L., Larsen, N. A., Duller, G., 1997. Temperature dependence of OSL decay curves: Experimental and theoretical aspects. *Radiation Measurements* 27(2), 161–170.
- Murray, A. S., Wintle, A. G., 2000. Luminescence dating of quartz using an improved single-aliquot regenerative-dose protocol. *Radiation Measurements* 32(1), 57–73.
- Pagonis, V., Kitis, G., Chen, R., 2003. Applicability of the Zimmerman predose model in the thermoluminescence of predosed and annealed synthetic quartz samples. *Radiation Measurements* 37(3), 267–274.

- Pagonis, V., Kitis, G., Furetta, C., 2006. Numerical and Practical Exercises in Thermoluminescence. Springer Science & Business Media.
- Pagonis, V., Chen, R., Wintle, A., 2007. Modelling thermal transfer in optically stimulated luminescence of quartz. *Journal of Physics D: Applied Physics* 40(4), 998–1006.
- Pagonis, V., Wintle, A. G., Chen, R., Wang, X. L., 2008a. A theoretical model for a new dating protocol for quartz based on thermally transferred OSL (TT-OSL). *Radiation Measurements* 43, 704–708.
- Pagonis, V., Balsamo, E., Barnold, C., Duling, K., McCole, S., 2008b. Simulations of the predose technique for retrospective dosimetry and authenticity testing. *Radiation Measurements* 43(8), 1343–1353.
- Pagonis, V., Ankjærgaard, C., Murray, A., Jain, M., Chen, R., Lawless, J. L., Greulich, S., 2010. Modelling the thermal quenching mechanism in quartz based on time-resolved optically stimulated luminescence. *Journal of Luminescence* 130(5), 902–909.
- Pagonis, V., Adamiec, G., Athanassas, C., Chen, R., Baker, A., Larsen, M., Thompson, Z., 2011. Simulations of thermally transferred OSL signals in quartz: Accuracy and precision of the protocols for equivalent dose evaluation. *Nuclear instruments and methods in physics research section B: Beam interactions with materials and atoms* 269(12), 1431–1443.
- Pagonis, V., Gochnour, E., Hennessey, M., Knowler, C., 2014. Monte Carlo simulations of luminescence processes under quasi-equilibrium (QE) conditions. *Radiation Measurements* 67, 67–76.
- Peng, J., Pagonis, V., 2016. Simulating comprehensive kinetic models for quartz luminescence using the R program KMS. *Radiation Measurements* 86, 63–70.
- R Development Core Team, 2016. *R: A language and environment for statistical computing*. Vienna, Austria. <http://www.R-project.org>,
- R Luminescence Development Team, 2016. *Luminescence: Comprehensive Luminescence Dating Data Analysis*. <https://CRAN.R-project.org/package=Luminescence>,
- Randall, J., Wilkins, M., 1945. Phosphorescence and electron traps. I. The study of trap distributions. *Proceedings of the Royal Society of London A: Mathematical, Physical and Engineering Sciences* 184(999), 366–389.
- Schmidt, C., Kreutzer, S., DeWitt, R., Fuchs, M., 2015. Radiofluorescence of quartz: A review. *Quaternary Geochronology* 27, 66–77.
- Singarayer, J., Bailey, R., 2004. Component-resolved bleaching spectra of quartz optically stimulated luminescence: preliminary results and implications for dating. *Radiation Measurements* 38, 111–118.
- Soetaert, K., Cash, J., Mazzia, F., 2012. Solving differential equations in R. Springer Science & Business Media.
- Spooner, N. A., 1994. On the optical dating signal from quartz. *Radiation Measurements* 23(2), 593–600.

- Urbach, F., 1930. Zur Lumineszenz der Alkalihalogenide II. Messungsmethoden; erste Ergebnisse; zur Theorie der Thermolumineszenz. Sitzungsberichte der Akademie der Wissenschaften in Wien, Mathematisch-Naturwissenschaftliche Klasse, Abt. IIa, Mathematik, Astronomie, Physik, Meteorologie und Technik 139, 363–372.
- Wickham, H., 2011. testthat: Get started with testing. The R Journal 3(1), 5–10.
- Wintle, A., 1975. Thermal Quenching of Thermoluminescence in Quartz. Geophysical Journal International 41(1), 107–113.
- Zimmerman, J., 1971. The radiation-induced increase of the 100 °C thermoluminescence sensitivity of fired quartz. Journal of Physics C: Solid State Physics 4(18), 3265–3276.

# 3 Quartz radiofluorescence: a modelling approach

Johannes Friedrich<sup>1</sup>, Vasilis Pagonis<sup>2</sup>, Reuven Chen<sup>3</sup>, Sebastian Kreutzer<sup>4</sup>, Christoph Schmidt<sup>1</sup>

<sup>1</sup> Chair of Geomorphology & BayCEER, University of Bayreuth, 95440 Bayreuth, Germany

<sup>2</sup> Physics Department, McDaniel College, Westminster, MD 21157, USA

<sup>3</sup> Raymond and Beverly Sackler School of Physics and Astronomy, Tel-Aviv University, Tel-Aviv 69978, Israel

<sup>4</sup> IRAMAT-CRP2A, Université Bordeaux Montaigne, Maison de l'Archéologie, Esplanade des Antilles, 33607 Pessac Cedex, France

*Journal of Luminescence* 186, 318 – 325, 2017

<https://doi.org/10.1016/j.jlumin.2017.02.039>

## Abstract

Modelling (natural) quartz luminescence (TL/OSL) phenomena appears to be quite common nowadays. The corresponding simulations are capable of giving valuable insights into the charge transport system. By contrast, simulating radiofluorescence (RF) of quartz has rather been neglected in the past. Here we present and discuss (1) the RF signals of natural quartz measured in the UV band and (2) simulations of these experiments executed using a three-energy-level model to explain the experimentally obtained results.

Two natural quartz samples were investigated at room temperature (RT) following different preheat procedures: (a) consecutively increasing preheat temperatures from 50 °C to 700 °C and (b) repeating a 500 °C preheat with subsequent UV-RF measurement at RT for eleven times. Based on the measurement and modelling results, we finally confirm theoretically the dependency of the UV-RF signal of quartz on the burial dose.

### 3.1 Introduction

Numerical simulations pave the way for a better understanding of luminescence phenomena, such as thermally stimulated and optically stimulated luminescence (TL, OSL) of various dosimeters (e.g., Chen & McKeever 1997; Chen & Pagonis 2004, 2011; Chruścińska 2009; Oniya 2015; Pagonis et al. 2003, 2014; Subedi et al. 2010). By contrast, simulating radioluminescence/radiofluorescence (henceforth radiofluorescence: RF) of natural quartz appears to have been neglected in the past.

RF is the luminescence emitted during exposure to ionizing radiation and for quartz believed to result from direct recombination of electrons with holes captured in recombination centres (cf. for a review: Schmidt et al. 2015). While quartz RF spectra are reported in the literature (e.g., Fujita & Hashimoto 2006; Martini et al. 2012a,b; Pagonis et al. 2014; Shimizu et al. 2006) simulation studies for a specific emission wavelength are missing so far. One recent study on simulating RF was published by Pagonis et al. (2009), but it is limited to  $\text{Al}_2\text{O}_3:\text{C}$ .

While the comprehensive quartz model developed by Bailey (2001) is capable of successfully simulating common TL and OSL luminescence phenomena (such as dose response, dose quenching, phototransfer, thermal activation) for the UV band, it fails for simulating experimentally obtained quartz RF signals. The results obtained by Bailey (2001: Sec. 3.4.4.) suggest that the shape of the simulated RF is correlated to the population of the so called reservoir centres. In more recent publications a link between the pre-dose effect (Zimmerman 1971a) and the RF behaviour is mentioned (Fasoli & Martini 2016; Martini et al. 2012a). The successful simulation of pre-dose effects on TL signals was published by, e.g., Adamiec (2005), Itoh et al. (2001), and Pagonis & Carty (2004) but not the effect of different preheat treatments on the RF signal.

This study is separated into two parts. The first part presents experimental results obtained by measuring quartz RF in the UV band (UV-RF) for different preheat temperatures as well as repeated cycles of heating and subsequent UV-RF measurement for a preheat temperature of 500 °C for two natural quartz samples. In the second part the empirical results are complemented by numerical simulations, i.e., three parameters from the original model (Bailey 2001) are adapted and modified to reproduce the signal dynamics seen in the experiments. To allow an understanding of the charge transport during heating and UV-RF, a simplified one-trap-two-centres model was developed.

Our numerical simulations demonstrate the potential of quartz UV-RF as a method of retrospective dosimetry, which so far has been almost neglected. While the study by Marazuev et al. (1995) appears to successfully demonstrate its general applicability, an elaborated explanation to understand the physical background of the obtained results is still missing. To the best of our knowledge, the RF signal dynamics in the UV and the burial dose estimation for natural quartz samples using RF signals have not been simulated and presented in the literature before.

## 3.2 Material and methods

### 3.2.1 Quartz samples

Two natural quartz samples were chosen for the measurements: (1) the quartz fraction of sample BT586 was extracted from a colluvial sample originating from the Trebgast valley in the north-west of Bayreuth (Germany) (Kolb et al. 2016). For this sample a palaeodose of  $\sim 24$  Gy was obtained. (2) a second quartz sample (BT1195) was extracted from the quartz ridge 'Pfahl' (Bavarian Forest, Germany), which is one of the largest hydrothermal quartz veins in Germany. This sample was extracted under daylight conditions and subsequently gently crushed with a steel mortar with frequent sieving in between. Subsequent chemical treatments followed routine preparation procedures for luminescence dating samples (e.g. Preusser et al. 2008). These are: HCl (30%), H<sub>2</sub>O<sub>2</sub> (30%), density separation using sodium-polytungstate, HF (40% for 60 min). In contrast to BT586 the sample BT1195 was bleached in a home made solar simulator (2 h with a Osram Duluxstar lamp). For both samples the used grain size fraction is 90–200  $\mu\text{m}$ . Two different pretreatments (natural and bleached) were used to investigate differences in the RF behaviour concerning these pretreatments.

### 3.2.2 Measurement conditions

RF measurements were carried out on a Freiberg Instruments *lexsyg research* reader (Richter et al. 2013) at the luminescence laboratory in Bayreuth. The reader is equipped with a  $^{90}\text{Sr}/^{90}\text{Y}$   $\beta$ -source ( $\sim 3.6$  Gy min<sup>-1</sup>), calibrated for coarse grain quartz on stainless steel cups. The  $\beta$ -source is specifically designed for RF measurements (Richter et al. 2012). Luminescence was detected through a Chroma BP 365/50 EX interference filter in front of a Hamamatsu H7360-02 photomultiplier tube allowing for a detection of the UV-RF signal between 315 nm and 415 nm. All measurements were performed in a nitrogen atmosphere. If not reported otherwise, preheating of the samples was performed with a constant heating rate of 5 K s<sup>-1</sup>. The channel time for the RF measurements was set to 1 s. The experimental data presented in this study are the arithmetic mean of two aliquots for each measurement. Reproducibility of RF signals using different aliquots was better than 5%. Further details on the UV-RF experiments are given in the text below.

### 3.2.3 Data analysis

Data analyses were carried out using the statistical programming environment **R** (R Development Core Team 2016) and the **R**-package 'Luminescence' (Kreutzer et al. 2012, 2016). For simulating the UV-RF signals the **R**-package 'RLumModel' (Friedrich et al. 2016a,b) was used. The code for the simulations presented here can be found in the supplementary material, Sec. A.2. Simulation results were cross-checked with *Mathematica*<sup>TM</sup> and *MATLAB*<sup>TM</sup>.

### 3.3 Quartz UV-RF measurements

#### 3.3.1 Preheat experiments

Martini et al. (2012a, 2014) reported that samples annealed at temperatures between 400 °C and 600 °C are showing an enhancement in the UV-RF intensity. To determine and better understand the correlation between preheat temperature and UV-RF signal intensity, UV-RF measurements were carried out for 10,000 s at room temperature ( $\sim 20$  °C) after preheating the samples to temperatures ranging from 50 °C to 700 °C using increments of 50 °C. The total absorbed dose after 10,000 s was  $\sim 600$  Gy.

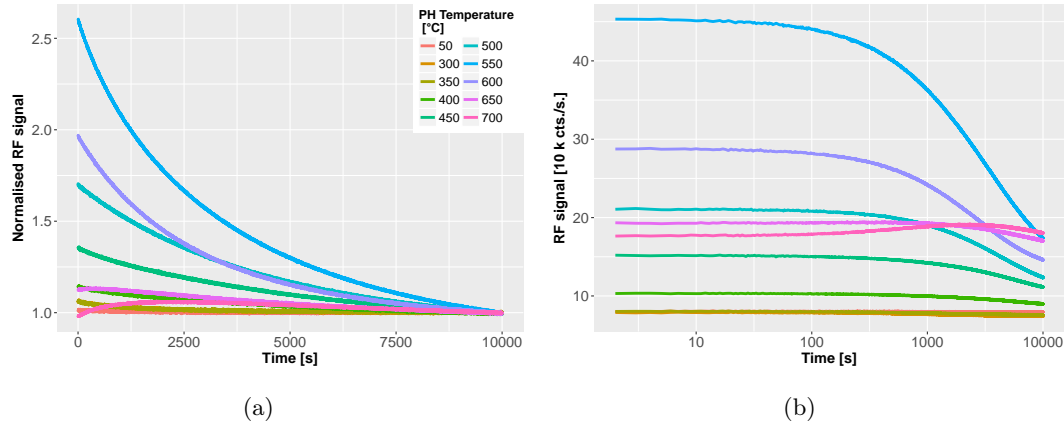
We expected a successive increase of the initial RF signal, triggered by the pre-dose effect, as described in Zimmerman (1971a) and Marazuev et al. (1995). A study by Krbetschek & Trautmann (2000) showed that high temperature annealing of quartz up to 700 °C can lead to a UV-RF signal characterized by an exponential increase followed by a linear decrease. This behaviour was not observed in any of the studies by Martini et al. (2014), although they used even higher temperatures (than reported by Krbetschek & Trautmann (2000), up to 1100 °C). In these studies no exponential increase at the begin of the measurement was observed, just an decrease of the UV-RF signal directly after starting the measurement.

Figure 3.1 (a) shows the UV-RF signals for sample BT586 after different preheat temperatures normalized to the last data point. For preheat temperatures from 50 °C to 350 °C no substantial differences within the signal shapes are visible and for the sake of clarity only the UV-RF curve for 50 °C is shown. The changes in these temperature interval are limited to a small decrease of the UV-RF signal in the first seconds followed by a stable signal until the end of the measurements.

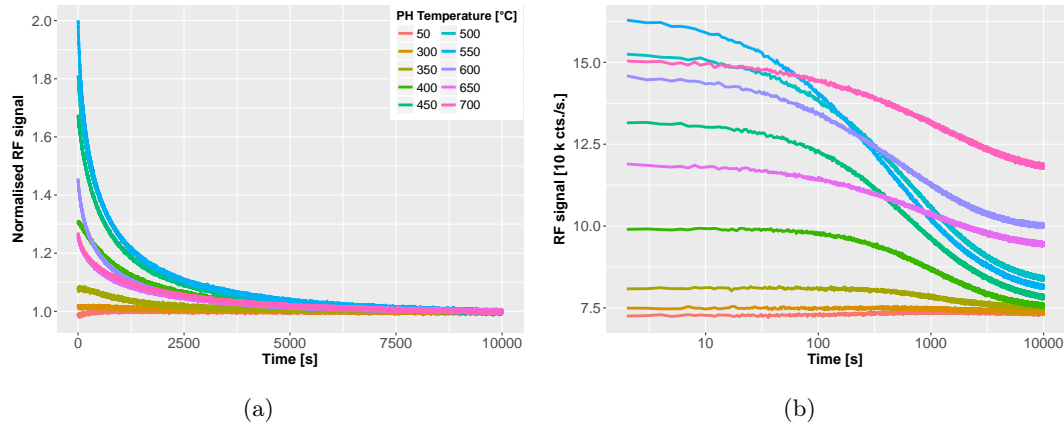
In the range from 400 °C to 550 °C an increase by a factor of  $\sim 1.2$  (400 °C) to  $\sim 2.6$  (550 °C) of the initial UV-RF signal was observed. From 600 °C to 700 °C the signal dynamics decreased by a factor of 2 (600 °C) down to 1 (700 °C). For the RF signal at 700 °C the maximum signal intensity is not observed at the very beginning of the measurements, but the signal builds up in the first channels (up to 3,000 s) and then decreases. A similar behaviour was described by Krbetschek & Trautmann (2000) for a quartz sample, after annealing it for 3 hours at 700 °C followed by  $\gamma$ -irradiation.

Figure 3.1 (b) shows all measured data, but on a logarithmic x-axis and not normalized. The strong increase in the first channel is caused by the opening of the shutter of the  $\beta$ -source. This takes up to  $\sim 0.5$  s and thus, the first channel comprises less counts than the following ones. Note the very high signal intensities and the behaviour of the RF signal at 700 °C. Figure 3.3 shows the initial signal of the RF curves from Figs. 3.1 and 3.2 normalized to the highest signal at 550 °C. Here all measured preheat temperatures are used and no differences are observed for preheat temperatures from 100 °C to 250 °C. For both samples a strong peak at 550 °C is observable. The sharp increase and decrease at lower and higher temperatures, respectively, indicate a change in the RF signal behaviour. The term 'initial signal' is used as the difference between the second and the last data point measured. A

similar behaviour to that of sample BT586 was observed for sample BT1195 (see Fig. 3.2 (a)). However, both samples show a slightly different behaviour as the signals with a preheat temperature from 50 °C to 250 °C first increase and at temperatures from 350 °C to 650 °C the decrease is getting steeper the higher the temperatures become. Such a rapid change in the signal dynamics is not observed for sample BT586 and the decrease of the signal is faster than for BT586. The differences between 650 °C and 700 °C are much smaller than for BT586. Figure 3.2 (b) shows that the signal intensities are lower by a factor  $\sim 3$  (for 550 °C) in contrast to sample BT586.



**Figure 3.1:** (a) UV-RF signal for sample BT586 for different preheat temperatures (hold for 120s) prior to the RF measurements. For each temperature a new aliquot was used. The values are normalized to the last data point of each measurement and the total absorbed dose is 600 Gy during each RF measurement. For the sake of clarity the UV-RF curves for preheat temperatures from 100 °C to 250 °C were removed, because no change was observed. (b) The same data as (a) but with absolute values and a logarithmic x-axis.



**Figure 3.2:** (a) UV-RF signal for sample BT1195 for different preheat temperatures (holding for 120s). The values are normalized to the last data point of each measurement. The total absorbed dose was 600 Gy during each RF measurement. For the sake of clarity the UV-RF curves for preheat temperatures from 100 °C to 250 °C were removed, because no change was observed. (b) The same data as (a) but with absolute values and a logarithmic x-axis.

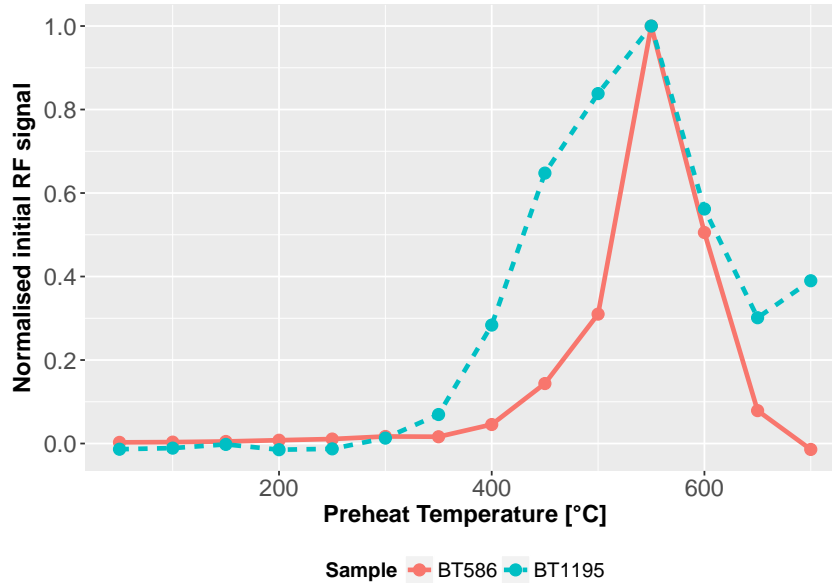


**Figure 3.3:** Initial UV-RF signal for different preheat temperatures (holding for 120 s) for samples BT586 and BT1195 normalized to the initial signal at 550 °C.

### 3.3.2 Signal stability tests

To test the UV-RF signal stability for repeated measurement cycles, a second experiment was designed measuring the RF signal 11 times with a constant preheat of 500 °C ( $5 \text{ K s}^{-1}$ , holding time 120 s) prior to each signal readout. A similar measurement was performed by Martini et al. (2012a: Fig. 4) and they observed an enhancement of the 3.44 eV (360 nm) band after each cycle. In contrast to Martini et al. (2012a) we did not measure a spectrum, but measured only the UV wavelength region (see section 3.2.2). Figure 3.4 (a) shows the results of these measurements, again normalized to the last data point. The first two cycles show different slopes than the other ones. For cycles 3 to 11 the slope of the curves is not changing, only the signal intensity increases. Subfigure (b) shows the same data as in the main figure, but on a logarithmic x-axis and with absolute count values for the RF signal. Here the successive increase of the initial signal by a factor of  $\sim 3$  over 11 cycles is observed as well as similar curve shapes. Analogue UV-RF signal behaviour was found for sample BT1195 (not shown here). Our results are in accordance with the results by Martini et al. (2012a) and show an increase of the initial signal intensity.

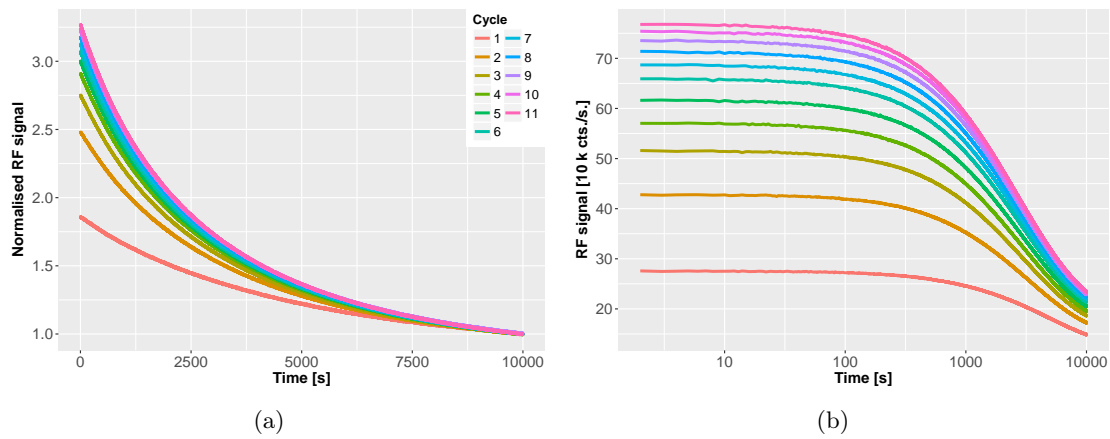


**Figure 3.4:** (a) UV-RF signals for sample BT586 for 11 cycles for a preheat at 500 °C for 120 s between each cycle. The total absorbed dose was 600 Gy for each RF cycle. The curves are normalized to the last data point. (b) The same data as (a) but with absolute values and a logarithmic x-axis.

## 3.4 Quartz UV-RF simulations

### 3.4.1 Defining the model

In a first simulation attempt to reproduce the obtained experimental results, the comprehensive quartz model developed by Bailey (2001) was used with minor modifications (see Table 3.2), since it is successful in simulating several TL and OSL phenomena in quartz. These modifications were necessary in order to simulate the RF curves obtained from our experiments.

Figure 3.5 shows the energy-band diagram the model is based on. To better understand the modifications applied later, the main aspects of the model by Bailey (2001) are listed briefly; for a detailed explanation of the levels, the reader is referred to Bailey (2001):

- Level 1 represents the 110 °C TL shallow electron trap, which gives rise to a TL peak at  $\sim 100$  °C when measured with a heating rate of  $5 \text{ K s}^{-1}$ ,
- level 2 represents a generic 230 °C TL level, as found in many sedimentary quartz samples. Photo-excitation of charge from this level is not allowed,
- levels 3 and 4 are usually termed 'fast' and 'medium' OSL components (e.g., Bailey et al. 1997) and yield TL peaks at  $\sim 330$  °C as well as give rise to the OSL emission used for dating,
- level 5 is a deep, thermally disconnected electron trap. This was proposed in order to explain several TL and OSL phenomena based on competition between energy levels,
- levels 6 – 9 are hole trapping centres acting as recombination centres for optically or thermally released electrons or for electrons which recombine directly after they reached the conduction band. Levels 6 and 7 are defined as thermally unstable, non-radiative recombination centres, similar to the hole reservoirs first introduced by Zimmerman (1971a,b) in order to explain the pre-dose sensitization phenomenon

in quartz. Level 8 is a thermally stable, radiative recombination centre termed the 'luminescence' (L) centre. Level 9 is defined as a thermally stable, non-radiative recombination centre termed 'killer' (K) centre. Holes can be thermally transferred from the two hole reservoirs (levels 6 and 7,  $R_1$  and  $R_2$ ) into the luminescence centre and the killer centre via the valence band.

Pagonis et al. (2008) stated that the levels 1, 6, 7, and 8 play a fundamental role for the pre-dose phenomenon, while we will argue in Sec. 3.4.3 that levels 5, 6, and 8 are vital for reproducing the UV-RF experimental results shown in Sec. 3.3 with the chosen model of Bailey (2001).

The following differential Eqs. (3.1) to (3.4) describe the charge flow in quartz in the context of luminescence production and are to be solved in this study. The total number of equations that need to be solved depends on the number of electron traps ( $q$ ) and hole centres ( $r$ ). For the case of the complete Bailey (2001) model  $q = 5$  and  $r = 4$ . In Sec. 3.4.3 we use a simplified model with  $q = 1$  and  $r = 2$ .

$$\frac{dn_i}{dt} = n_c \cdot (N_i - n_i) \cdot A_i - n_i \cdot P \cdot \sigma_{0i} \cdot e^{-E_{th_i}/(k_B \cdot T)} - n_i \cdot s_i \cdot e^{-E_i/(k_B \cdot T)} \quad (3.1)$$

$$\frac{dn_j}{dt} = n_v \cdot (N_j - n_j) \cdot A_j - n_j \cdot s_j \cdot e^{-E_j/(k_B \cdot T)} - n_c \cdot n_j \cdot B_j \quad (3.2)$$

$$\frac{dn_c}{dt} = R - \sum_{i=1}^q \left( \frac{dn_i}{dt} \right) - \sum_{j=q+1}^{q+r} (n_c \cdot n_j \cdot B_j) \quad (3.3)$$

$$\frac{dn_v}{dt} = R - \sum_{j=q+1}^{q+r} \left( \frac{dn_j}{dt} \right) - \sum_{j=q+1}^{q+r} (n_c \cdot n_j \cdot B_j) \quad (3.4)$$

A short description of the used abbreviations is given in Table 3.1 and in detail in Bailey (2001).

Table 3.3 shows in schematic form the steps simulated for the experiments shown in Sec. 3.2. After each excitation stage in the simulations a relaxation period is introduced in which the temperature of the sample is kept constant at 20 °C for 60 s after the excitation has stopped ( $R = 0$ ), and the concentrations of  $n_c$  and  $n_v$  decay to negligible values. When the temperature of the next simulation step is not the same as in the current step, the numerical solution simulates a cooling or heating period with a constant rate of  $\beta = 5 \text{ K s}^{-1}$ .

Bailey (2001) originally administered the burial dose at an elevated temperature of 220 °C and used a very high dose rate of  $0.01 \text{ Gy s}^{-1}$  (step 7 in Table 3.3).

ABBREVIATION	DESCRIPTION	UNIT
$n_c$	Concentration of electrons in the conduction band	$\text{cm}^{-3}$
$n_v$	Concentration of holes in the valence band	$\text{cm}^{-3}$
$N_i$	Concentration of electron traps	$\text{cm}^{-3}$
$n_i$	Concentration of trapped electrons	$\text{cm}^{-3}$
$s_i$	Frequency factor for electron traps	$\text{s}^{-1}$
$E_i$	Electron trap depth below the conduction band	eV
$N_j$	Concentration of hole centres	$\text{cm}^{-3}$
$n_j$	Concentration of trapped holes in centres	$\text{cm}^{-3}$
$s_j$	Frequency factor for hole centres	$\text{s}^{-1}$
$E_j$	Hole depth above the valence band	eV
$A_i$	Conduction band to electron trap transition probability	$\text{cm}^3 \text{s}^{-1}$
$A_j$	Valence band to hole centre transition probability	$\text{cm}^3 \text{s}^{-1}$
$B_j$	Conduction band to hole centre transition probability	$\text{cm}^3 \text{s}^{-1}$
$P$	Stimulation photon flux	
$\sigma_{0i}$	Photo eviction constant	$\text{s}^{-1}$
$E_{th_i}$	Thermal assistance energy	eV
$k_B$	Boltzmann constant	$\text{eV K}^{-1}$
$T$	Absolute temperature	K
$R$	Ionisation rate (pair production rate)	$\text{cm}^{-3} \text{s}^{-1}$
$t$	Time	s

**Table 3.1:** Description of the abbreviations used in the differential equations.

LEVELS		$N [\text{cm}^{-3}]$	$E [\text{eV}]$	$s [\text{s}^{-1}]$	$A [\text{cm}^3 \text{s}^{-1}]$	$B [\text{cm}^3 \text{s}^{-1}]$	$\sigma_0 [\text{s}^{-1}]$	$E_{th} [\text{eV}]$	
1	110 °C TL	1.5 E+07	0.97	5 E+12	1 E-08	-	0.75	0.1	
2	230 °C TL	1 E+07	1.55	5 E+14	1 E-08	-	-	-	
3	OSL <sub>F</sub>	1 E+09	1.7	5 E+13	1 E-09	-	6	0.1	
4	OSL <sub>M</sub>	2.5 E+08	1.72	5 E+14	5 E-10	-	4.5	0.13	
5	Deep	5 E+10	2	<b>1.95</b>	1 E+10	1 E-10	-	-	
6	R <sub>1</sub> -centre	3 E+08	<b>3 E+09</b>	1.43	<b>1.8</b>	5 E+13	5 E-07	5 E-09	-
7	R <sub>2</sub> -centre	1 E+10	1.75	5 E+14	1 E-09	5 E-10	-	-	
8	L-centre	1 E+11	5	1 E+13	1 E-09	1 E-10	-	-	
9	K-centre	5 E+09	5	1 E+13	1 E-10	1 E-10	-	-	

**Table 3.2:** The Qtz-A<sub>1</sub> parameters of Bailey (2001) are shown together with their modified values used in the simulations presented in this study (bold values).

1	Geological dose irradiation of 1,000 Gy at 1 Gy s <sup>-1</sup> at 20 °C
2	Relaxation stage - 60 s at 20 °C
3	Geological time - heat from 20 °C to 350 °C at 5 °C s <sup>-1</sup>
4	Relaxation for geological time, 60 s at 20 °C
5	Illuminate for 100 s at 200 °C - repeated daylight exposures over long time
6	Relaxation stage - 60 s at 20 °C
7	Burial dose - 50 Gy at 20 °C at 10 <sup>-11</sup> Gy s <sup>-1</sup>
8	Relaxation stage - 60 s at 20 °C
9	Preheat to temperatures from 50 °C to 500 °C (in 50 °C increments) for 120 s
10	Radiofluorescence for 10,000 s at 20 °C at 0.006 Gy s <sup>-1</sup>

**Table 3.3:** The simulation steps for the UV-RF simulation. For each new preheat temperature a new (simulated) aliquot was used. The line after step 8 indicates the end of the sample history. Steps 9 and 10 represent the simulated measurements in the laboratory.

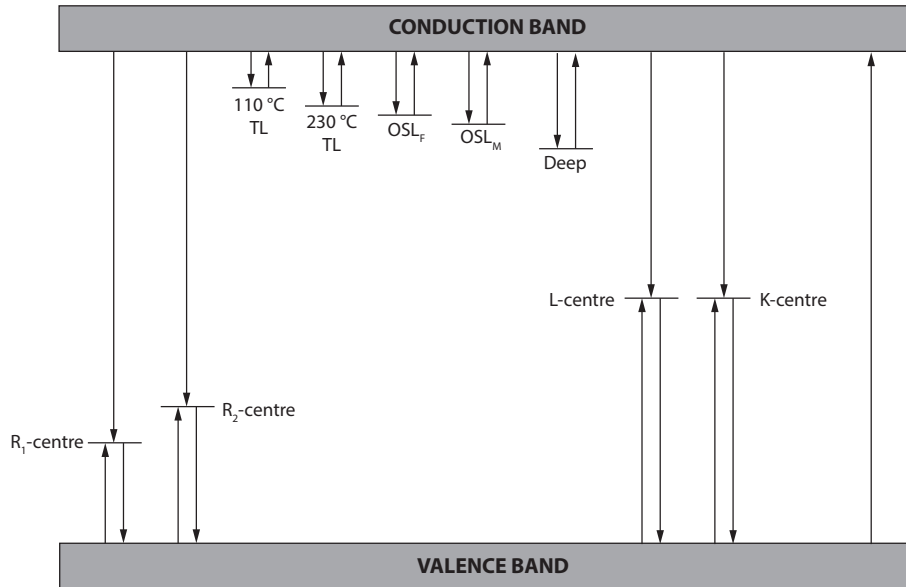


**Figure 3.5:** Schematic diagram of the comprehensive Bailey (2001) model for quartz.

In the modified step 7 above, we used a much lower dose rate of  $10^{-11} \text{ Gy s}^{-1}$  for the burial dose. This dose rate is closer to the typical environmental dose rate values, and an irradiation temperature of  $20^\circ\text{C}$  (Pagonis et al. 2011). Step 1 in Table 3.3 is simulated with a dose rate of  $1 \text{ Gy s}^{-1}$  in order to reduce computation times. Step 2 (‘geological time’) is used to empty shallow electron traps and hole centres. Thus, thermally unstable traps and centres are minimally populated after step 3. This conditions are supported by measurements of natural quartz samples (for details see Bailey 2001: Sec. 2.5).

It is well known for quartz that thermal transfer can take place from the hole reservoirs (level 6 and 7 in Table 3.2) into the L-centre (level 8 in Table 3.2), causing sensitivity changes in general and specifically the pre-dose effect (Zimmerman 1971a,b).

As discussed in Bailey (2001), the ionization rate  $R$  depends on the exact experimental conditions, namely the strength of the irradiation source and the irradiation geometry. The choice of the  $R$  value in the Bailey (2001) model is arbitrary; hence we adjusted this value so that the simulated RF results are similar to our experimental RF data.

For the simulations shown here we used the same ionization rate as Bailey (2001), except for step 10 of the simulation sequence (Table 3.3), where we employed a dose rate of  $0.006 \text{ Gy s}^{-1}$ , which is an order of magnitude smaller than the experimental dose rate. With such a dose rate, we obtained good accordance between UV-RF experiments and simulations, so that our modelling approach for the first time quantitatively reproduces UV-RF of natural quartz samples.

### 3.4.2 Matching experimental results and simulations

Figure 3.6 (a) shows the result of the RF simulations for different preheat treatments (see Table 3.3, step 9). The signals decrease over the observation time, but, as in the experimental

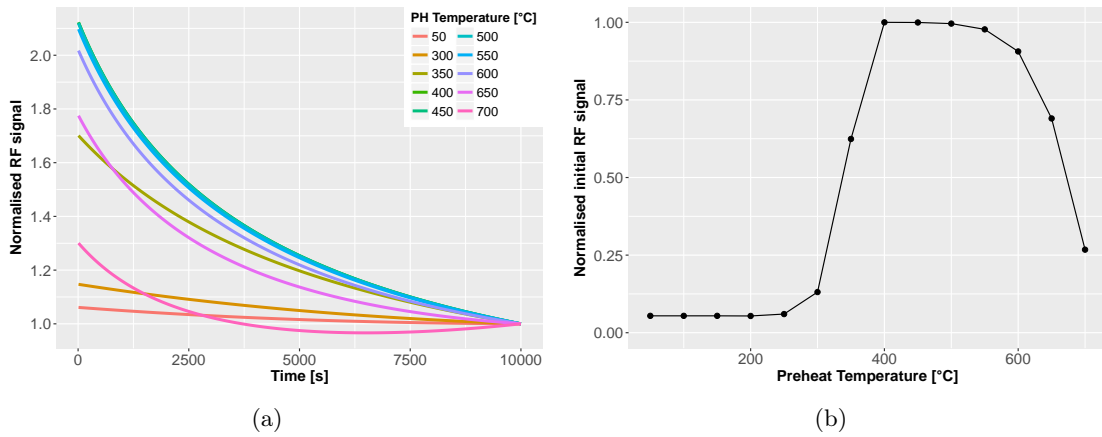


**Figure 3.6:** (a) Simulation of the sequence presented in Table 3.3 with the parameters from Table 3.2. The RF signal is normalized to the last signal value at 10,000 s. Subfigure (b) shows the simulated initial RF signal from the main figure. The values on the y-axis are normalized to the highest value of all initial signals.

data, for low temperatures signal dynamics are very weak. At a preheat temperature of 300 °C a change in the decay curve shape is observable. For preheat temperatures from 550 – 700 °C the signal intensity decreases again.

Besides the signal intensity, the most striking observation is the change in the decaying UV-RF signal. This effect can be related to a changing proportion of holes in the R-centres and L-centre. With higher preheat temperatures the concentration in the L-centre increases, see Fig. 3.9. The decay of the UV-RF signal can be linked with a decreasing competition between the recombination centres and the L-centre. This observation and a detailed explanation of this effect will be presented elsewhere.

This seems to qualitatively reproduce the experimental results from Figs. 3.1 and 3.2: Figure 3.6 (b) shows that the simulated initial RF signal does not change for low temperatures and at temperatures about 300 °C a massive increase of the signal occurs until a maximum value is reached at 400 °C. The higher the preheat temperatures are from now on the smaller is the initial signal intensity. Thus this simulation enables to reproduce qualitatively the signal dynamics and the signal height of the measured RF signal. However, the accordance is not quantitatively perfect for both natural samples.

To quantitatively simulate experimental RF signals, a more accurate determination of the model parameters (Table 3.2) is necessary, which is, however, not part of this study. Nevertheless, the behaviour of sample BT586 for a preheat temperature of 700 °C was not reproducible by our numerical simulations.

The second set of experiments was the successive preheat and RF measurement for 11 cycles, see Fig. 3.4 (a). The simulation for this sequence is shown in Fig. 3.7 and, as in the experiments with natural samples, a continuous growth of the initial signal intensity was observed from cycle to cycle. Note that before the first UV-RF measurement a preheat to 500 °C was performed. Otherwise, the signal for the first cycle would not decrease over

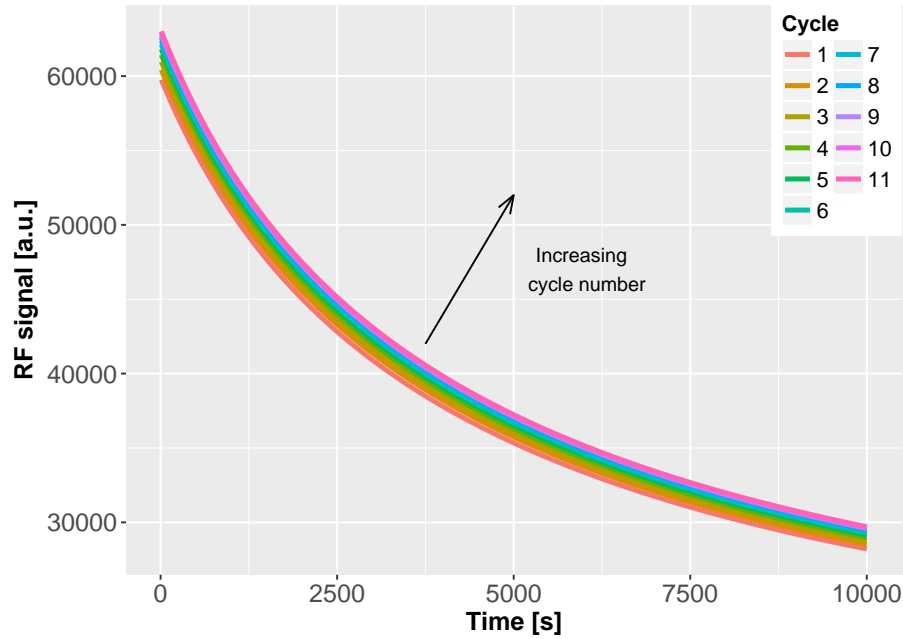


**Figure 3.7:** Simulation of the experimental results from Fig 3.4. Following the sample history, a preheat to 500 °C and a subsequent RF step were simulated, see steps 9 and 10 in Table 3.3.

time. In contrast to the experimental data, the signal for cycle 1 has the same curvature as all other cycles and so only the signal height is changing for each new cycle.

### 3.4.3 Further simulation results

In order to understand the charge movements of the UV-RF signal with different preheat temperatures, we simplified the used quartz model down to three-energy-levels, which produces approximately the same results as the complete model, but is easier to interpret.

For this purpose the deep electron trap, the  $R_1$ -centre and the L-centre were chosen. Figures 3.8 (a) and (b) show the same simulations as Figs. 3.6 and 3.7 but with only three energy levels and the results appear to be in very good accordance with the results obtained for the comprehensive Bailey (2001) model. Signal intensities from this simplified three-energy-level model are  $\sim 30\%$  higher than compared to the complete parameter set in the original model, which can be explained by the absence of competing traps in which electrons can be captured. Thus, the probability of a direct recombination with the L-centre is higher and consequently a higher signal intensity is observed. The curve shape after normalizing to the last value of the RF signal is in very good agreement with Fig. 3.6, justifying the application of the simplified model for further analyses.

In the following we used the simplified three-energy-level model. To better understand the dynamics of the charge flows in the system, a closer look at the numerical solutions is necessary. For this we investigated the concentrations of the deep trap and the two hole centres at the beginning of the RF step (see Table 3.3, step 10).

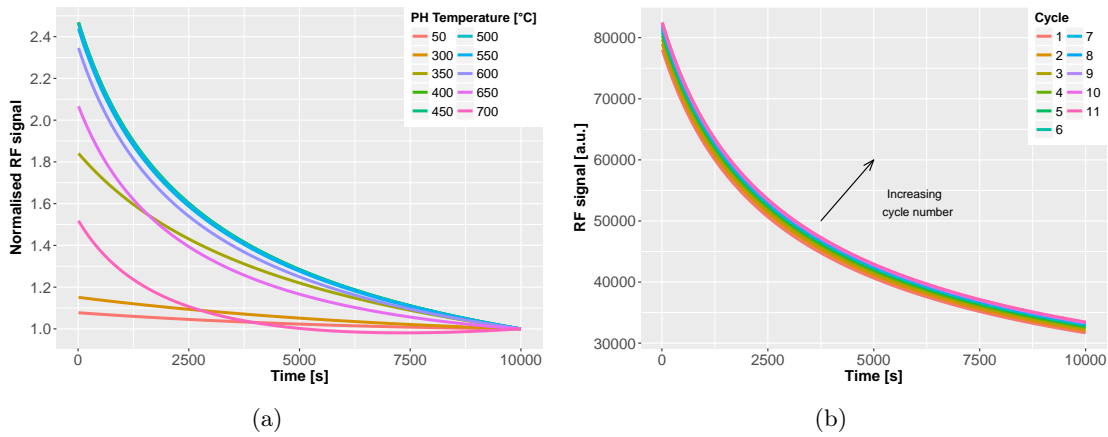


**Figure 3.8:** (a) Same simulation as for Figs. 3.6 and 3.7 (b) but using the simplified model with energy levels 5, 6, and 8 only (see Table 3.2).

Figure 3.9 shows the concentration of electrons in the deep trap and holes in the R- and L-centre for the simplified model as a function of the preheat temperature after the preheat step and hence before the beginning of the RF simulation. The concentrations are normalized to the total amount of electrons in the system. The results of Fig. 3.9 strongly indicate that the model successfully describes the pre-dose activation process, which is believed to result from holes transferring from the R- into the L-centre during the heating of the sample in the temperature range 300 – 400 °C (Zimmerman 1971a). If the preheat temperature increases, the concentration of holes in the L-centre is increased, while the corresponding concentration of holes in the hole reservoir R decreases by the same total amount. The results of Fig. 3.9 also show that an activation temperature in the region of 300 – 400 °C is sufficiently high to transfer all holes from the hole reservoir R into the luminescence centre L. In contrast to the simulations by Pagonis et al. (2008: Fig. 2b), the concentration of electrons does not remain constant during even higher temperatures, but decreases and so does the number of holes in the L-centre. This is possible because the temperatures are high enough to release electrons from the deep electron trap and charge neutrality forces the number of available holes to decrease; consequently the intensity of the luminescence signal decreases. This mechanism may explain the measured and simulated initial RF signal in Figs. 3.3 and 3.6 and it is capable of explaining why the decrease of the UV-RF signal is much weaker at temperatures above 550 °C.

Furthermore we investigated the behaviour for the initial UV-RF signal for different burial doses (see step 7 in Table 3.3). Figure 3.10 (a) shows the initial signal for different preheat temperatures from 50 °C to 500 °C and for different simulated burial doses in step 7 in the sample history of the quartz sample (see Table 3.3). The higher the simulated burial dose, the higher are the initial signals as well as the peak at 400 °C. A detailed view is provided by Fig. 3.10 (b): The initial RF signal at a preheat temperature of 450 °C is plotted against the simulated burial dose and an increasing dose-response curve can be

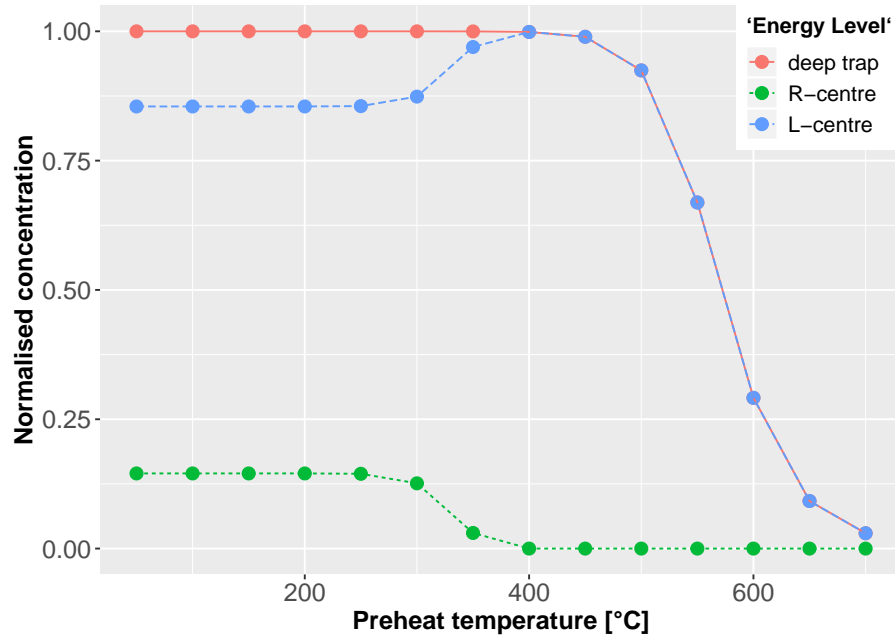


**Figure 3.9:** The concentration of electrons in the deep trap and holes in the R-centre and the L-centre after the preheat step (step 9 in Table 3.3) for the simplified three-energy-level model. The values are normalized to the total amount of electrons.

extracted from the simulated data. Note that Fig. 3.10 (a) only provides 6 different burial doses. Figure 3.10 (b) shows the numerical solution for burial doses from 0 Gy to 10,000 Gy using increments of 500 Gy.

In summary, the results of these simulations show that the initial signal of the quartz UV-RF depends on the burial dose. A multiple aliquot additive dose (MAAD) protocol with convenient preheat temperatures might be used for this purpose. Marazuev et al. (1995) first used this technique to determine the equivalent dose of quartz extracted from bricks in Chernobyl, but they used X-ray excitation. In their experiments, they focused on the difference between the initial signal and the signal after a certain time, the final kinetic equilibrium, and they used a preheat of 510 °C for 10 minutes. In contrast to our simulation findings, they observed a linearity in their dose-response curve for very low doses only. Nevertheless, our results indicate that with the UV-RF technique a determination of the equivalent dose in quartz is possible and needs to be (re-)investigated in a separate study.

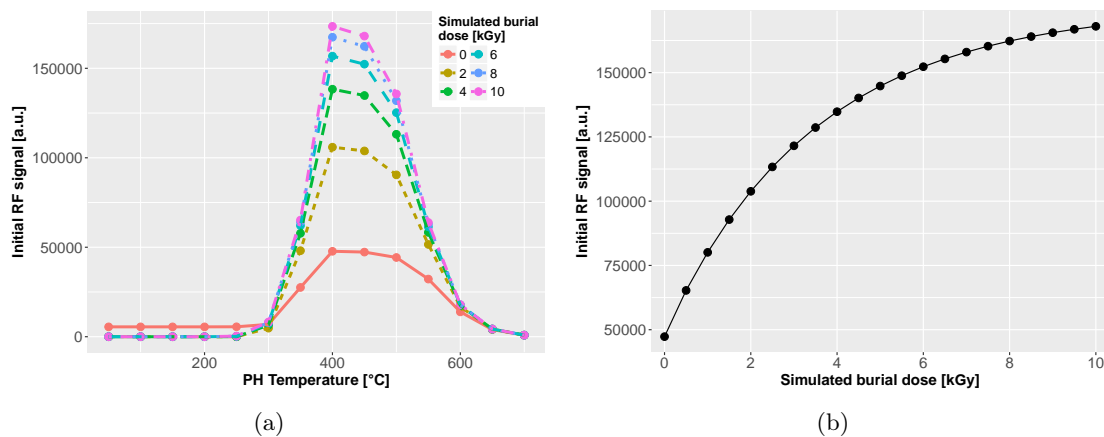


**Figure 3.10:** Simulations for different burial doses for step 7 in the sample history (see step 7 in Table 3.3). (a) shows initial RF signals for different preheat temperatures and for 6 different burial doses. (b) is a detailed view on the initial RF signal at 450 °C. The initial signal was plotted against the simulated burial dose.

### 3.5 Discussion

'Modeling is important for the purpose of determining if suggested mechanisms can indeed produce the effects observed in the practice' (McKeever & Chen 1997). The presented model and the interpretation of the results show indeed the accordance of model predictions and experimental results. Nevertheless it is important to test the model to determine 'what is possible with the model, and what is not possible' (McKeever & Chen 1997). We have run several tests with the parameter set presented in Table 3.2 (TL peaks shift with different heating rates, thermal activation characteristics, dose-recovery tests, OSL behaviour; see supplementary material in Sec. A.2) and all investigated phenomena produced meaningful results.

Nevertheless, simulated results should always be handled with care, as they describe a phenomenological point of view. To use the dependency of the initial signal height on the burial dose as a dating method one important requirement is the zeroing of the luminescence signal. From Fig. 3.10 one can deduce that a non zero signal of the initial RF signal for a preheat temperature of 450 °C is obtained in simulations for a burial dose equal to zero. The growth of the initial RF signal with the burial dose is a result of the dose dependence of the hole concentration in the luminescence centres (see Fig. 3.5). The concentration of this centre, however, is growing also before the zeroing event and optical bleaching is not sufficient to reduce it down to zero. Figure 3.9 shows that this is in principle possible when heating a sample to very high temperatures. This is in accordance with the published literature for determining an equivalent dose with quartz UV-RF, because they used bricks to determine the radiation dose related to the Chernobyl accident (Marazuev et al. 1995). When burning these bricks all electron traps and hole centres were emptied and the requirement of a complete zeroing the signal was fulfilled.

Nevertheless, Marazuev et al. (1995) also determined equivalent doses for natural quartzes but they also mentioned that this UV-RF approach will work for small doses only. Investigating this in detail is not part of this contribution.

As described in Schmidt et al. (2015), RF offers new insights into the recombination centres, due to the fact that quartz RF signals are believed to correspond to the direct recombination of electrons from the conduction band. Schmidt et al. (2015) argue that the RF technique provides information primarily on the recombination centres involved. Our results seem to confirm these ideas, since the increase of the initial RF signal appears to be a consequence of the movement from reservoir centres to luminescence centres. In addition, our preheat experiments and simulations indicate that the deep traps play a fundamental role in the description of quartz RF signals. At high temperatures the deep traps get emptied and so does the concentration of holes in the luminescence centres (see Fig. 3.9).

It should also be noted that the rapid change in the initial RF height occurs after the transition from  $\alpha$ - to  $\beta$ - quartz at a temperature of 573 °C (at normal pressure). Due to the fact that all RF measurements were performed at RT and the samples were cooled down from the preheat temperatures to RT in nitrogen atmosphere, a transition back from  $\beta$ - to  $\alpha$ -quartz appears to be likely. This transition is not part of the simulations but in the simulations this behaviour is indicated by emptying the deep electron traps.

## 3.6 Conclusions

A systematic investigation of UV-RF signals on two samples quartz samples (BT586 and BT1196) after preheat temperatures ranging from 50 °C to 700 °C was presented. For both samples the behaviour was similar: for low temperatures no differences in the UV-RF signal dynamics and in the initial signal height was observed. For preheat temperatures > 400 °C a significant rise in the initial height was noticeable as well as a decreasing signal. The initial signal was increasing until a peak was reached at a preheat of 550 °C. From this temperature on, the signal intensity was decreasing rapidly. For sample BT586 a change in the signal dynamics was detected for very high preheat temperatures: the signal is not decreasing during the complete stimulation time but builds up until 3,000 s and then decreases. Note that BT1195 was completely bleached before the measurements and BT586 still carries its natural dose. Nevertheless, both samples show a very similar behaviour.

Another preheat experiment showed that the initial RF signals are rising, if repeated cycles of preheating to 500 °C for 120 s and subsequent RF measurements were executed. These dynamics are similar to what is already known as the 'pre-dose' effect in quartz. This observation was similar for both samples.

In order to simulate these experimental results, a slightly modified Bailey (2001) model was used successfully. The different initial signal intensities and dynamics of the UV-RF signal could be simulated with good accordance between numerical and experimental results.

In addition to the successful simulation of the experimental data, we used a simplified model with three energy levels to obtain further insights. A theoretical explanation of the observed decrease of the initial signal height for high preheat temperatures is given, because the deep electron traps are emptied and the available concentration of holes in the luminescence centre L is decreasing and so are the signal intensities. Simulations additionally showed that the height of the RF signal depends on the burial dose of the sample. Brik et al. (1994) and Marazuev et al. (1995) reported this and used this fact to determine the burial dose. However, further experiments and studies are needed to establish this pre-dose method.

### 3.7 Acknowledgements

Initial UV-RF measurements and preparation of the samples BT586 and BT1195 were carried out within the framework of the project “*Radiofluorescence of quartz: Challenges towards a dating application*” (DFG, 2013 – 2015, SCHM 3051/2-1 und FU 417/16-1 and DAAD-PPP USA, 2013 – 2014, Prof. Dr. Markus Fuchs, id: 56022859). JF is gratefully supported by the DFG (2015 – 2018, “*Modelling quartz luminescence signal dynamics relevant for dating and dosimetry*”, SCHM 3051/4-1). SK was supported by the ANR (n° ANR-10-LABX-52). We also thank the two anonymous reviewers for their helpful suggestions.

## References

- Adamiec, G., 2005. Investigation of a numerical model of the pre-dose mechanism in quartz. *Radiation Measurements* 39(2), 175–189.
- Bailey, R. M., Smith, B. W., Rhodes, E. J., 1997. Partial bleaching and the decay form characteristics of quartz OSL. *Radiation Measurements* 27(2), 123–136.
- Bailey, R. M., 2001. Towards a general kinetic model for optically and thermally stimulated luminescence of quartz. *Radiation Measurements* 33(1), 17–45.
- Brik, A. B., Degoda, V. Y., Marazuev, Y. A., 1994. X-ray luminescence dosimetry of irradiated quartz. *Journal of Applied Spectroscopy* 60(5), 398–400.
- Chen, R., McKeever, S. W. S., 1997. *Theory of Thermoluminescence and Related Phenomena*. World Scientific, Singapore.
- Chen, R., Pagonis, V., 2004. Modelling thermal activation characteristics of the sensitization of thermoluminescence in quartz. *Journal of Physics D: Applied Physics* 37, 159–164.
- Chen, R., Pagonis, V., 2011. *Thermally and Optically Stimulated Luminescence: A Simulation Approach*. John Wiley & Sons, Chichester.
- Chruścińska, A., 2009. Modelling the thermal bleaching of OSL signal in the case of a competition between recombination centres. *Radiation Measurements* 44, 329–337.
- Fasoli, M., Martini, M., 2016. The composite nature of the thermoluminescence UV emission of quartz. *Journal of Luminescence* 173, 120–126.
- Friedrich, J., Kreutzer, S., Schmidt, C., 2016a. *RLumModel: Solving Ordinary Differential Equations to Understand Luminescence*. (R package version 0.1.2). CRAN. <http://CRAN.R-project.org/package=RLumModel>,
- Friedrich, J., Kreutzer, S., Schmidt, C., 2016b. Solving ordinary differential equations to understand luminescence: 'RLumModel', an advanced research tool for simulating luminescence in quartz using R. *Quaternary Geochronology* 35, 88–100.
- Fujita, H., Hashimoto, T., 2006. Influence of Radioluminescence on Optically Stimulated Luminescence from Natural Quartz Grains. *Radioisotopes* 55, 117–123.
- Itoh, N., Stoneham, D., Stoneham, A. M., 2001. The predose effect in thermoluminescent dosimetry. *Journal of Physics: Condensed Matter* 13(10), 2201–2209.
- Kolb, T., Fuchs, M., Zöller, L., 2016. Deciphering fluvial landscape evolution by luminescence dating of river terrace formation: a case study from Northern Bavaria, Germany. *Zeitschrift für Geomorphologie, Supplementary Issues* 60(1), 29–48.
- Krbetschek, M., Trautmann, T., 2000. A spectral radioluminescence study for dating and dosimetry. *Radiation Measurements* 32(5), 853–857.
- Kreutzer, S., Schmidt, C., Fuchs, M. C., Dietze, M., Fischer, M., Fuchs, M., 2012. Introducing an R package for luminescence dating analysis. *Ancient TL* 30(1), 1–8.
- Kreutzer, S., Dietze, M., Burow, C., Fuchs, M. C., Schmidt, C., Fischer, M., Friedrich, J., 2016. *Luminescence: Comprehensive Luminescence Dating Data Analysis*. (R package version 0.6.2). <https://CRAN.R-project.org/package=Luminescence>,

- Marazuev, Y. A., Brik, A. B., Degoda, V. Y., 1995. Radioluminescent dosimetry of  $\alpha$ -quartz. *Radiation Measurements* 24(4), 565–569.
- Martini, M., Fasoli, M., Villa, I., Guibert, P., 2012a. Radioluminescence of synthetic and natural quartz. *Radiation Measurements* 47(9), 846–850.
- Martini, M., Fasoli, M., Galli, A., Villa, I., Guibert, P., 2012b. Radioluminescence of synthetic quartz related to alkali ions. *Journal of Luminescence* 132(4), 1030–1036.
- Martini, M., Fasoli, M., Villa, I., 2014. Defect studies in quartz: Composite nature of the blue and UV emissions. *Nuclear Instruments and Methods in Physics Research Section B: Beam Interactions with Materials and Atoms* 327, 15–21.
- McKeever, S. W. S., Chen, R., 1997. Luminescence models. *Radiation Measurements* 27(5), 625–661.
- Oniya, E. O., 2015. Dependence of heating rates of thermal activation on thermal activation characteristics of 110 °C TL peak of quartz: A simulation approach. *Radiation Physics and Chemistry* 115, 171–178.
- Pagonis, V., Kitis, G., Chen, R., 2003. Applicability of the Zimmerman predose model in the thermoluminescence of predosed and annealed synthetic quartz samples. *Radiation Measurements* 37(3), 267–274.
- Pagonis, V., Carty, H., 2004. Simulation of the experimental pre-dose technique for retrospective dosimetry in quartz. *Radiation Protection Dosimetry* 109(3), 225–234.
- Pagonis, V., Balsamo, E., Barnold, C., Duling, K., McCole, S., 2008. Simulations of the predose technique for retrospective dosimetry and authenticity testing. *Radiation Measurements* 43(8), 1343–1353.
- Pagonis, V., Lawless, J. L., Chen, R., Andersen, C., 2009. Radioluminescence in  $\text{Al}_2\text{O}_3:\text{C}$  - analytical and numerical simulation results. *Journal of Physics D: Applied Physics* 42(17), 175107.
- Pagonis, V., Adamiec, G., Athanassas, C., Chen, R., Baker, A., Larsen, M., Thompson, Z., 2011. Simulations of thermally transferred OSL signals in quartz: Accuracy and precision of the protocols for equivalent dose evaluation. *Nuclear instruments and methods in physics research section B: Beam interactions with materials and atoms* 269(12), 1431–1443.
- Pagonis, V., Chithambo, M. L., Chen, R., Chruścińska, A., Fasoli, M., Li, S. H., Martini, M., Ramseyer, K., 2014. Thermal dependence of luminescence lifetimes and radioluminescence in quartz. *Journal of Luminescence* 145, 38–48.
- Preusser, F., Degering, D., Fuchs, M., Hilgers, A., Kadereit, A., Klasen, N., Krbetschek, M., Richter, D., Spencer, J. Q. G., 2008. Luminescence dating: basics, methods and applications. *Quaternary Science Journal* 57(1-2), 95–149.
- R Development Core Team, 2016. *R: A language and environment for statistical computing*. Vienna, Austria. <http://www.R-project.org>,
- Richter, D., Pintaske, R., Dornich, K., Krbetschek, M., 2012. A novel beta source design for uniform irradiation in dosimetric applications. *Ancient TL* 30(2), 57–63.

- Richter, D., Richter, A., Dornich, K., 2013. Lexsyg - A new system for luminescence research. *Geochronometria* 40(4), 220–228.
- Schmidt, C., Kreutzer, S., DeWitt, R., Fuchs, M., 2015. Radiofluorescence of quartz: A review. *Quaternary Geochronology* 27, 66–77.
- Shimizu, N., Mitamura, N., Takeuchi, A., Hashimoto, T., 2006. Dependence of radioluminescence on TL-properties in natural quartz. *Radiation Measurements* 41(7), 831–835.
- Subedi, B., Kitis, G., Pagonis, V., 2010. Simulation of the influence of thermal quenching on thermoluminescence glow-peaks. *physica status solidi (a)* 207(5), 1216–1226.
- Zimmerman, J., 1971a. The radiation-induced increase of the 100 °C thermoluminescence sensitivity of fired quartz. *Journal of Physics C: Solid State Physics* 4(18), 3265–3276.
- Zimmerman, J., 1971b. The radiation-induced increase of thermoluminescence sensitivity of the dosimetry phosphor LiF (TLD-100). *Journal of Physics C: Solid State Physics* 4(18), 3277–3291.

## 4 The basic principles of quartz radiofluorescence dynamics in the UV - analytical, numerical and experimental results

Johannes Friedrich<sup>1</sup>, Mauro Fasoli<sup>2,3</sup>, Sebastian Kreutzer<sup>4</sup>, Christoph Schmidt<sup>1</sup>

<sup>1</sup> Chair of Geomorphology & BayCEER, University of Bayreuth, 95440 Bayreuth, Germany

<sup>2</sup> Dipartimento di Scienza dei Materiali, Università degli Studi di Milano Bicocca, via R. Cozzi 55, I-20125 Milano, Italy

<sup>3</sup> INFN, Sezione di Milano Bicocca, Piazza della Scienza 1, I-20126 Milano, Italy

<sup>4</sup> IRAMAT-CRP2A, Université Bordeaux Montaigne, Maison de l'Archéologie, Esplanade des Antilles, 33607 Pessac Cedex, France

*Journal of Luminescence* 192, 940 – 948, 2017

<https://doi.org/10.1016/j.jlumin.2017.08.012>

### Abstract

An analytical solution for the behaviour of quartz radiofluorescence (RF) in the UV-band is described based on a kinetic model involving one (deep) electron trap and two kinds of recombination centres. This model has been previously used to provide a qualitative description of quartz UV-RF. The derived numerical solution of differential equations describing charge transport in quartz can successfully reproduce experimental data. Here, this set of differential equations is solved analytically by assuming a dynamic balance during the RF stimulation. The analytical results are compared with numerical solutions and experimentally derived data. With the analytical solutions a better understanding of common natural quartz UV-RF behaviour is provided, and several experimentally observed phenomena can now be explained. Furthermore, the comparison of two different kinetic models shows that the characteristic decay of the UV-RF signal in preheated quartz is attributed to an increasing competition of radiative and non-radiative centres during RF.

## 4.1 Introduction

In the last years publications showed radiofluorescence (RF) spectra of natural and synthetic quartz (e.g., Chithambo & Niyonzima (2017), Krbetschek & Trautmann (2000), Martini et al. (2012, 2014), Poolton et al. (2001), and Schilles et al. (2001)). One of the main spectral components in all (natural) quartz samples is the UV emission around 360 nm, also called C band (Fasoli & Martini 2016; Martini et al. 2014). Krbetschek & Trautmann (2000) analysed the RF signal characteristics for many materials and the results for quartz suggested, that many different signal dynamics can be measured in the UV band: a constant signal, a linearly or exponentially decreasing and/or increasing signal or even an exponential increase with a linear decrease subsequently (see Krbetschek & Trautmann (2000: Fig. 1)).

Further quartz RF experiments showed a systematic pattern of the initial signal and the change of the signal dynamics, however, an explanation was still missing (Friedrich et al. 2017). This work investigates the behaviour of quartz UV-RF signals in a theoretical manner. Analytical solutions of coupled ordinary differential equations (ODEs) are presented and three special cases are discussed in detail as well as a comparison between numerical and analytical solutions of these ODEs.

Numerical and analytical solutions should be capable of reproducing the so far known phenomena of quartz RF. These are on the one hand the change in the initial signal intensity and on the other hand the change of the (initial) slope of RF signals after different preheat temperatures. Especially the wide variation of signal dynamics is still not sufficiently explained.

The analytical solutions help to obtain a better understanding of the behaviour of quartz UV-RF. The comparison between these solutions and experimental data of known luminescence phenomena in quartz, such as the pre-dose effect (Zimmerman 1971), contribute to decipher the basic principles of quartz UV-RF.

## 4.2 Description of the model

We showed previously (e.g., Friedrich et al. (2017)) that it is possible to simulate UV-RF phenomena with a three-energy-level model by solving the corresponding ODEs. The model consists of a deep electron trap and two recombination centres L, which is radiative, and R, a non-radiative competitor, also called reservoir centre. The charge transitions in the model during an RF measurement are indicated in Fig. 4.1.

The following set of coupled differential equations describes the charge transport in quartz:

$$\frac{dn}{dt} = A_n \cdot (N - n) \cdot n_c \quad (4.1)$$

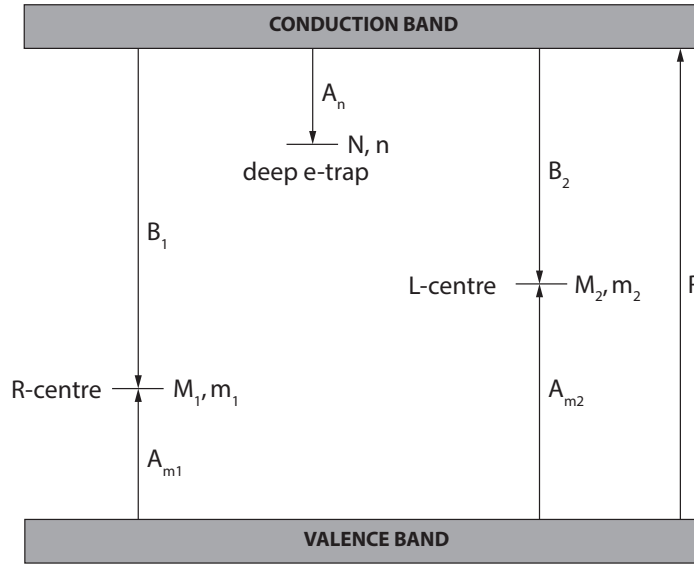


**Figure 4.1:** Energy-band-scheme of the three-level model employed to simulate RF at room temperature. The arrows indicate the allowed transitions of electrons/holes during RF. All indices with  $1$  indicate the parameters belonging to the R-centre and  $2$  those belonging to the L-centre. A detailed description of the parameters is given in table 4.1.

$$\frac{dm_1}{dt} = A_{m_1} \cdot (M_1 - m_1) \cdot n_v - B_1 \cdot m_1 \cdot n_c \quad (4.2)$$

$$\frac{dm_2}{dt} = A_{m_2} \cdot (M_2 - m_2) \cdot n_v - B_2 \cdot m_2 \cdot n_c \quad (4.3)$$

$$\frac{dn_c}{dt} = R - A_n \cdot (N - n) \cdot n_c - B_1 \cdot m_1 \cdot n_c - B_2 \cdot m_2 \cdot n_c \quad (4.4)$$

$$\frac{dn_v}{dt} = R - A_{m_1} \cdot (M_1 - m_1) \cdot n_v - A_{m_2} \cdot (M_2 - m_2) \cdot n_v, \quad (4.5)$$

where  $M_1$  ( $\text{cm}^{-3}$ ) is the concentration of non-radiative hole centres with instantaneous occupancy of  $m_1$  ( $\text{cm}^{-3}$ ),  $M_2$  ( $\text{cm}^{-3}$ ) is the concentration of radiative hole centres with instantaneous occupancy of  $m_2$  ( $\text{cm}^{-3}$ ),  $N$  ( $\text{cm}^{-3}$ ) is the concentration of the electron trapping state with instantaneous occupancy of  $n$  ( $\text{cm}^{-3}$ ).  $n_c$  and  $n_v$  are the concentrations ( $\text{cm}^{-3}$ ) of the electrons and holes in the conduction band (CB) and valence band (VB), respectively.  $R$  ( $\text{cm}^{-3} \text{ s}^{-1}$ ) is the rate of production of electron-hole pairs, which is proportional to the excitation dose rate,  $A_{m_1}$  and  $A_{m_2}$  ( $\text{cm}^3 \text{ s}^{-1}$ ) are the trapping probability

coefficients of free holes into centres 1 and 2, respectively.  $B_1$  and  $B_2$  ( $\text{cm}^3 \text{s}^{-1}$ ) are the recombination probability coefficients for free electrons with holes in centres 1 and 2, and  $A_n$  ( $\text{cm}^3 \text{s}^{-1}$ ) is the retrapping probability coefficient of free electrons into the active trapping state N.

The RF signal intensity obtained from the recombination of electrons from the conduction band into the recombination centre (L-centre) is given by:

$$I(t) = B_2 \cdot m_2 \cdot n_c \quad (4.6)$$

### 4.3 Derivation of the analytical expressions

As common in kinetic models, an assumption about the charge flow during the measurement has to be made: After a very short transitional period, a dynamic balance is established between the irradiation process creating pairs of electrons and holes on the one hand, and the relaxation process of electrons and holes into the various energy levels on the other hand. So we can assume that during this dynamic balance the concentrations of electrons in the CB and of holes in the VB change very slowly, so that assumption (4.7) holds.

$$\frac{dn_v}{dt} = \frac{dn_c}{dt} = 0 \quad (4.7)$$

The concentrations at the beginning of the RF measurement are:

$$\begin{aligned} m_1(0) &= m_{10} \\ m_2(0) &= m_{20} \\ n(0) &= n_0 = m_{10} + m_{20} \end{aligned} \quad (4.8)$$

The last line in Eq. (4.8) results from charge neutrality. With these assumptions and Eq. (4.4) we obtain the following expression for the initial concentration of electrons of the conduction band:

$$\begin{aligned} n_c &= \frac{R}{A_n \cdot (N - n) + B_1 \cdot m_1 + B_2 \cdot m_2} \\ \rightarrow n_{c0} &= \frac{R}{A_n \cdot (N - n_0) + B_1 \cdot m_{10} + B_2 \cdot m_{20}} \end{aligned} \quad (4.9)$$

The derivation of the expression for  $n_{v0}$  is obtained in a similar manner:

$$\begin{aligned} n_v &= \frac{R}{A_{m_1} \cdot (M_1 - m_1) + A_{m_2} \cdot (M_2 - m_2)} \\ \rightarrow n_{v0} &= \frac{R}{A_{m_1} \cdot (M_1 - m_{10}) + A_{m_2} \cdot (M_2 - m_{20})} \end{aligned} \quad (4.10)$$

Our goal is to obtain an analytical solution for the initial RF signal and the slope of the RF signal at the start of excitation. We derived a Taylor series at  $t = 0$  with the first two terms being  $C_1$  and  $C_2$ :

$$I(t) = C_1 + C_2 \cdot t + O(t^2) = I(0) + \left. \frac{dI}{dt} \right|_{t=0} \cdot t + O(t^2) \quad (4.11)$$

For the calculation of  $C_1$  Eqs. (4.7) – (4.9) are used:

$$\begin{aligned} C_1 &= I(0) = B_2 \cdot m_{20} \cdot n_{c0} \\ &= B_2 \cdot m_{20} \cdot \frac{R}{A_n \cdot (N - n_0) + B_1 \cdot m_{10} + B_2 \cdot m_{20}} \end{aligned} \quad (4.12)$$

Hence Eq. (4.12) describes the initial RF intensity (intensity at  $t \sim 0$ ). This is similar to the results calculated by Pagonis et al. (2009: Eq. 15) and has the same consequence: the initial signal intensity is directly proportional to the production-rate  $R$  of electron-hole pairs. This was already shown experimentally with  $\text{Al}_2\text{O}_3\text{:C}$  in Aznar (2005: Fig. 3.9 a).

The derivation of the slope of  $C_2$  is more complex and will be described in detail in Appendix 4.A.1. The result is Eq. (4.13):

$$\begin{aligned} C_2 &= \frac{B_2 \cdot R^2}{(A_n \cdot (N - n_0) + B_1 \cdot m_{10} + B_2 \cdot m_{20})^2} \\ &\cdot \left( m_{20} \cdot \frac{A_n \cdot (N - n_0)(A_n - B_2) + m_{10} \cdot (B_1^2 - B_2 \cdot B_1)}{A_n \cdot (N - n_0) + B_2 \cdot m_{20}} \right. \\ &\left. + \frac{A_n \cdot (N - n_0) \cdot A_{m_2} \cdot (M_2 - m_{20}) - B_1 \cdot A_{m_1} \cdot (M_1 - m_{10}) \cdot m_{20}}{A_{m_1} \cdot (M_1 - m_{10}) + A_{m_2} \cdot (M_2 - m_{20})} \right) \end{aligned} \quad (4.13)$$

Equation (4.13) indicates another experimentally observed phenomenon: The slope of the RF signal is proportional to the square of the electron-hole production rate  $R$ . Again, these results are similar to those reported by Aznar (2005: Fig 3.9 b) for  $\text{Al}_2\text{O}_3\text{:C}$ .

Note that all the experimental results cited so far were derived from  $\text{Al}_2\text{O}_3\text{:C}$  as phosphor. The energy-band-model is identical to the one for quartz, but with different parameters. Therefore, a general comparison appears possible.

## 4.4 Comparison of analytical expressions and numerical results

A comparison between analytical and numerical solutions of the initial signal ( $C_1$ ), the slope of the signal ( $C_2$ ), and the concentrations of levels  $n$ ,  $m_1$  and  $m_2$  is given below for different cases. The parameters for the calculations are similar to the ones by Bailey (2001) (levels 5, 6, and 8), except that the concentrations of the electron trap ( $N$ ), the non-radiative

PARAMETER	VALUE	UNIT	DESCRIPTION
$A_n$	1 E-10	$\text{cm}^3 \text{s}^{-1}$	Conduction band to electron trap transition probability
$B_1$	5 E-09	$\text{cm}^3 \text{s}^{-1}$	Conduction band to R-centre transition probability
$B_2$	1 E-10	$\text{cm}^3 \text{s}^{-1}$	Conduction band to L-centre transition probability
$A_{m_1}$	5 E-07	$\text{cm}^3 \text{s}^{-1}$	Valence band to R-centre transition probability
$A_{m_2}$	1 E-09	$\text{cm}^3 \text{s}^{-1}$	Valence band to L-centre transition probability
$M_1$	1 E+11	$\text{cm}^{-3}$	Concentration of R-centre
$M_2$	1 E+11	$\text{cm}^{-3}$	Concentration of L-centre
$N$	1 E+11	$\text{cm}^{-3}$	Concentration of electron trap
$R$	3 E+05	$\text{cm}^{-3} \text{s}^{-1}$	Ionisation rate (pair production rate)

**Table 4.1:** Used parameters for the comparison between analytical and numerical solutions.

( $M_1$ ), and the radiative centre ( $M_2$ ) are equal. This was done in order to compare different filling levels of the traps and centres, respectively. Otherwise it could not be ensured that one of the traps/centres is completely filled, due to charge neutrality. The parameter  $R$  is equivalent to  $0.01 \text{ Gy s}^{-1}$ . Note that these parameters were not chosen to describe RF signals quantitatively, but to compare analytical and numerical results (see Sec. 4.4.1 and 4.4.2) and to explore the general behaviour of RF signals (see Sec. 4.5). All used parameters are listed in Table 4.1.

The numerical solutions were calculated by solving Eqs. (4.1) – (4.5) with different starting conditions for the deep electron trap, the R- and the L-centre. All calculations were performed in **R** (R Core Team 2017) with the **R**-package 'deSolve' (Soetaert et al. 2012). The code is part of the supplementary material (see Sec. A.3).

#### 4.4.1 Case I: empty R-centre ( $m_1 = 0$ )

This case describes the initial condition when all holes are located in the L-centre and the same amount of electrons is stored in the deep electron trap, due to charge neutrality. This case can occur after annealing a sample to temperatures high enough to empty the R-centre completely.

Equations (4.12) and (4.13) simplify to:

$$C_1 = B_2 \cdot m_{2_0} \cdot \frac{R}{A_n \cdot (N - n_0) + B_2 \cdot m_{2_0}} \quad (4.14)$$

$$C_2 = \frac{B_2 \cdot R^2}{(A_n \cdot (N - n_0) + B_2 \cdot m_{2_0})^2} \cdot \left( \frac{m_{2_0} \cdot A_n \cdot (N - n_0)(A_n - B_2)}{A_n \cdot (N - n_0) + B_2 \cdot m_{2_0}} + \frac{A_n \cdot (N - n_0) \cdot A_{m_2} \cdot (M_2 - m_{2_0}) - B_1 \cdot A_{m_1} \cdot M_1 \cdot m_{2_0}}{A_{m_2} \cdot (M_2 - m_{2_0}) + A_{m_1} \cdot M_1} \right) \quad (4.15)$$

The concentration of holes in the R- and L-centre as well as for the electrons in the deep trap are derived in Appendix 4.A.2. The behaviour of these solutions will be investigated

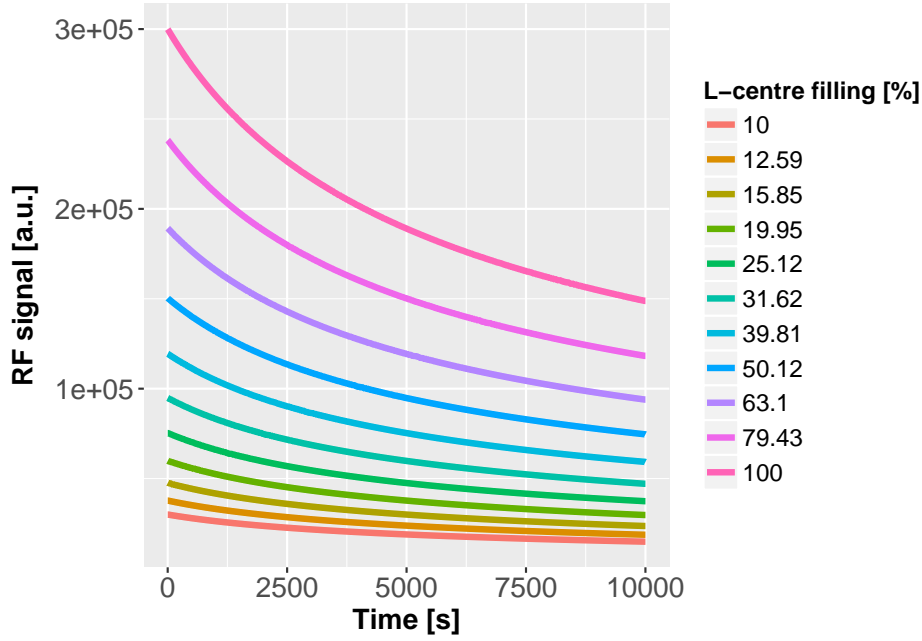


**Figure 4.2:** Different UV-RF curves when solving Eqs. (4.1) – (4.5) numerically. Eleven different starting concentrations of the L-centre were calculated. Note that the initial RF signal and the slope are further analysed in Figs. 4.3 and 4.4.

for different degrees of filling of the L-centre at the beginning of the simulations. The degree of filling ranges from  $1 \text{ cm}^{-3}$  to  $1 \text{ E}+11 \text{ cm}^{-3}$ .

Figure 4.2 shows the results when solving Eqs. (4.1) – (4.5) numerically for eleven different starting conditions (filling levels) for the L-centre. Figure 4.3 displays the dependency of the initial RF signal on the filling of the L-centre at the beginning of the calculations for the same data as plotted in Fig. 4.2. The first result is that the derived analytical solution matches the numerical solutions. Furthermore a linear dependency is identifiable between the filling of the L-centre and the height of the initial RF signal. Note that the same amount of electrons is in the deep electron trap as holes in the L-centre. So the linearity of the initial signal is an interplay between the increasing probability of a conduction band electron to recombine (because of the filling of the electron trap) and the availability of holes to recombine. The linear relationship is not obvious. Figure 4.4 shows the dependency of the slope of the UV-RF signal on the filling of the L-centre. Again an excellent match between analytical and numerical solutions is recognisable. The results of analysing the three-energy-level models show that the slope of the RF signal is linearly related to the filling of the L-centre.

#### 4.4.2 Case II: empty R-centre and empty electron trap ( $m_{10} = 0, n_0 = 0$ )

The second case describes the possibility of a completely vacant situation and thus a quartz sample just after mineralization or (in a wider sense) a very young sample. It is obvious that the initial signal is zero, because no holes to recombine are available in the L-centre.

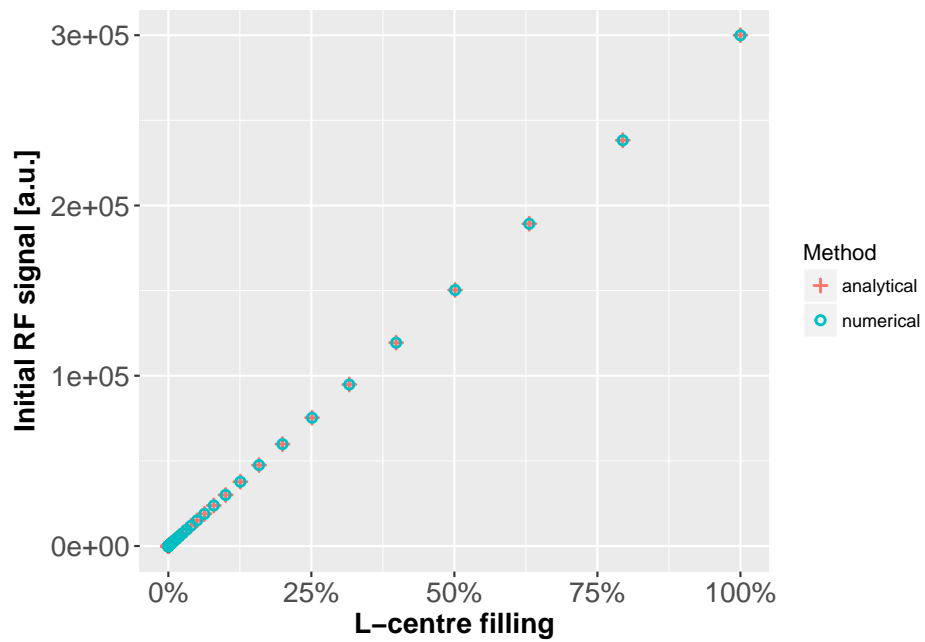


**Figure 4.3:** The analytically and numerically derived solutions for the initial RF signal for different degrees of filling of the L-centre.

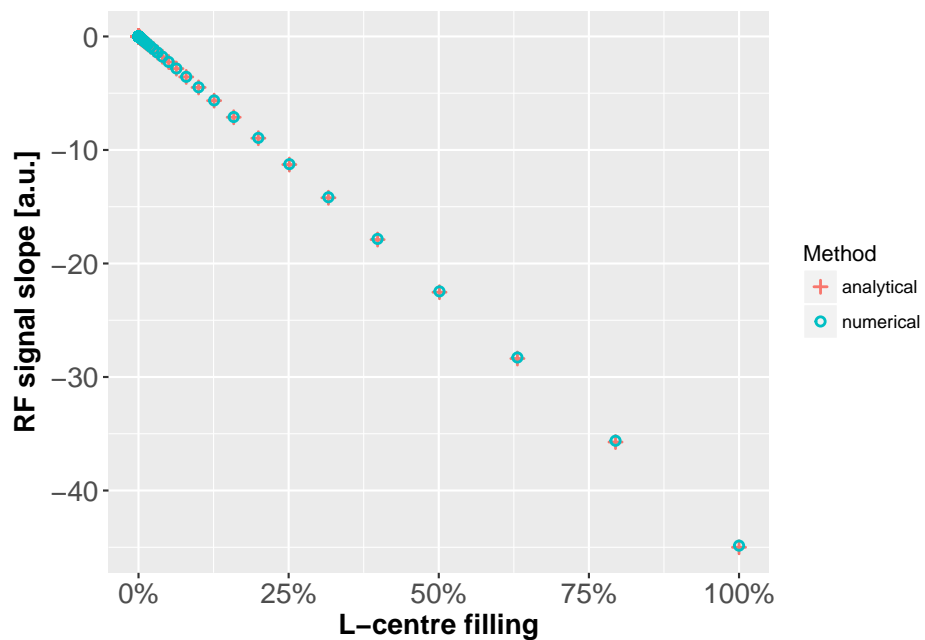


**Figure 4.4:** Slope of the RF signal against the filling of the L-centre.

Using Eqs. (4.12) and (4.13) and the initial conditions  $m_1 = 0, n_0 = 0$  results in:

$$C_1 = 0 \tag{4.16}$$

$$C_2 = R^2 \cdot \frac{B_2 \cdot A_{m_2} \cdot M_2}{A_{m_1} \cdot M_1 + A_{m_2} \cdot M_2} > 0 \tag{4.17}$$

The numerical solution of this case is exactly the same and a plot as in Figs. 4.3 and 4.4 is not necessary, because no change in the filling of the L-centre is possible. This case indicates, that the slope of the RF signal can also be positive.

#### 4.4.3 Case III: Random distribution of holes

To simulate an arbitrary filling of the L- and R-centre at the start of the simulation, 100,000 different combinations of L- and R-centre concentrations were calculated. The sum of holes in the R- and L-centre was limited to  $1 \text{ E}+11 \text{ cm}^{-3}$ , the maximum concentration of electrons in the deep trap (see Sec. 4.4). The goal of this approach was to gain a better understanding of the behaviour of the RF signal for random distributions of charge carriers. Figure 4.5 illustrates the result of the analytical calculations for the initial RF signal in a 3D plot. The special cases from Secs. 4.4.1 and 4.4.2 are shown therein.

The basic conclusion is that the initial RF signal is the higher the larger the occupancy of the L-centre and the less the concentration of holes in the R-centre is at the beginning of a simulation. As expected, different combinations of starting concentrations lead to a continuous distribution of the height of the RF signal.

Figure 4.6 shows the slope of the RF signal at the beginning of a simulation for the same starting concentrations as in Fig. 4.5. The special cases described in Secs. 4.4.1 and 4.4.2 are also included in this figure. The general trend shows a sharp decline of the RF signal (steep negative slope) when the initial concentration of holes in the L-centre is very high and the concentration of holes in the R-centre is small. Further analysis of the data showed that  $\sim 14\%$  of all calculated combinations of starting conditions lead to a positive slope signal and  $\sim 86\%$  to a negative slope. However, in most cases the negative slope is small. Hence, short simulation times will lead to a (visibly) stable signal, see histogram in Fig. 4.7. So for measurements of 10,000 s, (e.g., performed in Friedrich et al. (2017)), a very small change in the RF signal is expected when measuring without any (thermal) pre-treatment. From literature it is well known that a preheat influences the UV-RF signal dynamics dramatically, similar to the pre-dose effect (Zimmerman 1971). A detailed overview for effects of the preheat to UV-RF signals can be found in Friedrich et al. (2017) and Martini et al. (2012, 2014).

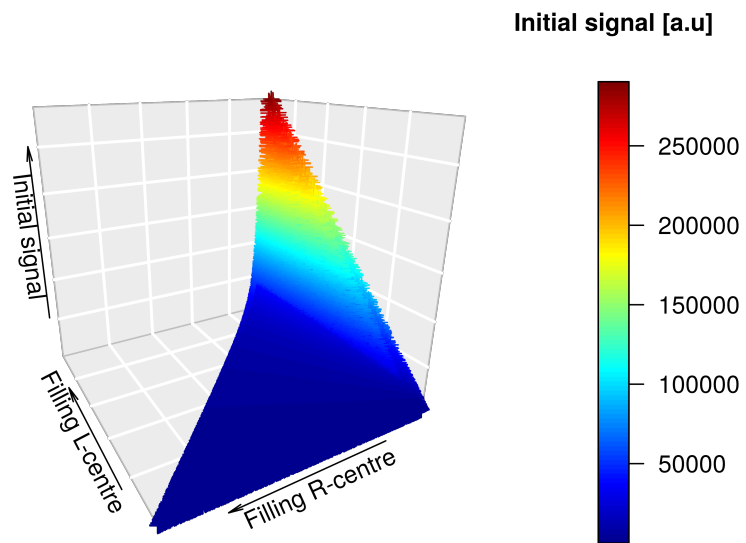


**Figure 4.5:** 3D plot of the initial RF signal for an arbitrary distribution of holes in the L- and R-centre. 100,000 different combinations of L- and R-centre concentrations were calculated.

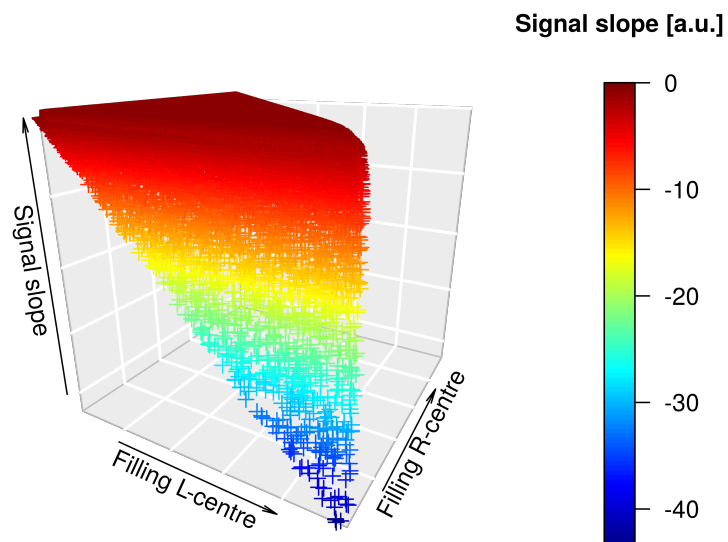


**Figure 4.6:** 3D plot of the initial RF signal slope for an arbitrary distribution of holes in the L- and R-centre. 100,000 different combinations of L- and R-centre concentrations were calculated.

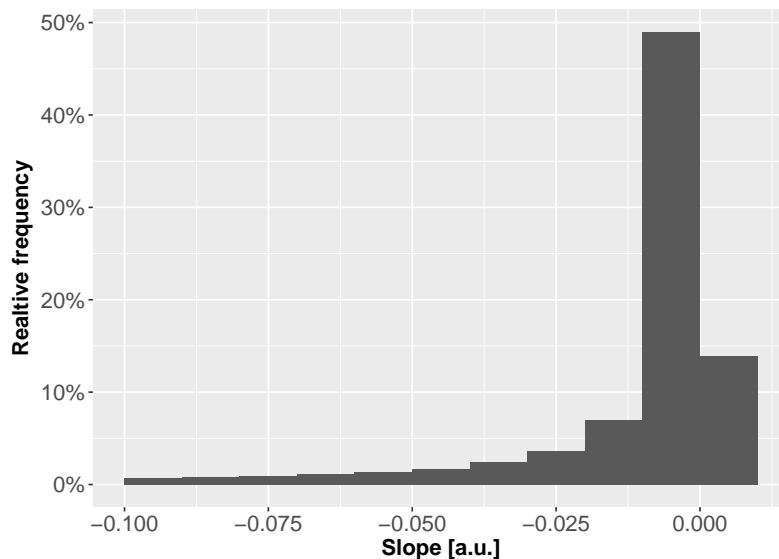


**Figure 4.7:** Histogram of the slope of the initial RF signal from -0.1 to the maximum value. About 14 % of all combinations lead to a positive slope signal.

## 4.5 Comparison with experimental results

### 4.5.1 Materials and methods

For our experiments we used three different types of natural quartz: a sediment quartz (BT586), a colourless (Hyaline) and a smoky quartz. These samples were already part of other studies, see Fasoli & Martini (2016), Friedrich et al. (2017), Martini et al. (2014), and Vaccaro et al. (2017). The crystals were crushed, grinded (colourless and smoky quartz), and sieved to select grains of 90 – 200  $\mu\text{m}$  in diameter. Subsequent chemical treatments for BT586 followed routine preparation procedures for luminescence dating samples, described in Preusser et al. (2008) and especially for BT586 in Friedrich et al. (2017). The RF measurements were carried out at room temperature (RT) using a home-made apparatus featuring, as detection system, a back illuminated UV-enhanced charge coupled device (CCD) (Jobin-Yvon Spectrum One 3000) coupled to a spectrograph operating in the 200 – 1100 nm range (Jobin-Yvon Triax 180). RF excitation was obtained by X-ray irradiation, through a Be window, using a Philips 2274 X-ray tube, with Tungsten target and operated at 20 kV. During each measurement, lasting 30 s, the sample was given a dose of  $6 \pm 1$  Gy, where the uncertainty is related to the dose calibration rather than to its repeatability that was quite good (1 %).

King et al. (2011) fitted cathodoluminescence curves (intensity against dose) with a power law approach without giving a physical explanation for the used formula. Based on our analytical solutions we advocate another approach, described in the following: From Eq. (4.30) it is known that the concentration of holes in the L-centre (in the framework of a completely empty R-centre) is a composite of two components: (1) The diffusion of holes

into the L-centre (saturating exponential) and (2) the loss of holes due to recombination (exponential decay). Therefore the following function is used to fit UV-RF signals after a strong preheat to 500 °C for 10 min:

$$\begin{aligned}
 I(t) &= \overbrace{A \cdot \left(1 - \exp\left(-\frac{t}{C}\right)\right)}^{\text{build up}} + \overbrace{B \cdot \exp\left(-\frac{t}{C}\right)}^{\text{decay}} \\
 &= A + \bar{B} \cdot \exp\left(-\frac{t}{C}\right),
 \end{aligned} \tag{4.18}$$

where  $\bar{B}$  is another constant with  $\bar{B} = B - A$ . From a series of publications it is known that a preheat to 500 °C leads to a strong decay of RF in the UV region at the start of the measurement. We normalise the UV-RF signal ( $I(0) = 1$ ), rename  $\bar{B}$  to  $B$  and use Eq. (4.18):

$$\begin{aligned}
 I(0) &= A + B \cdot \exp\left(\frac{0}{C}\right) = 1 \\
 \Rightarrow A + B &= 1 \\
 \Leftrightarrow B &= 1 - A
 \end{aligned} \tag{4.19}$$

Using Eq. (4.19) in Eq. (4.18):

$$\begin{aligned}
 I(t) &= A + (1 - A) \cdot \exp\left(-\frac{t}{C}\right) \\
 &= A \cdot \underbrace{\left(1 - \exp\left(-\frac{t}{C}\right)\right)}_{\text{saturating function}} + \underbrace{\exp\left(-\frac{t}{C}\right)}_{\text{decaying function}}
 \end{aligned} \tag{4.20}$$

Time  $t$  can be substituted by dose  $D$  via a known dose rate  $\dot{D}$ :

$$\begin{aligned}
 D &= \dot{D} \cdot t \\
 \Rightarrow I(D) &= A \cdot \left(1 - \exp\left(-\frac{D}{C}\right)\right) + \exp\left(-\frac{D}{C}\right)
 \end{aligned} \tag{4.21}$$

The more general function from Eq. (4.18) with three parameters is used for fitting UV-RF signals from samples lacking any thermal pre-treatments.

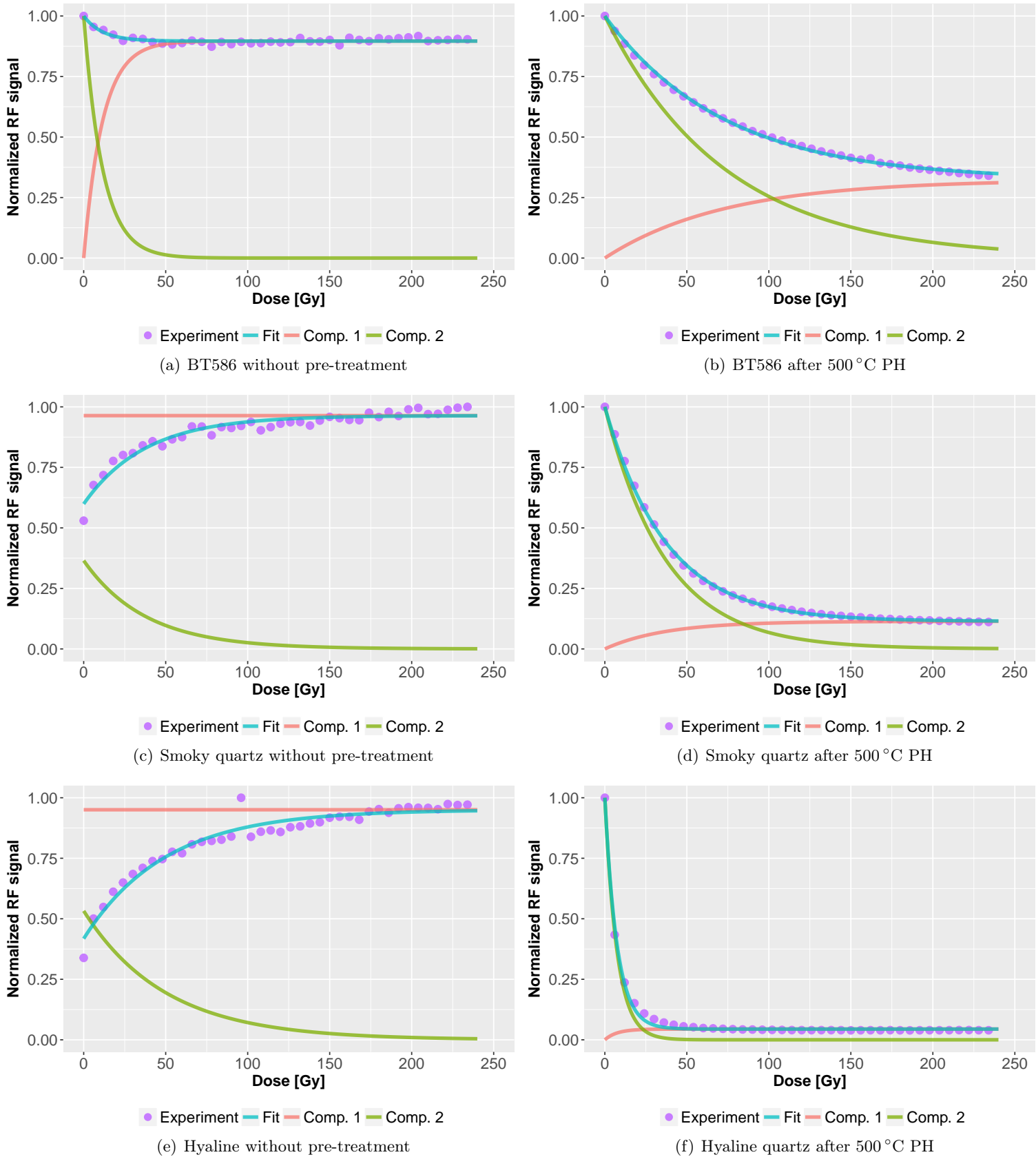
#### 4.5.2 Measurements in the UV

Figure 4.8 shows the results of the spectra measurements in the C band. The signal means from  $360 \pm 10$  nm were used to calculate the signal dynamics in the C band. Note that also the X band can superpose to the C band, especially for un-annealed samples. Nevertheless, spectra from all quartz samples show no contribution from the X band to the C band. A detailed overview over emission bands is given by Fasoli & Martini (2016). Figures 4.8

(a), (c), and (e) show the C band from untreated quartz samples BT586, Hyaline and the smoky quartz, respectively. In contrast Figs. 4.8 (b), (d), and (f) show the C band dynamics for the samples BT586, Hyaline and the smoky quartz after a preheat to 500 °C for 10 min, respectively. As mentioned in Sec. 4.5.1 the signals from all preheated samples (Fig. (b), (d), and (f)) were fitted with Eq. (4.21) with a good agreement between the fit and the experimental data. Also plotted in Fig. 4.8 are the components (see Eq. (4.21)). Component 1 describes the saturating part and component 2 the decaying part of the fitting function. The fitting function used for the untreated samples, except BT 586 (Subfig. (a)), was Eq. (4.18) with three fitting parameters. Component 1 describes the constant part with parameter  $A$  and component 2 equals  $B \cdot \exp(-\frac{t}{C})$ . Although Subfig. (a) presents an untreated sample the fitting with Eq. (4.18) failed. But because of the decreasing part of the curve Eq. (4.21) fits very well. Note that using Eq. (4.18) in Subfig. (c) and (e) leads to a value of  $A \approx 1$  since the data asymptotically approach this value at the end of the measurement. When substituting  $A = 1$ , we also get a fitting function with two parameters.

### 4.5.3 Interpretation

The experimental data support the theoretical findings from Sec. 4.3: A change in the concentration of holes in the R- and L-centre leads to a different behaviour of the signal dynamics. Due to the preheat to 500 °C the concentration of holes in the R-centre decreases and accordingly the concentration of holes in the L-centre increases (Zimmerman 1971). The result from this is that all three samples show a strong signal decay in the C band after the preheat. In contrast to that the untreated samples exhibit an increasing signal during RF measurements (Subfig (c) and (e)) or a slightly decreasing signal (Subfig. (a)). This is in accordance with the analytical findings that a random distribution of holes between the L- and R-centre leads to a diversity of signal dynamics, see Fig. 4.7.



**Figure 4.8:** (a), (c), and (e) show the UV-RF signal dynamics in the C band for untreated quartz samples. (b), (d), and (f) show the UV-RF signal dynamics in the C band for preheated quartz samples (500 °C). All signals from preheated samples as well as the signal from untreated sample BT586 were fitted with Eq. (4.21). Data displayed in Subfig. (c) and (e) were fitted using Eq. (4.18), where parameter  $B$  is negative.

## 4.6 Discussion

Bailey (2001) already mentioned the difference between the model by Zimmerman (1971) and the one presented by himself: In Bailey (2001) the recombination of electrons and holes within the R-centre is allowed and hence the R-centre is in competition with the L-centre for free electrons in the conduction band. During RF/irradiation  $R$  electron-hole pairs are produced and  $R$  free electrons are available in the conduction band. When assuming that a recombination within the R-centres is not allowed and we consider case I from Sec. 4.4.1 (empty R-centre at the beginning of the simulation) then a constant UV-RF signal with the signal intensity of  $R$  is the result of the simulations, see Fig. 4.9. All electrons available in the conduction band have to recombine in the L-centre. Figure 4.10 shows the concentration of holes in the R-centre during RF simulation. When using the model by Zimmerman (1971) this number grows linearly and the concentration of holes in the R-centre after 10,000s of irradiation is  $3 \text{ E}+05 \cdot 1 \text{ E}+04 = 3 \text{ E}+09$  holes. In contrast, the concentration of holes in the R-centre is smaller in the model by Bailey (2001). Holes can be removed due to recombination with electrons in the R-centre. As irradiation time progresses in the simulation, the competition between R- and L-centre is becoming bigger. This results in a decreasing RF curve (see Fig. 4.9). Comparing this to experimental data, the model by Bailey (2001) appears to be more appropriate for simulating RF phenomena. But note that neither the model by Bailey (2001) nor the one by Zimmerman (1971) were developed to simulate RF.

Furthermore, the comparison of different models shows that the most important fact of UV-RF simulation is the competition for electrons between the recombination centres (R- and L-centres). That is one of the reasons why simulating experimental UV-RF results with an OTOR (One-Trap-One-Recombination centre) model has to fail.

Although the analytical expressions derived in this study are helpful to understand the basics of quartz UV-RF, there is no mathematical description of the UV-RF curve as known from OSL (Chen & McKeever 1997; Chen & Leung 2003). With the approach of linearisation (Eq. (4.11)) we are not able to describe the behaviour for long simulation times. We know from experimental results that the slopes of the UV-RF curves after preheating are not constant and after long irradiation an equilibrium is reached (Brik et al. 1994; Friedrich et al. 2017; Marazuev et al. 1995; Shimizu et al. 2006).

The results suggest that different RF behaviour of thermally un-treated quartz can be an indicator for diverse charge distributions. The reason could be a different geological origin or sample history for the quartz grains. To confirm this, further investigations are needed, especially in combination with other analysis methods like inductively coupled plasma mass spectrometry (ICP-MS) or scanning electron microscope (SEM).

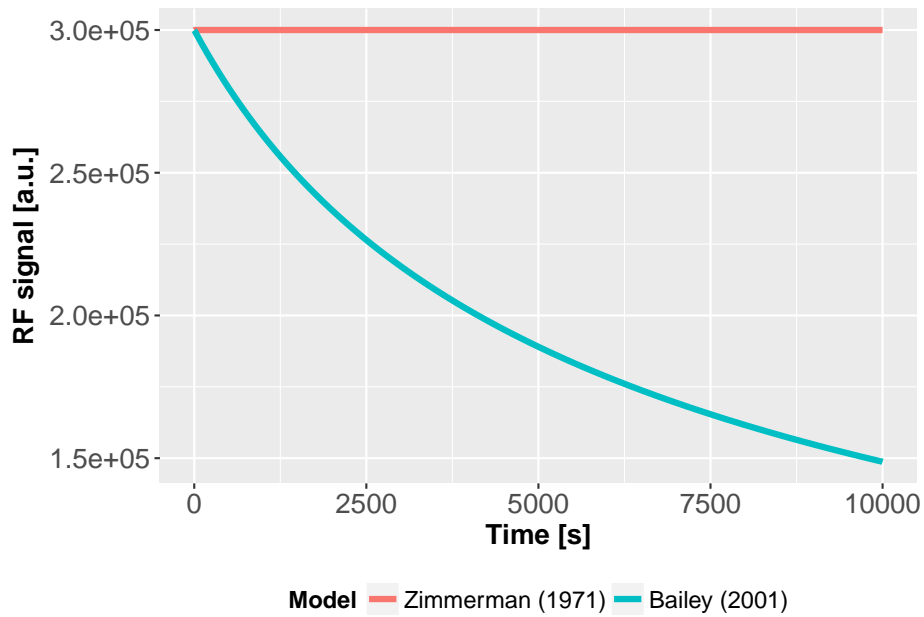


**Figure 4.9:** Comparison of the model by Bailey (2001) and Zimmerman (1971) for a simulated UV-RF signal. The starting condition was  $m_{1_0} = n_0 = M_1$ , see case I in Sec. 4.4.1.

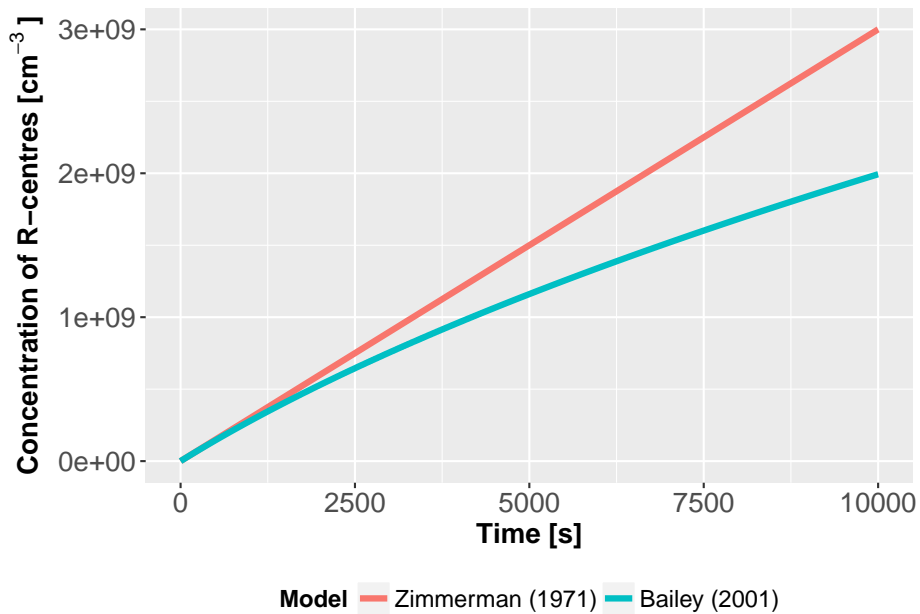


**Figure 4.10:** Comparison between the model by Bailey (2001) and Zimmerman (1971) for the concentration of holes in the R-centre for the same simulation as shown in Fig. 4.9. The starting condition was  $m_{1_0} = n_0 = M_1$ , see case I in Sec. 4.4.1.

## 4.7 Conclusion

We investigated the dynamics of the quartz UV-RF signal from a theoretical point of view and compared these results to experimentally obtained data. A three-energy-level model was used to derive analytical solutions of the initial signal intensity and the slope of the RF signal at the beginning of the simulation.

By comparing the analytical solutions with numerical solutions and the experimental results, it is possible to explain some basic principles of quartz UV-RF. Our derived analytical solutions for the initial signal and the slope of the RF signal in quartz are in excellent agreement with the numerical solutions. The results obtained show that the change in the signal shape is dependent on the filling of the L- and R-centre at the beginning of the measurement or simulation. Preheat experiments confirm this behaviour: Increasing the concentration of holes in the L-centre by thermally depleting the R-centre leads to higher and steeper initial signals. Heating to even higher temperatures causes decreased and flatter initial RF signals. At high temperatures the deep electron trap is emptied and so the concentration of holes in the L-centre decreases due to recombination. Referring to Figs. 4.3 and 4.4, this leads to a shift on the x-axis to the left along the trajectory indicated by the plotted data points. Consequently, a smaller RF intensity and a flatter RF signal is expected. This was confirmed experimentally (Friedrich et al. 2017).

When measuring the C band of quartz without any thermal pre-treatment, we can expect a variety of signal dynamics during the measurement. This variety can occur due to different conditions of quartz formation and associated variations in relative abundance of defect concentrations or diverse thermal, mechanical or chemical treatments prior to RF analysis.

The main fact responsible for the observation of decaying UV-RF signals with time/dose is the increasing competition for electrons between the L-centre and other recombination centres. This shows a comparison between different kinetic quartz models.

Furthermore we presented a mathematical description of the UV-RF signal in quartz and fitted experimental results with a two-component function. For preheated samples we obtained a very good agreement between experimental data and the fit. The application of the derived two-component formula describing the RF signal shape is not restricted to the UV emission, but may be extended to other emission bands in the future.

## 4.8 Acknowledgements

JF is gratefully supported by the DFG (2015 – 2018, “*Modelling quartz luminescence signal dynamics relevant for dating and dosimetry*”, SCHM 3051/4-1). The work of SK is financed by a programme supported by the ANR - n° ANR-10-LABX-52. We also thank the anonymous reviewer for his/her helpful suggestions.

## 4.A Appendix

### 4.A.1 Derivation of the coefficient $C_2$

$$\begin{aligned}
 C_2 &= \left. \frac{d(B_2 \cdot m_2 \cdot n_c)}{dt} \right|_{t=0} \\
 &= B_2 \cdot \left[ n_c \cdot \frac{dm_2}{dt} + m_2 \cdot \frac{d}{dt} \left( \frac{R}{A_n \cdot (N - n) + B_2 \cdot m_2 + B_1 \cdot m_1} \right) \right] \Big|_{t=0} \\
 &= B_2 \cdot \left[ n_c \cdot \frac{dm_2}{dt} + m_2 \cdot R \cdot \frac{A_n \frac{dn}{dt} - B_2 \cdot \frac{dm_2}{dt} - B_1 \cdot \frac{dm_1}{dt}}{(A_n \cdot (N - n) + B_2 \cdot m_2 + B_1 \cdot m_1)^2} \right] \Big|_{t=0} \\
 &= B_2 \cdot \left[ n_c \cdot \frac{dm_2}{dt} + \frac{n_c^2 \cdot m_2}{R} \cdot \left( A_n \frac{dn}{dt} - B_2 \cdot \frac{dm_2}{dt} - B_1 \cdot \frac{dm_1}{dt} \right) \right] \Big|_{t=0}
 \end{aligned} \tag{4.22}$$

order  $\frac{dm_2}{dt}$

$$C_2 = \frac{B_2 \cdot n_c}{R} \cdot \left[ (R - m_2 \cdot n_c \cdot B_2) \cdot \frac{dm_2}{dt} + n_c \cdot m_2 \cdot \left( A_n \frac{dn}{dt} - B_1 \cdot \frac{dm_1}{dt} \right) \right] \Big|_{t=0} \tag{4.23}$$

Use Eqs. (4.1), (4.2) and (4.3) and order:

$$\begin{aligned}
 C_2 &= \frac{B_2 \cdot n_c}{R} \cdot [(R - m_2 \cdot n_c \cdot B_2) \cdot (A_{m_2} \cdot (M_2 - m_2) \cdot n_v - B_2 \cdot m_2 \cdot n_c) \\
 &\quad + n_c \cdot m_2 \cdot (A_n^2 \cdot (N - n) \cdot n_c - B_1 \cdot A_{m_1} \cdot (M_1 - m_1) \cdot n_v + B_1^2 \cdot m_1 \cdot n_c)] \Big|_{t=0}
 \end{aligned} \tag{4.24}$$

$$\begin{aligned}
 C_2 &= \frac{B_2 \cdot n_{c_0}}{R} \cdot [(R - m_{2_0} \cdot n_{c_0} \cdot B_2) \cdot (A_{m_2} \cdot (M_2 - m_{2_0}) \cdot n_{v_0} - B_2 \cdot m_{2_0} \cdot n_{c_0}) \\
 &\quad + n_{c_0} \cdot m_{2_0} \cdot (A_n^2 \cdot (N - n_0) \cdot n_{c_0} - B_1 \cdot A_{m_1} \cdot (M_1 - m_{1_0}) \cdot n_{v_0} + B_1^2 \cdot m_{1_0} \cdot n_{c_0})]
 \end{aligned} \tag{4.25}$$

Use Eq. (4.9):  $R - m_{2_0} \cdot n_{c_0} \cdot B_2 = n_{c_0} \cdot (A_n \cdot (N - n_0) + B_1 \cdot m_{1_0})$

$$\begin{aligned}
 C_2 &= \frac{B_2 \cdot n_{c_0}^2}{R} \cdot [(A_n \cdot (N - n_0) + B_1 \cdot m_{1_0}) \cdot (A_{m_2} \cdot (M_2 - m_{2_0}) \cdot n_{v_0} - B_2 \cdot m_{2_0} \cdot n_{c_0}) \\
 &\quad + m_{2_0} \cdot (A_n^2 \cdot (N - n_0) \cdot n_{c_0} - B_1 \cdot A_{m_1} \cdot M_1 \cdot n_{v_0} + B_1^2 \cdot m_{1_0} \cdot n_{c_0})]
 \end{aligned} \tag{4.26}$$

Collect terms involving  $n_{c_0}$  and  $n_{v_0}$  and substitute with Eqs. (4.9) and (4.10).

$$\begin{aligned}
 C_2 = & \frac{B_2 \cdot n_{c_0}^2}{R} \cdot [n_{c_0} \cdot m_{2_0} \cdot (A_n^2 \cdot (N - n_0) + B_1^2 \cdot m_{1_0} - B_2 \cdot (A_n \cdot (N - n_0) + B_1 \cdot m_{1_0})) \\
 & + n_{v_0} \cdot ((A_n \cdot (N - n_0) + B_1 \cdot m_{1_0}) \cdot A_{m_2} \cdot (M_2 - m_{2_0}) - B_1 \cdot A_{m_1} \cdot (M_1 - m_{1_0}) \cdot m_{2_0})]
 \end{aligned} \tag{4.27}$$

$$\begin{aligned}
 C_2 = & \frac{B_2 \cdot R^2}{(A_n \cdot (N - n_0) + B_2 \cdot m_{2_0} + B_1 \cdot m_{1_0})^2} \\
 & \cdot \left( m_{2_0} \cdot \frac{A_n \cdot (N - n_0)(A_n - B_2) + m_{1_0} \cdot (B_1^2 - B_2 \cdot B_1)}{A_n \cdot (N - n_0) + B_2 \cdot m_{2_0}} \right. \\
 & \left. + \frac{A_n \cdot (N - n_0) \cdot A_{m_2} \cdot (M_2 - m_{2_0}) - B_1 \cdot A_{m_1} \cdot (M_1 - m_{1_0}) \cdot m_{2_0}}{A_{m_2} \cdot (M_2 - m_{2_0}) + A_{m_1} \cdot (M_1 - m_{1_0})} \right)
 \end{aligned} \tag{4.28}$$

#### 4.A.2 Derivation of the concentration of holes in the R- and L-centre (for $m_{1_0} = 0$ )

Using Eqs. (4.9) and (4.10) and  $m_{1_0} = 0$

##### 4.A.2.1 Concentration of holes in the L-centre

$$\begin{aligned}
 \frac{dm_2}{dt} = & A_{m_2} \cdot (M_2 - m_2) \cdot n_v - B_2 \cdot m_2 \cdot n_c \\
 = & \frac{A_{m_2} \cdot (M_2 - m_2) \cdot R}{A_{m_2} \cdot (M_2 - m_{2_0}) + A_{m_1} \cdot M_1} - \frac{B_2 \cdot m_2 \cdot R}{A_n \cdot (N - n_0) + B_2 \cdot m_{2_0}}
 \end{aligned} \tag{4.29}$$

Solving this differential equation with boundary condition  $m_2(0) = m_{2_0}$ :

$$m_2 = \frac{B_2 \cdot m_{2_0} \cdot (A_{m_2} \cdot M_2 + A_{m_1} \cdot M_1 \cdot e^{-D \cdot t \cdot R}) + A_{m_2} \cdot A_n \cdot (N - n_0) \cdot (M_2 \cdot (1 - e^{-D \cdot t \cdot R}) + m_{2_0})}{B_2 \cdot (A_{m_2} \cdot M_2 + A_{m_1} \cdot M_1) + A_{m_2} \cdot A_n \cdot (N - n_0)} \tag{4.30}$$

with

$$D = \frac{B_2 \cdot (A_{m_2} \cdot M_2 + A_{m_1} \cdot M_1) + A_{m_2} \cdot A_n \cdot (N - n_0)}{(A_{m_2} \cdot (M_2 - m_{2_0}) + A_{m_1} \cdot M_1) \cdot (B_2 \cdot m_{2_0} + A_n \cdot (N - n_0))} \tag{4.31}$$

For  $t \rightarrow 0$ :  $m_2 \rightarrow m_{2_0}$

For  $t \rightarrow \infty$ :  $m_2 \rightarrow$  finite value (depending on parameters)

#### 4.A.2.2 Concentration of holes in the R-centre

The analytical function for  $m_1$ , the concentration of holes in the R-centre. It is solved in the same manner as Eq. (4.30)

$$m_1 = \frac{A_{m_1} \cdot M_1 \cdot (1 - e^{-E \cdot t \cdot R}) \cdot (A_n \cdot (N - n_0) + B_2 \cdot m_{2_0})}{B_1 \cdot (A_{m_2} \cdot (M_2 - m_{2_0}) + A_{m_1} \cdot M_1) + A_{m_1} \cdot (B_2 \cdot m_{2_0} + A_n \cdot (N - n_0))} \quad (4.32)$$

with

$$E = \frac{B_1 \cdot (A_{m_2} \cdot (M_2 - m_{2_0}) + A_{m_1} \cdot M_1) + A_{m_1} \cdot (B_2 \cdot m_{2_0} + A_n \cdot (N - n_0))}{(A_{m_2} \cdot (M_2 - m_{2_0}) + A_{m_1} \cdot M_1) \cdot (B_2 \cdot m_{2_0} + A_n \cdot (N - n_0))} \quad (4.33)$$

It is obvious that for  $t \rightarrow 0$   $m_1 \rightarrow 0$

For  $t \rightarrow \infty$ :  $m_1 \rightarrow$  finite value (depending on parameters)

$m_1$  is a saturating exponential growth curve.

#### 4.A.2.3 Concentration of electrons in the deep trap

From Eq. (4.1) we obtain the following analytical expression for the concentration of electrons in the deep trap. The electron concentration in the deep trap increases continuously with irradiation time during RF and has a saturating exponential form.

$$n = N - (N - n_0) \cdot e^{-A_n \cdot F \cdot t} \quad (4.34)$$

with

$$F = \frac{R}{A_n \cdot (N - n_0) + B_2 \cdot m_{2_0}} \quad (4.35)$$

For  $t \rightarrow 0$ :  $n \rightarrow n_0$

For  $t \rightarrow \infty$ :  $n \rightarrow N$

## References

- Aznar, M. C., 2005. Real-time in vivo luminescence dosimetry in radiotherapy and mammography using  $\text{Al}_2\text{O}_3:\text{C}$ . Risø-PhD-12 (EN). Risø National Laboratory, Roskilde (Denmark).
- Bailey, R. M., 2001. Towards a general kinetic model for optically and thermally stimulated luminescence of quartz. *Radiation Measurements* 33(1), 17–45.
- Brik, A. B., Degoda, V. Y., Marazuev, Y. A., 1994. X-ray luminescence dosimetry of irradiated quartz. *Journal of Applied Spectroscopy* 60(5), 398–400.
- Chen, R., McKeever, S. W. S., 1997. *Theory of Thermoluminescence and Related Phenomena*. World Scientific, Singapore.
- Chen, R., Leung, P., 2003. The decay of OSL signals as stretched-exponential functions. *Radiation measurements* 37(4), 519–526.
- Chithambo, M., Niyonzima, P., 2017. Radioluminescence of annealed synthetic quartz. *Radiation Measurements* 106, 35–39.
- Fasoli, M., Martini, M., 2016. The composite nature of the thermoluminescence UV emission of quartz. *Journal of Luminescence* 173, 120–126.
- Friedrich, J., Pagonis, V., Chen, R., Kreutzer, S., Schmidt, C., 2017. Quartz radiofluorescence: a modelling approach. *Journal of Luminescence* 186, 318–325.
- King, G., Finch, A., Robinson, R., Taylor, R., Mosselmans, J., 2011. The problem of dating quartz 2: Synchrotron generated X-ray excited optical luminescence (XEOL) from quartz. *Radiation Measurements* 46(10), 1082–1089.
- Krbetschek, M., Trautmann, T., 2000. A spectral radioluminescence study for dating and dosimetry. *Radiation Measurements* 32(5), 853–857.
- Marazuev, Y. A., Brik, A. B., Degoda, V. Y., 1995. Radioluminescent dosimetry of  $\alpha$ -quartz. *Radiation Measurements* 24(4), 565–569.
- Martini, M., Fasoli, M., Villa, I., Guibert, P., 2012. Radioluminescence of synthetic and natural quartz. *Radiation Measurements* 47(9), 846–850.
- Martini, M., Fasoli, M., Villa, I., 2014. Defect studies in quartz: Composite nature of the blue and UV emissions. *Nuclear Instruments and Methods in Physics Research Section B: Beam Interactions with Materials and Atoms* 327, 15–21.
- Pagonis, V., Lawless, J. L., Chen, R., Andersen, C., 2009. Radioluminescence in  $\text{Al}_2\text{O}_3:\text{C}$  - analytical and numerical simulation results. *Journal of Physics D: Applied Physics* 42(17), 175107.
- Poolton, N., Bulur, E., Wallinga, J., Bøtter-Jensen, L., Murray, A., Willumsen, F., 2001. An automated system for the analysis of variable temperature radioluminescence. *Nuclear Instruments and Methods in Physics Research Section B: Beam Interactions with Materials and Atoms* 179(4), 575–584.
- Preusser, F., Degering, D., Fuchs, M., Hilgers, A., Kadereit, A., Klasen, N., Krbetschek, M., Richter, D., Spencer, J. Q. G., 2008. Luminescence dating: basics, methods and applications. *Quaternary Science Journal* 57(1-2), 95–149.

- R Core Team, 2017. *R: A Language and Environment for Statistical Computing*. R Foundation for Statistical Computing. Vienna, Austria. <https://www.R-project.org/>,
- Schilles, T., Poolton, N., Bulur, E., Bøtter-Jensen, L., Murray, A., Smith, G., Riedi, P., Wagner, G., 2001. A multi-spectroscopic study of luminescence sensitivity changes in natural quartz induced by high-temperature annealing. *Journal of Physics D: Applied Physics* 34(5), 722–731.
- Shimizu, N., Mitamura, N., Takeuchi, A., Hashimoto, T., 2006. Dependence of radioluminescence on TL-properties in natural quartz. *Radiation Measurements* 41(7), 831–835.
- Soetaert, K., Cash, J., Mazzia, F., 2012. *Solving differential equations in R*. Springer Science & Business Media.
- Vaccaro, G., Panzeri, L., Paleari, S., Martini, M., Fasoli, M., 2017. EPR investigation of the role of germanium centers in the production of the 110 °C thermoluminescence peak in quartz. *Quaternary Geochronology* 39, 99–104.
- Zimmerman, J., 1971. The radiation-induced increase of the 100 °C thermoluminescence sensitivity of fired quartz. *Journal of Physics C: Solid State Physics* 4(18), 3265–3276.

# 5 On the dose rate dependence of radiofluorescence signals of natural quartz

Johannes Friedrich<sup>1</sup>, Mauro Fasoli<sup>2,3</sup>, Sebastian Kreutzer<sup>4</sup>, Christoph Schmidt<sup>1</sup>

<sup>1</sup> Chair of Geomorphology & BayCEER, University of Bayreuth, 95440 Bayreuth, Germany

<sup>2</sup> Dipartimento di Scienza dei Materiali, Università degli Studi di Milano Bicocca, via R. Cozzi 55, I-20125 Milano, Italy

<sup>3</sup> INFN, Sezione di Milano Bicocca, Piazza della Scienza 1, I-20126 Milano, Italy

<sup>4</sup> IRAMAT-CRP2A, Université Bordeaux Montaigne, Maison de l'Archéologie, Esplanade des Antilles, 33607 Pessac Cedex, France

*Radiation Measurements* 111, 19 – 26, 2018

<https://doi.org/10.1016/j.radmeas.2018.02.006>

## Abstract

The general behaviour of the main UV emission during radiofluorescence (RF) in natural quartz with dose rates ranging from 10 – 500 mGy s<sup>-1</sup> is analysed. RF emission spectra were recorded and deconvolved to extract information on the C band, which is often the main emission of quartz annealed at a temperature close to 500 °C. Our results confirmed theoretical findings, e.g., the direct proportionality of the initial RF signal of the C band with dose rate and the direct proportionality of the initial slope with the squared dose rate. Furthermore, numerical simulations employing a three-energy-level model and experimental data are in agreement. A first concept of using quartz UV-RF for dosimetric application is given based on the findings that different absorbed doses resulting from different dose rates match well into a single UV-RF decay curve.

## 5.1 Introduction

Thermoluminescence (TL) and optically stimulated luminescence (OSL) are well established methods to determine the energy dose absorbed by natural minerals, such as quartz and feldspar. A key aspect in the accuracy of luminescence dating is the reproducibility of natural processes in the laboratory. However, typical dose rates applied in the laboratory differ by several orders of magnitude from the dose rate in nature. The effect of different dose rates on TL signals of quartz were investigated in different studies: Groom et al. (1978) reported a decrease of TL up to a factor of 5 with increased dose rate in powdered samples of Brazilian crystalline quartz when irradiated with a  $^{60}\text{Co}$  source at dose rates ranging from  $1.4 \text{ mGy s}^{-1}$  to  $3.3 \text{ Gy s}^{-1}$ . An opposite effect of higher TL response in quartz for larger dose rates was reported in Kvasnička (1979, 1983) using dose rates of  $0.02 \text{ mGy s}^{-1}$  to  $20 \text{ mGy s}^{-1}$ . Chen & McKeever (1997) pointed out that this discrepancy may be well described by the different (but overlapping) dose rate ranges. For a detailed overview of TL response to different dose rates see Chen & McKeever (1997: Sec. 4.6). Besides the experimental results, numerical models exist which help to understand the effect of different dose rates. McKeever et al. (1980) demonstrated numerically that an OTOR (one-trap-one-recombination centre) model is able to show a dose rate dependence of luminescence intensity, as well as does the model presented by Chen et al. (1981). Kijek & Chruścińska (2016, 2017) also investigated the difference between OSL dose response curves in the laboratory and in nature, where the dose rates differ by about ten orders of magnitude. They conclude that the difference between the growth curves is highly dependent on the filling of a deep electron trap.

This work investigates the dependence of the UV radiofluorescence (RF) signal of quartz on different dose rates. Radiofluorescence is the luminescence emitted during exposure to ionising radiation and for quartz believed to result from direct recombination of electrons with holes captured in recombination centres (cf. Schmidt et al. (2015) for a review). Therefore, RF allows direct insight into the charge redistribution during the irradiation process. As a result of the signal origin mentioned above, the number of generated free electrons in the quartz crystal should be proportional to the dose rate, and the initial RF intensity itself is related to the electron concentration in the conduction band (Friedrich et al. 2017c). These theoretical findings lead to the following hypotheses:

- The initial RF signal is directly proportional to the dose rate,
- the RF signal slope is directly proportional to the squared dose rate.

In this work we test these hypotheses through measurements on natural quartz for different dose rates. Furthermore, we present simulations of the measurements and compare them with experimentally obtained results.

## 5.2 Materials and methods

### 5.2.1 Quartz samples

Two different types of quartz were analysed in our investigation: a natural sedimentary quartz (BT586; Friedrich et al. (2017a,c)) and a coastal dune quartz (FB; Kreutzer et al. (2017a) and Schmidt et al. (2018)). Both samples were already part of different studies. Grains of 90 – 200  $\mu\text{m}$  in diameter were used. Both samples were annealed at 500 °C in the muffle oven: BT586 for 10 min and FB for 30 min, see Kreutzer et al. (2017a). For each measurement a new aliquot with the same amount of grains was used allowing a quantitative comparison of the results.

### 5.2.2 Measurement conditions

The RF measurements were carried out at room temperature (RT) using a home-made apparatus featuring, as detection system, a back illuminated UV-enhanced charge coupled device (CCD) (Jobin - Yvon Spectrum One 3000) coupled to a spectrograph operating in the 200 – 1100 nm range (Jobin - Yvon Triax 180). RF excitation was obtained by X-irradiation, through a Be window, using a Philips 2274 X-ray tube with Tungsten target and operated at 32 kV (0.6 – 29.6 mA). During each of the 41 consecutive measurements, everyone lasting 30 s, the samples were irradiated with dose rates ranging from 10 – 500 mGy s<sup>-1</sup>. Due to a software issue a delay of 4 s between each spectra recording was monitored which leads to an effective measurement time of 34 s. Hence doses from 13.6 – 680 Gy were absorbed. All the RF spectra were corrected for the spectral response of the detection systems.

### 5.2.3 Data analysis

Data analyses were carried out using the software *OriginPro9* and the statistical software **R** with a Levenberg-Marquardt algorithm (Marquardt 1963) for deconvolution of spectra into Gaussian components (R Core Team 2017). For simulating the UV-RF signals the **R**-package 'RLumModel' (Friedrich et al. 2016, 2017b) was used. The code for the simulations presented here can be found in the supplementary material, see Sec. A.4.

## 5.3 Results

Fasoli & Martini (2016) reported seven bands when deconvolving quartz RF spectra into Gaussian components. The recorded spectra in this paper were fitted with six Gaussian components, called the O, A, B, X, C and D band, without the M band being present in the spectra. The M band appears only when quartz samples are annealed at temperatures higher than 700 °C (Fasoli & Martini 2016). The values for the energy  $E$  [eV] and the full width at half maximum [eV] (FWHM) of individual, fitted emission bands are summarised in Table 5.1 and are the same as in Fasoli & Martini (2016: Table 1). Figure 1.10 shows

the results of these numerical fits, showing six Gaussian components for quartz sample BT586 and a dose rate of  $100 \text{ mGy s}^{-1}$ . Deconvolving the spectra indicated that the X band is not detectable in most of our recorded spectra and so we used the peak integral from  $3.37 - 3.47 \text{ eV}$  (see Fig. 1.10) to monitor the C band intensity changes, because there is no contribution from the X band despite the overlap.

BAND	E [eV]	$\sim \lambda_{\text{max}}$ [nm]	FWHM [eV]
O	1.92	635	0.39
A	2.51	490	0.46
B	2.79	440	0.46
X	3.06	395	0.89
C	3.42	360	0.58
M	3.73	330	0.45
D	3.93	315	0.49

**Table 5.1:** Spectral parameters of the emission bands resulting from Gaussian deconvolution of the spectra.

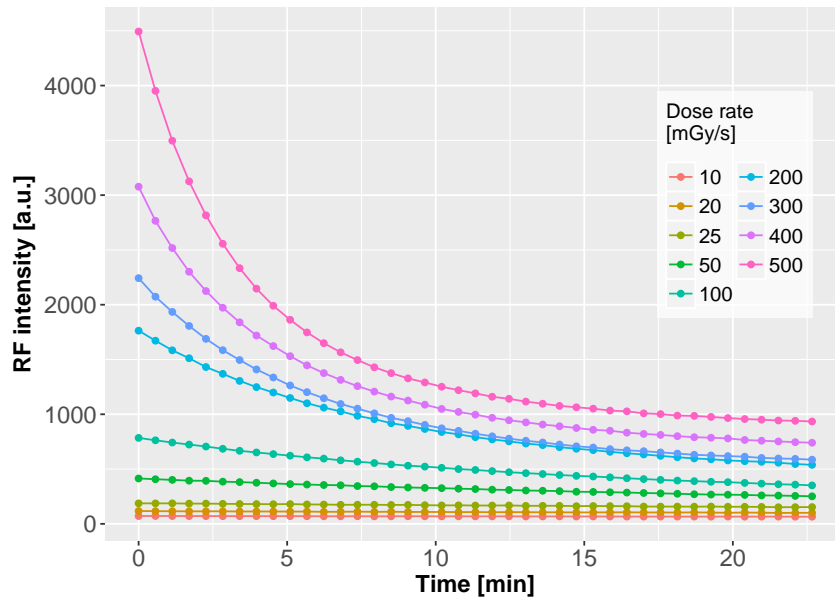
### 5.3.1 Effect of different dose rates on the C band (3.42 eV)

The effect of different dose rates on the C band, which is the dominant band when annealing quartz at  $500^\circ\text{C}$  (Friedrich et al. 2017a; Martini et al. 2012), was investigated in detail. Figure 5.1 shows the change of RF intensity in the C band with dose for (a) BT586 and (b) FB when using different dose rates. Some basic observations can be summarised as follows:

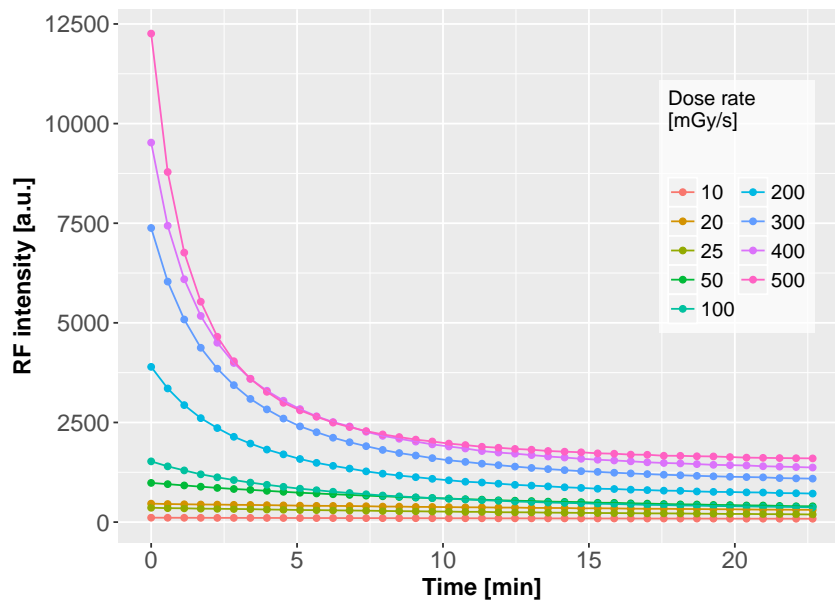
- The higher the dose rate, the higher the signal intensity,
- the higher the dose rate, the higher the intensity difference between the first and the last measurement,
- the C band in sample FB decreases much faster than in BT586.

Normalising the data to the first data point results in Fig. 5.2. A similar pattern is observed for both quartz samples: The higher the dose rate, the steeper is the slope of the signal obtained. The intensity of the C band of BT586 drops down to  $\sim 20\%$  of the initial intensity and for FB to  $\sim 12\%$  for the highest dose rate of  $500 \text{ mGy s}^{-1}$ . This minimum level is reached faster for sample FB than for sample BT586.

Nevertheless, when translating the time axis into a dose axis, the curves for sample FB overlap very well, see Fig. 5.3. That nearly all nine measured curves fit into one common curve was not necessarily expected since the dose rate differs more than one order of magnitude. The same behaviour was observed for sample BT586 (not shown here).



(a) Results for BT586



(b) Results for FB

**Figure 5.1:** RF intensity versus time for the C band (3.37 – 3.47 eV) for different dose rates. Subfigure (a) shows the results for BT586 and (b) for FB.

### 5.3.2 Analysis

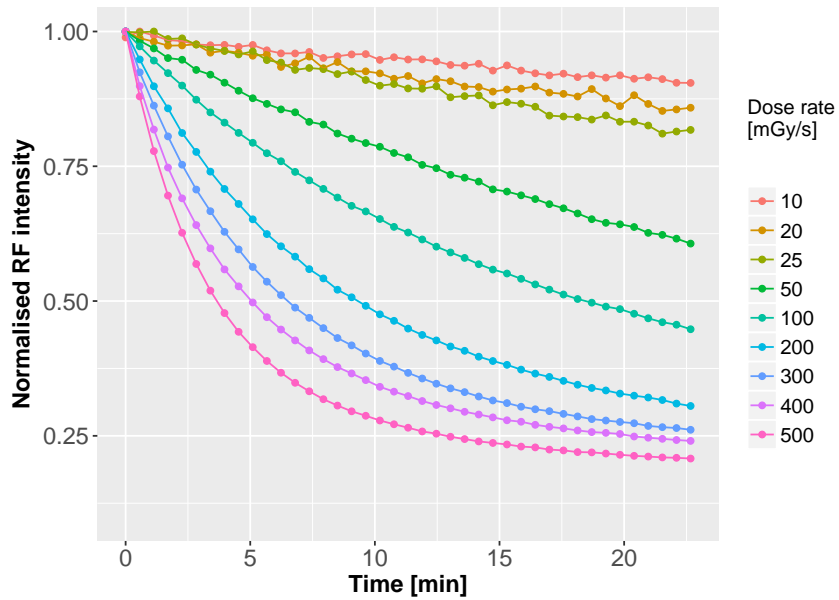
We analyse the results described in Sec. 5.3.1 for the initial signal (first data point) and the initial slope of the curves (first data point minus second data point). For  $\text{Al}_2\text{O}_3:\text{C}$  and a three-energy-level model for quartz it was already shown theoretically that the initial signal and the dose rate are linearly related, as well as is the case for the slope of the curve and the squared dose rate (Friedrich et al. 2017c; Pagonis et al. 2009). For quartz an experimental test for this behaviour is given in the next subsections.

#### 5.3.2.1 Initial signal

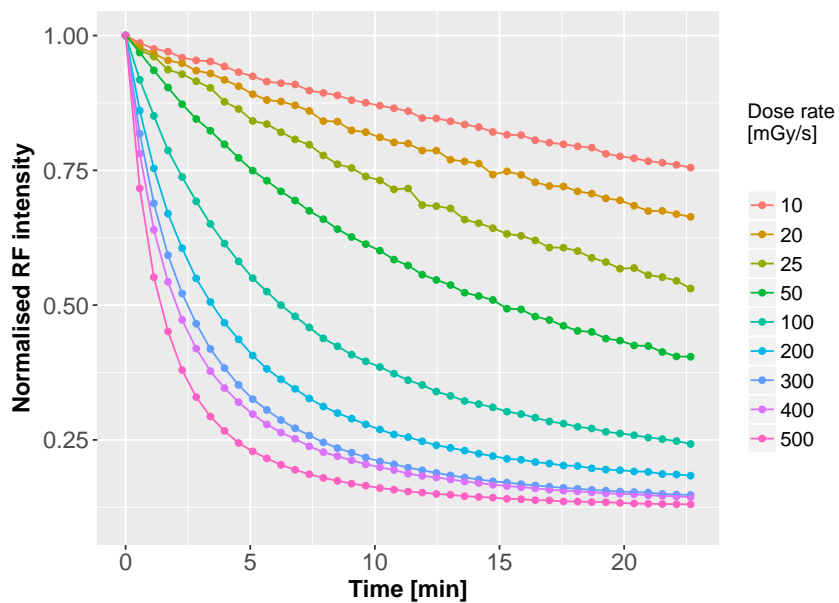
The initial signal is defined as the intensity of the C band in the first of the 41 measurement cycles. Figure 5.4 shows the initial signal against the dose rate for both quartz samples, BT586 and FB, respectively. A linear fit (Fig. 5.4) confirms direct proportionality with  $R^2 = 0.988$  (BT586) and  $R^2 = 0.993$  (FB). Note that the fit to the dataset of initial signal versus dose rate cannot be perfect since every measurement was started before opening the shutter of the source manually resulting in a short lag between the start of the irradiation and the beginning of the RF spectrum acquisition. Thus, the values presented in the y-axis in Fig. 5.4 are systematically underestimated by  $\sim 5\%$ . Nevertheless, the linear dependence of the initial signal on the dose rate is obvious for both quartz samples.

#### 5.3.2.2 Signal dynamics

We further analyse the initial slope of the RF signal. 'Initial slope' is here defined as the absolute difference between the counts of the first two measurements. Since the difference on the time axis is always constant, we omit it in the calculation of the so called 'slope'. As derived for  $\text{Al}_2\text{O}_3:\text{C}$  in Pagonis et al. (2009) and shown experimentally for  $\text{Al}_2\text{O}_3:\text{C}$  in Aznar (2005), the initial slope is proportional to the square of the dose rate for this phosphor. For quartz this was shown theoretically by Friedrich et al. (2017c). Figure 5.5 displays the dependence of the initial slope on the squared dose rate for the two quartz samples. The fits obtained here are better than the ones for the initial signal in Sec. 5.3.2.1 with  $R^2$  of 0.997 and 0.999 for BT586 and FB, respectively. The theoretical findings are, therefore, verified experimentally.



(a) Results for BT586



(b) Results for FB

**Figure 5.2:** Same data as in Fig. 5.1 normalised to the first data point. Subfigure (a) shows the results for BT586 and (b) for FB.

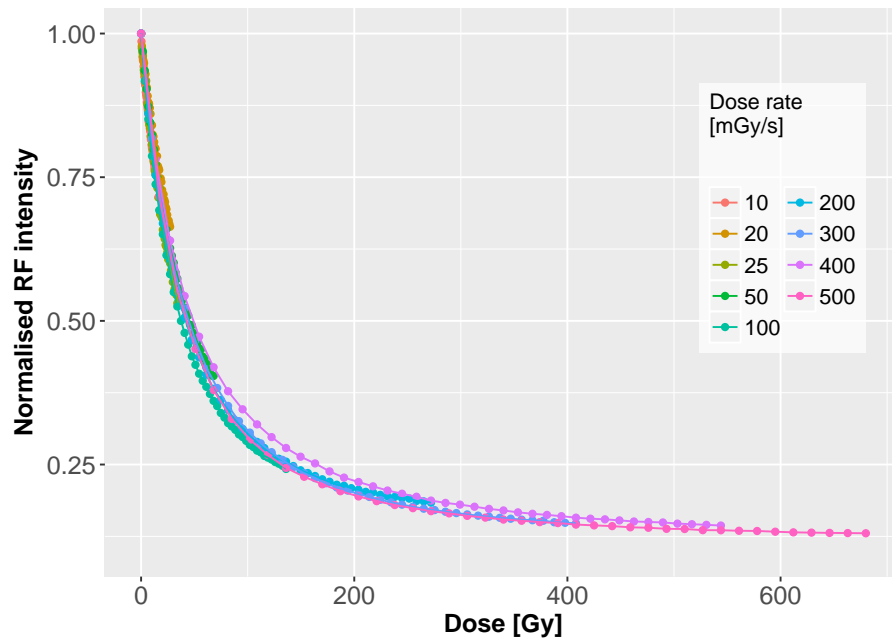


**Figure 5.3:** Translation of the data from Fig. 5.2 (b) to a dose-axis. The measurement time was  $\sim 23$  min, so doses from 13.6 – 680 Gy were applied.

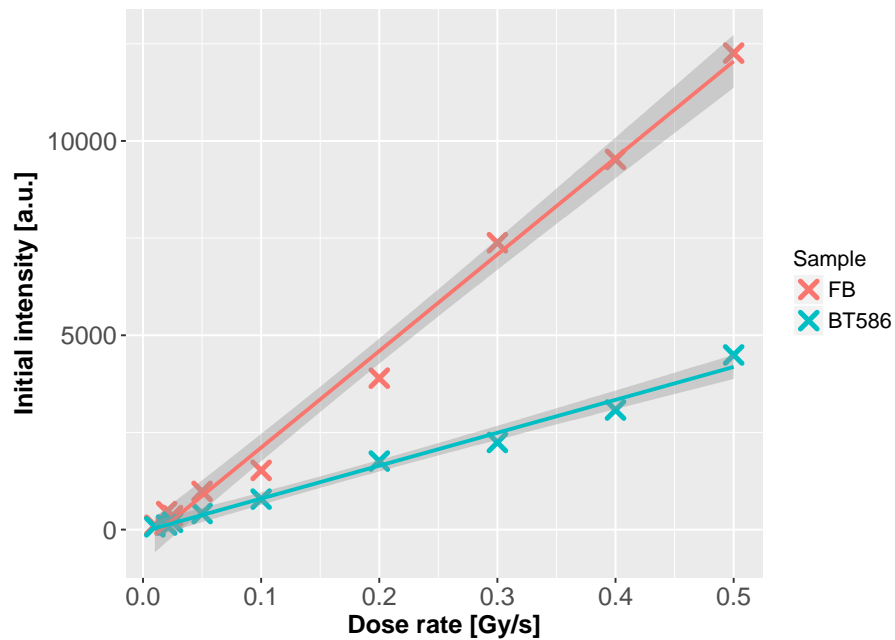


**Figure 5.4:** First data point of Fig. 5.1 versus dose rate for quartz samples BT586 and FB. The grey shaded area is the 95 % confidence level interval.

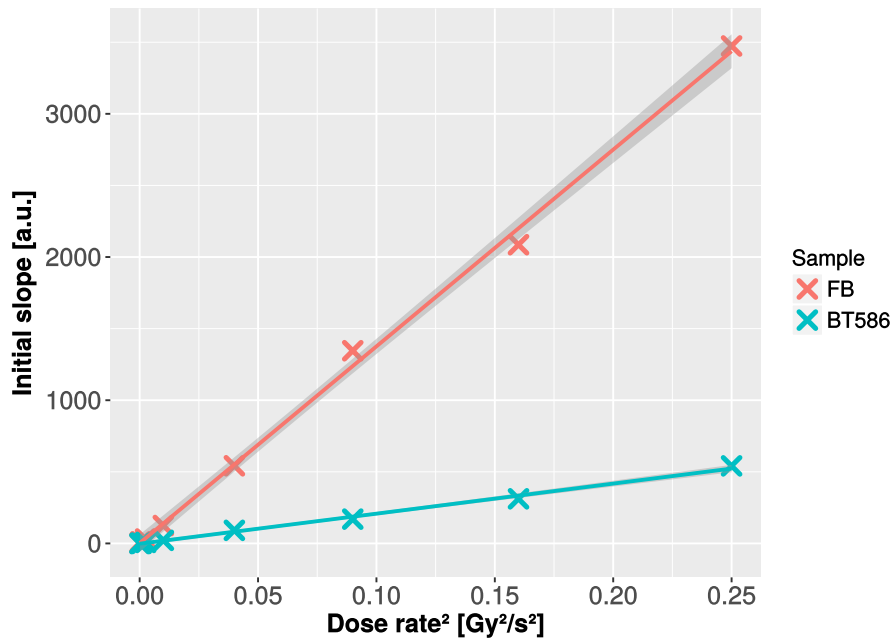


**Figure 5.5:** Initial slope (second data point minus first data point) of the UV-RF signal plotted against the square of dose rate for quartz samples BT586 ( $R^2 = 0.997$ ) and FB ( $R^2 = 0.999$ ). The grey shaded area is the 95 % confidence level interval.

## 5.4 Simulations

In order to understand the charge transfer during the measurements with different dose rates, we performed numerical simulations using the **R**-package 'RLumModel' (Friedrich et al. 2016, 2017b). The code is part of the supplementary material in Sec A.4. The model is designed for describing the UV-RF signal and capable of mimicking the behaviour of the C band.

### 5.4.1 Defining the model

A three-energy-level model was used to mimic the experimental results. A detailed overview of the model can be found in Friedrich et al. (2017c).

The following differential equations (5.1) – (5.4) describe the charge flow in quartz in the context of luminescence production. The total number of equations that need to be solved depends on the number of electron traps ( $q$ ) and hole centres ( $r$ ). For the case of the three-energy-level model  $q = 1$  and  $r = 2$ .

ABBREVIATION	DESCRIPTION	UNIT
$n_c$	Concentration of electrons in the conduction band	$\text{cm}^{-3}$
$n_v$	Concentration of holes in the valence band	$\text{cm}^{-3}$
$N_i$	Concentration of electron traps	$\text{cm}^{-3}$
$n_i$	Concentration of trapped electrons	$\text{cm}^{-3}$
$s_i$	Frequency factor for electron traps	$\text{s}^{-1}$
$E_i$	Electron trap depth below the conduction band	eV
$N_j$	Concentration of hole centres	$\text{cm}^{-3}$
$n_j$	Concentration of trapped holes in centres	$\text{cm}^{-3}$
$s_j$	Frequency factor for hole centres	$\text{s}^{-1}$
$E_j$	Hole trap depth above the valence band	eV
$A_i$	Conduction band to electron trap transition probability	$\text{cm}^3 \text{s}^{-1}$
$A_j$	Valence band to hole centre transition probability	$\text{cm}^3 \text{s}^{-1}$
$B_j$	Conduction band to hole centre transition probability	$\text{cm}^3 \text{s}^{-1}$
$k_B$	Boltzmann constant	$\text{eV K}^{-1}$
$T$	Absolute temperature	K
$R$	Ionisation rate (pair production rate)	$\text{cm}^{-3} \text{s}^{-1}$
$t$	Time	s

**Table 5.2:** Description of the abbreviations used in the differential equations (5.1) – (5.4).

LEVELS	$N$ [ $\text{cm}^{-3}$ ]	$E$ [eV]	$s$ [ $\text{s}^{-1}$ ]	$A$ [ $\text{cm}^3 \text{s}^{-1}$ ]	$B$ [ $\text{cm}^3 \text{s}^{-1}$ ]
1 Deep	5 E+10	1.95	1 E+10	1 E-10	-
2 R-centre	1 E+10	1.75	5 E+13	5 E-07	5 E-09
3 L-centre	1 E+11	5	1 E+13	1 E-09	5 E-10

**Table 5.3:** Simulation parameters

$$\frac{dn_i}{dt} = n_c \cdot (N_i - n_i) \cdot A_i - n_i \cdot s_i \cdot e^{-E_i/(k_B \cdot T)} \quad (5.1)$$

$$\frac{dn_j}{dt} = n_v \cdot (N_j - n_j) \cdot A_j - n_j \cdot s_j \cdot e^{-E_j/(k_B \cdot T)} - n_c \cdot n_j \cdot B_j \quad (5.2)$$

$$\frac{dn_c}{dt} = R - \sum_{i=1}^q \left( \frac{dn_i}{dt} \right) - \sum_{j=q+1}^{q+r} (n_c \cdot n_j \cdot B_j) \quad (5.3)$$

$$\frac{dn_v}{dt} = R - \sum_{j=q+1}^{q+r} \left( \frac{dn_j}{dt} \right) - \sum_{j=q+1}^{q+r} (n_c \cdot n_j \cdot B_j) \quad (5.4)$$

A short description of the used abbreviations is given in Table 5.2 and in detail in Bailey (2001). For the three energy levels used here no photosensitive traps were implemented and thus no corresponding terms are existing in Eqs. (5.1) – (5.4).

---

1	Geological dose irradiation of 1,000 Gy at 1 Gy s <sup>-1</sup> at 20 °C
2	Relaxation stage - 60 s at 20 °C
3	Geological time - heat from 20 °C to 350 °C at 5 °C s <sup>-1</sup>
4	Relaxation for geological time, 60 s at 20 °C
5	Burial dose - 20 Gy at 20 °C at 10 <sup>-11</sup> Gy s <sup>-1</sup>
6	Relaxation stage - 60 s at 20 °C
7	Preheat to 500 °C for 10 min
8	Radiofluorescence for 23 min at 20 °C at different dose rates

---

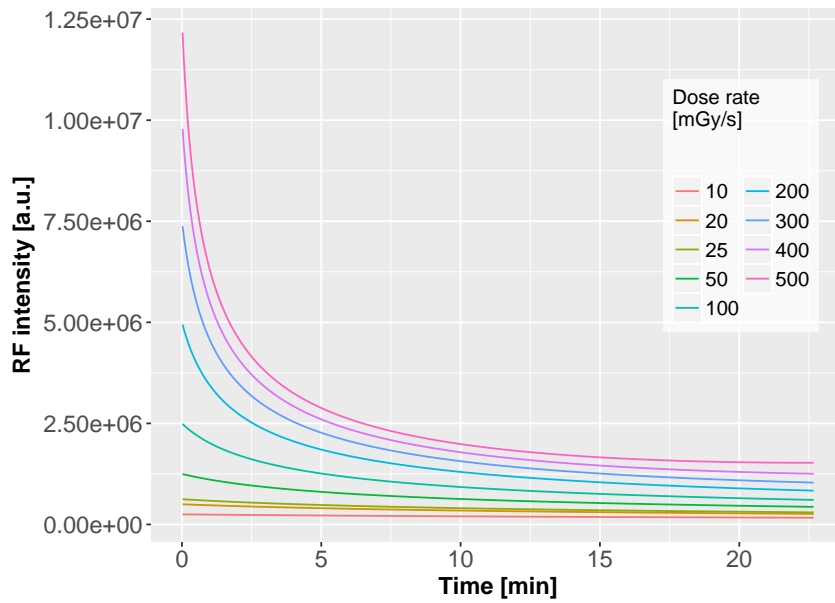
**Table 5.4:** Single steps for the simulations. Steps 7 and 8 represent the simulated measurements in the laboratory.

Table 5.4 lists the simulation steps for the experiments shown in Sec. 5.3. After each excitation stage in the simulations a relaxation period is introduced in which the temperature of the sample is kept constant at 20 °C for 60 s after the excitation has stopped ( $R = 0$ ) and the concentrations of  $n_c$  and  $n_v$  decay to negligible values. When the temperature of the next simulation step is not the same as in the current step, the numerical solution simulates a cooling or heating period with a constant rate of  $\beta = 5 \text{ K s}^{-1}$ . As pair production rate  $R$ , a value of  $6.3 \text{ E}+07 \text{ cm}^{-3} \text{ s}^{-1}$  was used.

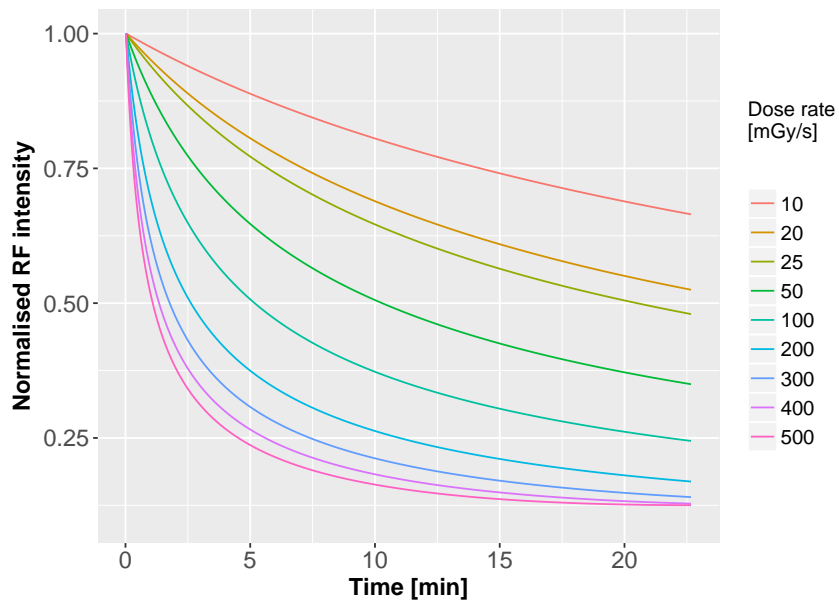
### 5.4.2 Matching experimental results and simulations

Figures 5.6 and 5.7 show the results from the numerical simulations. The parameters listed in Table 5.3 were used to reproduce the experimental results obtained for the FB quartz (see Figs. 5.1 (b), 5.2 (b), 5.4 (red line) and 5.5 (red line)). Note that the absolute values of Fig. 5.7 (a) are not meaningful, because the numerical simulation only qualitatively describes the behaviour of the C band. Matching the absolute values is possible if the parameters in Table 5.3 are downscaled. Nevertheless, when normalising to the first data point the order of the signals is the same in both, the results of the experiments and the simulations. The simulations suggest that the three-energy-level model is sufficient to describe the experimental findings. One indicator is the decrease of the C band down to  $\sim 12\%$  of the initial intensity, which is similar to the experiments, see Fig. 5.2 (b). Another indicator is the curve shape which is also similar to the experimental results.

We also performed an analysis of the initial signal intensity and the initial slope of the RF signal. The results are shown in Fig. 5.7 and closely resemble the experimental data from Sec. 5.3.2. In summary, the results from the numerical solutions are confirmed by the experimental data.

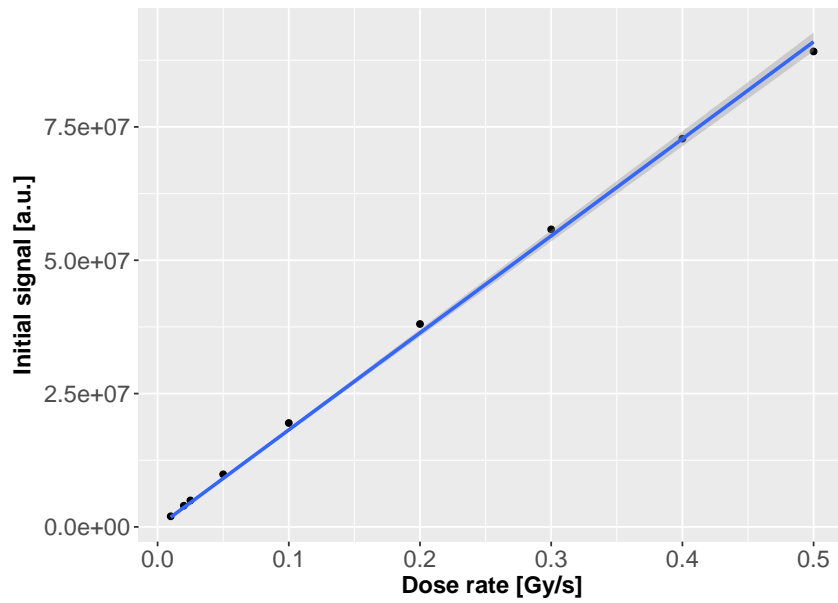


(a)

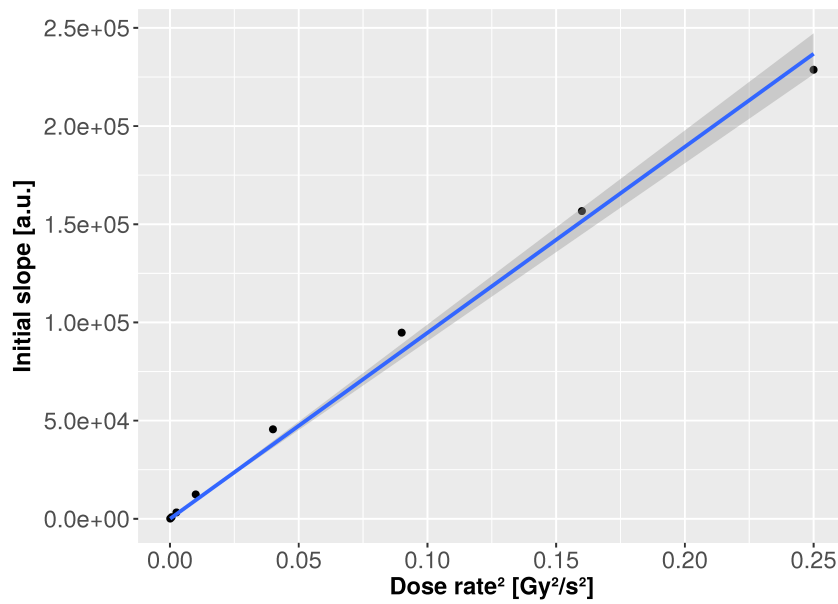


(b)

**Figure 5.6:** Simulation of the experimental results from Figs. 5.1 and 5.2. The simulation parameters were adjusted to fit the results of sample FB. Subfigure (a) shows the absolute values of the simulation and (b) is normalised to the first data point.



(a)



(b)

**Figure 5.7:** Simulation of the experimental results from Fig. 5.5. Subfigure (a) shows the change of the initial signal with dose rate and subfig. (b) the change of the initial slope with the squared dose rate. The grey shaded area is the 95% confidence level interval.

## 5.5 Discussion

### 5.5.1 Curve fitting

Friedrich et al. (2017c) derived an analytical expression for the UV-RF signal dynamics after high temperature annealing ( $\sim 500^\circ\text{C}$ ), see Eq. (4.20). This formula describes the luminescence intensity  $I$  as a function of time  $t$  with two parameters,  $A$  and  $C$ .

$$I(t) = A \cdot \left(1 - \exp\left(-\frac{t}{C}\right)\right) + \exp\left(-\frac{t}{C}\right) \quad (5.5)$$

Friedrich et al. (2017c) successfully used this function to fit their data acquired with one single dose rate. We also fitted the data presented in Sec. 5.3 to Eq. (5.5) and further analysed parameter  $C$ . From Friedrich et al. (2017c) it is known that the concentration of holes in the L-centre (in the framework of a completely empty R-centre) is a composite of two components: (1) The diffusion of holes into the L-centre (saturating exponential) and (2) the loss of holes due to recombination (exponential decay). The parameter  $C$  therefore can be handled as a 'lifetime' of the C band during irradiation. The term  $C^{-1}$  is the decay parameter and in this case the recombinations per second. Hence the expression  $C^{-1}$  should be depended on the dose rate (parameter  $R$  in the model) because the higher the dose rate the higher the probability of recombinations.

Figure 5.8 (a) shows the experimental data from sample BT586 (dots) as well as fits to Eq. (5.5) (lines). A good agreement between experiments and fits was found for sample BT586, as well as for sample FB (not shown here). From these fits the parameter  $C$  is extracted and the decay rate  $C^{-1}$  is plotted against the dose rate, see Fig. 5.8 (b). Except for low dose rates, a linear relation was found between the decay rate  $C^{-1}$  and the dose rate. The fits in Fig. 5.8 (a) and the linearity in subfig. (b) match well for sample BT586 but not for sample FB. One reason for this could be the less accurate fitting of the decaying UV-RF curves for sample FB compared to BT586.

Nevertheless, both samples indicate a linear relationship between the dose rate and the decay rate of the UV-RF signal. This is in concordance with the results obtained in Sec. 5.3.2. Note that in Sec. 5.3.2 the initial signal and the slope of the first two signal points were used to analyse the data. In contrast to that, we used the fit of the complete UV-RF signal here.

	<b>LEVELS</b>	$N$ [cm <sup>-3</sup> ]	$E$ [eV]	$s$ [s <sup>-1</sup> ]	$A$ [cm <sup>3</sup> s <sup>-1</sup> ]	$B$ [cm <sup>3</sup> s <sup>-1</sup> ]	$\sigma_0$ [s <sup>-1</sup> ]	$E_{th}$ [eV]
1	110 °C TL	1.5 E+07	0.97	5 E+12	1 E-08	-	0.75	0.1
2	230 °C TL	1 E+07	1.55	5 E+14	1 E-08	-	-	-
3	OSL <sub>F</sub>	1 E+09	1.7	5 E+13	1 E-09	-	6	0.1
4	OSL <sub>M</sub>	2.5 E+08	1.72	5 E+14	5 E-10	-	4.5	0.13
5	Deep	5 E+10	1.95	1 E+10	1 E-10	-	-	-
6	R <sub>1</sub> -centre	1 E+10	1.8	5 E+13	5 E-07	5 E-09	-	-
7	R <sub>2</sub> -centre	1 E+10	1.75	5 E+14	1 E-09	5 E-10	-	-
8	L-centre	1 E+11	5	1 E+13	1 E-09	5 E-10	-	-
9	K-centre	5 E+09	5	1 E+13	1 E-10	1 E-10	-	-

**Table 5.5:** Model parameters used for simulating the data shown in Fig. 5.9. The parameters for the deep electron trap, R<sub>1</sub>-centre and L-centre are identical to the ones presented in Table 5.3.

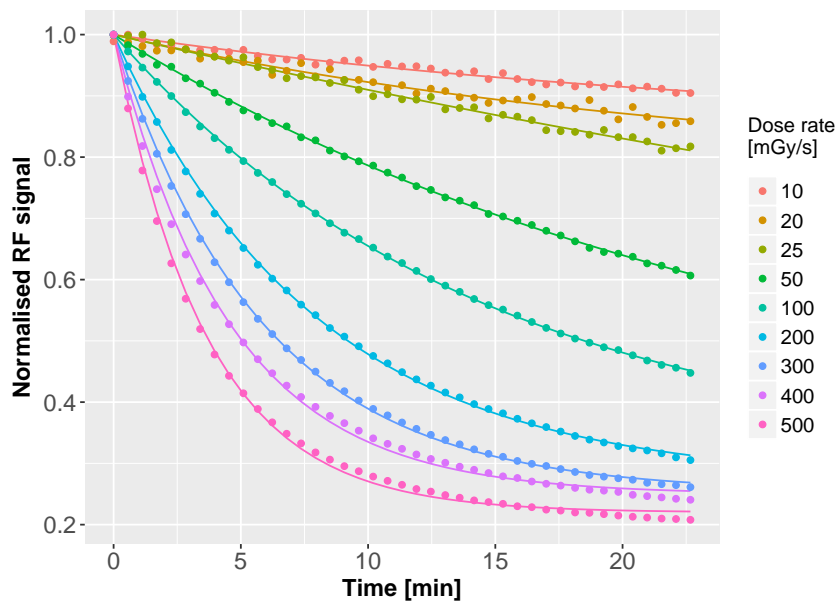
### 5.5.2 Expanded numerical model

The numerical model presented in Sec. 5.4.1 is a three-energy-level model with a limited explanatory power. We now present a comprehensive quartz model which describes more than the effects outlined in Sec. 5.3.1, e.g., the 110 °C TL peak or OSL behaviour. Therefore, we merge the parameters presented in Table 5.3 and the ones published in Friedrich et al. (2017a: Table 2). Table 5.5 shows the used parameters (nomenclature as in Bailey (2001)) for the comprehensive model. The pair production rate is the same as used for the three-energy-level model, 6.3 E+07 cm<sup>-3</sup> s<sup>-1</sup>.

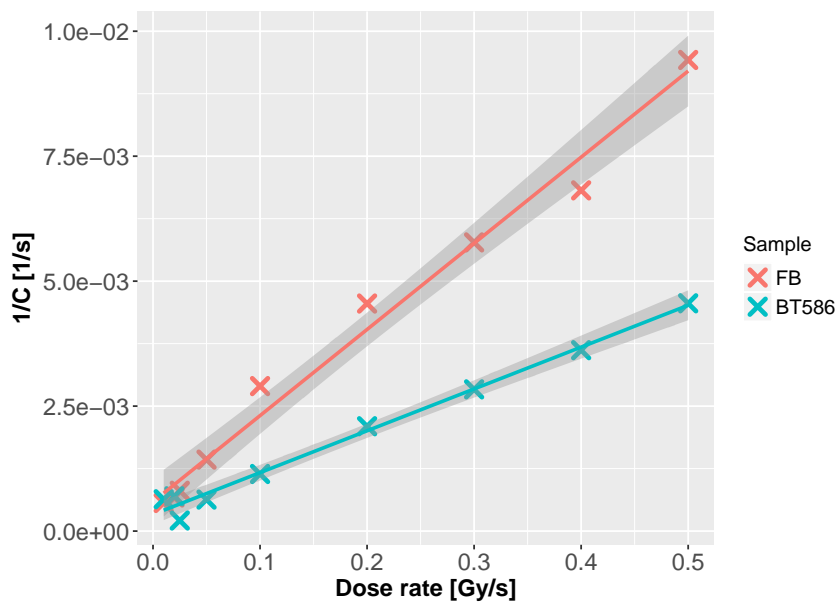
Figure 5.9 shows the same simulation as presented in Sec. 5.4.2 for the three-energy-level model. No obvious differences can be found in the simulation results between Figs. 5.6 and 5.9. This supports again the fact that the R<sub>1</sub> and L-centre play the most important role when simulating UV-RF signals (Friedrich et al. 2017a,c). Several tests with the comprehensive parameter set (TL peak shift with different heating rates, thermal activation characteristics, dose-recovery tests, OSL behaviour; see supplementary material in Sec. A.4) were performed and all investigated phenomena produced meaningful results. This parameter set is included in version 0.2.3 of the **R**-package 'RLumModel' (Friedrich et al. 2016, 2017b).

### 5.5.3 Potential for an application?

An application using the here presented findings could be the determination of absorbed doses. Figure 5.3 shows that sections of RF decay curves recorded with different dose rates overlap, hence proving - within the range of dose rates used in our experiments - the independency of RF signal characteristics on dose rate. This is a basic requirement for accurate dating. Similar to the IR-RF dating approach for K-feldspar developed by Erfurt & Krbetschek (2003) and Krbetschek et al. (2000) and recent applications of this method (e.g., Frouin et al. (2015, 2017)) the UV-RF signal of quartz could be exploited to determine an unknown dose when the quartz was heated before (e.g., ceramics, heated lithics, volcanic or volcanically heated rocks).



(a) Experimental data and corresponding fits for sample BT586



(b) Analysis of decay parameter  $C^{-1}$

**Figure 5.8:** Analysis of the UV-RF signals of sample BT586 using Eq. (5.5). Subfigure (a) shows the experimental data (dots) and fits to Eq. (5.5) (lines). Subfigure (b) shows the plot of the fitting parameter  $C^{-1}$  (decay rate) against the dose rate for both used samples. The grey shaded area is the 95 % confidence level interval.

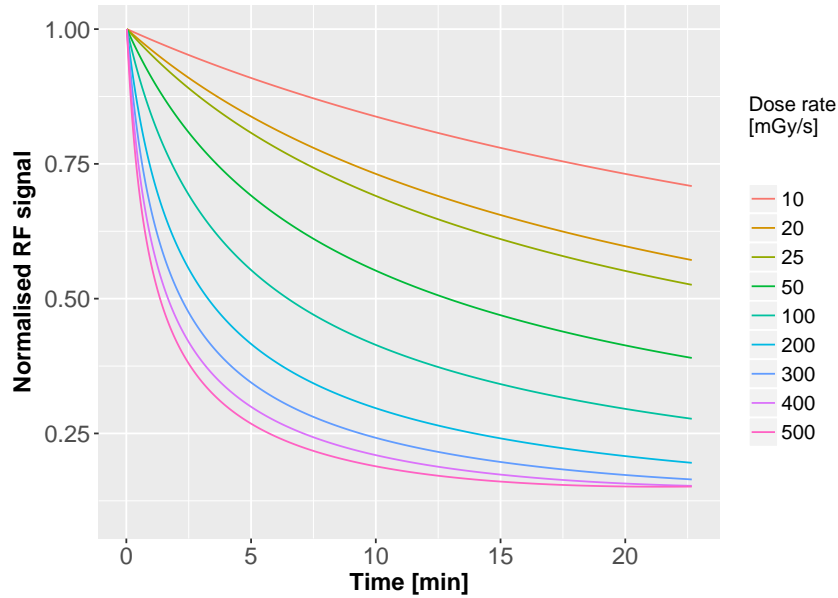


**Figure 5.9:** Simulation of the experimental results from Fig 5.5 with model parameters presented in Table 5.5. The results are similar to the ones obtained with the three-energy-level model given in Table 5.3 and Fig. 5.6.

The basic idea of this method is that the natural signal is horizontally translated onto the regenerated dose axis until it overlaps the regenerated signal. The length of the sliding along the x-axis is taken as the equivalent dose (Buylaert et al. 2012; Frouin et al. 2015).

To test this hypothesis we executed numerical simulations and first measurements. The numerical solutions indicate a good dose recovery when using the protocol presented in Table 5.6. In this example an unknown dose of 1 ks (60 Gy) was successfully recovered by our approach, see Fig. 5.10. To reset the signal a preheat to 500 °C was executed and subsequently the regenerated curve was measured. We now explain the measurement protocol in detail (see Table 5.6):

Step 1) is necessary to avoid sensitivity changes during UV-RF measurements/simulations (Friedrich et al. 2017a).

Step 2) gives a dose of 1 ks which has to be recovered by the protocol.

In step 3) a so called 'laboratory' signal ( $RF_{lab}$ ) is simulated. This signal will be shifted onto the x-axis towards the regenerated curve (see next step). This signal can be interpreted as additive dose on the laboratory dose  $RF_{lab}$ .

Step 4) describes a regenerative cycle: First a preheat to 500 °C to reset the UV-RF signal and subsequently the measurement of the  $RF_{reg}$  signal is executed. Note that the  $RF_{reg}$  signal also starts at 0 ks but is superimposed by the  $RF_{dose}$  signal.

Now the  $RF_{lab}$  signal is shifted along the x-axis until congruence with the regenerated curve  $RF_{reg}$  is reached (red arrow). The dashed vertical line in Fig. 5.10 at 1 ks indicates the calculated equivalent dose and the best match between  $RF_{lab}$  and  $RF_{reg}$ . This is the dose which was applied before in  $RF_{lab}$ .

STEP	DESCRIPTION	EXPLANATION
1	Preheat to 500 °C for 120 s and RF at RT for 2 ks (5 times)	Signal stabilisation
2	Preheat to 500 °C for 120 s and RF at RT for 1 ks ( $RF_{\text{dose}}$ )	Irradiation
3	RF for 1 ks ( $RF_{\text{lab}}$ )	'Natural' signal
4	Preheat to 500 °C for 120 s and RF at RT for 10 ks ( $RF_{\text{reg}}$ )	Regeneration

Table 5.6: Protocol for dose recovery with UV-RF.

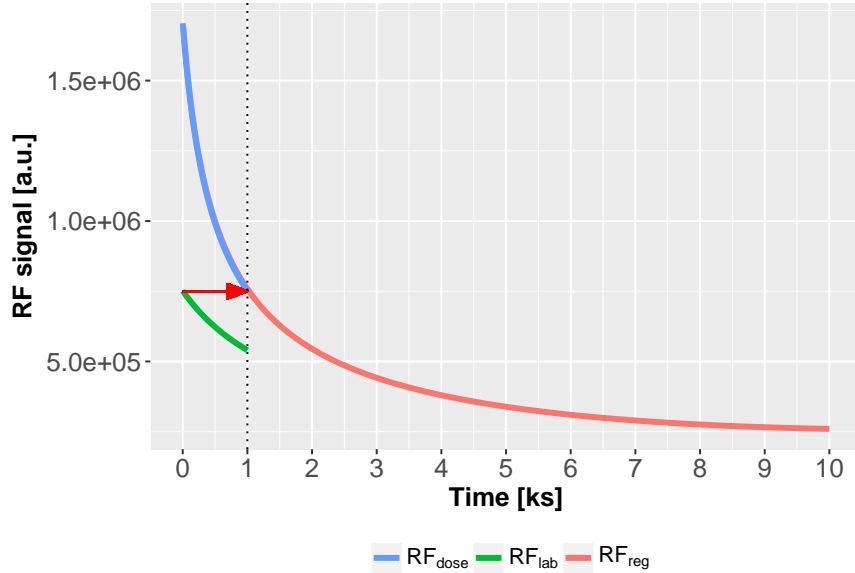


**Figure 5.10:** Simulations of the protocol given in Table 5.6. Curve  $RF_{\text{lab}}$  is shifted along the x-axis until congruence with the regenerated curve  $RF_{\text{reg}}$  is reached. In that way, the dose given in  $RF_{\text{dose}}$  can be determined. Note that  $RF_{\text{dose}}$  and  $RF_{\text{reg}}$  are on top of each other because after step 1 in Table 5.6 no sensitivity changes are expected.

For a detailed explanation of the shifting mechanism, see Frouin et al. (2017: Fig. 1) and for calculation details see the function `analyse_IRSAR.RF()` in the **R**-package 'Luminescence' (Kreutzer et al. 2012, 2017b). First measurements are promising regarding the recovery of  $RF_{\text{dose}}$  and further results will be presented in Sec. 8.2.

## 5.6 Conclusion

We investigated the dose rate dependence for UV-RF signals of natural quartz. Dose rates ranging from 10 – 500 mGy s<sup>-1</sup> were used to detect the UV-RF signal from 3.37 – 3.47 eV (C band). We observed:

1. Both natural quartz samples (two sedimentary quartz samples from different origin (geology, evolution, depositional environment), BT586 and FB) show a similar behaviour.
2. The higher the dose rate, the higher is the RF signal intensity in the C band.
3. The measured signal intensity of the C band grows linearly with the dose rate.
4. The measured initial slope of the C band grows linearly with squared dose rate.

5. All experiments support theoretically derived results.
6. Fitting experimental results to theoretically derived functions showed that the decay rate of the UV-RF curves is linearly dependent on the dose rate.
7. Our numerical simulations are capable of mimicking the experimental results. We showed that UV-RF signal production appears to be mainly an interplay between R- and L-centres. The three-energy-level model as well as the comprehensive model are able to reproduce the experimental results.
8. Numerical solutions and first measurements showed that it is possible to recover an absorbed dose of 60 Gy using quartz UV-RF.

## 5.7 Acknowledgements

JF is gratefully supported by the DFG (2015 – 2018, “*Modelling quartz luminescence signal dynamics relevant for dating and dosimetry*”, SCHM 3051/4-1). The work of SK is financed by a programme supported by the ANR - n° ANR-10-LABX-52. We also thank the anonymous reviewer for his/her helpful suggestions.

## References

- Aznar, M. C., 2005. Real-time in vivo luminescence dosimetry in radiotherapy and mammography using  $\text{Al}_2\text{O}_3:\text{C}$ . Risø-PhD-12 (EN). Risø National Laboratory, Roskilde (Denmark).
- Bailey, R. M., 2001. Towards a general kinetic model for optically and thermally stimulated luminescence of quartz. *Radiation Measurements* 33(1), 17–45.
- Buylaert, J.-P., Jain, M., Murray, A., Thomsen, K., Lapp, T., 2012. IR-RF dating of sand-sized K-feldspar extracts: A test of accuracy. *Radiation Measurements* 47(9), 759–765.
- Chen, R., McKeever, S. W., Durrani, S., 1981. Solution of the kinetic equations governing trap filling. Consequences concerning dose dependence and dose-rate effects. *Physical Review B* 24(9), 4931–4994.
- Chen, R., McKeever, S. W. S., 1997. *Theory of Thermoluminescence and Related Phenomena*. World Scientific, Singapore.
- Erfurt, G., Krbetschek, M., 2003. IRSAR—A single-aliquot regenerative-dose dating protocol applied to the infrared radiofluorescence (IR-RF) of coarse-grain K feldspar. *Ancient TL* 21(1), 35–42.
- Fasoli, M., Martini, M., 2016. The composite nature of the thermoluminescence UV emission of quartz. *Journal of Luminescence* 173, 120–126.
- Friedrich, J., Kreutzer, S., Schmidt, C., 2016. Solving ordinary differential equations to understand luminescence: 'RLumModel', an advanced research tool for simulating luminescence in quartz using R. *Quaternary Geochronology* 35, 88–100.
- Friedrich, J., Pagonis, V., Chen, R., Kreutzer, S., Schmidt, C., 2017a. Quartz radiofluorescence: a modelling approach. *Journal of Luminescence* 186, 318–325.
- Friedrich, J., Kreutzer, S., Schmidt, C., 2017b. *RLumModel: Solving Ordinary Differential Equations to Understand Luminescence*. (R package version 0.2.3). CRAN. <https://CRAN.R-project.org/package=RLumModel>,
- Friedrich, J., Fasoli, M., Kreutzer, S., Schmidt, C., 2017c. The basic principles of quartz radiofluorescence dynamics in the UV - analytical, numerical and experimental results. *Journal of Luminescence* 192, 940–948.
- Frouin, M., Huot, S., Mercier, N., Lahaye, C., Lamothe, M., 2015. The issue of laboratory bleaching in the infrared-radiofluorescence dating method. *Radiation Measurements* 81, 212–217.
- Frouin, M., Huot, S., Kreutzer, S., Lahaye, C., Lamothe, M., Philippe, A., Mercier, N., 2017. An improved radiofluorescence single-aliquot regenerative dose protocol for K-feldspars. *Quaternary Geochronology* 38, 13–24.
- Groom, P., Durrani, S., Khazal, K., McKeever, S., 1978. The Dose-Rate Dependence of Thermoluminescence Response and Sensitivity in Quartz in Séminaire de recherches consacrées à la datation par thermoluminescence, Oxford, 1978. *Pact. Revue du Groupe Européen*

- d'Etudes pour les Techniques Physiques, Chimiques et Mathématiques Appliquées à l'Archéologie Rixensart (2), 200–210.
- Kijek, N., Chruścińska, A., 2016. Natural and laboratory OSL growth curve - Verification of the basic assumption of luminescence dating. *Radiation Measurements* 90, 233–237.
- Kijek, N., Chruścińska, A., 2017. On the equivalence of natural and laboratory growth curves in luminescence dating - The effect of deep traps and luminescence centres. *Radiation Measurements* 106, 477–482.
- Krbetschek, M., Trautmann, T., Dietrich, A., Stolz, W., 2000. Radioluminescence dating of sediments: methodological aspects. *Radiation Measurements* 32(5), 493–498.
- Kreutzer, S., Schmidt, C., Fuchs, M. C., Dietze, M., Fischer, M., Fuchs, M., 2012. Introducing an R package for luminescence dating analysis. *Ancient TL* 30(1), 1–8.
- Kreutzer, S., Friedrich, J., Sanderson, D., Adamiec, G., Chruścińska, A., Fasoli, M., Martini, M., Polymeris, G. S., Burbidge, C. I., Schmidt, C., 2017a. Les sables de Fontainebleau: A Natural Quartz Reference Sample and its Characterisation. *Ancient TL* 35(2), 21–31.
- Kreutzer, S., Dietze, M., Burow, C., Fuchs, M. C., Schmidt, C., Fischer, M., Friedrich, J., 2017b. *Luminescence: Comprehensive Luminescence Dating Data Analysis*. (R package version 0.7.5). <http://CRAN.R-project.org/package=Luminescence>,
- Kvasnička, J., 1979. Dose rate and flux density of cosmic muons estimated by TLD method. *Health physics* 36(4), 521–524.
- Kvasnička, J., 1983. TL response dependence on the dose rate and its consequences. *The International journal of applied radiation and isotopes* 34(4), 713–715.
- Marquardt, D. W., 1963. An algorithm for least-squares estimation of nonlinear parameters. *Journal of the society for Industrial and Applied Mathematics* 11(2), 431–441.
- Martini, M., Fasoli, M., Villa, I., Guibert, P., 2012. Radioluminescence of synthetic and natural quartz. *Radiation Measurements* 47(9), 846–850.
- McKeever, S. W. S., Chen, R., Groom, P., Durrani, S., 1980. Dose-rate dependence of thermoluminescence response. *Nuclear Instruments and Methods* 175(1), 43–44.
- Pagonis, V., Lawless, J. L., Chen, R., Andersen, C., 2009. Radioluminescence in Al<sub>2</sub>O<sub>3</sub>:C - analytical and numerical simulation results. *Journal of Physics D: Applied Physics* 42(17), 175107.
- R Core Team, 2017. *R: A Language and Environment for Statistical Computing*. R Foundation for Statistical Computing. Vienna, Austria. <https://www.R-project.org/>,
- Schmidt, C., Kreutzer, S., DeWitt, R., Fuchs, M., 2015. Radiofluorescence of quartz: A review. *Quaternary Geochronology* 27, 66–77.
- Schmidt, C., Friedrich, J., Adamiec, G., Chruścińska, A., Fasoli, M., Kreutzer, S., Martini, M., Panzeri, L., Polymeris, G. S., Przegiętka, K., Valla, P. G., King, G. E., Sanderson, D. C., 2018. How reproducible are kinetic parameter constraints of quartz luminescence? An interlaboratory comparison for the 110 °C TL peak. *Radiation Measurements* 110, 14–24.



# 6 Radiofluorescence as a Detection Tool for Quartz Luminescence Quenching Processes

Johannes Friedrich<sup>1</sup>, Sebastian Kreutzer<sup>2</sup>, Christoph Schmidt<sup>1</sup>

<sup>1</sup> Chair of Geomorphology, University of Bayreuth, 95440 Bayreuth, Germany

<sup>2</sup> IRAMAT-CRP2A, UMR 5060 CNRS - Université Bordeaux Montaigne, Maison de l'Archéologie, Esplanade des Antilles, 33607 Pessac Cedex, France

*Radiation Measurements* 120, 33 – 40, 2018

<https://doi.org/10.1016/j.radmeas.2018.03.008>

## Abstract

Thermal quenching is a well-known phenomenon in quartz, which describes the decrease in luminescence efficiency (light output) with sample temperature. In the present work, the UV radiofluorescence (RF) signals of three different quartz samples during cooling from 500 °C to room temperature were monitored and analysed. Resulting thermal quenching parameters  $W$  (activation energy) and  $K$  (constant) agree with published values, except for one sample. Another quenching process in quartz is the reduction of luminescence sensitivity following irradiation (dose quenching), mainly known for TL and OSL of old samples with large palaeodoses. Here, the intensity of the 110 °C TL peak and the OSL signal were used to monitor the dose quenching effect. UV-OSL and UV-TL signals are analysed and found to be very similar. The UV-RF recorded during irradiation in between repeated cycles of TL and OSL measurements differs at high doses from a continuously recorded reference signal. Furthermore, numerical simulations are presented to decipher the charge transport processes in quartz. In summary, thermal quenching simulations are capable of mimicking experimental findings and confirm that UV-RF is a valuable tool to determine thermal quenching parameters. Dose quenching simulations differ from experimental results in the high dose range but help to understand the basic principle of dose quenching: charge competition of different centres.

## 6.1 Introduction

The mineral quartz has been studied intensively for thermoluminescence (TL) and optically stimulated luminescence (OSL) in dosimetry and dating applications. In this respect, it is of paramount importance to understand the response of luminescence signals to variables such as the absorbed dose or the temperature before and during measurement. For instance, the effect of thermal quenching in quartz is known latest since the observation by Wintle (1975) and has become subject to several publications during the last decades (e.g., McKeever & Chen (1997), Nanjundaswamy et al. (2002), Petrov & Bailiff (1997), Schilles et al. (2001), and Subedi et al. (2011)). It describes the decrease of luminescence production efficiency with rising sample temperature (Aitken 1985; Wintle 1975), and the Mott-Seitz mechanism can be used to illustrate this quenching process: An electron in the excited state of the luminescence centre can undergo either a radiative transition to the ground state or a thermally stimulated, but non-radiative transition, while the probability for the non-radiative pathway increases with temperature (Bøtter-Jensen et al. 2003; Pagonis et al. 2010). The luminescence efficiency  $I(T)$  as a function of sample temperature can be quantified in the form of Eq. (6.1) (Gurney & Mott 1939; Wintle 1975).

$$I(T) = \frac{1}{1 + K \cdot \exp\left(\frac{-W}{k_B \cdot T}\right)} \quad (6.1)$$

In Eq. (6.1),  $W$  [eV] is the activation energy for the quenching process,  $K$  is a constant,  $k_B$  is the Boltzmann constant [eV K<sup>-1</sup>] and  $T$  is the absolute temperature [K]. Quartz is well known to exhibit thermal quenching of the luminescence responsible for the so-called 325 °C UV-TL peak (Wintle 1975). Emission spectra indicate that the OSL emission, detected in the UV, is produced by the same type of recombination centre as the 325 °C UV-TL peak (Franklin et al. 1995; Spooner 1994). Wintle (1975) performed RF measurements to determine the thermal quenching activation energy  $W$  in quartz. Therefore, the sample was heated at a constant rate from room temperature (RT) to  $\sim 380$  °C during RF detection centred at 465 nm. As mentioned by Poolton et al. (2001), this can produce an overlay of TL and RF signals, which is not the same linear combination of TL and RF (if measured separately) at all temperatures, since the deep traps have longer filling times than the shallow traps. Own measurements confirmed this effect, hampering the determination of the quenching energy. To circumvent this limitation, Levy (1991), Petrov & Bailiff (1997), and Poolton et al. (2001) suggested measuring RF while cooling the sample, e.g., from 500 °C to RT. This approach has the advantage that TL traps (leading to peaks in the range 20 – 500 °C) do not contribute to the RF signal. Poolton et al. (2001) successfully determined quenching energies for quartz in that way and obtained results comparable with the values determined by Wintle (1975) and Schilles et al. (2001), the latter obtained by spectrally resolved TL. The phenomenon of thermal quenching was simulated by Pagonis et al. (2010) by solving ordinary differential equations (ODEs) describing the Mott-Seitz effect.

Another quenching effect in quartz is so-called 'dose quenching'. This term describes the reduction of luminescence efficiency following irradiation (Bailey 2001, 2004). Other names for this effect are 'radiation quenching' (Huntley et al. 1996) or 'R-fading' (Shlukov et al. 1993). Shlukov et al. (1993) reported a decrease of their dose-response curve (for the TL peak at 300 °C) at the initial stage (0 – 2,500 Gy) instead of a growth for a quartz sample in natural dose saturation. For larger doses (> 2,500 Gy), the dose-response curve increases again. They also mentioned that the higher the initially absorbed dose, the higher is the effect of dose quenching. Similar observations were made for OSL by Godfrey-Smith (1991) and Huntley et al. (1996) for old samples (natural radiation dose ~ 600 Gy).

The nature of the TL, OSL, and RF UV-emissions of quartz were widely investigated (e.g., Fasoli & Martini (2016), Itoh et al. (2002), and Martini et al. (2009, 2012)). The reader is referred to these publications for an overview of the role of different ions for luminescence production.

To better understand quenching processes in quartz, we performed UV-RF measurements on three different quartz samples. The RF signal of quartz provides the unique opportunity to directly observe changes in luminescence efficiency either simultaneous to temperature change (thermal quenching) or incrementally during repeated additive irradiation (dose quenching). We show that RF measurements are a means to determine thermal quenching parameters in an easy-to-apply procedure. We also demonstrate that dose quenching processes are tightly coupled to changes in UV-RF signals. Furthermore, dose quenching simulations were performed to present a possible mechanism for dose quenching in quartz; they suggest that charge competition between centres is the main reason for this effect, in agreement with the findings of Bailey (2001, 2004).

## 6.2 Materials and methods

### 6.2.1 Quartz samples

Three natural quartz samples were chosen for the measurements: (1) The quartz fraction was extracted from a colluvial sample originating from the Trebgast valley in the north-west of Bayreuth, Germany (lab code BT586; Kolb et al. (2016)). (2) A second sample (lab code BT1195) was extracted from the quartz ridge 'Pfahl' (Bavarian Forest, Germany), which is one of the largest hydrothermal quartz veins in Germany. This sample was prepared under daylight conditions and gently crushed with a steel mortar with frequent sieving in between. (3) The third sample was extracted from Oligocene coastal dune sand from the Fontainebleau Sand Formation (France; batch FB with used subsamples FB1A and FB2A) and annealed at 490 °C for 30 min, for details see Kreutzer et al. (2017b)). For thermal quenching measurements sample FB1A, and for dose quenching measurements FB2A was used. Subsequent chemical treatments for samples BT586 and BT1195 followed routine preparation procedures for quartz luminescence dating samples to enrich the quartz fraction (e.g., Preusser et al. (2008)). These are: HCl (30 %), H<sub>2</sub>O<sub>2</sub> (30 %), density separation

using sodium-polytungstate, HF (40% for 60 min). While sample BT586 was not exposed to daylight, BT1195 was bleached in a home-made solar simulator (2 h with an Osram Duluxstar lamp). For BT586 and BT1195 the used grain size fraction is 90 – 200  $\mu\text{m}$ , for FB 150 – 250  $\mu\text{m}$ .

UV-RF studies were already published for sample BT586 (Friedrich et al. 2017a,c, 2018) and for BT1195 (Friedrich et al. 2017a). A detailed kinetic analysis of the 110 °C TL peak for sample FB is presented by Schmidt et al. (2018).

## 6.2.2 Measurement conditions

All measurements were carried out on Freiberg Instruments lexsyg research readers (Richter et al. 2013) at the luminescence laboratories in Bayreuth (thermal quenching experiments) and Bordeaux (dose quenching experiments). For thermal quenching measurements six aliquots per sample and for radiation quenching, two aliquots per sample were measured.

### 6.2.2.1 Setup for thermal quenching measurements

The reader in Bayreuth is equipped with a  $^{90}\text{Sr}/^{90}\text{Y}$   $\beta$ -source ( $\sim 3.3 \text{ Gy min}^{-1}$ , calibrated for coarse grain quartz on stainless steel cups) and specifically designed for RF measurements (Richter et al. 2012). Luminescence was recorded through a Delta BP 365/50 EX interference filter (5 mm) in front of a Hamamatsu H7360-02 photomultiplier tube allowing detection of the UV-RF signal between 315 nm and 415 nm. The channel time for the RF measurements was set to 1 s throughout all measurements. Further details on the UV-RF experiments are given in the text below.

### 6.2.2.2 Setup for dose quenching measurements

For dose quenching measurements in Bordeaux the lexsyg research was equipped with a Hoya U340 glass filter (2.5 mm) in conjunction with a Semrock BrightLine HC 340/26 (5 mm) in front of a Hamamatsu H7360-02 photomultiplier tube. The OSL signal was stimulated using blue LEDs (458 nm, 26 mW  $\text{cm}^{-2}$ ) for 40 s and recorded at 125 °C. TL signals were recorded through a Schott-KG 3 glass filter (3 mm) in conjunction with a Delta BP 365/50 EX interference filter (5 mm). During TL measurements, the samples were heated from RT to 160 °C with 2 K  $\text{s}^{-1}$ . The channel time for all OSL or TL measurements was 0.1 s. For RF measurements in Bordeaux, the setup was similar to that used in Bayreuth (Sec. 6.2.1). If not reported otherwise, preheating the samples was performed with a heating rate of 5 K  $\text{s}^{-1}$ .

## 6.2.3 Data analysis

Data analysis was carried out using the **R**-package 'Luminescence' (Kreutzer et al. 2012, 2017a; R Core Team 2017). For simulating the UV-RF signals, the **R**-package 'RLumModel' (Friedrich et al. 2016, 2017b) was used.

## 6.3 Measurements

### 6.3.1 Thermal quenching

For determining the thermal quenching activation energy of the quartz samples in the UV, the sequence as follows was used:

1. Stabilisation: 5 cycles of preheating to 500 °C with 5 K s<sup>-1</sup> and irradiation with 120 Gy
2. Preheat to 500 °C for 120 s
3. Detection of RF during cooling from 500 °C to RT with 1 K s<sup>-1</sup>.

A stabilisation step was performed to omit a sensitivity change during the main measurement in step 3. It is known from previous UV-RF studies that RF sensitivity changes in the course of repeated cycles of preheating and irradiation (Friedrich et al. 2017a; Martini et al. 2012). In step 3, the same cooling ramp as mentioned in Poolton et al. (2001) of 1 K s<sup>-1</sup> was used. For all UV-RF curves, the signal normalised to the first data point was plotted against temperature after subtraction of steady emission, as suggested in Wintle (1975). The *lexsyg research* reader records the real temperature of the thermocouple. Thus it is possible to fit Eq. (6.1) to actual temperature data instead of using a nominal, extrapolated or recalculated temperature scale. Equation (6.1) was fitted to the measured data where  $K$  was chosen such that

$$K = \exp\left(\frac{W}{k_B \cdot T_{1/2}}\right), \quad (6.2)$$

where  $T_{1/2}$  is the temperature at which the UV-RF curve reaches half of its initial intensity (Wintle 1975). Figure 6.1 shows the result of the UV-RF measurements and the corresponding fit using Eq. (6.1) for sample BT1195. Note that the UV-RF curve was detected during cooling, but Fig. 6.1 shows the x-axis in increasing order;  $T_{1/2}$  is  $\sim 150$  °C. The observation of Fig. 6.1 is: The higher the measurement temperature, the lower is the UV-RF intensity, following Eq. (6.1). Table 6.1 summarises the results of all three samples. The quenching energies  $W$  and constants  $K$  for samples BT1195 and FB1A are in the range 0.63 – 0.66 eV and 3 – 9 E+07, respectively. These results are in agreement with published values (Poolton et al. 2001; Schilles et al. 2001; Wintle 1975); for a comprehensive comparison see Table 1 in Subedi et al. (2011)). Sample BT586 shows smaller values than expected:  $W = 0.51 \pm 0.02$  eV and  $K = 2 \pm 2$  E+06. Poolton et al. (2001) and Schilles et al. (2001) used annealed quartz for their experiments. For comparison, we annealed sample BT586 for 10 min at 500 °C in the muffle oven and the results for  $W$  and  $K$  slightly changed:  $W = 0.55 \pm 0.01$  eV,  $K = 5.3 \pm$  E+06. In addition to that, we also evaluated thermal quenching parameters for sample BT586 without any stabilisation of the UV-RF signal (step 1 in our sequence) and obtain significant lower values:  $W = 0.44 \pm 0.03$  eV,  $K = 3 \pm 2$  E+05. Further discussion of the results is given in Sec. 6.5.1.

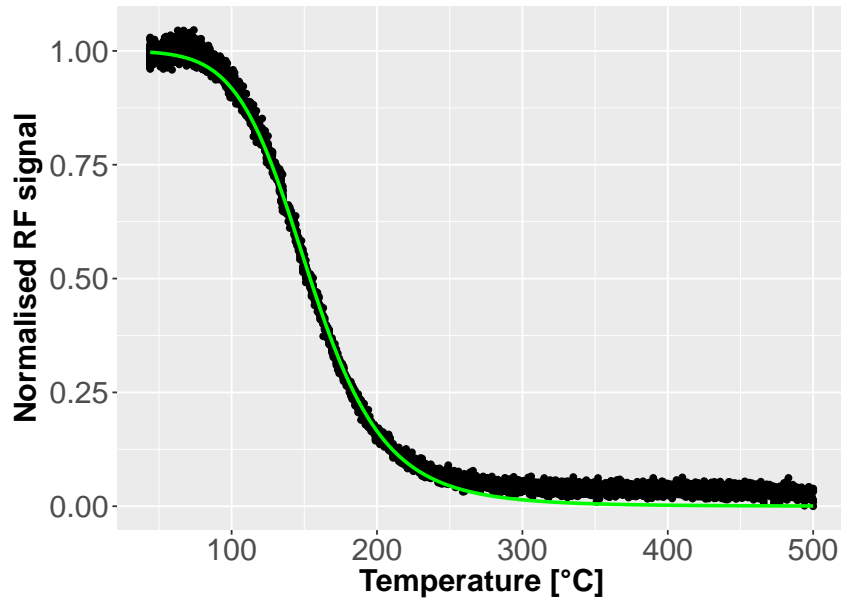


**Figure 6.1:** Normalised UV-RF curve during cooling from 500 °C to RT with 1 K s<sup>-1</sup> for sample BT1195. Also included is the fit to Eq. (6.1) (green).

	<b>BT586</b>	<b>BT1195</b>	<b>FB1A</b>
$W$ [eV]	$0.51 \pm 0.02$	$0.63 \pm 0.03$	$0.66 \pm 0.02$
$K$	$2 \pm 2 \text{ E}+06$	$3 \pm 2 \text{ E}+07$	$9 \pm 4 \text{ E}+07$
$T_{1/2}$ [°C]	$144 \pm 1$	$155 \pm 1$	$149 \pm 1$

**Table 6.1:** Summary of arithmetic average of  $W$ ,  $K$  and  $T_{1/2}$  derived from fitting of Eq. (6.1) and (6.2) to the experimentally obtained RF curves. The given uncertainty range ( $1 \sigma$  standard deviation) reflects the variety of different aliquots.

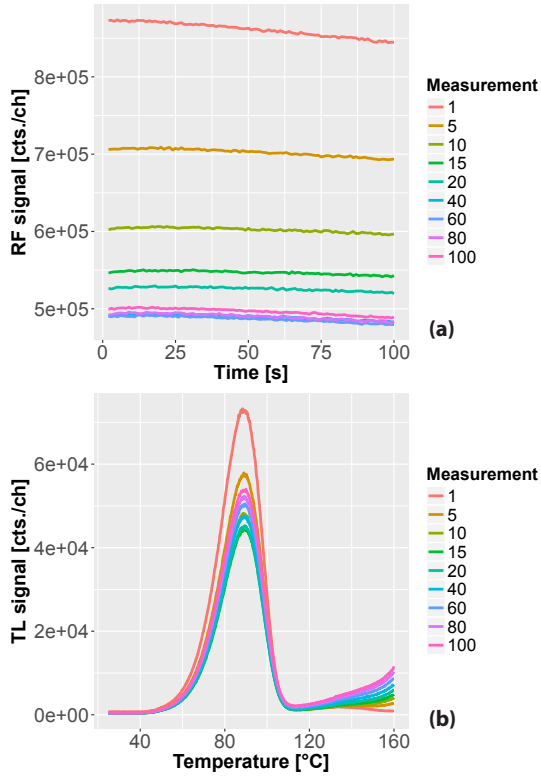


**Figure 6.2:** (a) UV-RF curves (b) UV-TL curves from quartz sample FB2A. For graphical reasons only nine out of 100 measured curves are shown. The sequence with which these results were obtained, is described in detail in Sec. 6.3.2

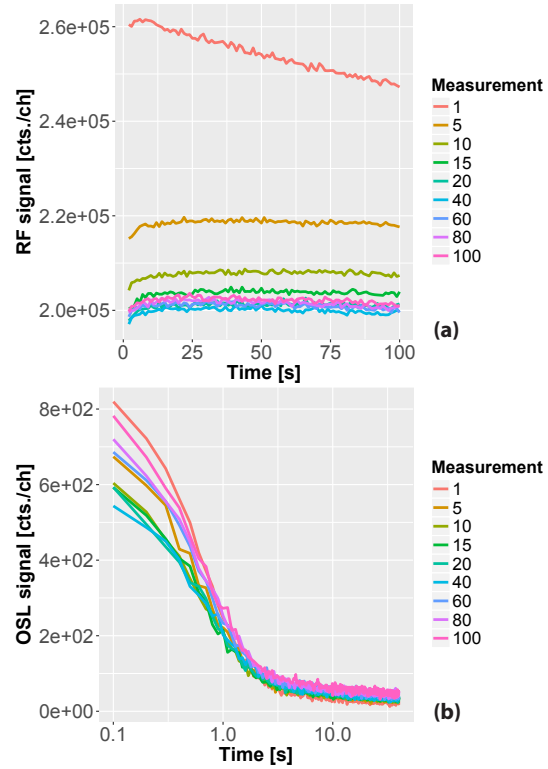


**Figure 6.3:** (a) UV-RF curves (b) OSL curves from quartz sample BT1195. For graphical reasons only nine out of 100 measured curves are shown.

### 6.3.2 Dose quenching

In this study, two different methods were used to observe dose quenching in quartz: (1) Indirectly via the 110 °C UV-TL peak and the initial OSL signal and (2) directly by measuring the UV-RF signal. Hence, the following sequence was applied:

1. Preheat to 500 °C with 5 K s<sup>-1</sup> for 120 s
2. Measure RF for 100 s ( $\sim 6$  Gy) at RT
3. Measure TL to 160 °C with 2 K s<sup>-1</sup> or OSL at 125 °C for 40 s
4. Repeat steps 2. and 3. 100 times

Step 1 was necessary for two reasons: (1) For enhancing the sensitivity of the TL and OSL signal and (2) for measuring a decreasing RF curve (Friedrich et al. 2017a,c). Step 2 serves as a direct indicator of dose quenching, whereas step 3 represents the indirect indicators, i.e. TL and OSL measurements. Steps 2 and 3 were repeated 100 times until an accumulated dose of  $\sim 600$  Gy was absorbed. Furthermore, a single RF curve was recorded for 10,000 s (also  $\sim 600$  Gy) for comparison with the discontinuous RF measurement when recording TL or OSL in between.

Figure 6.2 shows the results when using the 110 °C TL peak as an indicator of dose

quenching for sample FB2A, while Fig. 6.3 analogously displays OSL curves for sample BT1195. For both approaches we observed the following similarities:

- A decreasing UV-RF signal (as expected after sequence step 1; Friedrich et al. (2017a,c) and Martini et al. (2012); see subfigures (a)).
- The behaviour of the indicator signals (TL in Fig. 6.2 (b), OSL in Fig. 6.3 (b)) is similar: From the first to the twelfth measurement, a decrease in signal intensity was observed. For subsequent measurements, the differences become small and can hardly be discriminated in the plot.

Figures 6.4 and 6.5 provide further insight into the signal characteristics. The behaviour for all 100 UV-RF and UV-TL signals during the sequence is shown in Fig. 6.4 for samples (a) BT1195 and (b) FB2A. The signal 'RF<sub>initial</sub>' is always the second channel of each UV-RF measurement since the first channel is affected by the opening of the shutter in front of the  $\beta$ -source. 'RF<sub>ref</sub>' is the reference UV-RF measurement without TL or OSL measurements in between. 'TL<sub>max</sub>' is the integrated signal including  $\pm 5$  channels from the maximum TL signal and 'OSL<sub>max</sub>' is the first second of the OSL signal. To compare RF, TL, and OSL signal dynamics across the 100 measurement cycles, all results were normalised to the first measurement. All three quartz samples (BT586 not shown here) reveal similar relative signal changes.

- The RF<sub>initial</sub> signal decreases until  $\sim 150$  Gy and shows a small but steady increase until the end of the measurement.
- The RF<sub>ref</sub> signal decreases during the entire measurement. Note that RF<sub>ref</sub> and RF<sub>initial</sub> are not superimposable and the decrease of the reference signal is steeper than that for the RF<sub>initial</sub> signal.
- TL<sub>max</sub> and OSL<sub>max</sub> decrease until a cumulative dose of  $\sim 100$  Gy and  $\sim 100 - 200$  Gy, respectively, and then show an increase during further measurement cycles, but do not retain the initial signal intensity.

The reason for the decreasing and afterwards increasing TL and OSL signals will be explained, supported by numerical simulations, in Sec. 6.4.2.

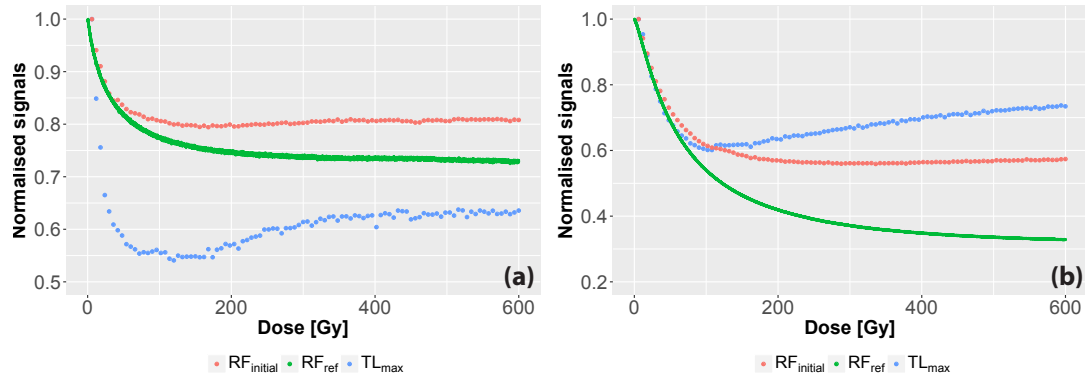


**Figure 6.4:** Combined signals for quartz sample (a) BT1195 and (b) FB2A for dose quenching measurements with the 110 °C TL peak as quenching indicator. In each graph, the second RF channel, the integrated ( $\pm 5$  channels from maximum) TL signal and the RF reference signal are plotted against dose.

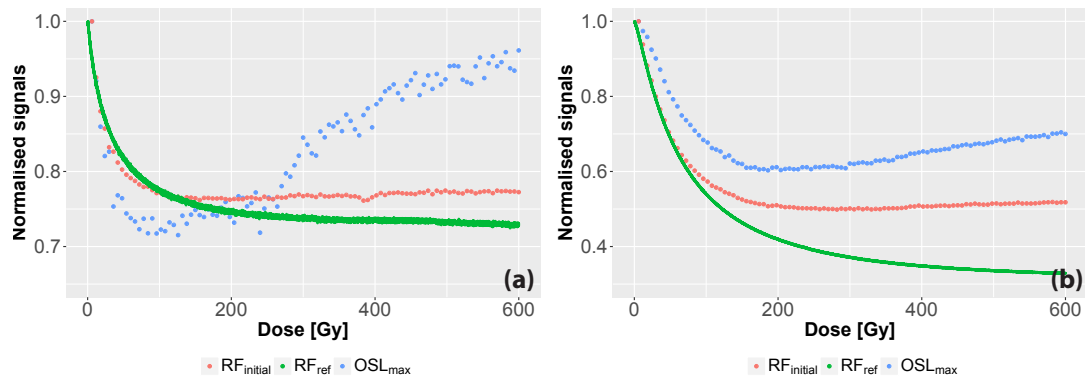


**Figure 6.5:** Combined signals for quartz (a) BT1195 and (b) FB2A for dose quenching measurements with the initial OSL signal as quenching indicator. In each graph, the second RF channel, the integrated (first second) OSL signal and the RF reference signal are plotted against dose.

## 6.4 Simulations

### 6.4.1 Defining the model

The model used for numerical simulations is the same as presented in detail in (Friedrich et al. 2017a) and is implemented in the **R**-package 'RLumModel' version 0.2.3 (Friedrich et al. 2016, 2017b). Since version 0.2.0, it is possible to simulate the process of sample irradiation during heating or cooling. The input parameters for  $W$  and  $K$  in the simulations were set to 0.64 eV and 2.8 E+07, respectively. For both thermal and dose quenching, the same model parameters were used and the sequences for the simulations are identical to those described in the experimental part in Sec. 6.3.1 and 6.3.2. Note that in Friedrich et al. (2017a) a dose rate for RF simulations lower by a factor of 10 was assumed in every RF step. This was equalised by multiplying the time by a factor of 10. In that way, the total absorbed dose was the same as in the experiments.

### 6.4.2 Matching experimental results and simulations

#### 6.4.2.1 Thermal quenching

Figure 6.6 shows the result of the simulation for RF during cooling from 400 °C to RT with 1 K s<sup>-1</sup>. The qualitative behaviour of the simulated UV-RF curve is very similar to the experimental data presented in Fig. 6.1. When fitting the data in the same way as described in Sec. 6.3.1, we obtain values of  $W = 0.67$  eV and  $K = 5.82$  E+07, which are very close to the input parameters of the model,  $W = 0.64$  eV and  $K = 2.80$  E+07. This agreement indicates that the UV-RF recorded during sample cooling seems to be an appropriate means for accurately determining the thermal quenching parameters in quartz.

#### 6.4.2.2 Dose quenching

Numerical solutions allow an insight into the change of charge concentration at distinct energy levels over time. Figure 6.7 (a) shows the numerical results for UV-RF simulations, and comparison with experimental data shown in Figs. 6.2 (a) and 6.3 (a) demonstrates similar change in signal intensity over measurement cycles, e.g., a decreasing signal for the first RF measurement. The qualitative behaviour of the simulated TL signal in Fig. 6.7 (b) is also comparable to the measured TL signals in Fig. 6.2 (b). A striking difference, however, is the behaviour of the signals  $RF_{\text{initial}}$  and  $RF_{\text{ref}}$ . In the simulations, almost no discrepancy between these signals is observed, while our experiments (see Figs. 6.4 and 6.5) clearly show deviations for cumulative doses exceeding  $\sim 50$  Gy. Figures 6.8 (a) and (b) reveal good agreement between numerical simulations and experimental data for the OSL experiments. In this case, in contrast to Fig. 6.7 (c), the signal for  $RF_{\text{ref}}$  and  $RF_{\text{initial}}$  are diverging for higher doses. However, in the experiments described in Sec. 6.3.2, the  $RF_{\text{ref}}$  signal is below the  $RF_{\text{initial}}$  signal. This is not the case for the numerical simulations and needs further investigations to see whether this is just a particular case for the used parameter set or

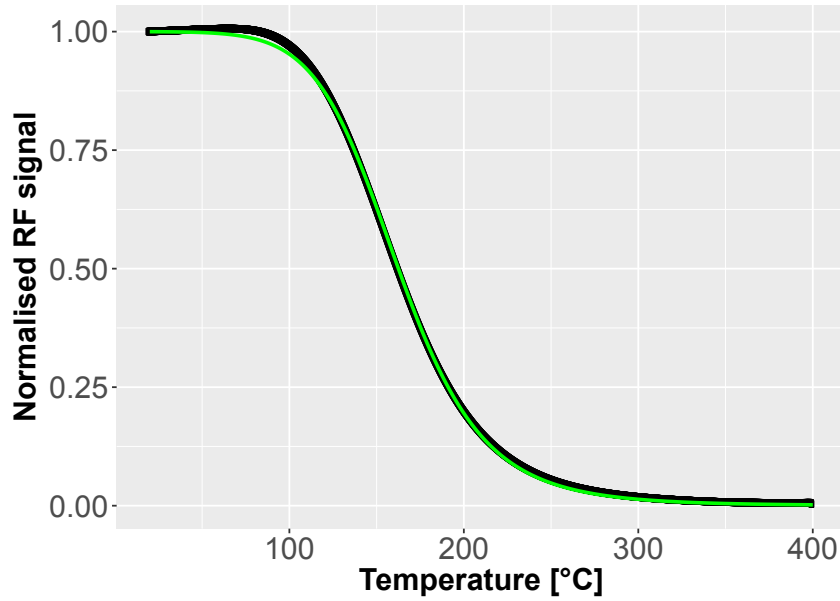


**Figure 6.6:** Simulated UV-RF curve during cooling from 400 °C to RT with  $1 \text{ K s}^{-1}$ . The used parameter set is the same as that presented in (Friedrich et al. 2017a). Used parameters for  $W$  and  $K$  were 0.64 eV and  $2.8 \text{ E}+07$ , respectively. The fit returns values in the same range as the inserted parameter values ( $W = 0.67 \text{ eV}$ ,  $K = 5.82 \text{ E}+07$ ).

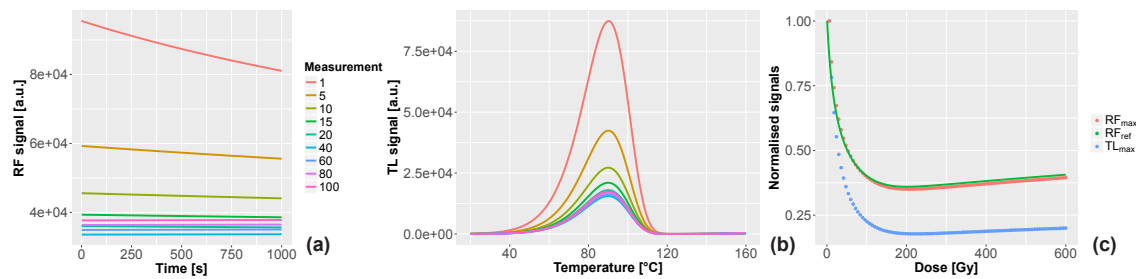


**Figure 6.7:** Simulated dose quenching experiment with the 110 °C TL peak as indicator. Subfigure (a) shows the simulated RF curves, (b) the simulated 110 °C TL peak and (c) the combined signals including a reference RF signal, as described in Sec. 6.3.2.

a general behaviour of the selected model. Nevertheless, as a first attempt and without modifying any parameters from the parameter set of Friedrich et al. (2017a) an acceptable agreement between experiments and simulations is obtained. Further investigations to determine the differences between simulations and experiments are required, but beyond the scope of this study.

To explain the similar behaviour of TL and OSL signals during the experimental sequence, we investigated the charge concentrations in related traps and centres by looking specifically at three different energy levels in the simulations: The reservoir centre R, the luminescence centre L and the 110 °C TL trap or the OSL fast component trap. For more details of the energy levels and their comprehensive description, see Bailey (2001). Figure 6.9 shows the normalised (to the highest point of each signal) charge concentrations in these traps and

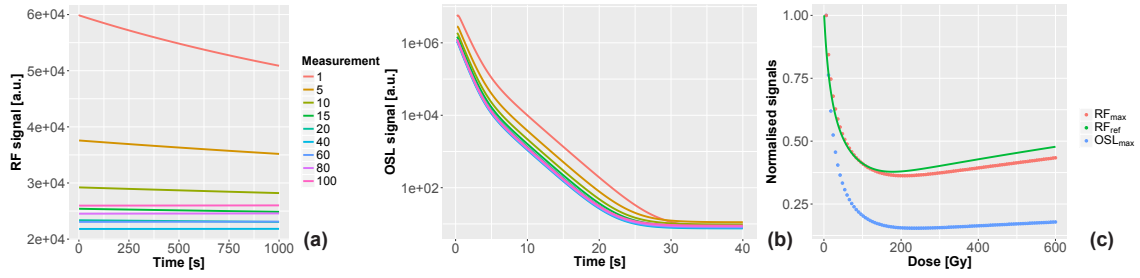


**Figure 6.8:** Simulated dose quenching experiment with OSL as indicator. Subfigure (a) shows the simulated RF curves, (b) the simulated OSL decay curve and (c) the combined signals including a reference RF signal, as described in Sec. 6.3.2.

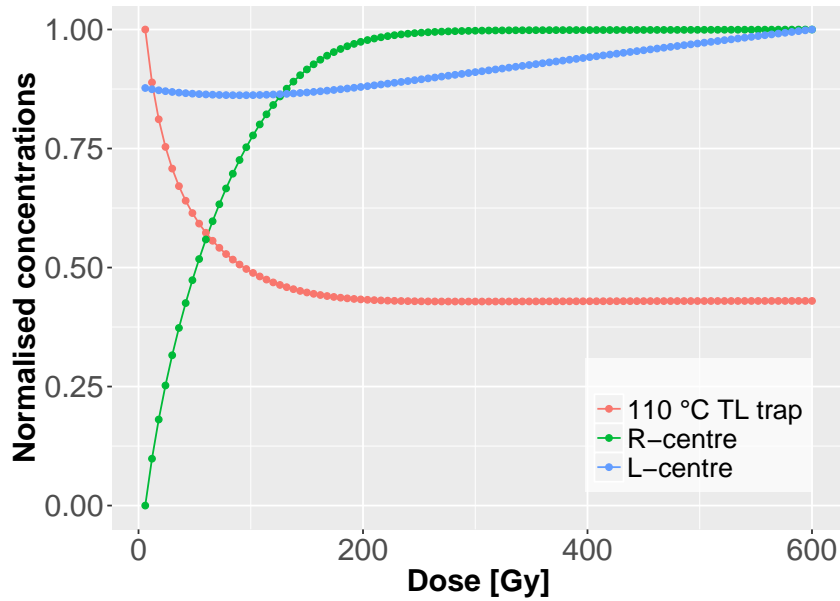


**Figure 6.9:** Charge concentrations in different energy levels normalised to the highest value of each concentration. Beyond  $\sim 150$  Gy, the hole concentration in the L-centre begins to increase what is the reason for the increasing luminescence signals.

centres for the sequence making use of the  $110^\circ\text{C}$  TL peak as quenching indicator. The case for OSL was not shown here since we observed only minimal differences between OSL simulations and the data displayed in Fig. 6.9. Thus, the following description should be valid for both the OSL fast component trap and the  $110^\circ\text{C}$  TL trap.

At the beginning of the simulation, the R-centre is empty due to the preheat to  $500^\circ\text{C}$ , while the L-centre hosts the highest concentration of holes. Note that a normalised concentration of 1 does not imply that the trap/centre is completely filled, it indicates only the highest filling level during the simulation. From cycle to cycle, the concentration of electrons in the OSL fast component trap or the  $110^\circ\text{C}$  TL trap decreases because the competition between R-centre and OSL fast component trap or  $110^\circ\text{C}$  TL trap for capturing electrons during irradiation increases. At the same time, the concentration of holes in the R-centre increases as well, while the concentration of holes in the L-centre remains nearly constant.

Holes produced in the valence band prefer to occupy the R-centre since initially it is empty and in the model the R-centre has a higher probability to capture a hole than the L-centre (Friedrich et al. 2017a). This competition holds until  $\sim 150$  Gy. Beyond  $\sim 150$  Gy, the concentration of holes in the R-centre and of electrons in the TL trap remains largely constant. From there on, holes created during irradiation move preferentially into the L-centre as the R-centre is not able to absorb more holes. This inflexion point marks the dose where the TL and OSL signals in Figs. 6.4 and 6.5 increase again, driven by a higher number of holes captured in the L-centre. To conclude, the TL and OSL signal behaviour can be described by a two-step process:

1. Decrease of the signal intensities due to low charge concentration in the associated electron trap,
2. increase of the signal intensities after the R-centre is saturated with holes and, consequently, the concentration of holes in the L-centre increases gradually.

## 6.5 Discussion

### 6.5.1 Thermal quenching

Our results for thermal quenching parameters  $W$  and  $K$ , except for sample BT586, are in agreement with other published values for quartz, e.g., Poolton et al. (2001), Schilles et al. (2001), Subedi et al. (2011), and Wintle (1975). Sample BT586 is known to exhibit a very slowly decaying UV-RF signal (see Fig. 1 in Friedrich et al. (2017a)) in contrast to BT1195 (Fig. 2 in Friedrich et al. (2017a)). This particular characteristic could be an indicator why this quartz behaves differently from all others. Many publications concerning thermal quenching in quartz used annealed samples for their research (Poolton et al. 2001; Schilles et al. 2001). Subedi et al. (2011) investigated the impact of preheating quartz before determining thermal quenching parameters and reported no change in thermal quenching parameters. Annealing quartz sample BT586 to  $500^\circ\text{C}$  for 10 min in the muffle oven shows a slightly different result: This procedure increases the thermal quenching parameters  $W$  and  $K$  by  $\sim 8\%$  and decreases the inter-aliquot scatter (smaller errors for  $W$  and  $K$ ). We further investigated the effect of stabilising the UV-RF signal before determining thermal quenching parameters. The results for the thermal quenching parameters are significantly smaller compared to those measured after cycles of preheating and irradiating. This observation supports the idea that stabilising the signal is important to determine thermal quenching parameters properly. Whereas Petrov & Bailiff (1997) and Poolton et al. (2001) determined thermal quenching parameters by cooling the sample, Wintle (1975) heated her sample during RF measurement. One reason why the approach by Wintle (1975) was working could be the low dose rate of the used  $\beta$ -source ( $0.1\text{ Gy min}^{-1}$ ). The RF measurements done by Poolton et al. (2001) and the present study were performed with a dose rate of  $4.5\text{ Gy min}^{-1}$  and  $3.3\text{ Gy min}^{-1}$ , respectively. However, further investigations are required

to better understand this behaviour. Nevertheless, the approach using UV-RF to determine thermal quenching parameters is very promising and easy to perform. The fitting is more robust due to a larger number of data points compared to measuring thermal quenching by use of TL or OSL curves.

### 6.5.2 Dose quenching

The phenomenon of dose quenching has not been given a lot of attention in the last decades, although known and corrected for in pre-dose dating (Aitken 1985). In OSL, the effect was observed when measuring old samples which are probably in-field saturation (Huntley et al. 1996). For our experiments, we decided to include a preheat to 500 °C for 2 min before measurements because we assume that this has nearly the same effect as a long storage of the mineral, concerning the centres: The R-centres are thermally unstable over long time scales and hence are occupied by holes only to a small fraction (Bailey 2001). The same effect can be mimicked by a preheat. With this assumption, the dose-response curves for TL and OSL were analysed and compared to known phenomena in literature. The dose-response curves for saturated quartz samples in Shlukov et al. (1993) and Huntley et al. (1996) for TL and OSL, respectively, showed a decrease in luminescence intensity after a laboratory dose was given. Shlukov et al. (1993) also reported increasing dose response after  $\sim 2.5$  kGy and named this effect 'dose pit' (Fig. 4 in their publication). This effect was not reported explicitly for OSL by Huntley et al. (1996). However, studying Fig. 8 in Huntley et al. (1996) in detail, an increasing signal after  $\sim 400$  Gy is observable. A common observation by Shlukov et al. (1993) and Huntley et al. (1996) was that the greater the initial charge (or: the older the sample), the greater the effect of dose quenching. This is in accordance with the explanation given in Sec. 6.4.2.2: The older the sample the higher the probability to get less populated R-centres and the greater the effect of observing a more intense luminescence signal in the first measurement than for subsequent measurements because there is no competition between R- and L-centres in the first measurement.

### 6.5.3 Limitation of our study

To support our interpretations, we performed simulations based on energy-band models. Such models are of phenomenological nature and usually do not consider the nature of lattice defects (traps and centres), which are bound to their geological origin and history (cf. Preusser et al. (2009) for an overview). In the future, it might be worthwhile to link our observations to luminescence characteristics found for specific lattice defects.

## 6.6 Conclusions

This study investigated the use of UV-RF signals as an indicator of thermal and dose quenching processes in natural quartz. Three such samples with different pre-treatments were analysed to draw general conclusions for quenching processes in quartz luminescence. Furthermore, we presented numerical studies to explain the experimentally obtained results.

In the case of thermal quenching, we presented measurements which combined cooling a sample from 500 °C to RT with recording the UV-RF signal, from which the quenching parameters  $W$  and  $K$  can be calculated directly. Our results for two out of three quartz samples (FB1A and BT1195) with  $W$  and  $K$  ranging from 0.63 eV to 0.66 eV and from 3 to 9 E+07, respectively, and are in accordance with published values (for the UV region), except for sample BT586. Here we obtained  $W = 0.51 \pm 0.02$  eV and  $K = 2 \pm 2$  E+06. Further investigations concerning the effect of pre-treatment before determining thermal quenching parameters yielded that cycles of annealing and irradiation are important to obtain robust values for  $W$  and  $K$ . Numerical simulations lead to a good match between modelled data and experiments. The main advantages of the here presented UV-RF method are:

- Direct observation of centre-driven processes leading to thermal quenching, without interference from electron traps,
- rapid measurements with an easy-to-apply sequence,
- robust fitting due to a large amount of recorded data points.

We observed dose quenching in two different ways: We used the 110 °C TL peak and the initial OSL signal as indirect indicator for quenching with increasing dose and compared these signals with measured RF signals (direct indicator) for a sequence of 100 consecutive cycles, each consisting of RF (6 Gy) and subsequent OSL/TL measurement. Both signals (TL and OSL) show a similar behaviour for all quartz samples: after a strong reduction of the signals until  $\sim 150$  Gy, the signals increased until the end of the measurements (600 Gy). This supports the idea that the 110 °C TL signal and OSL share the same recombination centres (Bailey et al. 1997; Chen et al. 2000; Franklin et al. 1995; Martini et al. 2009). The increasing TL/OSL signals beyond  $\sim 150$  Gy can be explained by saturated R-centres and hence an increasing hole population in the L-centre and consequently a higher signal intensity.

Unexpected was the behaviour of the signal  $RF_{\text{ref}}$  measured without any TL or OSL measurements in between the cycles, in contrast to the  $RF_{\text{initial}}$  signal. Both signals behave differently for high doses in the sense that the  $RF_{\text{initial}}$  signal shows a higher intensity than the continuously measured  $RF_{\text{ref}}$  signal. This effect was not observed in the numerical simulations. An explanation may be a kind of recuperation effect between two RF measurements (pers. communication with M. Fasoli) but this effect needs further investigations.

## 6.7 Acknowledgements

We are thankful to two anonymous reviewers for constructive comments. Initial UV-RF measurements and preparation of the samples BT586 and BT1195 were carried out within the framework of the project “*Radiofluorescence of quartz: Challenges towards a dating application*” (DFG, 2013 – 2015, SCHM 3051/2-1 und FU 417/16-1 and DAAD-PPP USA, 2013 – 2014, Prof. Dr. Markus Fuchs, id: 56022859). The work of SK was financed by a programme supported by the ANR - n° ANR-10-LABX-52, that of JF by the DFG (DFG, 2015 – 2018, “*Modelling quartz luminescence signal dynamics relevant for dating and dosimetry*”, SCHM 3051/4-1). JF thanks the committee of the International LED meeting 2017 in Cape Town, South Africa, for the student award.

## References

- Aitken, M. J., 1985. Thermoluminescence dating. Academic press.
- Bailey, R. M., Smith, B. W., Rhodes, E. J., 1997. Partial bleaching and the decay form characteristics of quartz OSL. *Radiation Measurements* 27(2), 123–136.
- Bailey, R. M., 2001. Towards a general kinetic model for optically and thermally stimulated luminescence of quartz. *Radiation Measurements* 33(1), 17–45.
- Bailey, R. M., 2004. Paper I - Simulation of dose absorption in quartz over geological timescales and its implications for the precision and accuracy of optical dating. *Radiation Measurements* 38(3), 299–310.
- Bøtter-Jensen, L., McKeever, S., Wintle, A., 2003. *Optically Stimulated Luminescence Dosimetry*. Elsevier Science.
- Chen, G., Li, S.-H., Murray, A., 2000. Study of the 110 °C TL peak sensitivity in optical dating of quartz. *Radiation Measurements* 32(5), 641–645.
- Fasoli, M., Martini, M., 2016. The composite nature of the thermoluminescence UV emission of quartz. *Journal of Luminescence* 173, 120–126.
- Franklin, A., Prescott, J. R., Scholefield, R., 1995. The mechanism of thermoluminescence in an Australian sedimentary quartz. *Journal of Luminescence* 63(5-6), 317–326.
- Friedrich, J., Kreutzer, S., Schmidt, C., 2016. Solving ordinary differential equations to understand luminescence: 'RLumModel', an advanced research tool for simulating luminescence in quartz using R. *Quaternary Geochronology* 35, 88–100.
- Friedrich, J., Pagonis, V., Chen, R., Kreutzer, S., Schmidt, C., 2017a. Quartz radiofluorescence: a modelling approach. *Journal of Luminescence* 186, 318–325.
- Friedrich, J., Kreutzer, S., Schmidt, C., 2017b. *RLumModel: Solving Ordinary Differential Equations to Understand Luminescence*. (R package version 0.2.3). CRAN. <https://CRAN.R-project.org/package=RLumModel>,
- Friedrich, J., Fasoli, M., Kreutzer, S., Schmidt, C., 2017c. The basic principles of quartz radiofluorescence dynamics in the UV - analytical, numerical and experimental results. *Journal of Luminescence* 192, 940–948.
- Friedrich, J., Fasoli, M., Kreutzer, S., Schmidt, C., 2018. On the dose rate dependence of radiofluorescence signals of natural quartz. *Radiation Measurements* 111, 19–26.
- Godfrey-Smith, D., 1991. Optical dating studies of sediment extracts. PhD thesis at the Simon Fraser University, Burnaby, Canada.
- Gurney, R., Mott, N., 1939. Luminescence in solids. *Transactions of the Faraday Society* 35, 69–73.
- Huntley, D., Short, M., Dunphy, K., 1996. Deep traps in quartz and their use for optical dating. *Canadian Journal of Physics* 74, 81–91.
- Itoh, N., Stoneham, D., Stoneham, A., 2002. Ionic and electronic processes in quartz: mechanisms of thermoluminescence and optically stimulated luminescence. *Journal of Applied Physics* 92(9), 5036–5044.

- Kolb, T., Fuchs, M., Zöller, L., 2016. Deciphering fluvial landscape evolution by luminescence dating of river terrace formation: a case study from Northern Bavaria, Germany. *Zeitschrift für Geomorphologie, Supplementary Issues* 60(1), 29–48.
- Kreutzer, S., Schmidt, C., Fuchs, M. C., Dietze, M., Fischer, M., Fuchs, M., 2012. Introducing an R package for luminescence dating analysis. *Ancient TL* 30(1), 1–8.
- Kreutzer, S., Murari, M. K., Frouin, M., Fuchs, M., Mercier, N., 2017a. Always remain suspicious: a case study on tracking down a technical artefact while measuring IR-RF. *Ancient TL* 35(1), 20–30.
- Kreutzer, S., Friedrich, J., Sanderson, D., Adamiec, G., Chruścińska, A., Fasoli, M., Martini, M., Polymeris, G. S., Burbidge, C. I., Schmidt, C., 2017b. Les sables de Fontainebleau: A Natural Quartz Reference Sample and its Characterisation. *Ancient TL* 35(2), 21–31.
- Levy, P. W., 1991. Radiation damage studies on non-metals utilizing measurements made during irradiation. *Journal of Physics and Chemistry of Solids* 52(1), 319–349.
- Martini, M., Fasoli, M., Galli, A., 2009. Quartz OSL emission spectra and the role of  $[\text{AlO}_4]^\ominus$  recombination centres. *Radiation Measurements* 44(5), 458–461.
- Martini, M., Fasoli, M., Villa, I., Guibert, P., 2012. Radioluminescence of synthetic and natural quartz. *Radiation Measurements* 47(9), 846–850.
- McKeever, S. W. S., Chen, R., 1997. Luminescence models. *Radiation Measurements* 27(5), 625–661.
- Nanjundaswamy, R., Lepper, K., McKeever, S., 2002. Thermal quenching of thermoluminescence in natural quartz. *Radiation Protection Dosimetry* 100(1-4), 305–308.
- Pagonis, V., Ankjærgaard, C., Murray, A., Jain, M., Chen, R., Lawless, J., Greilich, S., 2010. Modelling the thermal quenching mechanism in quartz based on time-resolved optically stimulated luminescence. *Journal of Luminescence* 130(5), 902–909.
- Petrov, S., Bailiff, I., 1997. Determination of trap depths associated with TL peaks in synthetic quartz (350 – 550 K). *Radiation Measurements* 27(2), 185–191.
- Poolton, N., Bulur, E., Wallinga, J., Bøtter-Jensen, L., Murray, A., Willumsen, F., 2001. An automated system for the analysis of variable temperature radioluminescence. *Nuclear Instruments and Methods in Physics Research Section B: Beam Interactions with Materials and Atoms* 179(4), 575–584.
- Preusser, F., Degering, D., Fuchs, M., Hilgers, A., Kadereit, A., Klasen, N., Krbetschek, M., Richter, D., Spencer, J. Q. G., 2008. Luminescence dating: basics, methods and applications. *Quaternary Science Journal* 57(1-2), 95–149.
- Preusser, F., Chithambo, M. L., Götte, T., Martini, M., Ramseyer, K., Sendezera, E. J., Susino, G. J., Wintle, A. G., 2009. Quartz as a natural luminescence dosimeter. *Earth-Science Reviews* 97(1), 184–214.
- R Core Team, 2017. *R: A Language and Environment for Statistical Computing*. R Foundation for Statistical Computing. Vienna, Austria. <https://www.R-project.org/>,
- Richter, D., Pintaske, R., Dornich, K., Krbetschek, M., 2012. A novel beta source design for uniform irradiation in dosimetric applications. *Ancient TL* 30(2), 57–63.

- Richter, D., Richter, A., Dornich, K., 2013. Lexsyg - A new system for luminescence research. *Geochronometria* 40(4), 220–228.
- Schilles, T., Poolton, N., Bulur, E., Bøtter-Jensen, L., Murray, A., Smith, G., Riedi, P., Wagner, G., 2001. A multi-spectroscopic study of luminescence sensitivity changes in natural quartz induced by high-temperature annealing. *Journal of Physics D: Applied Physics* 34(5), 722–731.
- Schmidt, C., Friedrich, J., Adamiec, G., Chruścińska, A., Fasoli, M., Kreutzer, S., Martini, M., Panzeri, L., Polymeris, G. S., Przegiętka, K., Valla, P. G., King, G. E., Sanderson, D. C., 2018. How reproducible are kinetic parameter constraints of quartz luminescence? An interlaboratory comparison for the 110 °C TL peak. *Radiation Measurements* 110, 14–24.
- Shlukov, A., Shakhovets, S., Voskovskaya, L., Lyashenko, M., 1993. A criticism of standard TL dating technology. *Nuclear Instruments and Methods in Physics Research Section B: Beam Interactions With Materials and Atoms* 73(3), 373–381.
- Spooner, N. A., 1994. On the optical dating signal from quartz. *Radiation Measurements* 23(2), 593–600.
- Subedi, B., Oniya, E., Polymeris, G. S., Afouxenidis, D., Tsirliganis, N. C., Kitis, G., 2011. Thermal quenching of thermoluminescence in quartz samples of various origin. *Nuclear Instruments and Methods in Physics Research Section B: Beam Interactions with Materials and Atoms* 269(6), 572–581.
- Wintle, A., 1975. Thermal Quenching of Thermoluminescence in Quartz. *Geophysical Journal International* 41(1), 107–113.



# 7 Making the Invisible Visible: Observing the UV-reversal Effect in Quartz using Radiofluorescence

Johannes Friedrich<sup>1</sup>, Sebastian Kreutzer<sup>2</sup>, Christoph Schmidt<sup>1</sup>

<sup>1</sup> Chair of Geomorphology, University of Bayreuth, 95440 Bayreuth, Germany

<sup>2</sup> IRAMAT-CRP2A, UMR 5060, CNRS - Université Bordeaux Montaigne, Maison de l'Archéologie, Esplanade des Antilles, 33607 Pessac Cedex, France

*Journal of Physics D: Applied Physics* 51, 335105, 2018

<https://doi.org/10.1088/1361-6463/aacfd0>

## Abstract

The pre-dose effect is one of the most well-known phenomena in quartz luminescence. It refers to an increase in dose sensitivity subsequent to radiation pre-exposure and annealing. A theoretical description of this phenomenon exists since the 1970s and is widely used in recent luminescence models. However, also the opposite effect has been described, the less known 'UV-reversal' effect which reduces the luminescence sensitivity due to illuminating the sample with far UV light. Both effects were detected with thermoluminescence (TL) following a small test dose and observing the effect indirectly using the response of the 110°C peak. We here present a more direct measurement of both phenomena via UV-Radiofluorescence (UV-RF), which is the luminescence emitted during irradiation. Therefore, the need of a TL measurement is obsolete. Furthermore, we were able to calculate a time rate of eviction of holes from the luminescence centre and implement this value into existing models to obtain a more comprehensive description of quartz luminescence. Numerical simulations are in good agreement with experimental data.

## 7.1 Introduction

Understanding charge transfer in quartz is of interest for a wide range of topics, especially for luminescence dating and dosimetry. During the last few decades different models were developed to explain luminescence production in minerals, starting with Halperin & Braner (1960) who were the first attempting to describe a single thermoluminescence (TL) peak based on three coupled first-order differential equations. These equations describe the transfer of electrons during heating. It has been known for a long time that irradiating and annealing quartz leads to dose-dependent sensitivity changes, also known as *pre-dose* effect. Zimmerman (1971) published an interpretation for this phenomenon which has commonly been accepted and implemented in more recent models (e.g., Bailey (2001), Chen & Leung (1999), Friedrich et al. (2017a), and Pagonis et al. (2008)). The basic energy level scheme given by Zimmerman (1971) includes one electron trapping state (T) and two hole states: reservoir (R) and luminescence (L) centres. During the excitation by  $\beta$ -radiation or  $\gamma$ -rays, electrons are raised from the valence to the conduction band, and can be localised in the trapping state T. Defect electrons (holes) can be captured by the R- or L-centre. Annealing to high temperatures ( $> 500^\circ\text{C}$ ) sensitises quartz by redistributing holes from non-luminescent centres (R-centre) to luminescence centres (L-centre) within the crystal lattice. The findings by Zimmerman (1971) suggested that this effect can be reversed by illuminating the sample with far UV light (UVC, 240 nm).

Zimmerman's experiments are summed up here: She pre-dosed quartz samples and measured the UV-TL sensitivity. After bleaching with UV light the samples were rapidly heated to different temperatures and the TL sensitivity being determined after each heating. The TL sensitivity after the UV bleaching was compared to the sensitivity before and the results showed that heating to  $150^\circ\text{C}$  or  $500^\circ\text{C}$  resulted in 40% and 95% of the prior TL sensitivity, respectively. From these findings Zimmerman (1971) suggested that the effect of UV bleaching is primarily the opposite of the effect of heating (UV-reversal effect). We can thus ascertain that all results were obtained *indirectly* via TL measurements. The aim of this study is to show the UV-reversal effect more directly via radiofluorescence measurements in the UV (UV-RF). Previous studies showed basic characteristics of UV-RF signals (Friedrich et al. 2017c):

- A decreasing UV-RF signal over time is expected when almost all of the holes are located in the L-centre (e.g., after strong annealing). The more holes are localised in the L-centre, the higher is the UV-RF intensity (linear relationship).
- No signal dynamics over time is expected when no significant amount of charge carriers is located either in the R- or the L-centre.
- In theory, an increasing signal over time is expected when most of the holes are located in the R-centre.

- Realising the last condition is difficult because heating transports holes most probably in the L-centre while during irradiation both centres are being filled. Nevertheless, numerical solutions in Friedrich et al. (2017c) showed that an increasing UV-RF signal will be expected when almost all holes are located in the R-centre.

The main idea behind this study is to confirm the model developed by Zimmerman (1971) more directly with UV-RF signals instead of TL signals after giving test doses (Zimmerman 1971). The hypotheses for our experiments are:

- We expect a less intense UV-RF signal after short UV bleaching times. According to the model by Zimmerman (1971) the concentration of holes in the R-centre is now higher than in the L-centre. Combining with the findings by Friedrich et al. (2017c) this should lead to a less intense UV-RF signal.
- After very long UV bleaching times a very low concentration of holes in the L-centre and a high concentration in the R-centre is expected. Consequently, we expect an increasing UV-RF signal after UV bleaching.
- Annealing the samples to different temperatures after UV bleaching will partly restore the hole distribution from before UV bleaching and thus a similar UV-RF signal dynamics than prior UV bleaching is expected.

## 7.2 Material and methods

### 7.2.1 Quartz samples

We analysed three different quartz samples: (I) a natural sedimentary quartz (BT1248), (II) quartz extracted from a colluvial sample originating from the Trebgast valley in the north-west of Bayreuth, Germany (BT586; Kolb et al. (2016)) and (III) a coastal dune quartz (FB1A; Kreutzer et al. (2017a) and Schmidt et al. (2018)). Sample FB1A was annealed at 500 °C in the muffle oven for 30 min, see Kreutzer et al. (2017a). Sample BT1248 was annealed at 700 °C for 60 min. The crystals were sieved to separate grains of 90 – 200  $\mu\text{m}$  in diameter. Subsequent chemical treatments followed routine preparation procedures for luminescence dating samples, described in Preusser et al. (2008) and especially for BT586 in Friedrich et al. (2017a) and for FB1A in Kreutzer et al. (2017a). For each measurement a new aliquot with the same amount of grains was used, allowing a quantitative comparison of the results. Figure 7.1 shows the emission spectra of two investigated quartz samples after annealing the samples to 500 °C for 10 min and recording the RF spectra with a dose rate of 12 Gy min<sup>-1</sup>. Note that this is the dose rate for Fig. 7.1 and not for the measurements presented elsewhere in the study. The measurement conditions for recording the spectra are the same as given in Friedrich et al. (2017c). In all samples a strong C band is apparent, which decreases with measurement time (Fasoli & Martini 2016). The detection window of the used photomultiplier (see Sec. 7.2.2) is covering the main emission peak at  $\sim 3.42$  eV.

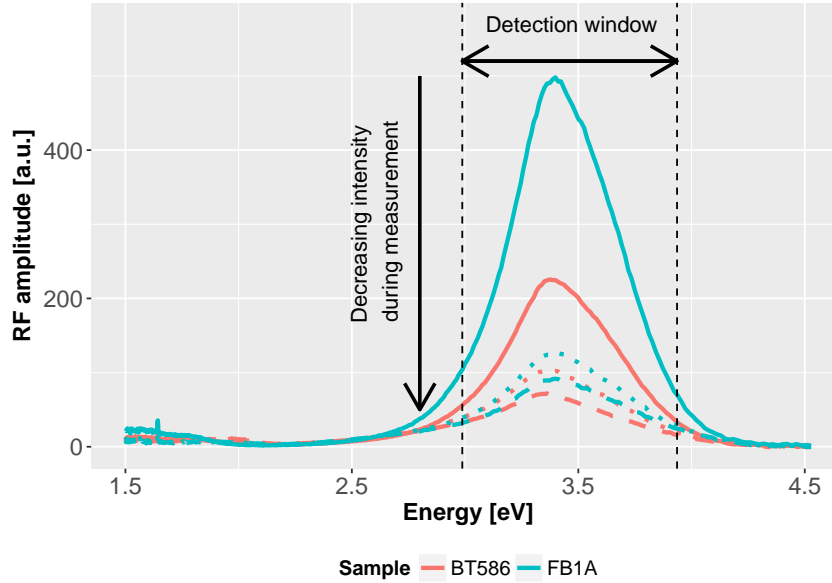


**Figure 7.1:** Radiofluorescence spectra measurements for two quartz samples. Different line types indicate different times/doses during the measurement (solid line:  $\sim 7$  Gy, dotted:  $\sim 143$  Gy, dashed:  $\sim 279$  Gy). A decreasing C band (peak maximum at  $\sim 3.42$  eV) is apparent in the two investigated samples. Vertical dotted lines mark the detection window, limited by the used filter, see Sec. 7.2.2.

## 7.2.2 Measurement conditions

All measurements were carried out on a Freiberg Instruments *leasyg research* reader (Richter et al. 2013) at the luminescence laboratory in Bayreuth. The reader is equipped with a  $^{90}\text{Sr}/^{90}\text{Y}$   $\beta$ -source ( $\sim 3.6$  Gy  $\text{min}^{-1}$ ), calibrated for coarse grain quartz on stainless steel cups. The  $\beta$ -source is specifically designed for RF measurements (Richter et al. 2012). Luminescence was detected through a Chroma BP 365/50 EX interference filter in front of a Hamamatsu H7360-02 photomultiplier tube allowing for a detection of the UV-RF signal between 315 nm and 415 nm (3.94 eV and 2.99 eV, respectively, see Fig. 7.1). All measurements were performed in a nitrogen atmosphere. The channel time for the RF measurements was set to 1 s. Further details on the UV-RF experiments are given in the text below. The UV-LEDs used for the bleaching experiments were produced by Seoul Viosys (product name *CUD7GF1B*) and emit light with a peak wavelength of 275 nm, a spectrum half width of 11 nm and an optical output power of 11.5 mW. The LEDs were mounted in a distance of 5 cm to the sample.

## 7.2.3 Data analysis

Data analyses were carried out using the statistical programming environment **R** (R Core Team 2017) and the **R**-package 'Luminescence' (Kreutzer et al. 2012, 2017b). For simulating the UV-RF signals in Sec. 7.4.2 and for the comprehensive quartz model, the **R**-packages 'deSolve' (Soetaert et al. 2012) and 'RLumModel' (Friedrich et al. 2016, 2017b) were used.

## 7.3 Quartz UV-RF measurements

### 7.3.1 Varying UV-bleaching times

In a first attempt, we varied the duration of the UV bleaching and measured the effect on the UV-RF signal. Table 7.1 shows the measurement protocol: In step 1 a stabilisation was performed to prevent sensitivity changes (Friedrich et al. 2017a). Step 2 is the reference UV-RF measurement at room temperature (RT) before the UV bleaching (step 3). Finally, RF is measured again after bleaching to detect changes caused by bleaching (step 4). We varied the bleaching time in step 3 from 2 min to 120 min.

Step	Description
1	Irradiate for 2 ks and anneal to 500 °C for 2 min (5x)
2	Radiofluorescence for 2 ks at RT
3	UV bleach for different times
4	Radiofluorescence for 2 ks at RT

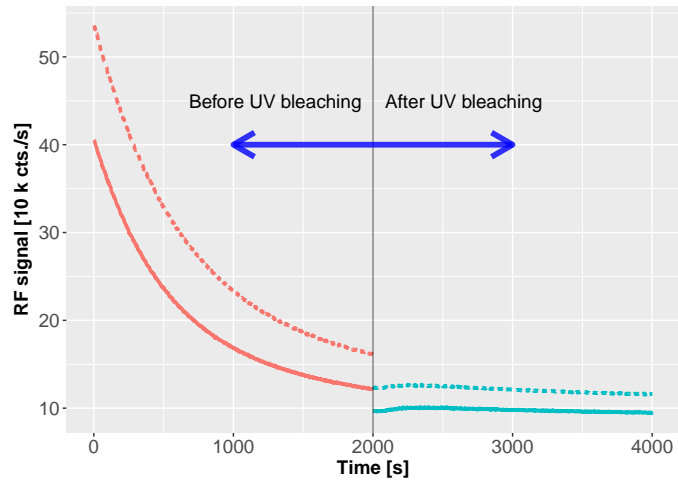
**Table 7.1:** Measurement protocol for varying bleaching times. All annealing steps were performed with 5 K s<sup>-1</sup>. For detailed information, see text.

Figure 7.2 shows results for every quartz sample. Subfigure (a) shows sample BT1248 after 10 min UV bleaching, (b) BT586 after 40 min and (c) FB1A after 120 min. Different line types indicate different measured aliquots. Note that there is a gap in time between the red and the blue lines, which is indicated with the vertical line after 2,000 s. This marks the bleaching event. The second RF measurement (step 4 in Table 7.1) was shifted to a start time of 2,000 s to see the effect of UV bleaching. Figure 7.3 shows in detail the change in the RF signal dynamics after different UV bleaching times for sample BT1248. All other samples show a similar behaviour (not shown here). The UV-RF signals are normalised to the last signal value at 2,000 s. A strong time dependency is evident, e.g., for bleaching times > 20 min the curve shape changes completely from a decreasing to an increasing signal.

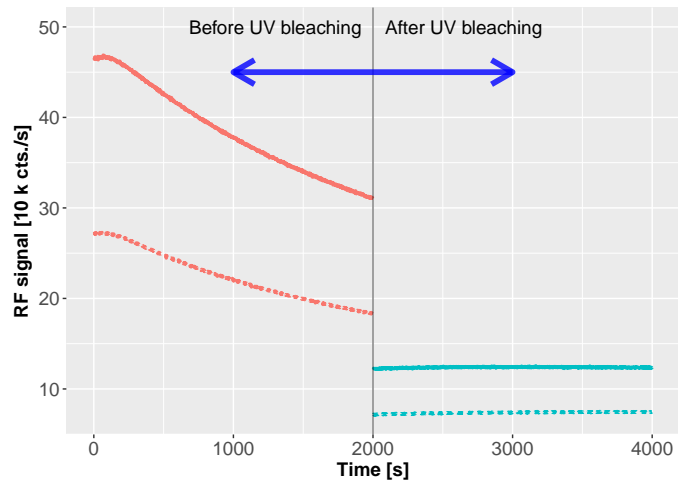
The ratio of the last channel of measurement step 2 to the first channel of step 4 is taken as indicator of the UV bleaching effect. Figures 7.2 and 7.3 already indicate that the effect of UV bleaching will be more intense after longer illumination times. A comprehensive analysis of all used samples is given in Fig. 7.4. Different dot colours indicate different samples. For every bleaching time two aliquots were measured per sample. The lines indicate a fit over dots belonging to one colour. The used fitting equation was:

$$y = A \cdot \exp(-B \cdot t) + C \quad (7.1)$$

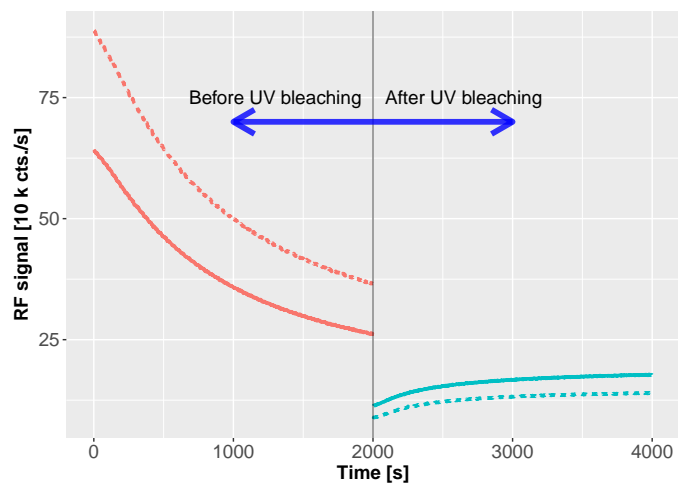
This equation describes an exponentially decaying function with time. Parameter  $A$  is a scaling factor,  $B$  [s<sup>-1</sup>] acts as a decay parameter and  $C$  is the residual component. The detailed estimation of the parameters is shown in Table 7.2.



(a) BT1248 10 min



(b) BT586 40 min



(c) FB1A 120 min

**Figure 7.2:** Typical results of different UV bleaching times for all measured quartz samples. Subfigure (a) BT1248 after 10 min UV bleaching, (b) BT586 after 40 min and (c) FB1A after 120 min. The vertical line indicates the bleaching event and different line types indicate different measured aliquots.

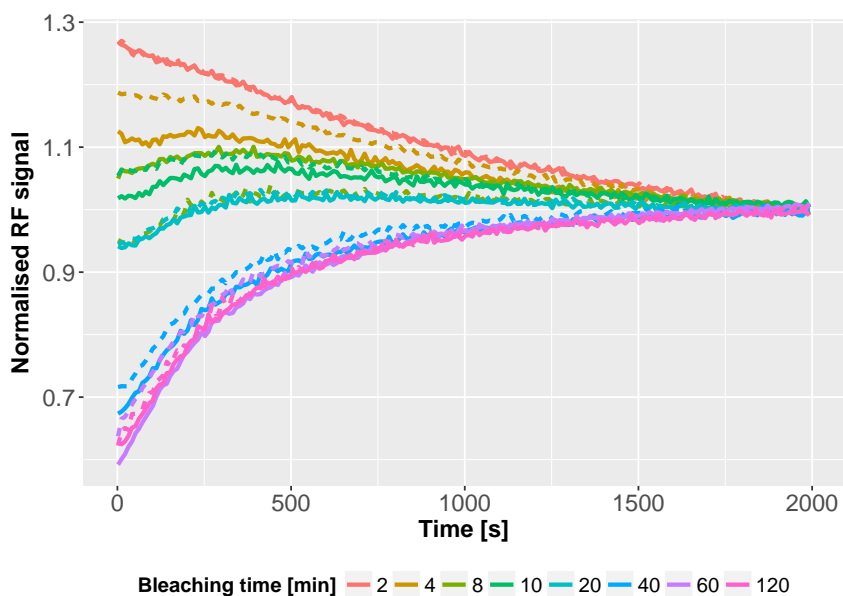


**Figure 7.3:** Normalised (to the last data point) UV-RF curves of sample BT1248 after different UV bleaching times ranging from 2 min to 120 min. Different line types indicate different measured aliquots.

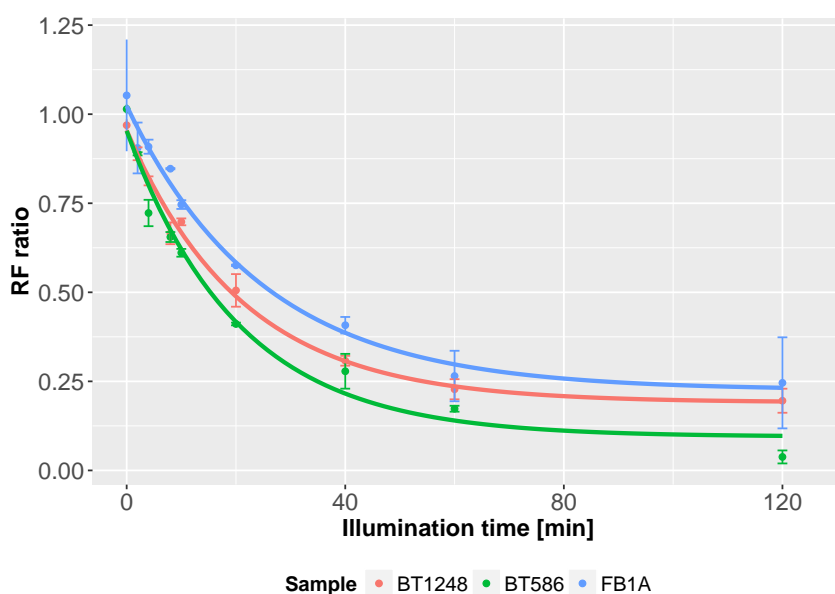


**Figure 7.4:** RF ratio of the last channel before UV bleaching and first channel after UV bleaching for all measured samples. The dots represent the mean value and the error bars the std. error for all measured aliquots. The lines indicate a fit according to Eq. (7.1).

	BT586	BT1248	FB1A
A	$0.85 \pm 0.04$	$0.76 \pm 0.02$	$0.80 \pm 0.05$
B [ $s^{-1}$ ]	$0.050 \pm 0.006$	$0.047 \pm 0.004$	$0.040 \pm 0.007$
C	$0.09 \pm 0.03$	$0.19 \pm 0.02$	$0.23 \pm 0.04$

**Table 7.2:** Estimation of fitted parameters in Fig. 7.4 with std. error from fitting procedure.

STEP	DESCRIPTION
1	Anneal to 500 °C for 2 min (5x)
2	Radiofluorescence for 2 ks at RT
3	UV bleach for 10 min
4	Anneal to different temperatures from 200 °C to 500 °C
5	Radiofluorescence for 2 ks at RT

**Table 7.3:** Measurement protocol detecting the UV-reversal effect.

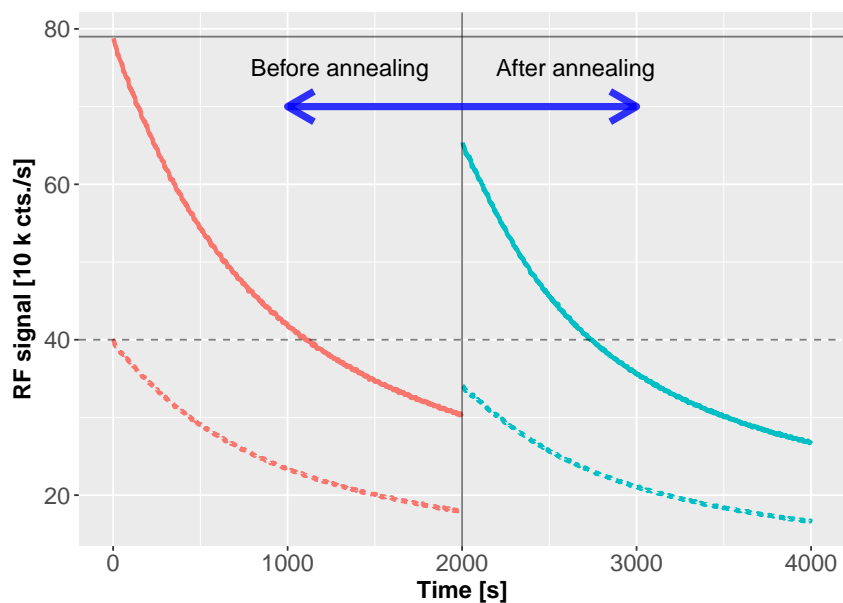
Table 7.2 identifies that the most sensitive parameter  $B$  is (within errors) identical for all three samples. Parameters  $A$  and  $C$  are also comparable between all samples. Therefore, we conclude that the UV bleaching characteristics of different quartz samples from different geological origins are similar. These results will be used in Sec. 7.4 to simulate the UV bleaching effect.

### 7.3.2 Detecting the UV-reversal effect

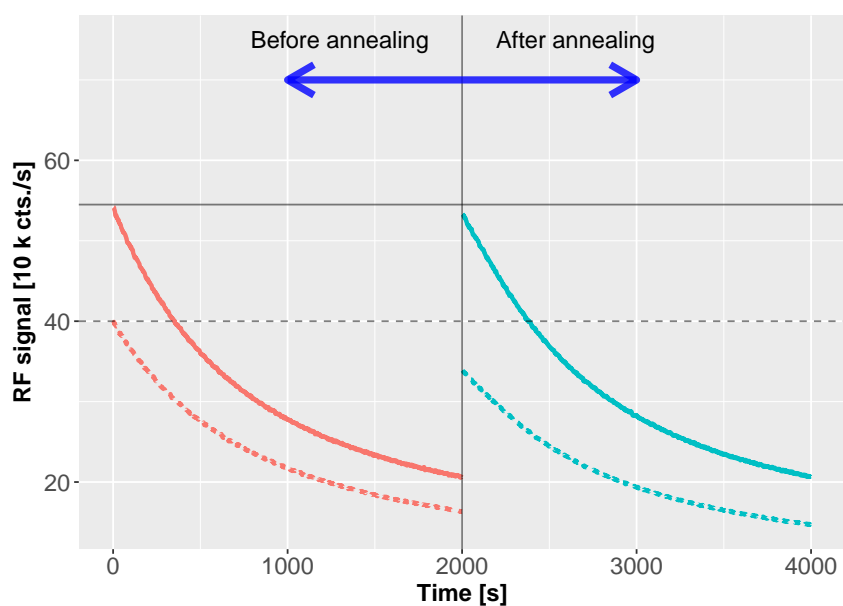
The UV-reversal effect was measured with the protocol given in Table 7.3: Step 1 and 2 correspond to step 1 and 2 in Table 7.1. The UV-bleaching was fixed to 10 min. The next step is the annealing to different temperatures and with step 5 the change in sensitivity caused by step 4 by measuring UV-RF was detected.

Figure 7.5 contains representative examples for different annealing temperatures: Subfigure (a) shows sample FB1A before (left side, red) and after (right side, blue) UV bleach and annealing to 300 °C. Different line types indicate different aliquots. The two horizontal lines show the UV-RF signal prior to UV bleach and annealing. In subfigure (b) an annealing temperature of 500 °C is shown. Again, the horizontal lines indicate the primary UV-RF signal. One aliquot (solid line) shows an almost complete recovery of the UV-RF signal. A complete overview of all measured samples is given in Fig. 7.6 and a possible interpretation of this analysis is:

- Temperatures  $< 300$  °C are not able to recover the primary UV-RF signal completely.
- Samples BT1248 and FB1A show higher signal intensities than the primary UV-RF signal for annealing temperatures of 350 °C and 400 °C.
- An annealing temperature of 500 °C is able to recover the primary UV-RF intensity, even with higher intensities than the primary UV-RF signal.
- All three measured quartz samples behave similarly.



(a)



(b)

**Figure 7.5:** Experimental results for sample FB1A before (red lines) and after (blue lines) UV bleach and annealing to (a) 300 °C and (b) 500 °C. This corresponds to step 2 (red lines) and 5 (blue lines) in Table 7.3. Different line types indicate different measured aliquots. Horizontal lines mark the initial signal intensity of step 2 and indicate if an annealing temperature is capable of fully recovering this intensity.

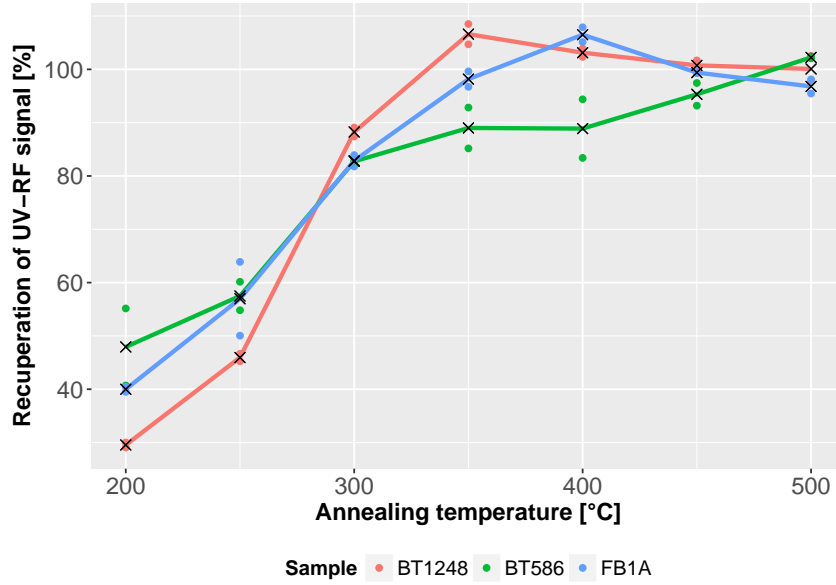


**Figure 7.6:** Recuperation of the primary RF signal (before UV bleaching) after UV bleaching and annealing to different temperatures. The line indicates the mean of the two measured aliquots (filled dots). Crosses are average values of the all measured aliquots.

## 7.4 Quartz UV-RF simulations

### 7.4.1 Defining the model

The simulation of the UV-reversal effect was already performed by Pagonis et al. (2006) but for TL measurements and without determining a parameter for the time rate of eviction of holes from the L-centre. In this study, this parameter as well as RF simulations were used to reproduce the experiments described above. It was previously shown that it is possible to simulate UV-RF phenomena with a three-energy-level model by solving the corresponding differential equations (e.g., Friedrich et al. (2017a,c)). The model consists of a deep electron trap and two recombination centres: The L-centre, which is radiative, and the R-centre, a non-radiative competitor, also called reservoir centre. In contrast to former publications we included a term in the equation for the L-centre (Eq. (7.4)) which describes the reduction of the hole centre concentration in time due to UV bleaching. Note that this term also changes the equation for the  $\frac{dn_v}{dt}$  (Eq. (7.6)).

The following set of coupled differential equations describes the charge transport in quartz:

$$\frac{dn}{dt} = A_n \cdot (N - n) \cdot n_c \quad (7.2)$$

$$\frac{dm_1}{dt} = A_{m_1} \cdot (M_1 - m_1) \cdot n_v - B_1 \cdot m_1 \cdot n_c \quad (7.3)$$

$$\frac{dm_2}{dt} = A_{m_2} \cdot (M_2 - m_2) \cdot n_v - B_2 \cdot m_2 \cdot n_c - m_2 \cdot \theta_{m_2} \cdot P \quad (7.4)$$

$$\frac{dn_c}{dt} = R - A_n \cdot (N - n) \cdot n_c - B_1 \cdot m_1 \cdot n_c - B_2 \cdot m_2 \cdot n_c \quad (7.5)$$

$$\frac{dn_v}{dt} = R - A_{m_1} \cdot (M_1 - m_1) \cdot n_v - A_{m_2} \cdot (M_2 - m_2) \cdot n_v + m_2 \cdot \theta_{m_2} \cdot P \quad (7.6)$$

where  $M_1$  ( $\text{cm}^{-3}$ ) is the concentration of non-radiative hole centres with instantaneous occupancy of  $m_1$  ( $\text{cm}^{-3}$ ),  $M_2$  ( $\text{cm}^{-3}$ ) is the concentration of radiative hole centres with instantaneous occupancy of  $m_2$  ( $\text{cm}^{-3}$ ),  $N$  ( $\text{cm}^{-3}$ ) is the concentration of the electron trapping state with instantaneous occupancy of  $n$  ( $\text{cm}^{-3}$ ).  $n_c$  and  $n_v$  are the concentrations ( $\text{cm}^{-3}$ ) of the electrons and holes in the conduction band (CB) and valence band (VB), respectively.  $R$  ( $\text{cm}^{-3} \text{ s}^{-1}$ ) is the rate of production of electron-hole pairs, which is proportional to the excitation dose rate,  $A_{m_1}$  and  $A_{m_2}$  ( $\text{cm}^3 \text{ s}^{-1}$ ) are the trapping probability coefficients of free holes into centres 1 and 2, respectively.  $B_1$  and  $B_2$  ( $\text{cm}^3 \text{ s}^{-1}$ ) are the recombination probability coefficients for free electrons with holes in centres 1 and 2, and  $A_n$  ( $\text{cm}^3 \text{ s}^{-1}$ ) is the retrapping probability coefficient of free electrons into the active trapping state  $N$ .  $\theta_{m_2}$  is the time rate of eviction of holes in the L-centre. Parameter  $P$  is a scaling value for the power density of the UV lamp. We choose a value of  $P = 0.014$  to obtain the best agreement with our experiments. Note that the last two parameters described are the analogue to the bleaching terms of electron traps published in former quartz models (Bailey 2001, 2002; Friedrich et al. 2017a; Pagonis et al. 2008). The RF signal intensity obtained from the recombination of electrons from the conduction band into the recombination centre (L-centre) is given by:

$$I(t) = B_2 \cdot m_2 \cdot n_c \quad (7.7)$$

### 7.4.2 Matching experimental results and simulations

The parameters for the calculations are similar to the ones by Friedrich et al. (2017a) (levels 5, 7, and 8). The parameter  $R$  is equivalent to  $0.01 \text{ Gy s}^{-1}$  and the simulated sequences are steps 2 to 4 in Table 7.1. Note that with Eq. (7.2) – (7.6) it is only possible to simulate the RF and UV bleaching steps, not any heating. Therefore, we assumed that after step 1 in Table 7.1 all holes are migrated towards the L-centre. Hence, the concentration of electrons in the deep electron trap  $N$  and the concentration of holes in the L-centre are identical because of charge neutrality. We set  $n_0 = m_{2_0} = 1 \text{ E}+09$  and  $m_{1_0} = 0$ .

PARAMETER	VALUE	UNIT	DESCRIPTION
$A_n$	1 E-10	$\text{cm}^3 \text{s}^{-1}$	Conduction band to electron trap transition probability
$B_1$	5 E-09	$\text{cm}^3 \text{s}^{-1}$	Conduction band to R-centre transition probability
$B_2$	5 E-10	$\text{cm}^3 \text{s}^{-1}$	Conduction band to L-centre transition probability
$A_{m_1}$	5 E-07	$\text{cm}^3 \text{s}^{-1}$	Valence band to R-centre transition probability
$A_{m_2}$	1 E-09	$\text{cm}^3 \text{s}^{-1}$	Valence band to L-centre transition probability
$M_1$	1 E+10	$\text{cm}^{-3}$	Concentration of R-centre
$M_2$	1 E+11	$\text{cm}^{-3}$	Concentration of L-centre
$N$	5 E+10	$\text{cm}^{-3}$	Concentration of electron trap
$R$	3 E+05	$\text{cm}^{-3} \text{s}^{-1}$	Ionisation rate (pair production rate)
$P$	0.0140		Scaling value for the power density of the UV lamp
$\theta_{m_2}$	0.046	$\text{s}^{-1}$	Time rate of eviction of holes from the L-centre

**Table 7.4:** Used parameters for the comparison between analytical and numerical solutions. No heating steps were included in this simulation.

Table 7.4 shows the used parameters. It is important that during RF simulation  $P = 0$  and  $R \neq 0$  and during UV bleaching simulation  $P \neq 0$  and  $R = 0$ .

Figure 7.7 shows the effect of the UV bleaching in the numerical model presented above. As in the experimental part (Sec. 7.3.1) the duration of the UV bleach was varied from 2 min to 120 min. The black line in Fig. 7.7 shows the RF before UV bleach (step 2 in Table 7.1) and the vertical line at 2,000 s indicates the UV bleaching step. Note that Fig. 7.7 is a summary of different runs of the models, each with another bleaching time. The colour at the right hand side of the plot indicates different bleaching times, identical to those used in the experiments. It can be noted that the behaviour is very similar to that seen in Fig. 7.3:

- There is a clear loss in signal intensity after the UV bleaching step
- Bleaching times  $> 20$  min change the dynamics of the RF signal

Figure 7.8 shows the same analysis as Fig. 7.4 but for numerical simulations. All calculations were executed in the same way as for the experimental data. Fitting of the curve obtained from Fig. 7.8 was executed. Parameter  $B$  is comparable with the experiments from Sec. 7.3.1. It is striking that parameter  $C$  is almost 0. This indicates that the bleaching is so effective that no charge remains in the L-centre after long UV bleaching times, which is contradictory to our findings from Sec. 7.3.1. The values for the fitted parameters are:  $A = 0.98 \pm 0.01$ ,  $B [\text{s}^{-1}] = 0.0434 \pm 0.0008$  and  $C = 0.01 \pm 0.01$ .

### 7.4.3 Simulations with a more comprehensive model

The numerical model presented in Sec. 7.4.1 is a three-energy-level model with a limited explanatory power. We now present a comprehensive quartz model which describes more than the effects outlined in Sec. 7.3, e.g., the 110 °C TL peak or OSL behaviour. Therefore, we merge the parameters presented in Table 7.4 and the ones published in Friedrich et al. (2017a: Table 2) while omitting the R<sub>2</sub>-centre because it behaves similar to the R<sub>1</sub>-centre.

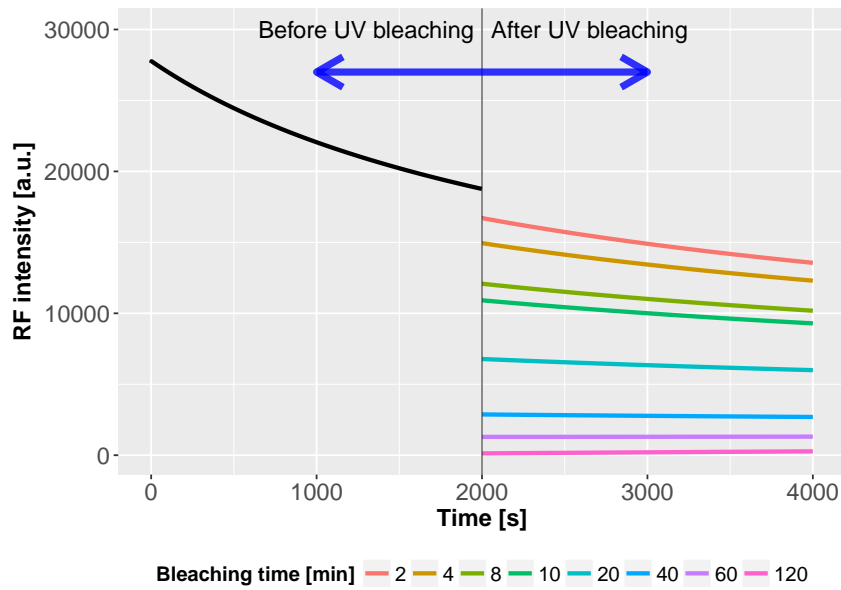


**Figure 7.7:** Simulation of different UV bleaching times ranging from 2 min to 120 min. The vertical line at 2,000 s marks the bleaching event.

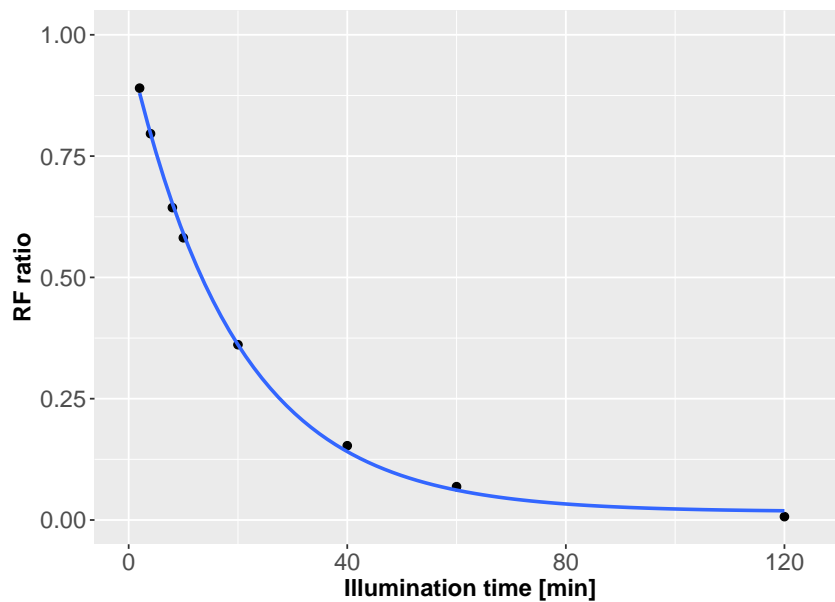


**Figure 7.8:** RF ratio calculated from Fig. 7.7. See Fig. 7.4 for the experimental analysis.

7 Making the Invisible Visible: Observing the UV-reversal Effect in Quartz using Radiofluorescence

	LEVELS	$N$ [cm <sup>-3</sup> ]	$E$ [eV]	$s$ [s <sup>-1</sup> ]	$A$ [cm <sup>3</sup> s <sup>-1</sup> ]	$B$ [cm <sup>3</sup> s <sup>-1</sup> ]	$\sigma_0$ [s <sup>-1</sup> ]	$E_{th}$ [eV]	$\theta$
1	110 °C TL	1.5 E+07	0.97	5 E+12	1 E-08	-	0.75	0.1	-
2	230 °C TL	1 E+07	1.55	5 E+14	1 E-08	-	-	-	-
3	OSL <sub>F</sub>	1 E+09	1.7	5 E+13	1 E-09	-	6	0.1	-
4	OSL <sub>M</sub>	2.5 E+08	1.72	5 E+14	5 E-10	-	4.5	0.13	-
5	Deep	5 E+10	1.95	1 E+10	1 E-10	-	-	-	-
6	R-centre	1 E+10	2	5 E+13	5 E-07	5 E-09	-	-	-
7	L-centre	1 E+11	5	1 E+13	1 E-09	5 E-10	-	-	0.046
8	K-centre	5 E+09	5	1 E+13	1 E-10	1 E-10	-	-	-

**Table 7.5:** Model parameters used for simulating the data shown in Figs. 7.9 and 7.10. The parameters for the deep electron trap, R- and L-centre are identical to the ones presented in Table 7.4.

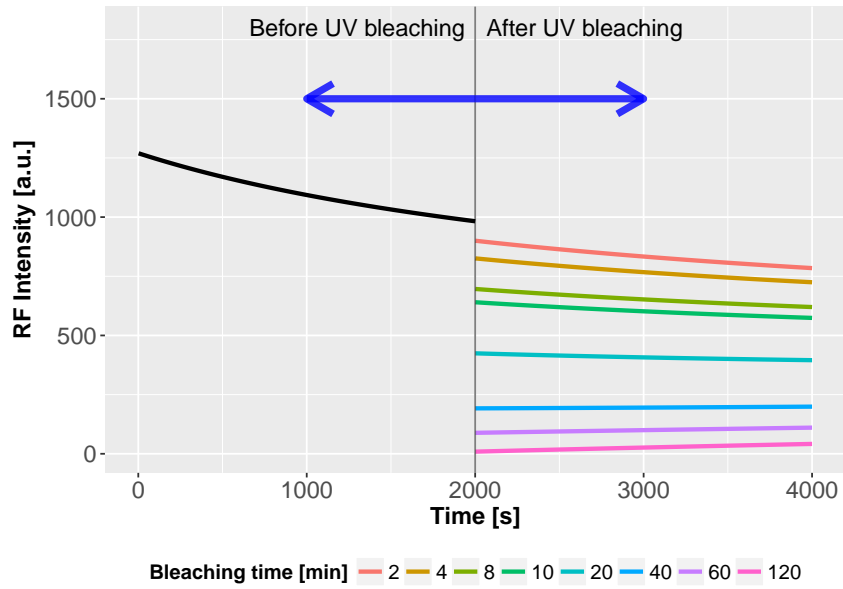
1	Geological dose irradiation of 1,000 Gy at 1 Gy s <sup>-1</sup> at 20 °C
2	Relaxation stage - 60 s at 20 °C
3	Geological time - heat from 20 °C to 350 °C at 5 °C s <sup>-1</sup>
4	Relaxation for geological time, 60 s at 20 °C
5	Illuminate for 100 s at 200 °C - repeated daylight exposures over long time
6	Relaxation stage - 60 s at 20 °C
7	Burial dose - 50 Gy at 20 °C at 10 <sup>-11</sup> Gy s <sup>-1</sup>
8	Relaxation stage - 60 s at 20 °C
9	Preheat to 500 °C for 120 s
10	Radiofluorescence for 2 ks at 20 °C with $R = 3e5$
11	UV bleach at 20 °C for different times
12	Radiofluorescence for 2 ks at 20 °C with $R = 3e5$

**Table 7.6:** The simulation steps for the UV-RF simulation with the comprehensive model. Steps 9 to 12 represent the simulated measurements in the laboratory and are comparable with steps 1 to 4 in Table 7.1.

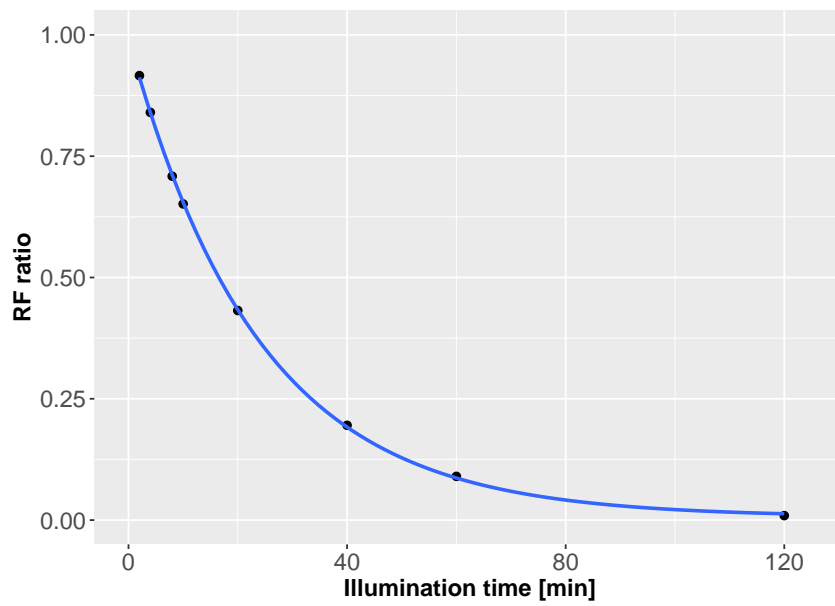
Table 7.5 shows the used parameters (nomenclature identical to Bailey (2001)) for the comprehensive model. Now we are able to simulate also heating events and the complete used sequence is listed in Table 7.6.

Figure 7.9 summarises the results of the UV-bleaching with the full quartz model. Subfigure 7.9 (a) is qualitatively comparable with Fig. 7.7. The signal intensity is different because more traps are available and able to capture electrons, resulting in a reduced recombination rate. This finding is in accordance with Friedrich et al. (2017a). In contrast to that, subfigure 7.9 (b) is quantitatively comparable with Fig. 7.8. This confirms that the suggested mechanism of bleaching the L-centre is able to explain the experimental observations.

We further analysed the behaviour of different optical power densities  $P$ , see Sec. 7.4.1. Figure 7.10 shows different values of  $P$  against calculations of parameter  $B$  (decay parameter of curves for different bleaching times, see Fig. 7.4). A linear fit describes the behaviour in a very good manner. An experimental proof is still pending but lies beyond the scope of this study.



(a) Simulation of different UV-bleaching times with the comprehensive model.



(b) RF ratio of last channel before UV bleaching and first channel after UV bleaching for comprehensive model. The line indicates a fit according to Eq. (7.1).

**Figure 7.9:** Results of the numerical simulations with the comprehensive quartz model.

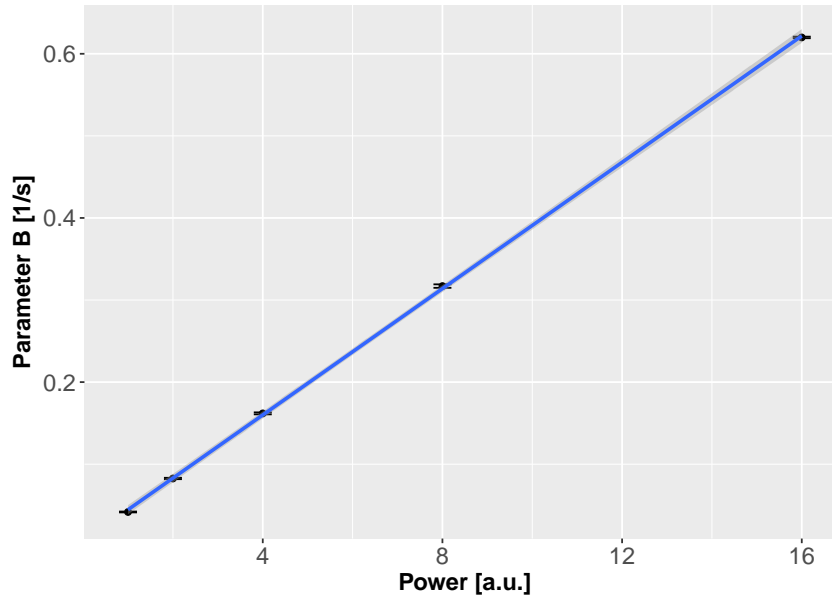


**Figure 7.10:** Results of the simulation of different values of parameter  $P$ , the power density of the UV light against the calculated decay parameter  $B$ . The line indicates an linear fit through all points and suggests a direct linearity.

## 7.5 Discussion

One major limitation of our approach is that the UV bleaching is supposed to have just an effect on the L-centre and not on other centres or traps. The UV bleaching produces electron hole pairs in the valence band and the holes can (with different probabilities) occupy any R- or L-centre, if the assumption of delocalised transitions holds. Nevertheless, we think it is valid to use this as a first concept of the proposed mechanism.

Another limitation is that the proposed models have only one L-centre for the UV emission. However, recent publications by Martini et al. (2014) and Fasoli & Martini (2016) show that the UV emission is a composite of different emissions. With our photomultiplier measurements it is not possible to distinguish between different emissions, because we record the wavelength range from 315 nm to 415 nm. Spectra measurements with subsequent deconvolution into Gaussian components would give a deeper insight into charge redistribution after UV bleaching. The measurements presented here are a continuation of the measurements done decades before by Zimmerman (1971) and furthermore first attempts towards a more complete picture of the charge transfer in quartz using UV-RF.

## 7.6 Conclusions

Our contribution presents a more direct view on the UV-reversal phenomenon, first observed by Zimmerman (1971). In contrast to the original publication we do not use TL measurements to interpret the effect of UV bleaching but UV-RF signals instead, enabling a more direct analysis. This is possible because in the last years the knowledge about signal dynamics of UV-RF increased and this measurement technique is widely available in modern luminescence readers (Lapp et al. 2012; Richter et al. 2012).

We performed UV bleaching experiments with LEDs of 275 nm emission wavelength and re-evaluated the UV-reversal effect in quartz. The advantage of UV-RF measurements is the direct view into involved luminescence centres. For instance, a reduction of available holes in the recombination centre is connected directly to a less intense UV-RF signal. Theoretical predictions of the UV-RF signal from previous publications were confirmed experimentally. We further executed numerical simulations to see if the proposed mechanism of hole redistribution during UV bleaching is also supported in existing quartz models. Therefore we used the results from our experiments, calculated a time rate of eviction of holes from the L-centre and used this as input for our numerical analysis. The numerical solutions are comparable with the experiments and confirm the proposed charge transport during UV bleaching.

We also analysed the recovery of the effect by heating the quartz sample to different temperatures after the UV bleaching and again confirmed the results by Zimmerman (1971) with our UV-RF measurements. Temperatures from 300 °C to 500 °C are able to recover the signal intensity before UV bleaching. Further numerical simulations showed the direct proportionality between the power of the UV bleaching and the calculated decay parameter.

Our approach can be considered as a starting point to obtain a wavelength-dependent description of photoexcitation of holes trapped in hole centres. More research concerned with other emission-bands is also recommended. This will help to better understand charge transfer in quartz. During the last few decades the main focus was on electron traps and their behaviour during heating or illumination. To obtain deeper insights into charge carrier transport in quartz it is essential to also understand the behaviour of luminescence centres. Radiofluorescence is a mighty tool for that purpose.

## 7.7 Acknowledgements

JF is gratefully supported by the DFG (2015 – 2018, “*Modelling quartz luminescence signal dynamics relevant for dating and dosimetry*”, SCHM 3051/4-1). SK received financial support from the LaScArBx. LaScArBx is a research programme supported by the ANR (ANR-10-LABX-52). We wish to thank Manfred Fischer for constructing the body of the UV bleaching unit.

## References

- Bailey, R. M., 2001. Towards a general kinetic model for optically and thermally stimulated luminescence of quartz. *Radiation Measurements* 33(1), 17–45.
- Bailey, R. M., 2002. Simulations of variability in the luminescence characteristics of natural quartz and its implications for estimates of absorbed dose. *Radiation Protection Dosimetry* 100, 33–38.
- Chen, R., Leung, P., 1999. Modeling the pre-dose effect in thermoluminescence. *Radiation Protection Dosimetry* 84(1-4), 43–46.
- Fasoli, M., Martini, M., 2016. The composite nature of the thermoluminescence UV emission of quartz. *Journal of Luminescence* 173, 120–126.
- Friedrich, J., Kreutzer, S., Schmidt, C., 2016. Solving ordinary differential equations to understand luminescence: 'RLumModel', an advanced research tool for simulating luminescence in quartz using R. *Quaternary Geochronology* 35, 88–100.
- Friedrich, J., Pagonis, V., Chen, R., Kreutzer, S., Schmidt, C., 2017a. Quartz radiofluorescence: a modelling approach. *Journal of Luminescence* 186, 318–325.
- Friedrich, J., Kreutzer, S., Schmidt, C., 2017b. *RLumModel: Solving Ordinary Differential Equations to Understand Luminescence*. (R package version 0.2.3). CRAN. <https://CRAN.R-project.org/package=RLumModel>,
- Friedrich, J., Fasoli, M., Kreutzer, S., Schmidt, C., 2017c. The basic principles of quartz radiofluorescence dynamics in the UV - analytical, numerical and experimental results. *Journal of Luminescence* 192, 940–948.
- Halperin, A., Braner, A., 1960. Evaluation of thermal activation energies from glow curves. *Physical Review* 117, 408–415.
- Kolb, T., Fuchs, M., Zöller, L., 2016. Deciphering fluvial landscape evolution by luminescence dating of river terrace formation: a case study from Northern Bavaria, Germany. *Zeitschrift für Geomorphologie, Supplementary Issues* 60(1), 29–48.
- Kreutzer, S., Schmidt, C., Fuchs, M. C., Dietze, M., Fischer, M., Fuchs, M., 2012. Introducing an R package for luminescence dating analysis. *Ancient TL* 30(1), 1–8.
- Kreutzer, S., Friedrich, J., Sanderson, D., Adamiec, G., Chruścińska, A., Fasoli, M., Martini, M., Polymeris, G. S., Burbidge, C. I., Schmidt, C., 2017a. Les sables de Fontainebleau: A Natural Quartz Reference Sample and its Characterisation. *Ancient TL* 35(2), 21–31.
- Kreutzer, S., Dietze, M., Burow, C., Fuchs, M. C., Schmidt, C., Fischer, M., Friedrich, J., 2017b. *Luminescence: Comprehensive Luminescence Dating Data Analysis*. (R package version 0.7.5). <http://CRAN.R-project.org/package=Luminescence>,
- Lapp, T., Jain, M., Thomsen, K. J., Murray, A. S., Buylaert, J.-P., 2012. New luminescence measurement facilities in retrospective dosimetry. *Radiation Measurements* 47(9), 803–808.

- Martini, M., Fasoli, M., Villa, I., 2014. Defect studies in quartz: Composite nature of the blue and UV emissions. *Nuclear Instruments and Methods in Physics Research Section B: Beam Interactions with Materials and Atoms* 327, 15–21.
- Pagonis, V., Chen, R., Kitis, G., 2006. Theoretical modelling of experimental diagnostic procedures employed during pre-dose dosimetry of quartz. *Radiation Protection Dosimetry* 119(1-4), 111–114.
- Pagonis, V., Balsamo, E., Barnold, C., Duling, K., McCole, S., 2008. Simulations of the predose technique for retrospective dosimetry and authenticity testing. *Radiation Measurements* 43(8), 1343–1353.
- Preusser, F., Degering, D., Fuchs, M., Hilgers, A., Kadereit, A., Klasen, N., Krbetschek, M., Richter, D., Spencer, J. Q. G., 2008. Luminescence dating: basics, methods and applications. *Quaternary Science Journal* 57(1-2), 95–149.
- R Core Team, 2017. *R: A Language and Environment for Statistical Computing*. R Foundation for Statistical Computing. Vienna, Austria. <https://www.R-project.org>,
- Richter, D., Pintaske, R., Dornich, K., Krbetschek, M., 2012. A novel beta source design for uniform irradiation in dosimetric applications. *Ancient TL* 30(2), 57–63.
- Richter, D., Richter, A., Dornich, K., 2013. Lexsyg - A new system for luminescence research. *Geochronometria* 40(4), 220–228.
- Schmidt, C., Friedrich, J., Adamiec, G., Chruścińska, A., Fasoli, M., Kreutzer, S., Martini, M., Panzeri, L., Polymeris, G. S., Przegiętka, K., Valla, P. G., King, G. E., Sanderson, D. C., 2018. How reproducible are kinetic parameter constraints of quartz luminescence? An interlaboratory comparison for the 110 °C TL peak. *Radiation Measurements* 110, 14–24.
- Soetaert, K., Cash, J., Mazzia, F., 2012. *Solving differential equations in R*. Springer Science & Business Media.
- Zimmerman, J., 1971. The radiation-induced increase of the 100 °C thermoluminescence sensitivity of fired quartz. *Journal of Physics C: Solid State Physics* 4(18), 3265–3276.



## 8 Further results

In this section previously unpublished results are presented. The first two subsections handle experimental data covering further quartz UV-RF measurements. Section 8.1 investigates the behaviour of different storage times to the UV-RF signal. The next chapter gives an experimental proof of the presented dose determination method given in Sec. 5.5.3. Sections 8.3 and 8.4 present additional modelling results: Section 8.3 presents a method to calculate model parameters from experimental data and Sec. 8.4 investigates the first RF simulations with the Monte-Carlo method.

### 8.1 Recuperation of the UV-RF signal after storing at RT

For using the quartz UV-RF signal for determining absorbed doses it has to be ensured that the signal is not fading. First results showed that the UV-RF signal is able to recover absorbed doses, see Ch. 5. This section contains tests on the signal stability over time. The following measurement sequence was applied:

1. Preheat to 500 °C with 5 K s<sup>-1</sup> for 120 s
2. Measure RF for 2,000 s ( $\sim$  120 Gy) at RT
3. Pause for different times
4. Measure RF for 2,000 s ( $\sim$  120 Gy) at RT

The pause times in step 3 range from 10 s to 30 d. All pause times  $\leq$  1 d were measured with a sequence inheriting a pause step. All other measurements were carried out in a two-stage process: Steps 1) and 2) given above were measured and afterwards the aliquot was stored in the sample wheel of the measurement device. After the pause time, a new sequence with step 4) was applied to these aliquots. Subfigures 8.2 a) and b) show the results for two aliquots with a waiting time of 10 min and 30 d, respectively. The second RF measurement (step 4) was shifted to a start time of 2,000 s to see the effect of the storage. The vertical line indicates the waiting event and different line types indicate different measured aliquots. A summary of all carried out storage experiments is given in Fig. 8.3. The ratio (after background subtraction) of the first channel of step 4 to the last channel of measurement step 2 is taken as indicator of the storage time. The value on the y-axis (recuperation) in Fig. 8.3 is then calculated via  $1 - ratio$ . Hence, a value of 0 % indicates that the signal before and after the waiting time is identical (0 % recuperation). Figure 8.1 shows the same data as presented in Fig. 8.2 (b) but just for one aliquot and with a normalised y-axis. A fitting of the RF curve before storage was executed, identical to the procedure given in

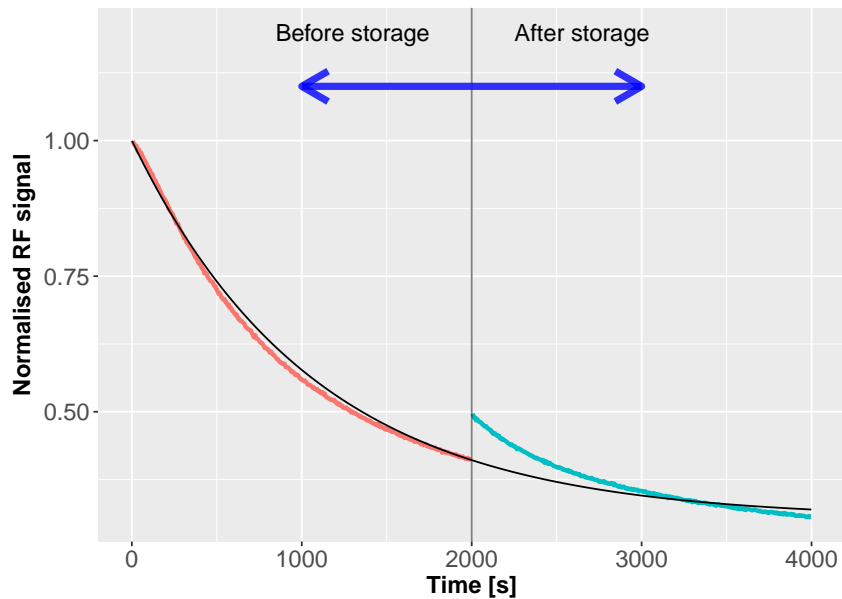
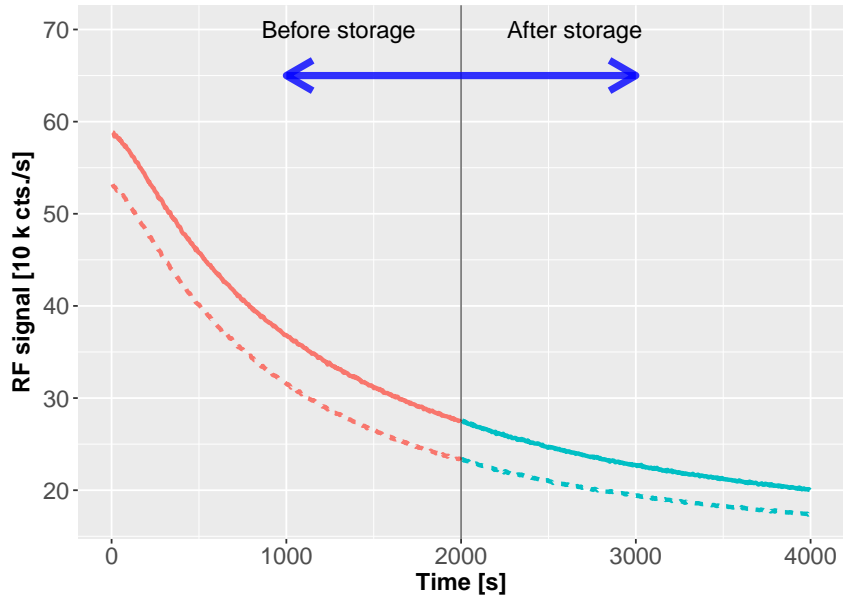


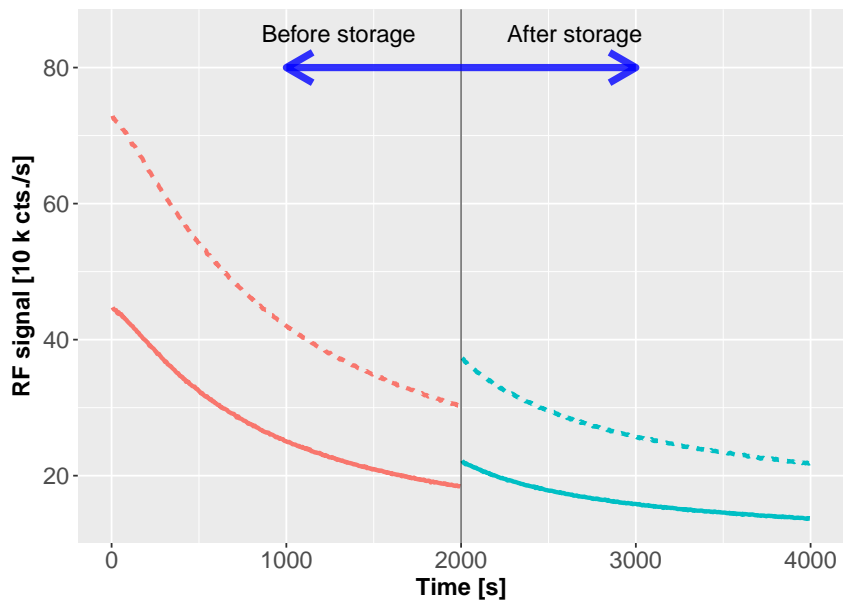
**Figure 8.1:** Result for sample FB1A for 30 d waiting with normalised y-axis and just one aliquot. The black line indicates the fit for the RF curve before storage but extended to the complete x-axis.

Ch. 4 and 5. The fitting parameters were calculated, and the fitting curve calculated but for the complete x-axis from 0 to 4,000 s. The results show that the first channels of the RF curve after storage show a higher intensity, but the tail of the curves overlap with the fitted curve.

The results from Fig. 8.3 suggest that even after 30 d storage the recuperation of the quartz UV-RF signal is still increasing. In the framework of the energy band model, a possible interpretation could be the migration of holes from the R- to L-centres due to a thermal release of holes at room temperature. In contrast to that is the finding, that released holes are preferable moving into R-centres than L-centres (see parameters  $A_6$  and  $A_8$  in the model published by Bailey (2001)). Following this line of argumentation, most freed holes are getting re-trapped into the R-centre. Further measurements with different quartz samples and different absorbed doses in measurement step 2) are necessary to obtain a consistent model for this kind of recuperation effect.



(a) 10 min



(b) 30 d

**Figure 8.2:** Result for sample FB1A for 10 min (a) and 30 d (b) waiting, respectively. The vertical line indicates the waiting event and different line types indicate different measured aliquots.

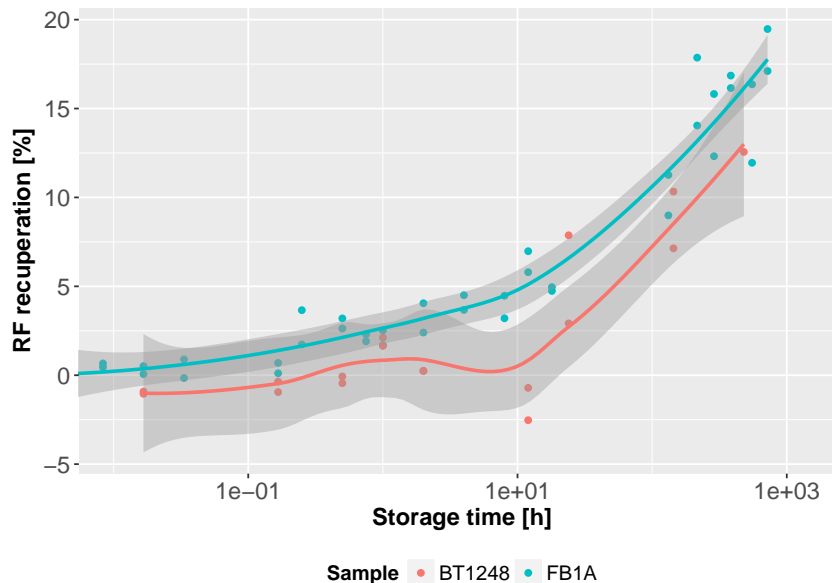


**Figure 8.3:** All measured storage times of sample BT1248 and FB1A against the recuperated UV-RF signal. The grey shaded area is the 95 % confidence level interval.

## 8.2 Determining absorbed doses with UV-RF

The basic idea for using the UV-RF signal for dose determination is given in Ch. 5. A detailed measurement protocol and further measurements will be given here. Two observations were important developing the idea of using UV-RF as dose determination:

- The UV-RF signal can be reset by preheating to 500 °C (see Ch. 3)
- The independency of the UV-RF signal characteristics on dose rate (see Ch. 5)

### 8.2.1 Measurement protocol

The basic idea of the method is that a quartz sample received a dose (in nature or in laboratory). After sample preparation in the laboratory, the *natural signal* is recorded by an RF measurement at room temperature. Afterwards, a preheat to 500 °C is executed to reset the UV-RF signal. The last step is to record the *regenerated signal*. To calculate an equivalent dose, the natural signal is horizontally translated onto the regenerated dose axis until it overlaps the regenerated signal. The length of the sliding along the x-axis is taken as the equivalent dose. This technique is used in IR-RF dating, e.g., Buylaert et al. (2012) and Frouin et al. (2015). Note the necessity that the quartz was heated before (e.g., ceramics, heated lithics, volcanic or volcanically heated rocks). Otherwise a decreasing UV-RF signal can not be guaranteed and the method may fail.

To test the basic idea of the technique, the measurement sequence in Table 8.1 was applied to different quartz samples. Note that the natural absorbed dose was mimicked in these experiments in order to know the exact absorbed dose. The dose rate of the source was  $\sim 0.06 \text{ Gy s}^{-1}$ , so 1 ks irradiation is  $\sim 60 \text{ Gy}$ .

STEP	DESCRIPTION	EXPLANATION
1	Preheat to 500 °C for 120 s and RF at RT for 2 ks (5 times)	Signal stabilisation
2	Preheat to 500 °C for 120 s	
3	RF at RT for different time ( $RF_{\text{dose}}$ )	Mimic natural irradiation
4	Pause (1 h at maintenance position)	
5	RF for 2 ks ( $RF_{\text{lab}}$ )	Natural signal
6	Preheat to 500 °C for 120 s	Signal reset
7	RF at RT for 10 ks ( $RF_{\text{reg}}$ )	Regenerated signal

**Table 8.1:** Protocol for dose recovery with UV-RF.

To calculate the equivalent dose the **R**-function `analyse_IRSAR.RF()` from the **R**-package *Luminescence* was used (Kreutzer et al. 2012, 2018). The function calculates the best fit by searching for the minimum of the squared residuals. It is also possible to set a vertical sliding range which compensates for sensitivity changes during the measurement steps and also to set the minimum and maximum channel range for the natural signal. This is important, because the study from Sec. 8.1 showed that the tail of the  $RF_{\text{lab}}$  fits into the virtual extension of the  $RF_{\text{dose}}$  curve. Hence, the hope is to obtain better results choosing the end of the  $RF_{\text{lab}}$  curve for the fitting procedure. Figure 8.4 visualises the described method for quartz sample FB1A, given a dose of 1 ks ( $RF_{\text{dose}}$ ). Afterwards, the signal  $RF_{\text{lab}}$  was recorded, which is the analogue to the *natural signal* in IR-RF dose determination. The signal  $RF_{\text{reg}}$  is recorded after annealing the sample to 500 °C for 120 s (step 6 in Table 8.1). It is important to notice, that the dose absorbed through the signal  $RF_{\text{dose}}$  is the dose to recover. In Fig. 8.4 the signal  $RF_{\text{lab}}$  was shifted 1 ks to the right. In a more real application the  $RF_{\text{dose}}$  signal is unknown but for a first test this signal can be interpreted as an artificial dose, similar to a dose-recovery test in the OSL technique. Calculating the equivalent dose with `analyse_IRSAR.RF()` results in Fig. 8.5. As can be guessed from Fig. 8.4, a x-axis shift of 1 ks will not perfect fit the regenerated curve and the calculated equivalent dose  $D_e$  of  $930 \pm 2$  s confirms this finding. Further experiments with this technique were conducted and several parameters changed:

- Changing the given dose to recover ( $RF_{\text{dose}}$ )
- Considering the channel range of the  $RF_{\text{lab}}$  signal to calculate the  $D_e$
- Test different quartz samples

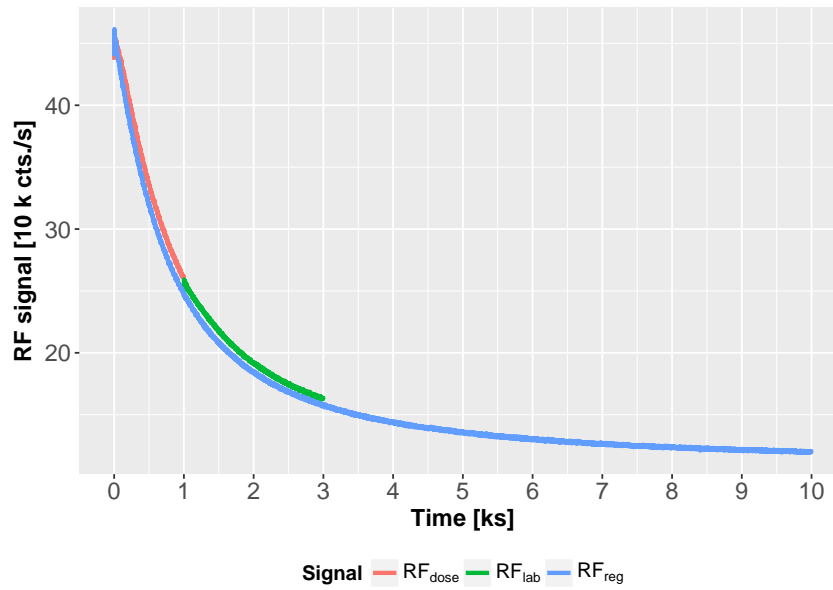


**Figure 8.4:** Example of the used dose determination technique. For explanations see text.

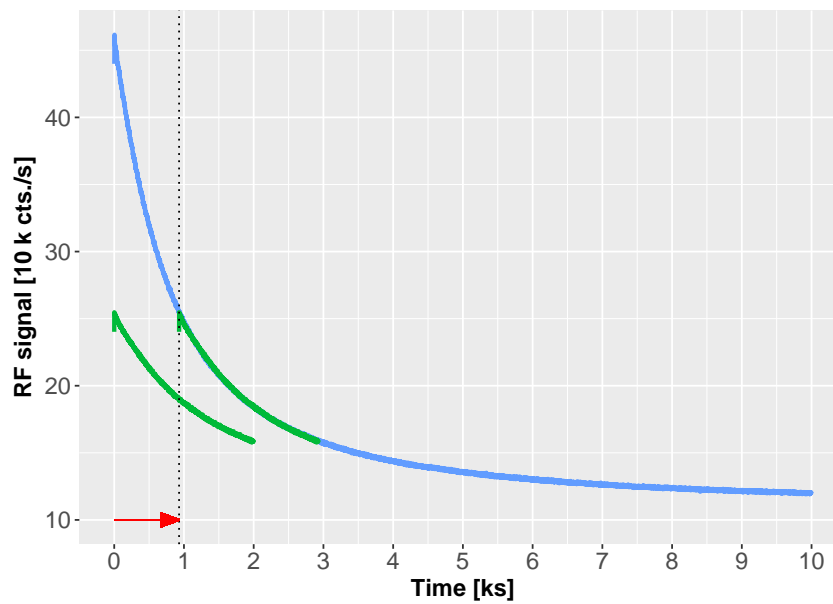


**Figure 8.5:** Procedure of curve shifting of RF<sub>lab</sub> onto the RF<sub>reg</sub> signal. The given dose of 1 ks was underestimated because the best fit results in  $930 \pm 2$  s.

### 8.2.2 Dose recovery tests

For testing the measurement protocol proposed above four different quartz samples were taken: (a) BT586, (b) FB1A, (c) BT1248, and (d) Hyaline. All these quartzes were already investigated in former studies, see Table 1.4.

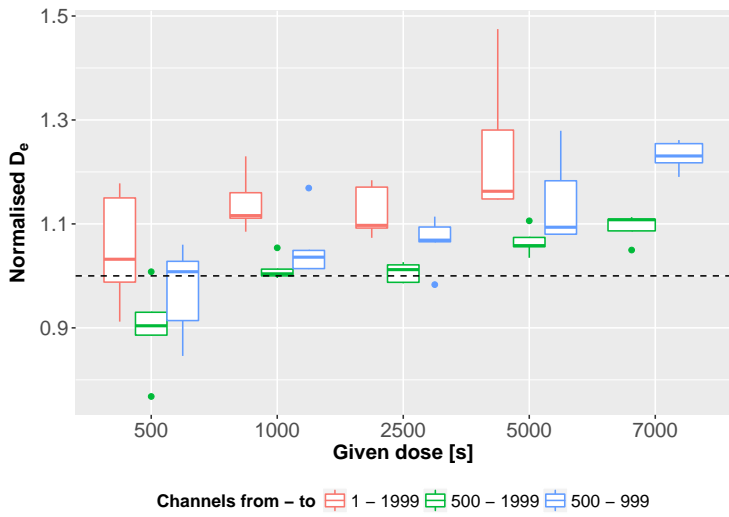
Five aliquots per given dose were used and the measurement protocol was the one given in Table 8.1. Figure 8.6 gives an overview about the results obtained from these experiments and the results can be summarised as follows:

- The error calculated with `analyse_IRSAR.RF()` is very small due to the huge amount of data points available. The error is never greater than  $\pm 8$  s.
- All quartz samples behave very differently and hence individual summaries are given:
- BT586
  - Using the complete channel range always yields the highest mean value and the highest scatter.
  - Calculating  $D_e$  with a channel range from 500 – 1,999 always results in the lowest values.
  - Absorbed doses of 1,000 s and 2,000 s are recovered in a good manner by removing the first 499 channels.
  - Smaller doses ( $< 5,000$  s) show better results than bigger doses, but this depends on the channel range used.
- FB1A
  - The given dose is always underestimated, except for one outlier at 5000 s.
  - No clear trend between different used channel ranges is observable.
- BT1248
  - Doses up to 2,500 s can be recovered with less than 5% deviation.
  - Doses higher than 2,500 s are systematically underestimated.
  - The channel range from 500 – 999 has the highest scatter in all measurements.
- Hyaline
  - The inter-aliquot scatter is low in this sample.
  - Doses up to 1,000 s are overestimated and higher doses are underestimated.
  - No clear trend concerning the channel ranges is observable.

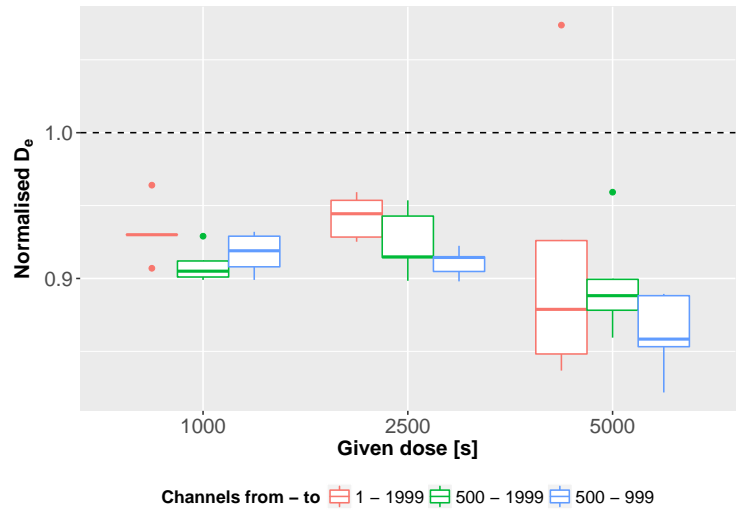
These results show that the presented protocol is able to recover absorbed doses in quartz using UV-RF. Of course there are many factors influencing the results and these factors have to be analysed in future studies. One point to consider for more accurate results is the more precise determination of the best channel range to use. Another one is the length of the annealing after the  $RF_{lab}$  signal. In this study 120 s were used but further tests have to show what the best annealing time for every sample is.

Brik et al. (1994) and Marazuev et al. (1995) also published a method determining absorbed doses with UV-RF but their main idea was to use the signal intensity at the begin of the UV-RF decay. They successfully recovered doses in the range of 1 – 10 Gy from natural quartz with UV-RF. Nevertheless, further investigations were never published. They performed an extrapolation to obtain the absorbed dose, similar to the pre-dose technique (Bailiff 1994). Own measurements were not able to verify the findings by Marazuev et al. (1995). The linearity for small doses was confirmed but the extrapolated doses were far off compared with single-aliquot regenerative-dose (SAR) measurements. Nevertheless, our simulations in Ch. 3 also showed the dependency of absorbed dose to the initial signal in quartz UV-RF.

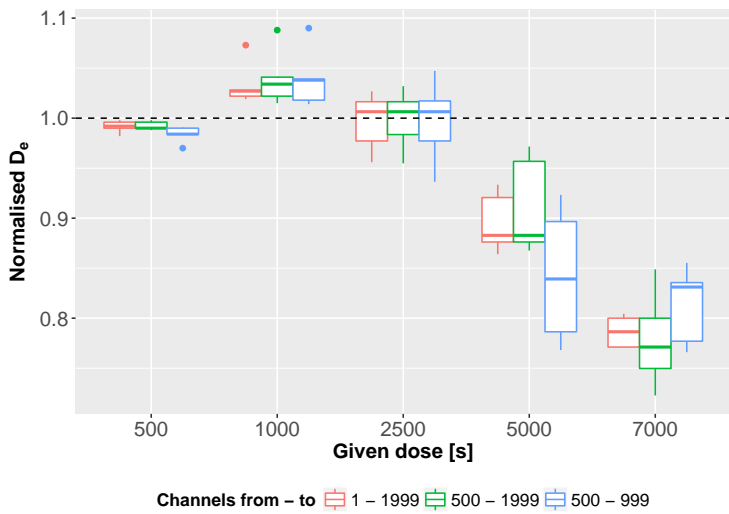
With the new approach presented here no interpolation is needed and the accuracy of the sliding technique is much higher. Furthermore, we used one aliquot to calculate a  $D_e$  and sensitivity changes are compensated with the vertical sliding option within the **R**-function `analyse_IRSAR.RF()`.



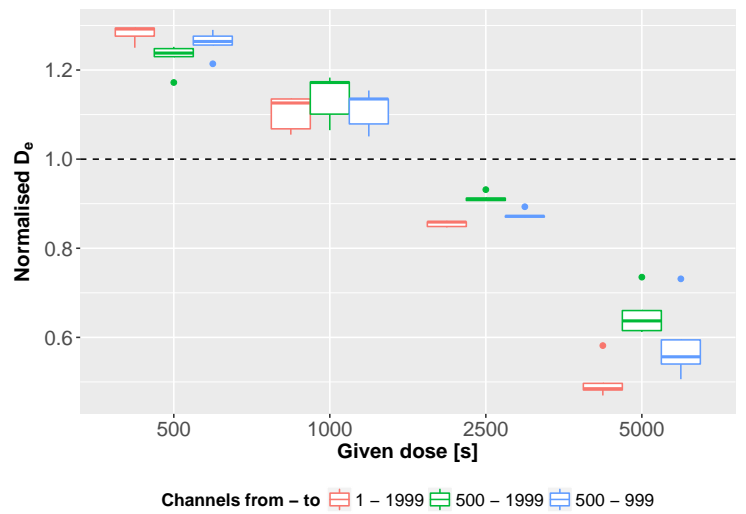
(a) BT586



(b) FB1A



(c) BT1248



(d) Hyaline

**Figure 8.6:** Boxplot of a dose-recovery-test with UV-RF for quartz sample (a) BT586, (b) FB1A, (c) BT1248, and (d) Hyaline. For every measurement 5 aliquots were used. Different colours identify different used channel ranges to calculate the equivalent dose  $D_e$ .

## 8.3 Inverse modelling

Models, such as quartz luminescence models, depend on constant parameters, many of which are poorly known and cannot be measured. Thus, one essential step in the process of model development is model calibration, during which these parameters are estimated by fitting the model to experimental data. The process of fitting a model to experimental data is known as *inverse modelling* (Soetaert & Petzoldt 2010). Many model equations are generally non-linear and so parameter estimation constitutes a non-linear optimization problem. The aim of the inverse modelling approach is to find parameters minimising a measure of badness of fit.

Inverse modelling is wide spread in hydrological modelling (see, e.g., Franssen et al. 2009) but was (to the best knowledge of the author) less used in luminescence modelling, except, e.g., in Adamiec et al. (2004, 2006). Knowing the most sensitive parameters of a model is of crucial importance for adjusting the model parameters. Hence, in this section (I) the influence of different parameters on luminescence signals (Sec. 8.3.1) and (II) the results by fitting these parameters to experimental data are investigated (Sec. 8.3.2).

### 8.3.1 Sensitivity analysis of quartz luminescence simulations

Saltelli et al. (2004) give a definition of sensitivity analysis:

The study of how uncertainty in the output of a model (numerical or otherwise) can be apportioned to different sources of uncertainty in the model input.

Different kinds of sensitivity analysis exist: a global sensitivity analysis and a local sensitivity analysis, which are explained in the following subsections and they will be helpful to estimate parameters most influencing the model output.

#### 8.3.1.1 Global sensitivity analysis

In global sensitivity analysis certain parameters are changed over a large range and the effect on certain model output variables assessed (Soetaert & Petzoldt 2010). In the case of luminescence models the model output variable normally belongs to the luminescence signal or the concentrations of certain energy levels. Global sensitivity analysis is a tool for obtaining an insight into the behaviour of the differential equations for varying different parameters of the model.

Figure 8.7 shows a global sensitivity analysis for parameter  $E$  over a range from 0.87 eV to 1.07 eV. 50 runs of the model were executed, each run with a different value for  $E$ . So with only varying the trap depth parameter  $E$  a wide range of different TL curves can be expected.

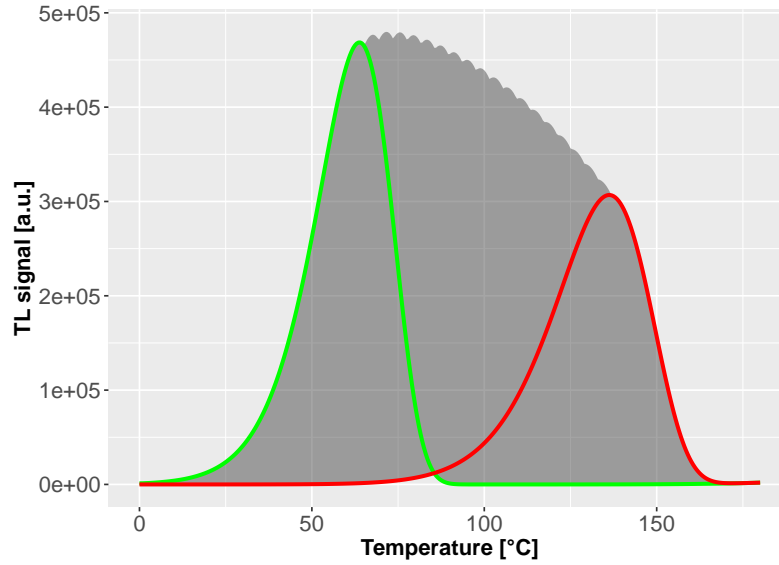


**Figure 8.7:** Global sensitivity analysis of a TL signal for  $E$  in the range between  $\pm 0.1$  eV around its nominal value of 0.97 eV. Marked are the TL curves belonging to the smallest and highest value of  $E$  (green: 0.87 eV; red: 1.07 eV).

### 8.3.1.2 Local sensitivity analysis

In local sensitivity, the effect of a parameter value in a very small region near its nominal value is estimated (Soetaert & Petzoldt 2010). In this context a perturbation of  $+1$  E-08 is used. The dimensionless value *sensitivity* of model output to a specific parameter is calculated via

$$\frac{\partial y}{\partial \Theta} \cdot \frac{w_{\Theta}}{w_y} \quad (8.1)$$

In term (8.1)  $y$  is an output variable (e.g. TL signal),  $\Theta$  is the parameter to be investigated,  $w_y$  is the scaling of variable  $y$  and  $w_{\Theta}$  is the scaling of parameter  $\Theta$ , usually equal to the parameter value (Soetaert & Petzoldt 2010). Equation 8.1 defines the sensitivity as the (weighted) local gradient in the direction of the parameter. An explanation for a sensitivity analysis of a simulated TL signal to parameter  $E$  is given in Fig. 8.8. Here a perturbation of  $+0.005$  eV was chosen to illustrate a sensitivity analysis. The TL peak for  $E = 0.975$  eV is shifted towards higher temperatures. But this implies that for the same value on the x-axis, e.g., 100 °C, the TL signal intensity is decreasing. In contrast to that, for temperatures higher than the intersection of both signals an increase in TL intensity takes place. With this kind of analysis it is possible to identify parameters that influence the output value most. These parameters have a higher absolute sensitivity value. As it makes no sense to fine-tune parameters that have little effect, this ranking serves to choose candidate parameters for model fitting (Soetaert & Petzoldt 2010). Figure 8.9 shows a sensitivity analysis of two parameters,  $E$  and  $s$ . Other parameter have been ignored because they do not have a high impact to the simulated TL curve compared to  $E$  and  $s$ .

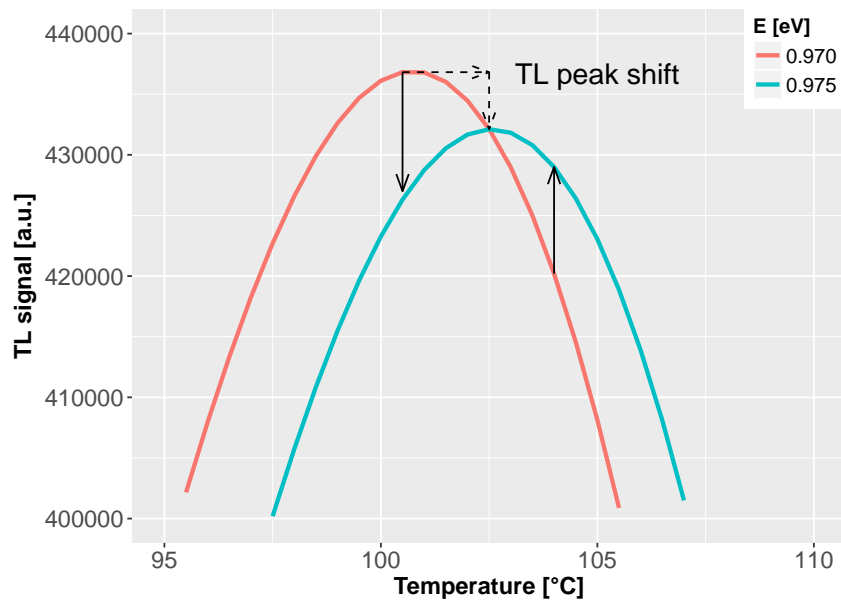


**Figure 8.8:** Explanation of a TL sensitivity analysis. Two simulated TL peaks with values of 0.970 and 0.975 eV for  $E$ , respectively.

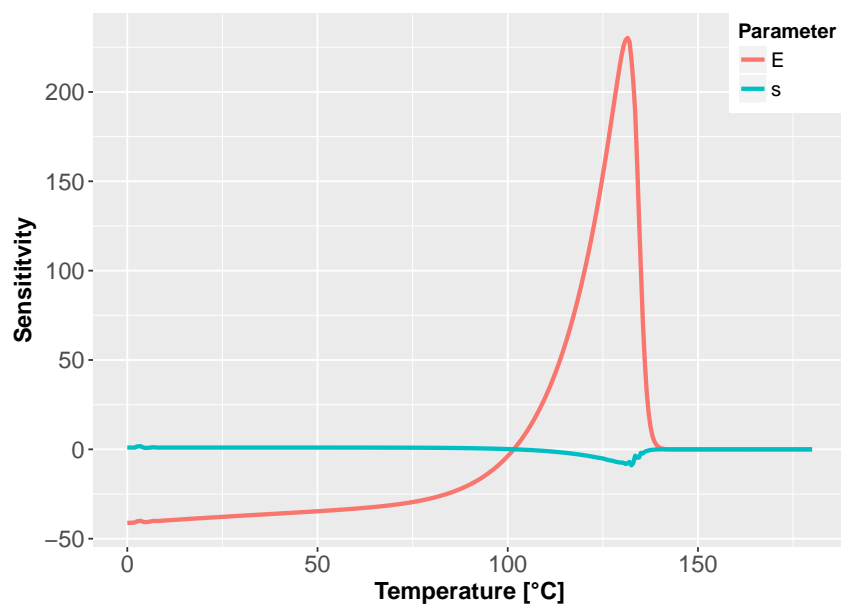


**Figure 8.9:** Sensitivity analysis of a TL simulation with parameters by Bailey (2001) for the 110 °C TL peak. The higher the absolute value at the y-axis, the higher the influence to the model output.

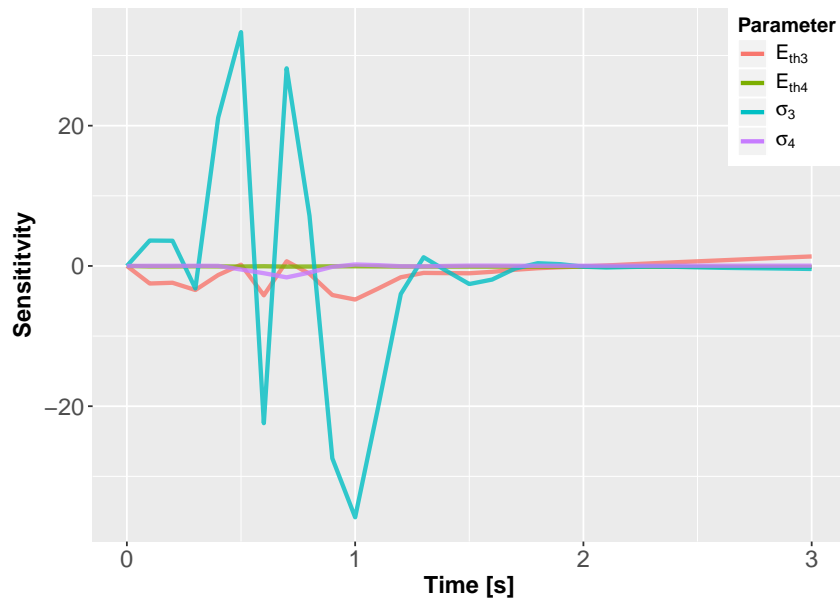


**Figure 8.10:** Sensitivity analysis of a OSL simulation with parameters by Bailey (2001) for the optical active traps level 3 and 4 and the corresponding parameters for thermal assistance energy  $E_{th}$  and photoionisation cross-section  $\sigma$ , see Ch. 1.4 and 1.6.

### 8.3.2 Finding appropriate model parameters

After finding parameters with most influence on luminescence signals with sensitivity analysis, the inverse modelling method can be executed with these parameters. For demonstrating the inverse modelling technique an open access dataset published by Schmidt et al. (2018)<sup>1</sup> was used to fit the model parameters published by Bailey (2001) to these experimental data. The data set *FB\_Mastersequence\_150.BIN* was used and the applied sequence was a TL measurement with a heating rate of  $1 \text{ K s}^{-1}$  subsequent to irradiating 1 Gy at room temperature. This sequence was simulated and the TL measurement was fitted to the model parameters  $E$  and  $s$  for level 1, the energy level corresponding to the  $110^\circ\text{C}$  TL peak. Figure 8.11 shows three different signals: (I) The experimental data (red), (II) the simulation with the new calculated parameters for  $E$  and  $s$  (green), and (III) the simulation with the original parameters by Bailey (2001) (blue). In Table 8.2 the new parameters used to simulate the results from Fig. 8.11 are listed. All other parameters in the model by Bailey (2001) were kept constant and just  $E_1$  and  $s_1$  have been changed. The results indeed indicate a better accordance than the standard parameters by Bailey (2001). However, it is possible that multiple combinations of  $E$  and  $s$  lead to the same TL curve. Nevertheless, further peak shape calculations were performed to obtain also values for  $E$  and  $s$ . The **R**-package *tgcd* (Peng et al. 2016) is able to automatically calculate glow curve parameters from an general-order empirical expression of Eq. (1.12) (see also Pagonis et al. (2006)).

<sup>1</sup><https://ecl.earthchem.org/view.php?id=1095>

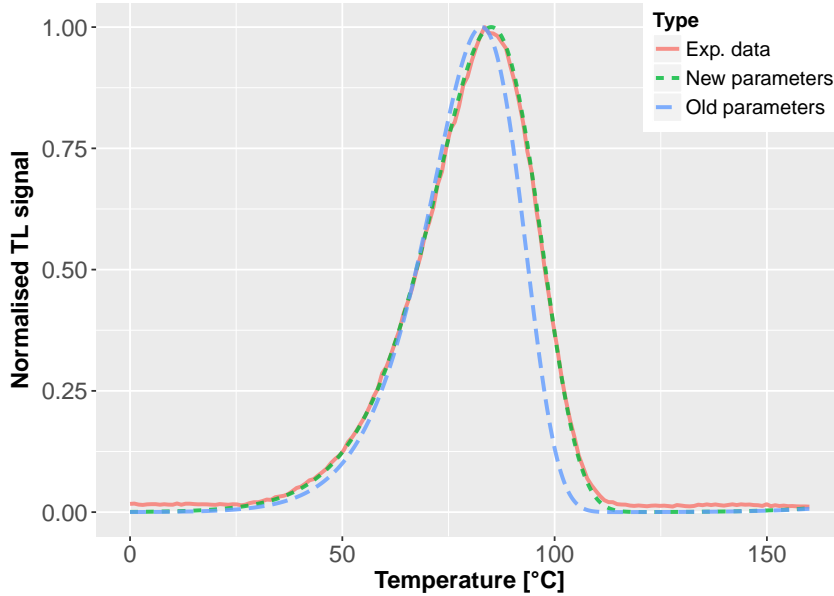


**Figure 8.11:** Result of the inverse modelling method for the 110 °C TL peak. Three different signals are shown: (I) The experimental data (red), (II) the simulation with the new calculated parameters for  $E$  and  $s$  (green, see Table 8.2), and (III) the simulation with the original parameters by Bailey (2001) (blue).

The results are comparable with the values obtained by the inverse modelling technique (Table 8.2). To further test the inverse modelling technique experimentally obtained OSL signals were fitted to OSL related parameters. The experimental OSL data has been taken from the **R**-package *Luminescence*, example data set *CWOSL.SAR.Data* and it is the natural signal of the SAR measurement given in these example data set (Kreutzer et al. 2018).

Parameters  $E_{th3}$  and  $\sigma_3$  (corresponding to the  $OSL_{fast}$  component) have most influence on the simulated OSL signals (Fig. 8.10). The results of the inverse modelling technique are shown in Table 8.2 and indicate a significant higher value of the photoionisation cross-section  $\sigma$ . This was expected because the experimental data show a much faster decay of the OSL signal than the initial parameters by Bailey (2001). The new parameters are able to mimic this behaviour in a good manner, see Fig. 8.12.

STIMULATION	PARAMETER	OLD VALUE	NEW VALUE	TGCD PACKAGE
TL	$E_1$ [eV]	0.97	0.85	0.85
TL	$s_1$ [ $s^{-1}$ ]	5.0 E+12	7.1 E+10	6.2 E+10
OSL	$E_{th3}$ [eV]	0.10	0.03	-*
OSL	$\sigma_3$ [ $s^{-1}$ ]	6.0	13.0	-*

**Table 8.2:** Change of parameter values before and after inverse modelling for TL and OSL simulations. The corresponding TL and OSL curves are given in Figs. 8.11 and 8.12. \*: The *tgcd* package is able to calculate glow curve parameters from TL, but not from OSL curves.

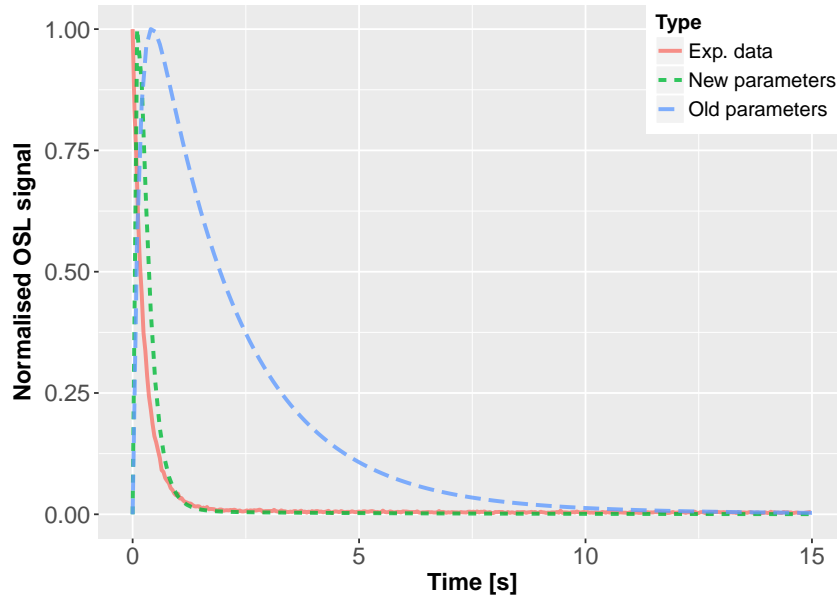


**Figure 8.12:** Result of the inverse modelling method for a natural OSL curve. Three different signals are shown: (I) The experimental data (red), (II) the simulation with the new calculated parameters for  $E$  and  $s$  (green, see Table 8.2), and (III) the simulation with the original parameters by Bailey (2001) (blue).

### 8.3.3 Software and integration

All presented analysis tools (global and local sensitivity, parameter determination with inverse modelling) are integrated in the **R**-package *RLumModel*, version 0.3.0. The core of the analyses is the **R**-package *FME* (Soetaert & Petzoldt 2010), which provides all necessary functions performing these analyses and is automatically loaded when starting *RLumModel*. In the following some examples demonstrate the usage of the package *RLumModel* to calculate the local sensitivity analysis presented in Fig. 8.9. For an introduction to *RLumModel* see Ch. 2.

```

1 library("RLumModel")
2
3 sequence <- list(
4   IRR = c(20, 10, 1),
5   TL = c(0, 180, 5))
6
7 model <- "Bailey2001"
8
9 parms <- extract_parameters2FME(model = model)
10
11 func_FME <- fit_RLumModel2data(
12   sequence = sequence,
13   model = model,
14   seq.step2fit = 2,
15   norm = FALSE)
16

```

```
17 local_sens <- FME::sensFun(func = func_FME,  
18                             parms = parms,  
19                             senspar = c("E1", "s1"))  
20  
21 plot(local_sens)
```

The code above simulates the given sequence from line 3 to 5: This sequence describes an irradiation at 20 °C with a dose of 10 Gy and a dose rate of 1 Gy s<sup>-1</sup>, which is followed by TL simulation from 0 °C to 180 °C with a heating rate of 5 °C s<sup>-1</sup>. Line 11 is the most important part of the analysis because a function named `func_FME()` is created which is compatible with functions provided by *FME*, e.g., `FME::sensFun()` in line 17. The argument `seq.step2fit` in line 14 is needed to submit that the second sequence step from the sequence will be analysed: the TL readout. Function `FME::sensFun()` is able to calculate the local sensitivity for parameters given in the argument `senspar`. In the case presented above the parameters  $E$  and  $s$  for the first energy level (the 110 °C TL peak) are needed. Note that further parameters can be submitted here, e.g., `senspar = c("E1", "s1", "A1")` for analysing the impact of the conduction band to electron trap probability of level 1 to the TL signal. Further examples are given in the help files of the **R**-package.

### 8.3.4 Conclusion

The method of inverse modelling is known in many different research areas but was not used in luminescence modelling until now. The advantage of this method is that experimental data can be used to calibrate luminescence models and find the most appropriate set of parameters for most of the measurements done in luminescence. Once found these parameters, the process of *forward modelling* can be started: using the model for forecasting and hypothesis testing.

With respect to luminescence modelling the advantage of this method is that in contrast to other parameter estimation methods, the kinetic order of the process plays no role. Due to the fact that the range of used electron traps and recombination centres can be set by the user, the retrapping is calculated by the interaction of the system via ODEs and is not fixed. Nevertheless, already Bräunlich et al. (1979) mentioned:

... it is extremely difficult to correlate by curve fitting alone, theory and experiment with any degree of confidence. Any measured and well-resolved glow peak that may reasonably be expected to be due to a single type of traps can be fitted with a solution of the single trap model by appropriately adjusting several out of a set of many model parameters.

So although the calculated parameters by inverse modelling and other techniques are comparable, different sets of parameters can lead to the same result. It is possible that non (physical) meaningful parameters are also solutions to the equations calculated by different methods because they mathematically solve the corresponding equations. A lot of care must be taken interpreting the results of fitting methods of physical problems.

## 8.4 Monte-Carlo simulations of RF

Monte-Carlo methods play an important role in statistical physics and during recent years their successful adaptation to luminescence phenomena like TL and OSL were performed by Mandowski & Świątek (1992, 1994, 1996, 1998), Mandowski (2002), Pagonis et al. (2014), Pagonis & Chen (2015), and Pagonis & Kulp (2017). The necessity of using Monte-Carlo methods in luminescence description is due to the existence of electron-hole pairs trapped close to each other and the assumption of a uniform spatial distribution of electron traps and centres does not hold (Chen et al. 2011). This is especially expected in materials with polycrystalline and low-dimensional structures, as well as in materials which underwent high dose irradiations and hence a creation of groups of defects (Chen et al. 2011; Pagonis et al. 2014).

All publications concerning luminescence and Monte-Carlo methods describe TL and/or OSL signals but no RF phenomena. The difference between these stimulation types is the availability of electrons and holes within the system. In TL/OSL simulations the existing number of electrons and holes stays stable or decreases with time, depending on whether a recombination occurs or not. In contrast to that, during RF the number of electrons and holes in the system can increase (capturing of electrons and holes in traps and holes, respectively), stay stable (recombination of electron and hole) or decrease (no electron-hole pair created, but a recombination occurred). These different mechanisms support the fact that other algorithms and approaches are needed to describe RF with the Monte-Carlo approach than published for TL or OSL until now.

### 8.4.1 Basics of Monte-Carlo simulations

For a general introduction in Monte-Carlo simulations see standard textbooks of statistical physics, e.g., Landau & Binder (2014). For an introduction into TL/OSL simulations using Monte-Carlo methods see Kulkarni (1994), Mandowski & Świątek (1992), and Pagonis et al. (2014). When simulating RF, a constant number of electron-hole-pairs are created during each time step. Each electron has a certain probability to either (I) get trapped in an electron trap, (II) recombine radiative with a L-centre or (III) recombine non-radiative with a R- or K-centre. Each hole created can move to all existing hole centres (R-, K- and L-centres). When considering the model presented in Fig. 4.1 with one electron trap, one R-centre and one L-centre and using the abbreviations mentioned in Ch. 4.2, the probability for each of the processes mentioned above is:

1. Electron recombining non-radiative with R-centre:

$$p_{1e} = \frac{B_1 \cdot m_1}{B_1 \cdot m_1 + B_2 \cdot m_2 + A_1 \cdot (N - n)} \quad (8.2)$$

2. Electron recombining radiative with L-centre

$$p_{2_e} = \frac{B_2 \cdot m_2}{B_1 \cdot m_1 + B_2 \cdot m_2 + A_1 \cdot (N - n)} \quad (8.3)$$

3. Electron gets trapped in an electron trap:

$$p_{3_e} = \frac{A_1 \cdot (N - n)}{B_1 \cdot m_1 + B_2 \cdot m_2 + A_1 \cdot (N - n)} \quad (8.4)$$

Analogous the probabilities for holes moving into R- or L-centres:

1. Trapping in R-centre:

$$p_{1_h} = \frac{(M_1 - m_1) \cdot A_{m_1}}{(M_1 - m_1) \cdot A_{m_1} + (M_2 - m_2) \cdot A_{m_2}} \quad (8.5)$$

2. Trapping in L-centre

$$p_{2_h} = \frac{(M_2 - m_2) \cdot A_{m_2}}{(M_1 - m_1) \cdot A_{m_1} + (M_2 - m_2) \cdot A_{m_2}} \quad (8.6)$$

Assuming that the concentrations at  $t = 0$  are  $n_0$ ,  $m_{1_0}$ , and  $m_{2_0}$ , during each timestep the following calculations are performed in Monte-Carlo simulation:

1.  $R$  electrons can be trapped or recombine, respectively.
2. For each of the  $R$  electrons  $p_{1_e}$ ,  $p_{2_e}$ , and  $p_{3_e}$  are calculated
  - Choose a random number  $r_e$  between 0 and 1
  - If  $r_e < p_{1_e}$ : recombination in R-centre (no signal):  $m_1 \rightarrow m_1 - 1$
  - If  $p_{1_e} < r_e < p_{1_e} + p_{2_e}$ : recombination in L-centre (signal):  $m_2 \rightarrow m_2 - 1$
  - If  $p_{1_e} + p_{2_e} < r_e$ : Trapping in electron trap (no signal):  $n \rightarrow n + 1$
3. For each of the  $R$  created holes calculate  $p_{1_h}$  and  $p_{2_h}$ 
  - Choose a random number  $r_h$  between 0 and 1
  - If  $r_h < p_{1_h}$ : Trapping of hole in R-centre:  $m_1 \rightarrow m_1 + 1$
  - Else: Trapping of hole in L-centre:  $m_2 \rightarrow m_2 + 1$
4. Go to the next timestep and repeat steps 1 – 4 until expected simulation time is reached.

Note that in Eq. (8.2) – (8.6) no concentration of the conduction or valence band appears.

The probability of trapping/recombination into the  $i$ -th trap is, in general:

$$p_{i_{e/h}} = \frac{\alpha_i \cdot V_i}{\sum_{j=1}^m \alpha_j \cdot V_j} \quad (8.7)$$

$\alpha_i$  is the trapping/recombination coefficient of the  $i$ -th trap and  $V_i$  is the density of vacancies (Kulkarni 1994). So the system of electron traps and hole centres can be expanded to any need. In the following the case of one electron trap and two recombination centres will be discussed in detail.

The process described above can now happen in separate systems, called *clusters*. Every cluster consists of a system of charge carriers, in the example above one electron trap, one R- and one L-centre, see Fig. 8.13. During the simulation the state in the cluster can change, according to the schema given above. The number of clusters is variable but the higher the number, the lower the statistical error (Pagonis et al. 2014). Figure 8.13 shows the situation for a cluster, where three electron-hole pairs are available. The electrons are captured in the only available electron trap (4 available, 3 filled) and the holes are located in R-centres (3 available, 2 filled) and L-centres (3 available, 1 filled).

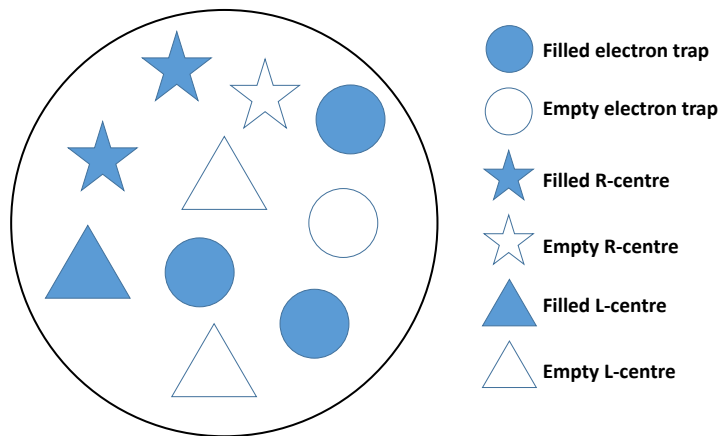


**Figure 8.13:** Example state of a cluster in the Monte-Carlo simulation of RF.

### 8.4.2 Performing Monte-Carlo simulations

Following Kulkarni (1994) and Mandowski & Świątek (1994), the following relation must be established:

$$\chi n, \chi m_1, \chi m_2, \chi N, \chi M_1, \chi M_2, \chi R \rightarrow \bar{n}, \bar{m}_1, \bar{m}_2, \bar{N}, \bar{M}_1, \bar{M}_2, \bar{R} \quad (8.8)$$

$$A_1/\chi, A_{m_1}/\chi, A_{m_2}/\chi, B_1/\chi, B_2/\chi \rightarrow \bar{A}_1, \bar{A}_{m_1}, \bar{A}_{m_2}, \bar{B}_1, \bar{B}_2 \quad (8.9)$$

$\chi$  stands for a constant having the dimension of a volume, see Mandowski & Świątek (1994).  $\bar{n}, \bar{m}_1, \bar{m}_2, \bar{N}, \bar{M}_1, \bar{M}_2$  have the meanings of absolute numbers of traps/centres and  $\bar{A}_1, \bar{A}_{m_1}, \bar{A}_{m_2}, \bar{B}_1, \bar{B}_2$  are the trapping and recombination probabilities in hole centres and the electron trap, respectively. The dashed parameters are used in the Monte-Carlo simulations. In contrast to earlier simulations of luminescence phenomena with Monte-Carlo methods, the electron-hole production-rate  $R$  also has to be changed by a factor  $\chi$ . From a physical point of view  $R$  has to be an integer number, because in a single cluster only an integer number of electron and holes can be available. The following Monte-Carlo simulations were conducted with the parameters in Table 8.3 and the maximum value for  $\chi$  is  $\frac{1}{3}$  E-05. The initial values for the energy levels are:  $m_{10} = 0$ ,  $m_{20} = 5$  E+10 and  $n_0 = 5$  E+10 to mimic an annealed quartz sample where all holes are located in the L-centre ( $M_2$ ). The RF signal is calculated by electrons recombining into this energy level.

PARAMETER	VALUE	UNIT
$\bar{A}_n$	1 E-10	s <sup>-1</sup>
$\bar{B}_1$	5 E-09	s <sup>-1</sup>
$\bar{B}_2$	1 E-10	s <sup>-1</sup>
$\bar{A}_{m_1}$	5 E-07	s <sup>-1</sup>
$\bar{A}_{m_2}$	1 E-09	s <sup>-1</sup>
$\bar{M}_1$	3 E+09	
$\bar{M}_2$	1 E+11	
$\bar{N}$	5 E+10	
$\bar{R}$	3 E+05	s <sup>-1</sup>

**Table 8.3:** Used parameters for the Monte-Carlo simulation of quartz UV-RF.

Figure 8.14 (a) shows three different cases for  $\chi$ :  $\frac{1}{3}$  E-03,  $\frac{1}{3}$  E-04, and  $\frac{1}{3}$  E-05. This corresponds to a total number of simulated electron-hole pairs per second from 100, 10 and 1, respectively. The number of calculated clusters was 100, 1,000, and 10,000, respectively. So the total number of simulated electron-hole pairs keeps constant. The coloured lines indicate the average signal of all simulated clusters and the grey area indicates the minimum and maximum RF signal from all clusters per timestep. Subfigure (b) shows the sum of all signals simulated in all clusters for every value of  $\chi$ . The y-axis is the same for all simulated cases of 100, 1,000, and 10,000 clusters. The cumulated signal for all analysed

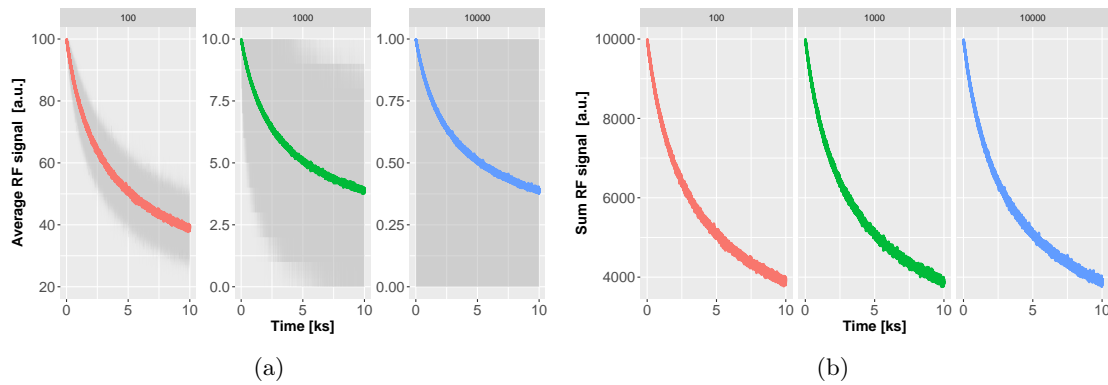


**Figure 8.14:** Results of Monte-Carlo simulations for different numbers of clusters. Subfigure a) shows the behaviour for a different number of clusters. The total number of simulated electron-hole creations was the same for all calculations. Subfigure b) shows the total number of RF signal as sum of all clusters.

cases is comparable and shows minimal difference coming from the stochastic nature of the simulations.

To further test the performance of the Monte-Carlo approach the experimental results from Ch. 5 were tried to simulate. So again Monte-Carlo simulations for the parameters in Table 8.3 were conducted and the value for the electron-hole production-rate (or: dose rate) was kept variable from  $30 - 30,000 \text{ s}^{-1}$ . The expectation is that the same as already mentioned in Ch. 5: The signal intensity of the simulated RF signal grows linearly with the dose rate. Furthermore, the initial slope should be steeper the higher the dose rate. Figure 8.15 shows the results for four different electron-hole production rates,  $30, 300, 3,000, \text{ and } 30,000 \text{ s}^{-1}$ . The results show indeed that the initial signal is linear dependent on the dose rate. Furthermore, Fig. 8.16 shows the same signals as given in Fig. 8.15 but normalised to the first data point and confirm the expectation that the decay of the RF signal is steeper, the higher the dose rate is.

### 8.4.3 Comparison with other numerical methods

From Ch. 3 to Ch. 7 it is known that numerical solutions of ODEs are able to reproduce RF phenomena in quartz. In this section a comparison between ODE and Monte-Carlo results is given. The former sections showed that the numerical solution of coupled ordinary differential equations can also lead to meaningful results. The same equations as given in Sec. 4.2, Eqs. (4.1) – (4.5), are solved with the parameters given in Table 8.3 for different values of  $R$  (electron-hole production rate). The results are calculated with the **R**-package *deSolve* (Soetaert et al. 2012) and are given in Fig. 8.16 as black lines. A very good agreement with the Monte-Carlo approach is reached, show that both methods are comparable. Nevertheless, the Monte-Carlo method is much more time consuming in calculation than the ODE method although the calculations can be done on different processors in parallel.

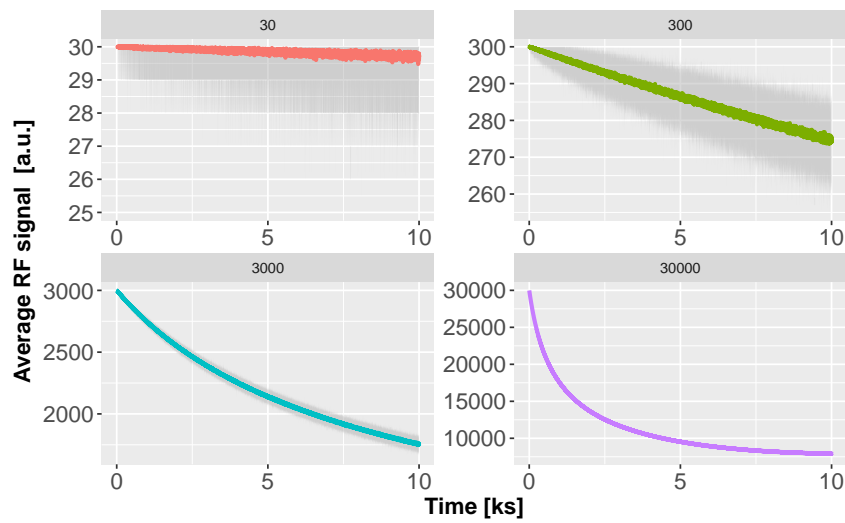


**Figure 8.15:** Average signal of 100 clusters with parameters from Table 8.3 and four different pair-production rates.

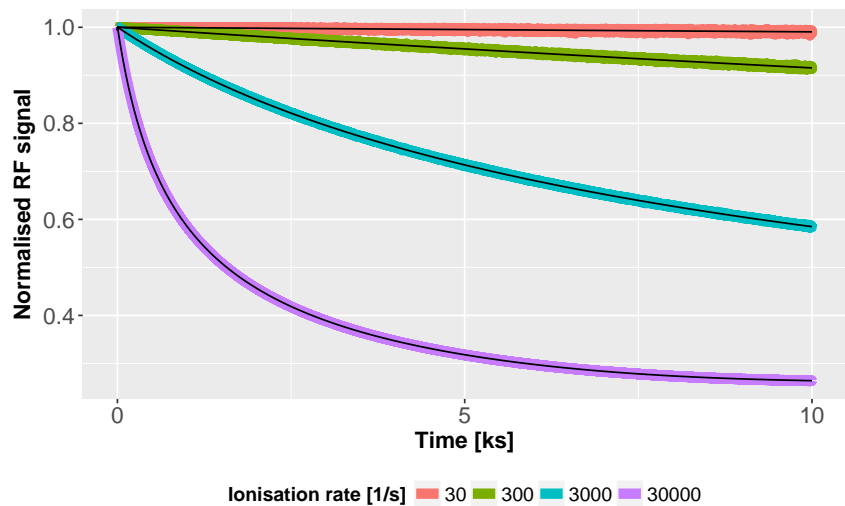


**Figure 8.16:** Same data as in Fig. 8.15 but normalised to the first data point. The black lines indicate the solutions solving the system of ODEs numerically, see Ch. 8.4.3.

#### 8.4.4 Discussion

The presented calculation method by using the statistical Monte-Carlo method is able to give the same results as using numerically methods solving sets of ODEs, see Fig. 8.16. Nevertheless, the number of carriers in one cluster is large and so the accordance between the solutions of both methods is not surprising. In order to achieve similar results as presented in Pagonis et al. (2014) the number of charge carriers in one cluster has to be very small. Pagonis et al. (2014) showed that for a big number of charge carriers (e.g., 100) no difference between the ODE and Monte-Carlo method exists. Only after reducing the number of charge carriers down to 20 significant changes between both methods occur and they become more divergent for even smaller numbers of charge carriers (see Pagonis et al. (2014: Fig.4)). Similar conclusions were made before by Mandowski & Świątek (1998). The implementation of the reduction of charge carriers to RF is not straightforward and the here presented results are just a starting point. The problem is that in TL/OSL Monte-Carlo simulations the number of charge carriers keeps constant (no signal) or decreases (signal). In RF simulations the situation is different because in each time step new electrons and holes are created and so the number of charge carrier in one cluster changes permanently. So, another design of clusters than presented in former Monte-Carlo TL/OSL studies has to be applied to reach the goal of reducing the cluster since further more.

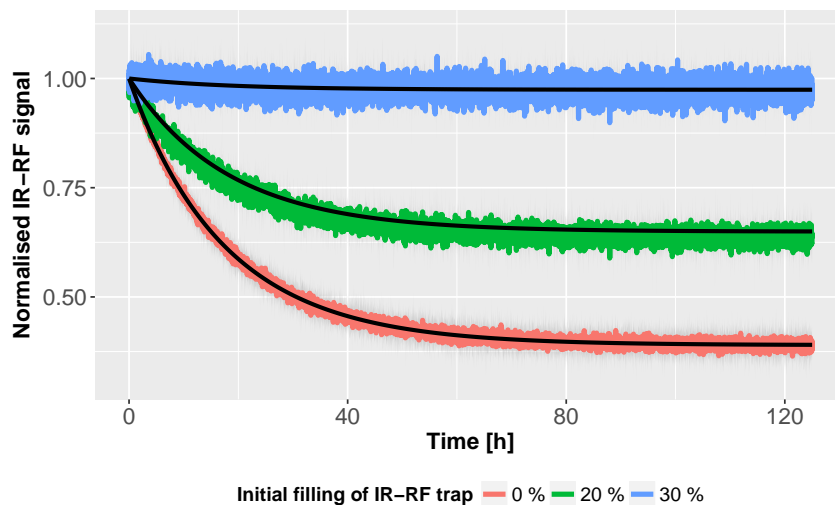


**Figure 8.17:** Results of the simulation of IR-RF with the model suggested by Trautmann et al. (1999) for different initial fillings of the IR-RF trap. The black lines indicate the ODE solutions which are in agreement with the Monte-Carlo results.

The idea of using Monte-Carlo methods in luminescence modelling in the past years was mainly applied to feldspar models, e.g. Pagonis & Chen (2015), Pagonis & Kulp (2017), and Pagonis et al. (2017). To further test the presented algorithm for Monte-Carlo simulations calculating RF signals, the model for infrared radiofluorescence (IR-RF) in feldspar published by Trautmann et al. (1999) was used. In contrast to quartz RF, it is suggested that the

PARAMETER	VALUE	UNIT
$\bar{A}_n$	1 E-16	s <sup>-1</sup>
$\bar{B}_1$	1 E-16	s <sup>-1</sup>
$\bar{B}_2$	1 E-16	s <sup>-1</sup>
$\bar{A}_{m_1}$	2 E-16	s <sup>-1</sup>
$\bar{A}_{m_2}$	2 E-16	s <sup>-1</sup>
$\bar{A}_{m_n}$	5 E-16	s <sup>-1</sup>
$\bar{M}_1$	5 E+17	
$\bar{M}_2$	1 E+18	
$\bar{N}$	5 E+17	
$\bar{R}$	5 E+12	s <sup>-1</sup>

**Table 8.4:** Used parameters for the Monte-Carlo simulation of feldspar IR-RF. In contrast to Table 8.3 the new parameter  $\bar{A}_{m_n}$  describes the probability of a hole transport into the IR-RF trap.

IR-RF signal is generated when electrons migrate from the conduction band into the electron trap. Nevertheless, Trautmann et al. (1999) also used a three-energy-level model to simulate IR-RF signals, which is very similar to the one presented for quartz UV-RF in this section. Just small changes in the ODE equations (due to an allowed transition of holes into the electron trap) as well as small adjustments on the parameters are needed, see Table 8.4. The used value of  $\chi$  was 1 E-10 and in order to reduce the computation time just 8 clusters were simulated. Figure 8.17 shows the results for two different simulation methods: The coloured curves show the average signal from the Monte-Carlo methods for 8 clusters while the black lines indicate the solutions of numerically solving the ODEs given in Trautmann et al. (1999). As expected, the signal does not show strong signal dynamic for simulated IR-RF because the IR-RF trap is 30 % filled before starting the simulation (Trautmann et al. 1999). The strongest decay in the simulated IR-RF signal is reached if the IR-RF trap is completely empty. And again, the ODE and the Monte-Carlo solutions match well.

The presented approach is just a starting point and shows the potential that Monte-Carlo simulations are able to simulate UV-RF signals in quartz and IR-RF signals in feldspar properly. In the future more complex scenarios of designing clusters are possible, e.g., exchange of charge carriers between different clusters.

## References

- Adamiec, G., Garcia-Talavera, M., Bailey, R. M., La Torre, P. I. de, 2004. Application of a genetic algorithm to finding parameter values for numerical simulation of quartz luminescence. *Geochronometria* 23, 9–14.
- Adamiec, G., Bluszcz, A., Bailey, R. M., Garcia-Talavera, M., 2006. Finding model parameters: Genetic algorithms and the numerical modelling of quartz luminescence. *Radiation Measurements* 41(7), 897–902.
- Bailey, R. M., 2001. Towards a general kinetic model for optically and thermally stimulated luminescence of quartz. *Radiation Measurements* 33(1), 17–45.
- Bailiff, I., 1994. The pre-dose technique. *Radiation Measurements* 23(2), 471–479.
- Bräunlich, P., Kelly, P., Fillard, J.-P., 1979. Thermally stimulated luminescence and conductivity. In: *Thermally stimulated relaxation in solids*. Springer, 35–92.
- Brik, A. B., Degoda, V. Y., Marazuev, Y. A., 1994. X-ray luminescence dosimetry of irradiated quartz. *Journal of Applied Spectroscopy* 60(5), 398–400.
- Buylaert, J.-P., Jain, M., Murray, A., Thomsen, K., Lapp, T., 2012. IR-RF dating of sand-sized K-feldspar extracts: A test of accuracy. *Radiation Measurements* 47(9), 759–765.
- Chen, R., Lawless, J., Pagonis, V., 2011. A model for explaining the concentration quenching of thermoluminescence. *Radiation Measurements* 46, 1380–1384.
- Franssen, H. H., Alcolea, A., Riva, M., Bakr, M., Wiel, N. van der, Stauffer, F., Guadagnini, A., 2009. A comparison of seven methods for the inverse modelling of groundwater flow. Application to the characterisation of well catchments. *Advances in Water Resources* 32(6), 851–872.
- Frouin, M., Huot, S., Mercier, N., Lahaye, C., Lamothe, M., 2015. The issue of laboratory bleaching in the infrared-radiofluorescence dating method. *Radiation Measurements* 81, 212–217.
- Kreutzer, S., Schmidt, C., Fuchs, M. C., Dietze, M., Fischer, M., Fuchs, M., 2012. Introducing an R package for luminescence dating analysis. *Ancient TL* 30(1), 1–8.
- Kreutzer, S., Burow, C., Dietze, M., Fuchs, M. C., Schmidt, C., Fischer, M., Friedrich, J., 2018. *Luminescence: Comprehensive Luminescence Dating Data Analysis*. (R package version 0.8.4). <https://CRAN.R-project.org/package=Luminescence>,
- Kulkarni, R., 1994. The development of the Monte Carlo method for the calculation of the thermoluminescence intensity and the thermally stimulated conductivity. *Radiation Protection Dosimetry* 51(2), 95–105.
- Landau, D. P., Binder, K., 2014. *A guide to Monte Carlo simulations in statistical physics*. Cambridge university press.
- Mandowski, A., Świątek, J., 1992. Monte Carlo simulation of thermally stimulated relaxation kinetics of carrier trapping in microcrystalline and two-dimensional solids. *Philosophical Magazine B* 65, 729–732.

- Mandowski, A., Świątek, J., 1994. Monte Carlo simulation of TSC and TL in spatially correlated systems. *Proceedings of 8th International Symposium on Electrets (ISE 8)*, IEEE, 461–466.
- Mandowski, A., Świątek, J., 1996. On the influence of spatial correlation on the kinetic order of TL. *Radiation Protection Dosimetry* 65, 25–28.
- Mandowski, A., Świątek, J., 1998. Thermoluminescence and trap assemblies - results of Monte Carlo calculations. *Radiation Measurements* 29, 415–419.
- Mandowski, A., 2002. The theory of thermoluminescence with an arbitrary spatial distribution of traps. *Radiation Protection Dosimetry* 100, 115–118.
- Marazuev, Y. A., Brik, A. B., Degoda, V. Y., 1995. Radioluminescent dosimetry of  $\alpha$ -quartz. *Radiation Measurements* 24(4), 565–569.
- Pagonis, V., Kitis, G., Furetta, C., 2006. *Numerical and Practical Exercises in Thermoluminescence*. Springer Science & Business Media.
- Pagonis, V., Gochnour, E., Hennessey, M., Knowler, C., 2014. Monte Carlo simulations of luminescence processes under quasi-equilibrium (QE) conditions. *Radiation Measurements* 67, 67–76.
- Pagonis, V., Chen, R., 2015. Monte Carlo simulations of TL and OSL in nanodosimetric materials and feldspars. *Radiation Measurements* 81, 262–269.
- Pagonis, V., Kulp, C., 2017. Monte Carlo simulations of tunneling phenomena and nearest neighbor hopping mechanism in feldspars. *Journal of Luminescence* 181, 114–120.
- Pagonis, V., Bernier, S., Santos Vieira, F. M. dos, Steele, S., 2017. The effect of crystal size on tunneling phenomena in luminescent nanodosimetric materials. *Nuclear Instruments and Methods in Physics Research Section B: Beam Interactions with Materials and Atoms* 412, 198–206.
- Peng, J., Dong, Z., Han, F., 2016. tged: An R package for analyzing thermoluminescence glow curves. *SoftwareX* 5, 112–120.
- Saltelli, A., Tarantola, S., Campolongo, F., Ratto, M., 2004. *Sensitivity Analysis in Practice: A Guide to Assessing Scientific Models*. John Wiley & Sons.
- Schmidt, C., Friedrich, J., Adamiec, G., Chruścińska, A., Fasoli, M., Kreutzer, S., Martini, M., Panzeri, L., Polymeris, G. S., Przegiętka, K., Valla, P. G., King, G. E., Sanderson, D. C., 2018. How reproducible are kinetic parameter constraints of quartz luminescence? An interlaboratory comparison for the 110 °C TL peak. *Radiation Measurements* 110, 14–24.
- Soetaert, K., Petzoldt, T., 2010. Inverse Modelling, Sensitivity and Monte Carlo Analysis in R Using Package FME. *Journal of Statistical Software* 33, 1–28.
- Soetaert, K., Cash, J., Mazzia, F., 2012. *Solving differential equations in R*. Springer Science & Business Media.
- Trautmann, T., Krbetschek, M., Dietrich, A., Stolz, W., 1999. Feldspar radioluminescence: a new dating method and its physical background. *Journal of Luminescence* 85(1), 45–58.

# Appendices



# A Supplementary material of publications

## A.1 Chapter 2

# Solving Ordinary Differential Equations to Understand Luminescence: 'RLumModel', an Advanced Research Tool for Simulating Luminescence in Quartz Using R (supplementary material)

*Johannes Friedrich, Sebastian Kreutzer, Christoph Schmidt*

## Introduction

This supplementary material is part of the article Friedrich et al. (2016) and contains additional **R**-coding examples and code completions.

## R-Code by examples

### Code example 2.4.1.1

```
##set heating rate
heating.rate <- seq(from = 2, to = 10, by = 2)

##model signals
##"verbose = FALSE" for no terminal output
## "TL$" for exact matching TL and not (TL)
model.output <- lapply(
  1:length(heating.rate), function(x){
    sequence <- list(
      IRR = c(20, 10, 1),
      TL = c(20, 400, heating.rate[x]))

    TL_data <- model_LuminescenceSignals(
      sequence = sequence,
      model = "Bailey2001",
      plot = FALSE,
      verbose = FALSE)

    return(get_RLum(TL_data, recordType = "TL$", drop = FALSE))
  })

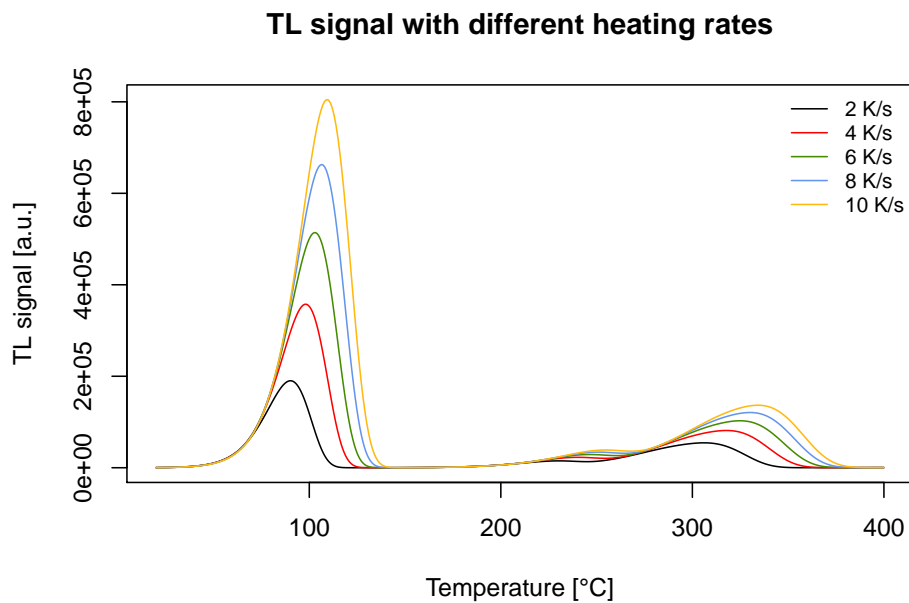
##merge output
model.output.merged <- merge_RLum(model.output)

##plot results
```

```

plot_RLum(
  object = model.output.merged,
  xlab = "Temperature [\u00B0C]",
  ylab = "TL signal [a.u.]",
  main = "TL signal with different heating rates",
  legend.text = paste(heating.rate, "K/s"),
  combine = TRUE)

```



### Code example 2.4.1.2

```

##set temperature
act.temp <- seq(from = 80, to = 600, by = 20)

##loop over temperature
model.output <- vapply(X = act.temp, FUN = function(x) {

  ##set sequence, note: sequence includes sample history
  sequence <- list(
    IRR = c(20, 1, 1e-11),
    IRR = c(20, 10, 1),
    PH = c(x, 1),
    IRR = c(20, 0.1, 1),
    TL = c(20, 150, 5)
  )

  ##run simulation
  temp <- model_LuminescenceSignals(
    sequence = sequence,
    model = "Pagonis2007",
    simulate_sample_history = TRUE,
    plot = FALSE,
    verbose = FALSE
  )

```

```

)

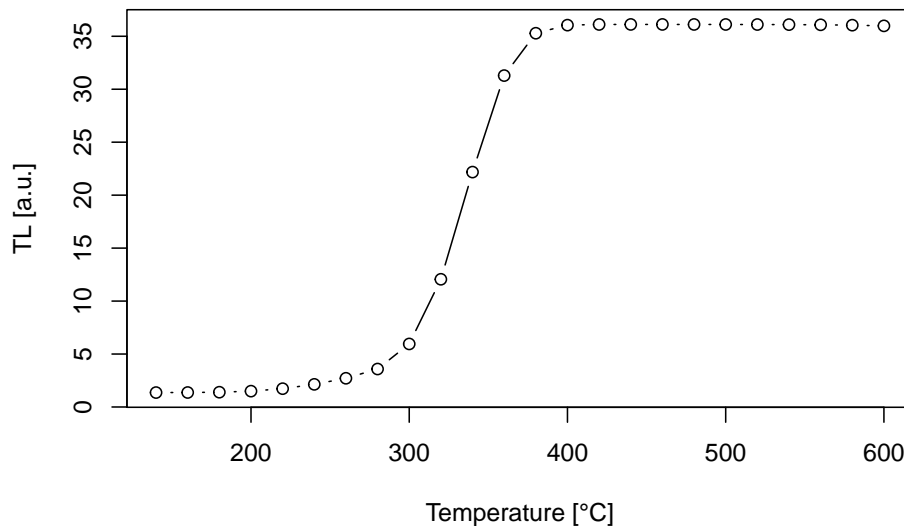
## "TL$" for exact matching TL and not (TL)
TL_curve <- get_RLum(temp, recordType = "TL$")

##return max value in TL curve
return(max(get_RLum(TL_curve)[,2]))

}, FUN.VALUE = 1)

##plot results
plot(
  act.temp[-(1:3)],
  model.output[-(1:3)],
  type = "b",
  xlab = "Temperature [\u00B0C]",
  ylab = "TL [a.u.]"
)

```



### Code example 2.4.1.3

```

##set optical power [%]
optical_power <- seq(0, 100, 20)

##loop over power
model.output <- lapply(optical_power, function(x){

  ##set sequence
  sequence <- list(
    IRR = c(20, 50, 1),
    PH = c(220, 10, 5),
    OSL = c(125, 50, x))

```

```

data <- model_LuminescenceSignals(
  sequence = sequence,
  model = "Bailey2004",
  plot = FALSE,
  verbose = FALSE)

##"OSL$" for exact matching TL and not (OSL)
return(get_RLum(data, recordType = "OSL$", drop = FALSE))

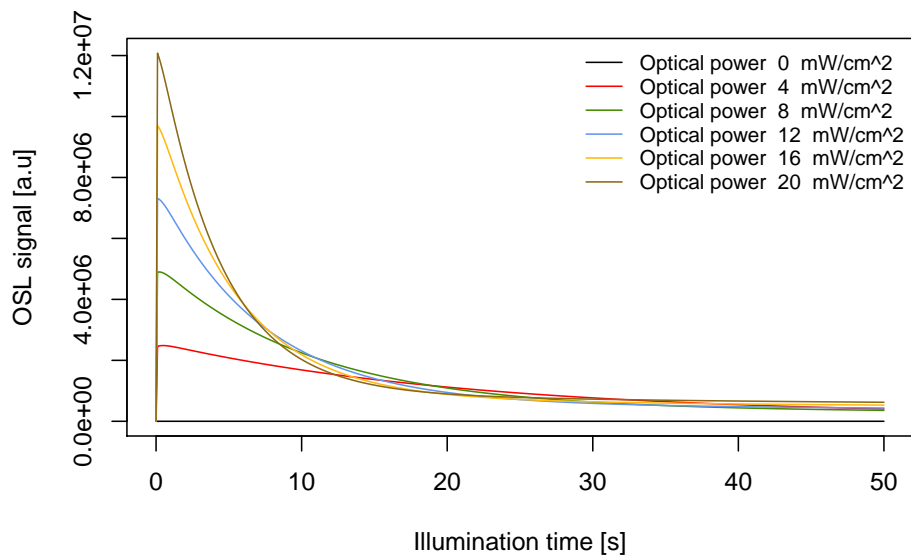
})

##merge output
model.output.merged <- merge_RLum(model.output)

##plot results
plot_RLum(
  object = model.output.merged,
  xlab = "Illumination time [s]",
  ylab = "OSL signal [a.u]",
  legend.text = paste("Optical power ", 20 * optical_power / 100, " mW/cm^2"),
  combine = TRUE
)

```

OSL combined



## Code example 2.4.1.4

```

##set OSL temperature
OSL.temp <- c(20,80,160,200,240)

##loop over temperature
model.output <- lapply(OSL.temp, function(x){

  ##set sequence

```

```

sequence <- list(OSL = c(x, 60, 100))

data <- model_LuminescenceSignals(
  sequence = sequence,
  model = "Bailey2001",
  plot = FALSE,
  verbose = FALSE
)

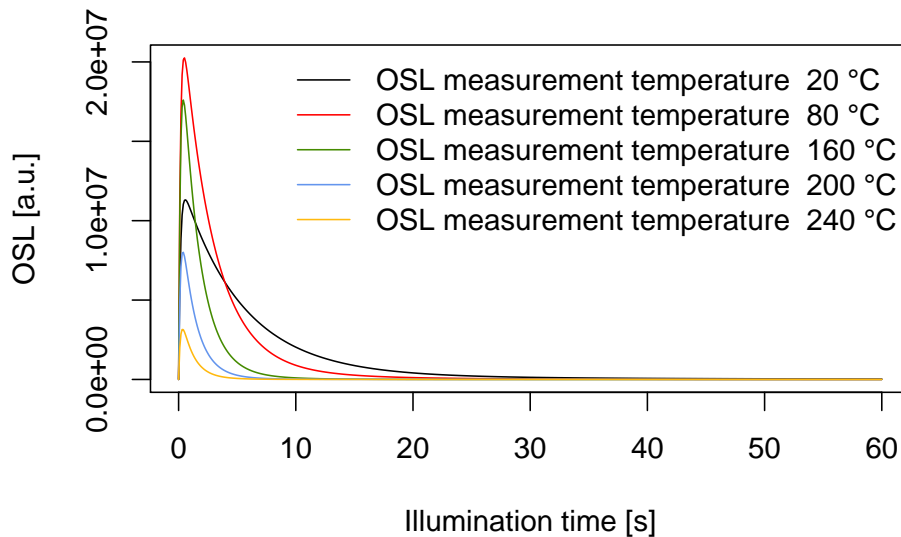
##"OSL$" for exact matching TL and not (OSL)
return(get_RLum(data, recordType = "OSL$", drop = FALSE))
})

##merge output
model.output.merged <- merge_RLum(model.output)

##plot results
plot_RLum(
  object = model.output.merged,
  xlab = "Illumination time [s]",
  ylab = "OSL [a.u.]",
  main = "OSL signal for different temperatures",
  legend.text = paste("OSL measurement temperature ", OSL.temp, "\u00B0C"),
  combine = TRUE,
  cex = 1.2)

```

**OSL signal for different temperatures**



**Code example 2.4.2a**

```

##set PH temperatures
PH_temp <- seq(from = 160, to = 300, by = 20)

##set RegDose
RegDose = c(0, 80, 140, 260, 320, 0, 80)

```

```

##loop over PH temperatures
DRT.output <- lapply(1:length(PH_temp), function(x){

  sequence <- list(
    RegDose = RegDose,
    TestDose = 20,
    PH = PH_temp[x],
    CH = PH_temp[x],
    OSL_temp = 125,
    Irr_2recover = 200
  )

  model.output <- model_LuminescenceSignals(
    sequence = sequence,
    model = "Pagonis2008",
    plot = FALSE,
    verbose = FALSE
  )

  results <- analyse_SAR.CWOSL(object = model.output,
    signal.integral.min = 1,
    signal.integral.max = 7,
    background.integral.min = 301,
    background.integral.max = 401,
    fit.method = "EXP",
    dose.points = RegDose,
    plot = FALSE)

  temp <- get_RLum(results)
  out <- data.frame(De = temp$De, De.error = temp$De.Error)
  return(out)
})

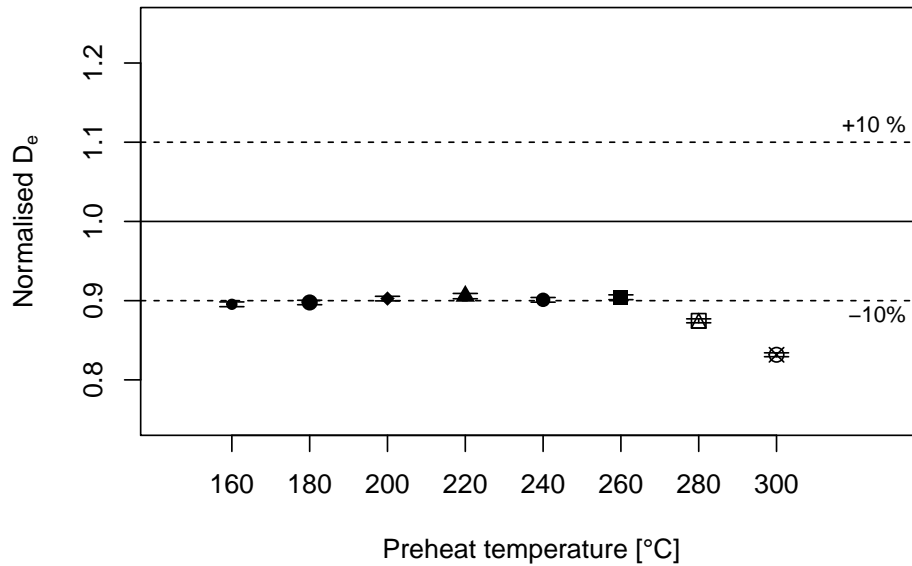
## [plot_GrowthCurve()] Fit: EXP (interpolation) | De = 179.08 | D01 = 101.52
## [plot_GrowthCurve()] Fit: EXP (interpolation) | De = 179.54 | D01 = 101.44
## [plot_GrowthCurve()] Fit: EXP (interpolation) | De = 180.52 | D01 = 101.34
## [plot_GrowthCurve()] Fit: EXP (interpolation) | De = 181.15 | D01 = 101.36
## [plot_GrowthCurve()] Fit: EXP (interpolation) | De = 180.21 | D01 = 101.78
## [plot_GrowthCurve()] Fit: EXP (interpolation) | De = 180.86 | D01 = 102.75
## [plot_GrowthCurve()] Fit: EXP (interpolation) | De = 174.91 | D01 = 107.31
## [plot_GrowthCurve()] Fit: EXP (interpolation) | De = 166.34 | D01 = 130.93

##output as data.frame for plot_DRTResults
DRT.result <- as.data.frame(do.call(rbind,DRT.output))

##plot DRT.results
plot_DRTResults(DRT.result, preheat = PH_temp, given.dose = 200)

```

### Dose recovery test



### Code example 2.4.2b

```
##set RegDose
RegDose = c(0, 80, 140, 260, 320, 0, 80)

##set sequence
sequence <- list(
  RegDose = RegDose,
  TestDose = 20,
  PH = 180,
  CH = 180,
  OSL_temp = 125
)

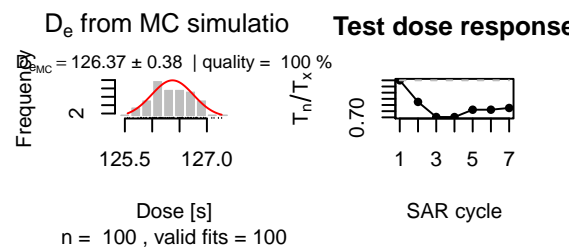
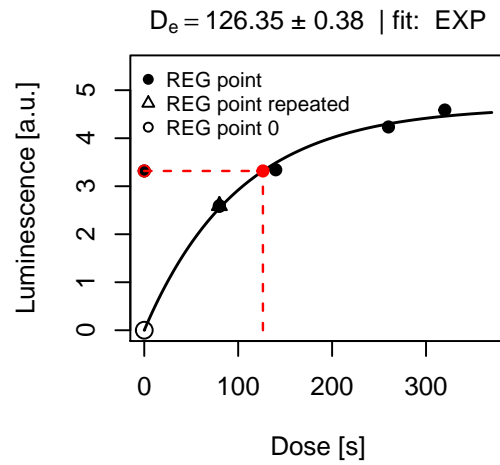
##model
model.output <- model_LuminescenceSignals(
  sequence = sequence,
  model = "Pagonis2008",
  plot = FALSE,
  verbose = FALSE
)

##analyse SAR sequence and plot only the resulting growth curve
results <- analyse_SAR.CWOSL(
  model.output,
  signal.integral.min = 1,
  signal.integral.max = 7,
  background.integral.min = 301,
  background.integral.max = 401,
  fit.method = "EXP",

```

```
dose.points = RegDose,
verbose = FALSE,
plot.single = c(6)
)
```

### Growth curve



## **A.2 Chapter 3**

# Quartz radiofluorescence: a modelling approach (supplementary material)

*Johannes Friedrich, Vasilis Pagonis, Rewen Chen, Sebastian Kreutzer, Christoph Schmidt*

## Introduction

This supplementary material is part of the article Friedrich et al. and contains additional **R**-coding examples and code completions.

## R-Code by examples

### Code example 1: TL signal with different heating rates

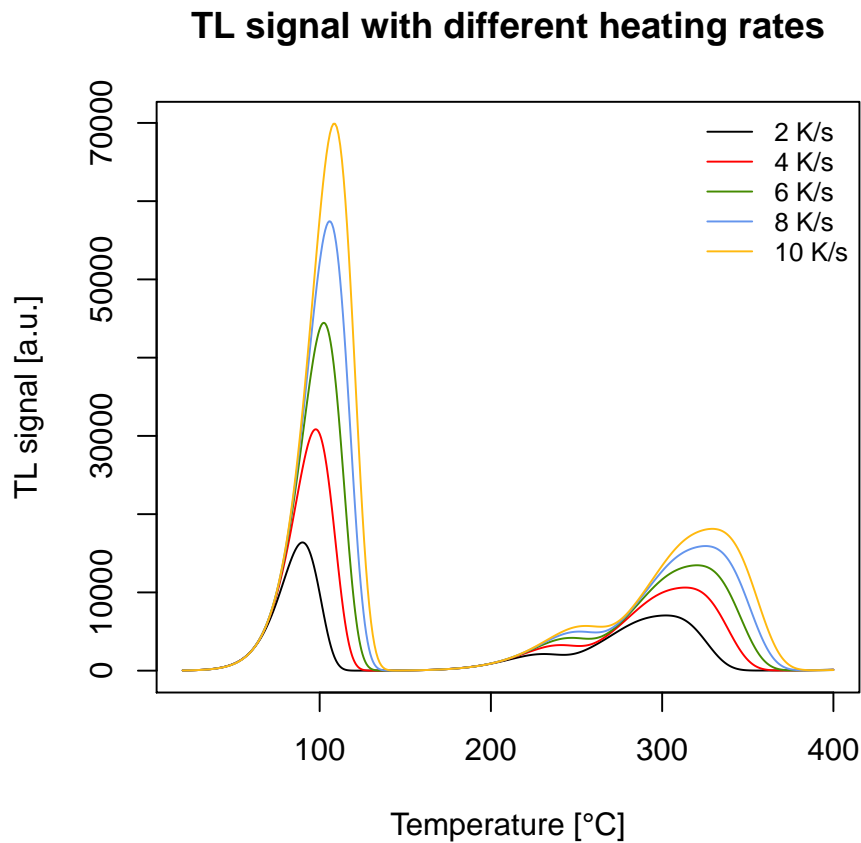
```
##set heating rate
heating.rate <- seq(from = 2, to = 10, by = 2)

##model signals
##"verbose = FALSE" for no terminal output
## "TL$" for exact matching TL and not (TL)
model.output <- lapply(
  1:length(heating.rate), function(x){
    sequence <- list(
      IRR = c(20, 10, 1),
      TL = c(20, 400, heating.rate[x]))

    TL_data <- model_LuminescenceSignals(
      sequence = sequence,
      model = "Friedrich2017",
      plot = FALSE,
      verbose = FALSE)

    return(get_RLum(TL_data, recordType = "TL$", drop = FALSE))
  })

##merge output
model.output.merged <- merge_RLum(model.output)
```



#### Code example 2: TAC

```
##set temperature
act.temp <- seq(from = 80, to = 600, by = 20)

##loop over temperature
model.output <- vapply(X = act.temp, FUN = function(x) {

  ##set sequence, note: sequence includes sample history
  sequence <- list(
    IRR = c(20, 1, 1e-11),
    IRR = c(20, 10, 1),
    PH = c(x, 1),
    IRR = c(20, 0.1, 1),
    TL = c(20, 150, 5)
  )

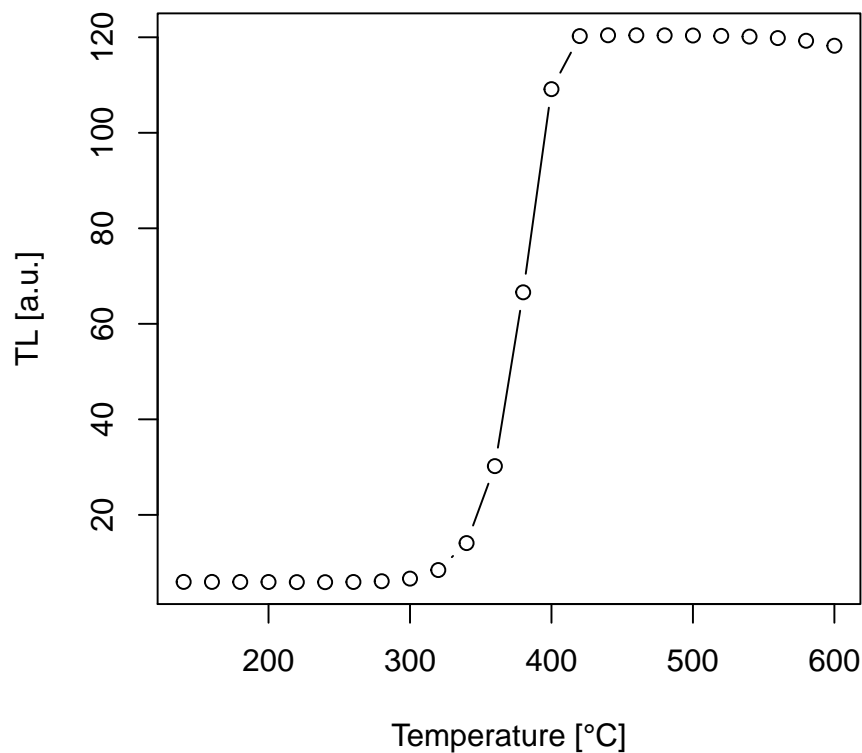
  ##run simulation
  temp <- model_LuminescenceSignals(
    sequence = sequence,
    model = "Friedrich2017",
    simulate_sample_history = TRUE,
    plot = FALSE,
    verbose = FALSE
  )
}
```

```

## "TL$" for exact matching TL and not (TL)
TL_curve <- get_RLum(temp, recordType = "TL$")

##return max value in TL curve
return(max(get_RLum(TL_curve)[,2]))
}, FUN.VALUE = 1)

```



### Code example 3: OSL signal for different optical powers

```

##set optical power [%]
optical_power <- c(0,20,40,60,80,100)

##loop over power
model.output <- lapply(optical_power, function(x){

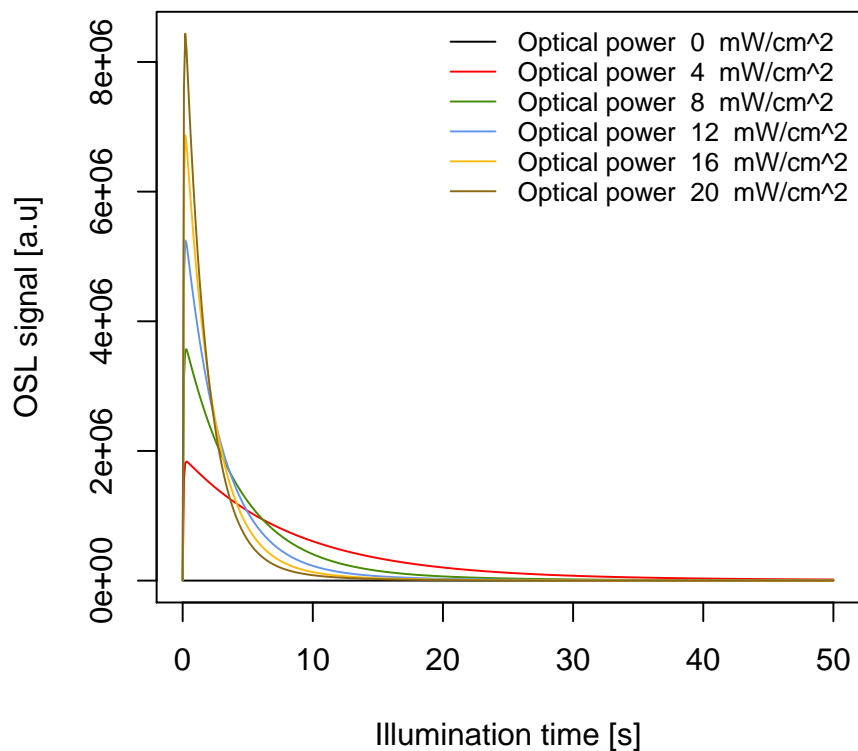
##set sequence
sequence <- list(
  IRR = c(20, 50, 1),
  PH = c(220, 10, 5),
  OSL = c(125, 50, x))

data <- model_LuminescenceSignals(
  sequence = sequence,
  model = "Friedrich2017",
  plot = FALSE,

```

```
verbose = FALSE)  
  
##"OSL$" for exact matching TL and not (OSL)  
return(get_RLum(data, recordType = "OSL$", drop = FALSE))  
})  
  
##merge output  
model.output.merged <- merge_RLum(model.output)
```

### OSL combined



### Code example 4: OSL signal for different reading temperatures

```
##set OSL temperature  
OSL.temp <- c(20, 80, 160, 200, 240)  
  
##loop over temperature  
model.output <- lapply(OSL.temp, function(x){  
  
  ##set sequence  
  sequence <- list(  
    OSL = c(x, 60, 100)  
  )  
  
  data <- model_LuminescenceSignals(  

```

```

sequence = sequence,
model = "Friedrich2017",
plot = FALSE,
verbose = FALSE
)

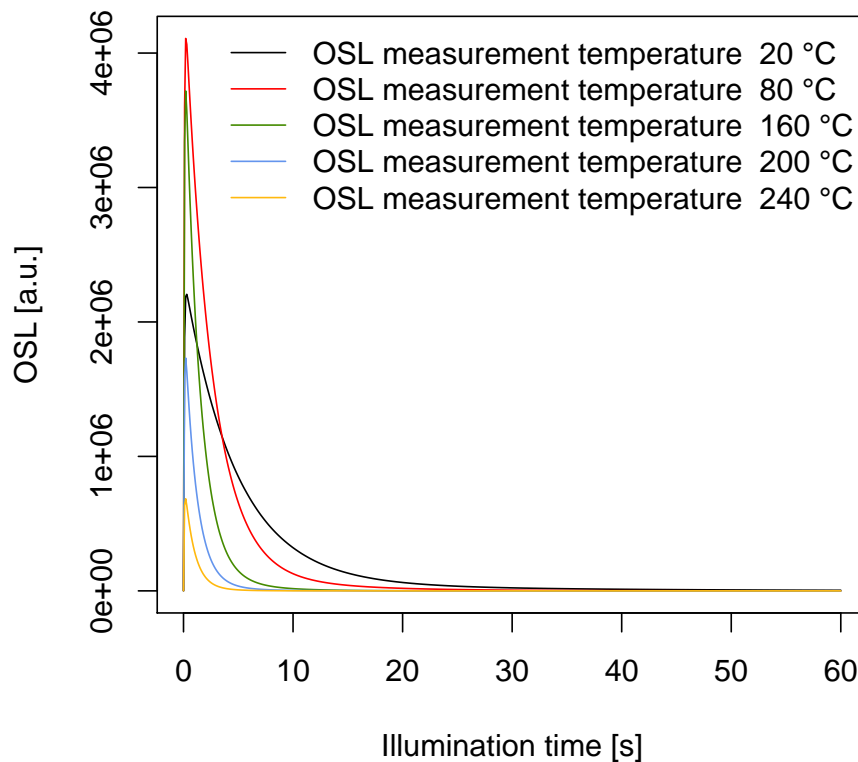
##"OSL$" for exact matching TL and not (OSL)
return(get_RLum(data, recordType = "OSL$", drop = FALSE))
})

##merge output
model.output.merged <- merge_RLum(model.output)

##plot results
plot_RLum(
  object = model.output.merged,
  xlab = "Illumination time [s]",
  ylab = "OSL [a.u.]",
  main = "OSL signal for different reading temperatures",
  legend.text = paste("OSL measurement temperature ",OSL.temp, "\u00B0C"),
  combine = TRUE,
  cex = 1.2)

```

### OSL signal for different reading temperatures



### Code example 5: DRT

```
##set PH temperatures
PH_temp <- seq(from = 160, to = 300, by = 20)

##set RegDose
RegDose = c(0, 20, 35, 65, 80, 0, 20)

##loop over PH temperatures
DRT.output <- lapply(1:length(PH_temp), function(x){

  sequence <- list(
    RegDose = RegDose,
    TestDose = 5,
    PH = PH_temp[x],
    CH = PH_temp[x],
    OSL_temp = 125,
    Irr_2recover = 50
  )

  model.output <- model_LuminescenceSignals(
    sequence = sequence,
    model = "Friedrich2017",
    plot = FALSE,
    verbose = FALSE
  )

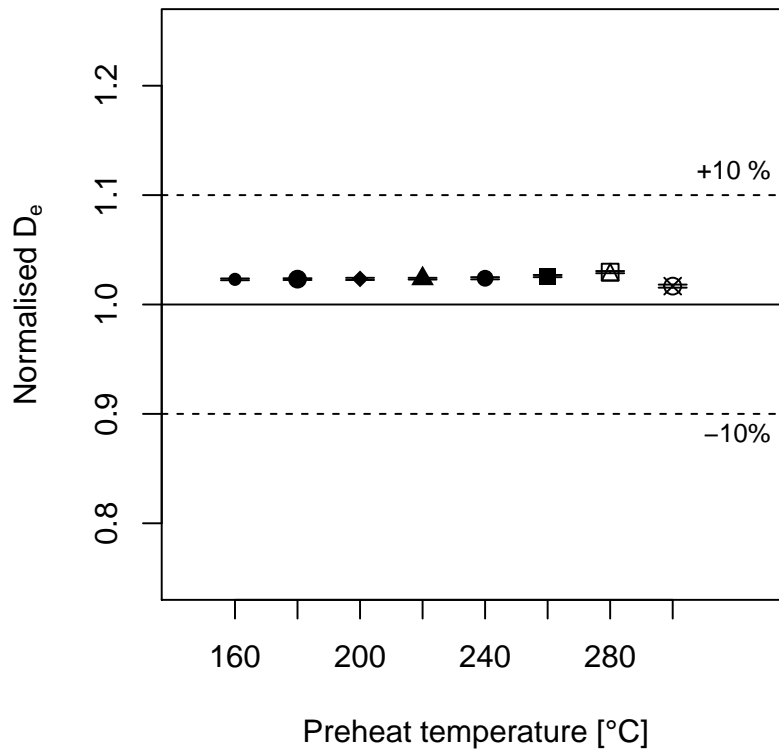
  results <- analyse_SAR.CWOSL(object = model.output,
    signal.integral.min = 1,
    signal.integral.max = 7,
    background.integral.min = 301,
    background.integral.max = 401,
    fit.method = "EXP",
    dose.points = RegDose,
    plot = FALSE)

  temp <- get_RLum(results)
  out <- data.frame(De = temp$De, De.error = temp$De.Error)
  return(out)
})

##output as data.frame for plot_DRTResults
DRT.result <- as.data.frame(do.call(rbind,DRT.output))

##plot DRT.results
plot_DRTResults(DRT.result, preheat = PH_temp, given.dose = 50)
```

## Dose recovery test



### Code example 6: SAR protocol

```
##set RegDose
RegDose = c(0, 20, 35, 65, 80, 0, 20)

##set sequence
sequence <- list(
  RegDose = RegDose,
  TestDose = 5,
  PH = 200,
  CH = 220,
  OSL_temp = 125
)

##model
model.output <- model_LuminescenceSignals(
  sequence = sequence,
  model = "Friedrich2017",
  plot = FALSE,
  verbose = FALSE
)

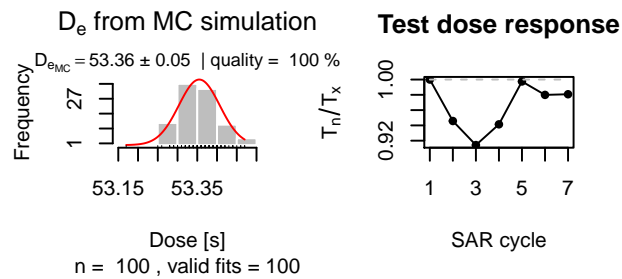
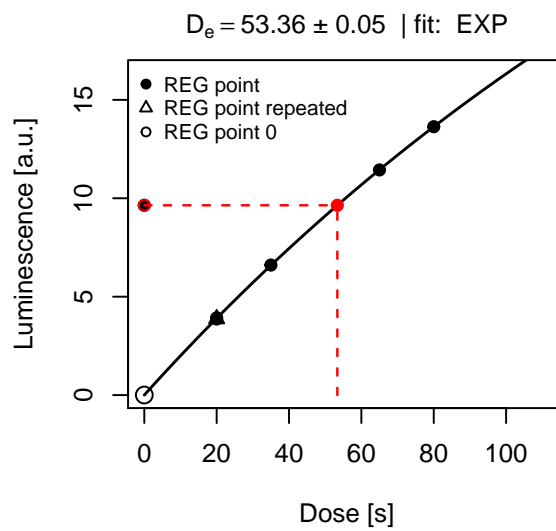
##analyse SAR sequence and plot only the resulting growth curve
```

```

results <- analyse_SAR.CWOSL(
  model.output,
  signal.integral.min = 1,
  signal.integral.max = 7,
  background.integral.min = 301,
  background.integral.max = 401,
  fit.method = "EXP",
  dose.points = RegDose,
  verbose = FALSE,
  plot.single = c(6)
)

```

### Growth curve



## A.3 Chapter 4

# The basic principles of quartz radiofluorescence dynamics in the UV - analytical, numerical and experimental results (supplementary material)

*Johannes Friedrich, Mauro Fasoli, Sebastian Kreutzer, Christoph Schmidt*

## Introduction

This supplementary material is part of the article Friedrich et al. (submitted) and contains additional **R**-coding examples and code completions.

All calculations presented here were executed with **R** version 3.4.0 and the **R**-package 'deSolve' version 1.14.

## Case I: empty R-centre

### Set parameters

```
times <- 0:10000

filling <- 10^seq(10, 11, 0.1)

parameters <- c(
  Am1 = 5e-7,
  Am2 = 1e-9,
  An = 1e-10,
  B1 = 5e-9,
  B2 = 1e-10,
  N = 1e11,
  M1 = 1e11,
  M2 = 1e11,
  R = 3e5)

RF_ODE <- function(t, state, parameters) {
  with(as.list(c(state, parameters)),{

    dn <- An*(N-n)*nc

    dm1 <- Am1*(M1-m1)*nv - B1*m1*nc
    dm2 <- Am2*(M2-m2)*nv - B2*m2*nc

    dnc <- R - nc*(An*(N-n) + B1*m1 + B2*m2)

    dnv <- R - Am2*(M2-m2)*nv - Am1*(M1-m1)*nv

    # return the rate of change
```

```

    list(c(dn, dm1, dm2, dnc, dnv), signal = m2*B2*nc)
  })
}

```

## Solve ODEs for different starting values

```

RF_list <- sapply(filling, function(x){

  state <- c(n = x,
            m1 = 0,
            m2 = x,
            nc = 0,
            nv = 0)

  result <- deSolve::ode(
    y = state,
    times = times,
    func = RF_ODE,
    parms = parameters,
    rtol = 1e-10,
    atol = 1e-10)

  return(result[, "signal"])

})

RF_list <- as.data.frame(RF_list)
colnames(RF_list) <- round(100 * filling/1e11, 2)
RF_list$time <- times

```

## Plot results

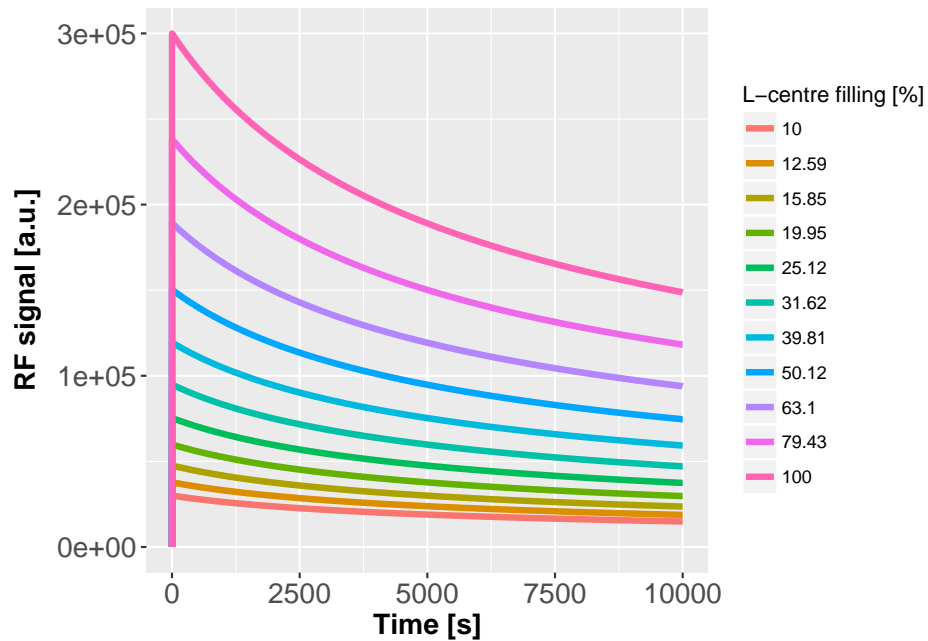
```

library(reshape2)
library(ggplot2)

RF_ggplot <- reshape2::melt(RF_list, id.vars = "time")

ggplot(RF_ggplot, aes(x = time, y = value, colour = variable)) +
  geom_line(aes(colour = variable), size = 1.5) +
  scale_colour_discrete(name = "L-centre filling [%]") +
  xlab("Time [s]") +
  ylab(expression(bold("RF signal [a.u.]"))) +
  theme(axis.text = element_text(size = 14),
        axis.title = element_text(size = 14, face = "bold"))

```



## Discussion

### Set parameters

```
state <- c(n = 1e11,
          m1 = 0,
          m2 = 1e11,
          nc = 0,
          nv = 0)

RF_ODE_Zimmerman <- function(t, state, parameters) {
  with(as.list(c(state, parameters)),{

    dn <- An*(N-n)*nc

    dm1 <- Am1*(M1-m1)*nv
    dm2 <- Am2*(M2-m2)*nv - B2*m2*nc

    dnc <- R - nc*(An*(N-n) + B2*m2)

    dnv <- R - Am2*(M2-m2)*nv - Am1*(M1-m1)*nv

    # return the rate of change
    list(c(dn, dm1, dm2, dnc, dnv), signal = m2*B2*nc)
  })
}
```

## Solve ODEs

```
result_Bailey <- deSolve::ode(
  y = state,
  times = times,
  func = RF_ODE,
  parms = parameters,
  rtol = 1e-10,
  atol = 1e-10)

result_Zimmerman <- deSolve::ode(
  y = state,
  times = times,
  func = RF_ODE_Zimmerman,
  parms = parameters,
  rtol = 1e-10,
  atol = 1e-10)
```

## Plot results

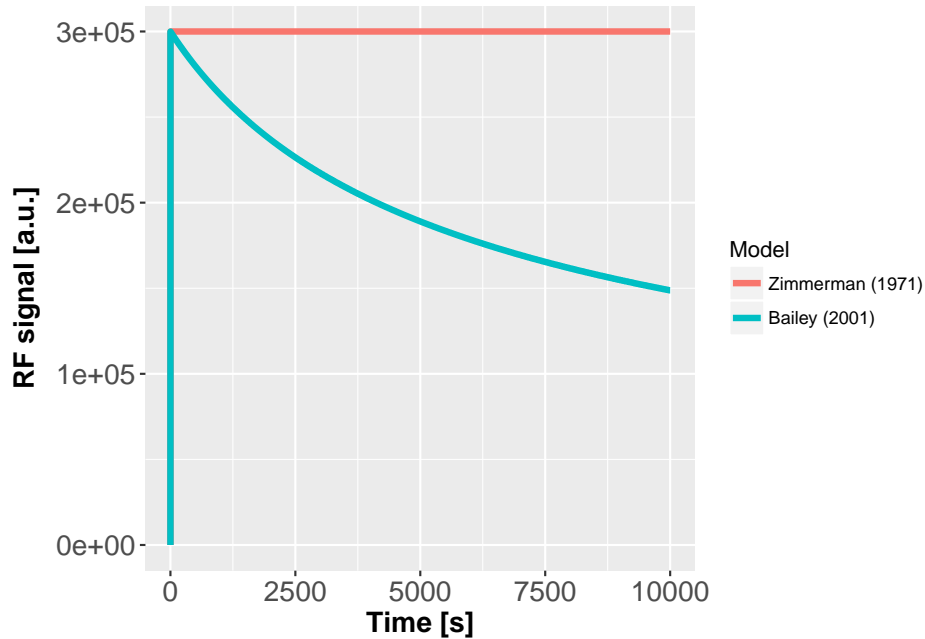
### Plot RF signal

```
RF_signal <- as.data.frame(cbind(time = times,
                                Zimmerman = result_Zimmerman[, "signal"],
                                Bailey = result_Bailey[, "signal"]))

colnames(RF_signal) <- c("time", "Zimmerman (1971)", "Bailey (2001)")

RF_signal <- reshape2::melt(RF_signal, id.vars = "time")

ggplot(RF_signal, aes(x = time, y = value, colour = variable)) +
  geom_line(aes(colour = variable), size = 1.5) +
  scale_colour_discrete(name = "Model") +
  xlab("Time [s]") +
  ylab(expression(bold("RF signal [a.u.]"))) +
  theme(axis.text = element_text(size = 14),
        axis.title = element_text(size = 14, face = "bold"))
```



Plot concentration of R-centre

```

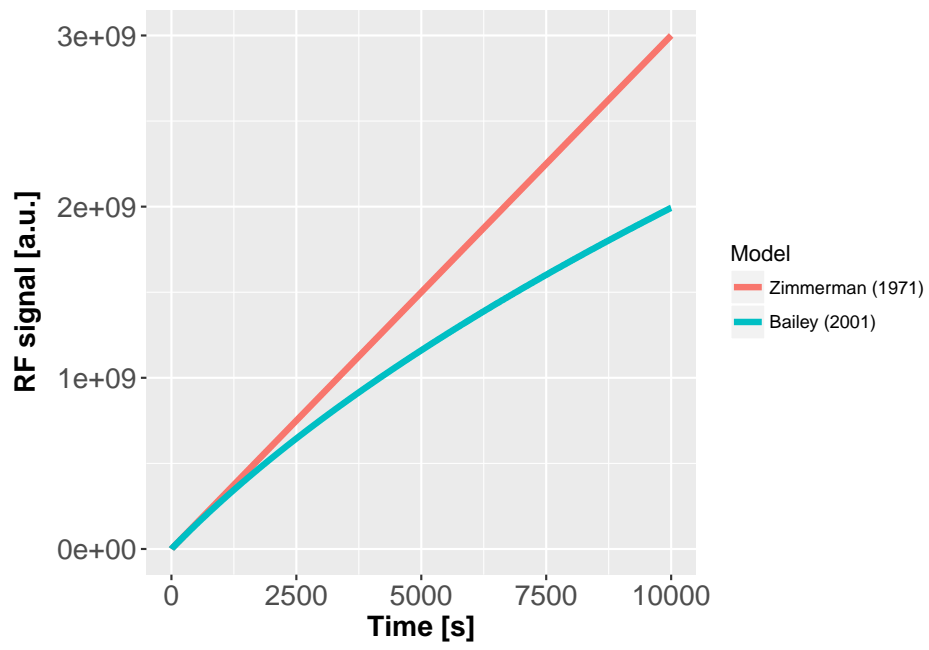
conc_m1 <- as.data.frame(cbind(time = times,
                              Zimmerman = result_Zimmerman[, "m1"],
                              Bailey = result_Bailey[, "m1"]))

colnames(conc_m1) <- c("time", "Zimmerman (1971)", "Bailey (2001)")

conc_m1 <- reshape2::melt(conc_m1, id.vars = "time")

ggplot(conc_m1, aes(x = time, y = value, colour = variable)) +
  geom_line(aes(colour = variable), size = 1.5) +
  scale_colour_discrete(name = "Model") +
  xlab("Time [s]") +
  ylab(expression(bold("RF signal [a.u.]"))) +
  theme(axis.text = element_text(size = 14),
        axis.title = element_text(size = 14, face = "bold"))

```



## **A.4 Chapter 5**

# On the dose-rate dependence of radiofluorescence signals of natural quartz (supplementary material)

*Johannes Friedrich, Mauro Fasoli, Sebastian Kreutzer, Christoph Schmidt*

## Introduction

This supplementary material is part of the article Friedrich et al. (submitted) and contains additional **R**-coding examples and code completions.

All calculations presented here were executed with **R** version 3.4.3 and the **R**-package ‘RLumModel’ version 0.2.3.

```
library(RLumModel)
```

## Use three-energy-level model

### Set parameters

```
own_parameters <- list(
  N = c(5e10, 1e10, 1e11),
  E = c(1.95, 1.75, 5),
  s = c(1e10, 5e13, 1e13),
  A = c(1e-10, 5e-7, 1e-9),
  B = c(0, 5e-9, 5e-10),
  Th = c(0),
  E_th = c(0),
  K = 2.8e7,
  W = 0.64,
  R = 6.3e7,
  model = "customized"
)

dose_rate <- c(10, 20, 25, 50, 100, 200, 300, 400, 500)
```

### Simulate RF signals

```
model.output <- lapply(
  dose_rate/1000, function(x){

  sequence <- list(
    IRR = c(20, 1000, 1),
    PAUSE = c(20, 60),
    PH = c(350, 5),
    PAUSE = c(20, 60),
```

```

IRR = c(20, 20, 1e-11),
PAUSE = c(20, 60),
# end sample history, begin laboratory

TL = c(20, 500, 10),
PAUSE = c(500, 600),
RF = c(20, 40*34*x, x)
)

RF_data <- model_LuminescenceSignals(
  model = "customized",
  sequence = sequence,
  own_parameters = own_parameters,
  plot = FALSE,
  verbose = FALSE
)

return(get_RLum(RF_data, recordType = c("RF$"), drop = FALSE))
})

RF_data <- merge_RLum(model.output)

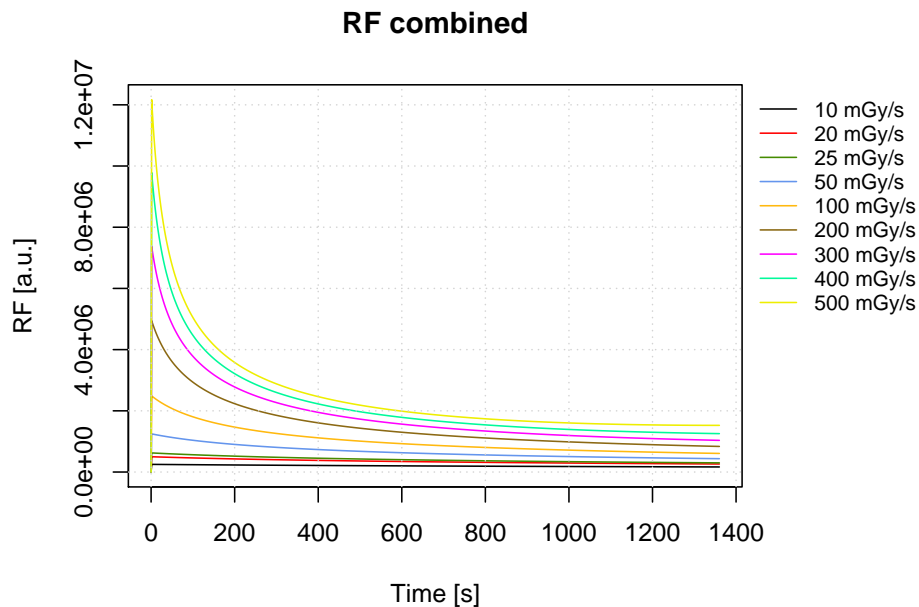
```

## Plot results

```

plot(RF_data,
  combine = T,
  legend.text = paste0(dose_rate, " mGy/s"),
  legend.pos = "outside")
grid()

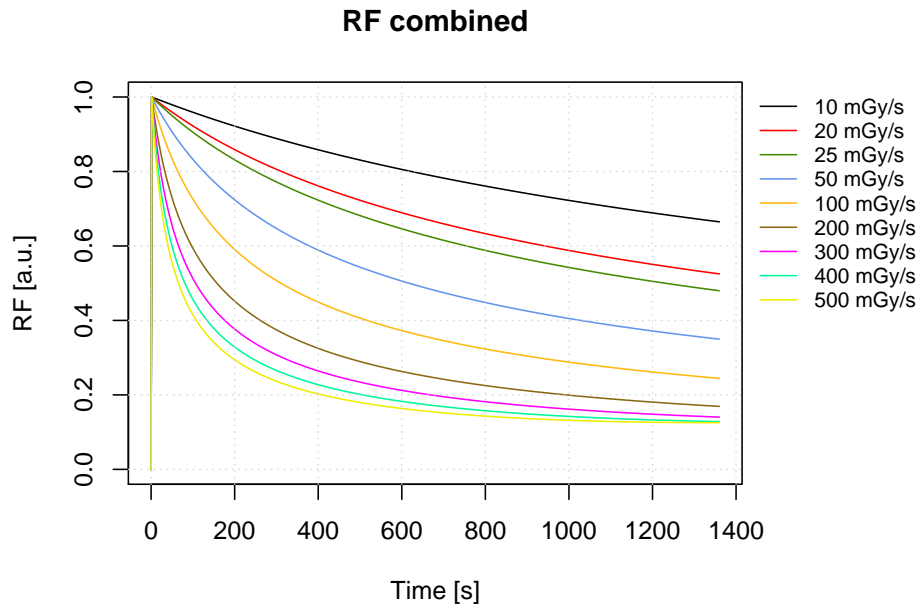
```



```

plot(RF_data,
     combine = T,
     norm = T,
     legend.text = paste0(dose_rate, " mGy/s"),
     legend.pos = "outside")
grid()

```



## Use Friedrich2018 model

### Simulate RF signals

#### Define sequence

```

dose_rate <- c(10, 20, 25, 50, 100, 200, 300, 400, 500)

model.output <- lapply(
  dose_rate/1000, function(x){

  sequence <- list(
    TL = c(20, 500, 10),
    PAUSE = c(500, 600),
    RF = c(20, 40*34*x, x)
  )

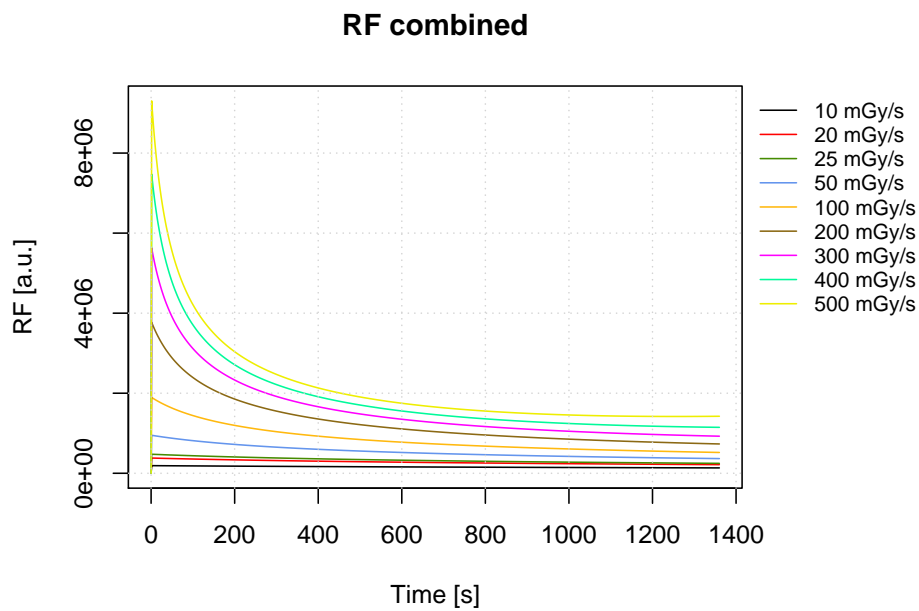
  RF_data <- model_LuminescenceSignals(
    model = "Friedrich2018",
    sequence = sequence,
    plot = FALSE,
    verbose = FALSE
  )
}

```

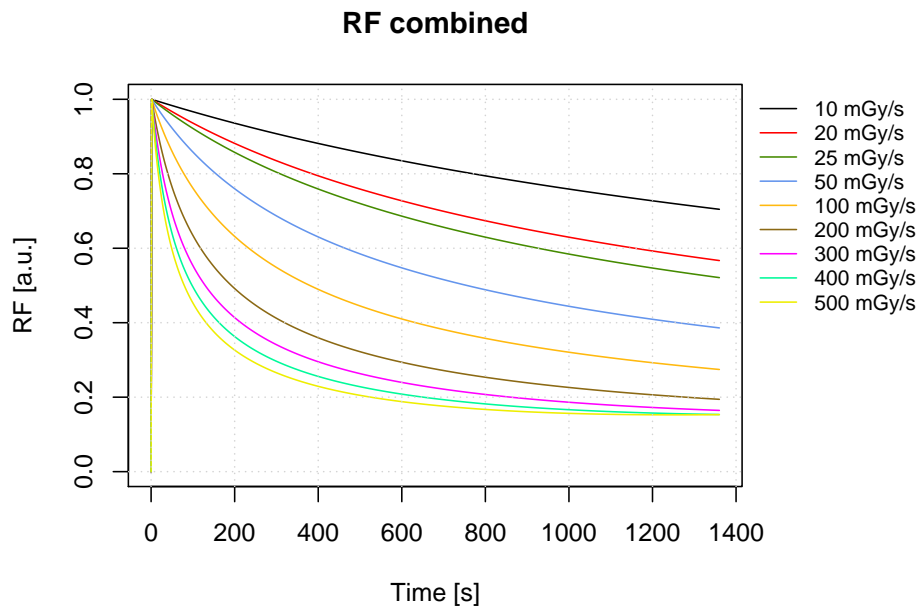
```
return(get_RLum(RF_data, recordType = c("RF$"), drop = FALSE))  
})  
RF_data <- merge_RLum(model.output)
```

## Results

```
plot(RF_data,  
     combine = T,  
     legend.text = paste0(dose_rate, " mGy/s"),  
     legend.pos = "outside")  
grid()
```



```
plot(RF_data,  
     combine = T,  
     norm = T,  
     legend.text = paste0(dose_rate, " mGy/s"),  
     legend.pos = "outside")  
grid()
```



## Common quartz phenomena

### TL signal with different heating rates

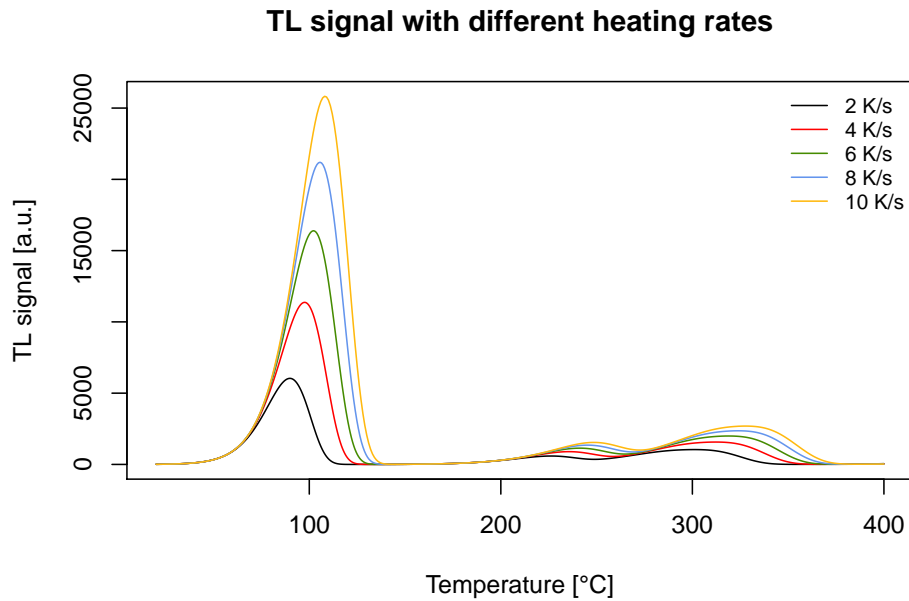
```
##set heating rate
heating.rate <- seq(from = 2, to = 10, by = 2)

##model signals
##"verbose = FALSE" for no terminal output
## "TL$" for exact matching TL and not (TL)
model.output <- lapply(
  1:length(heating.rate), function(x){
    sequence <- list(
      IRR = c(20, 10, 1),
      TL = c(20, 400, heating.rate[x]))

    TL_data <- model_LuminescenceSignals(
      sequence = sequence,
      model = "Friedrich2018",
      plot = FALSE,
      verbose = FALSE)

    return(get_RLum(TL_data, recordType = "TL$", drop = FALSE))
  })

##merge output
model.output.merged <- merge_RLum(model.output)
```



## TAC

```
##set temperature
act.temp <- seq(from = 80, to = 600, by = 20)

##loop over temperature
model.output <- vapply(X = act.temp, FUN = function(x) {

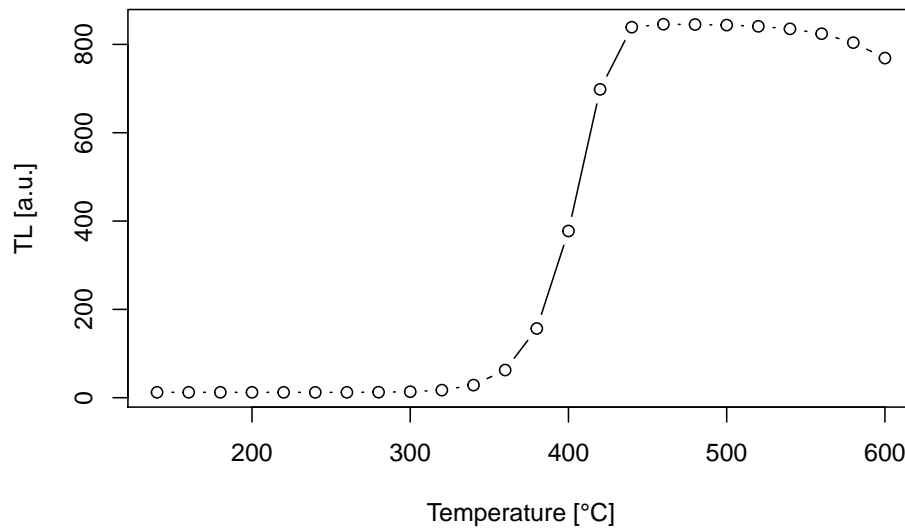
  ##set sequence, note: sequence includes sample history
  sequence <- list(
    IRR = c(20, 1, 1e-11),
    IRR = c(20, 10, 1),
    PH = c(x, 1),
    IRR = c(20, 0.1, 1),
    TL = c(20, 150, 5)
  )

  ##run simulation
  temp <- model_LuminescenceSignals(
    sequence = sequence,
    model = "Friedrich2018",
    simulate_sample_history = TRUE,
    plot = FALSE,
    verbose = FALSE
  )

  ## "TL$" for exact matching TL and not (TL)
  TL_curve <- get_RLum(temp, recordType = "TL$")

  ##return max value in TL curve
  return(max(get_RLum(TL_curve)[,2]))
})
```

```
}, FUN.VALUE = 1)
```



#### OSL signal for different optical powers

```
##set optical power [%]
optical_power <- c(0,20,40,60,80,100)

##loop over power
model.output <- lapply(optical_power, function(x){

  ##set sequence
  sequence <- list(
    IRR = c(20, 50, 1),
    PH = c(220, 10, 5),
    OSL = c(125, 50, x))

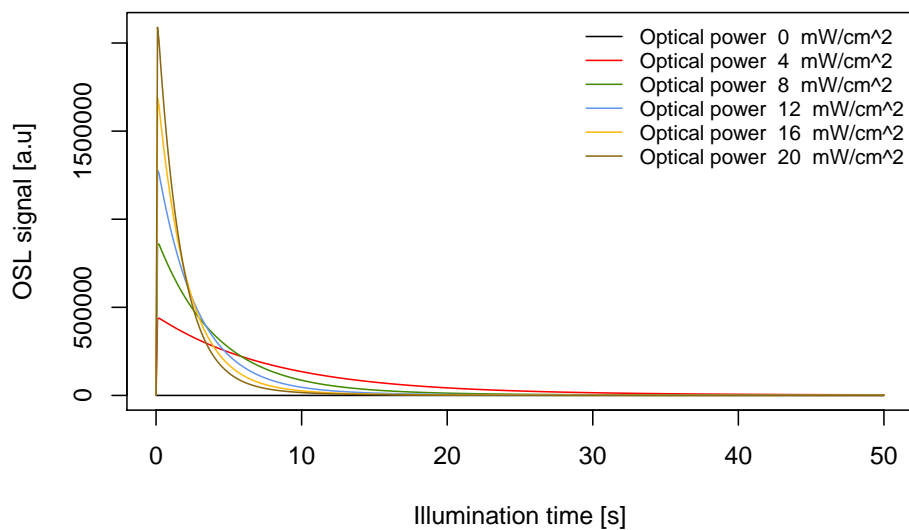
  data <- model_LuminescenceSignals(
    sequence = sequence,
    model = "Friedrich2018",
    plot = FALSE,
    verbose = FALSE)

  ##"OSL$" for exact matching TL and not (OSL)
  return(get_RLum(data, recordType = "OSL$", drop = FALSE))

})

##merge output
model.output.merged <- merge_RLum(model.output)
```

### OSL combined



### OSL signal for different reading temperatures

```
##set OSL temperature
OSL.temp <- c(20, 80, 160, 200, 240)

##loop over temperature
model.output <- lapply(OSL.temp, function(x){

  ##set sequence
  sequence <- list(
    OSL = c(x, 60, 100)
  )

  data <- model_LuminescenceSignals(
    sequence = sequence,
    model = "Friedrich2018",
    plot = FALSE,
    verbose = FALSE
  )

  ##"OSL$" for exact matching TL and not (OSL)
  return(get_RLum(data, recordType = "OSL$", drop = FALSE))
})

##merge output
model.output.merged <- merge_RLum(model.output)

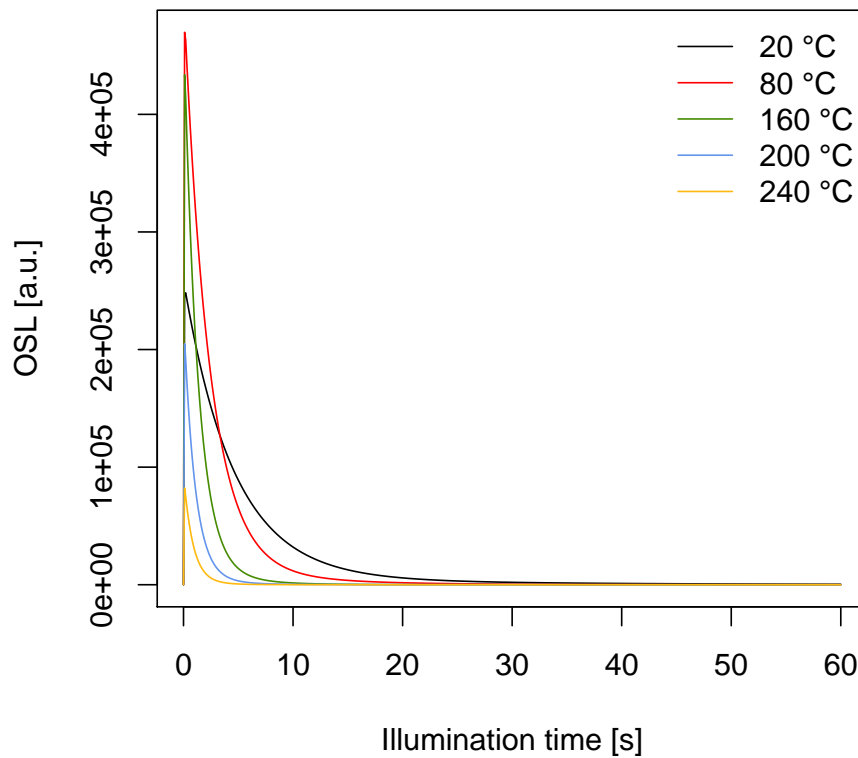
##plot results
plot_RLum(
  object = model.output.merged,
  xlab = "Illumination time [s]",
  ylab = "OSL [a.u.]",
```

```

main = "OSL signal for different reading temperatures",
legend.text = paste(OSL.temp, "\u00B0C"),
combine = TRUE,
cex = 1.2)

```

### OSL signal for different reading temperatures



### DRT

```

##set PH temperatures
PH_temp <- seq(from = 160, to = 300, by = 20)

##set RegDose
RegDose = c(0, 8, 15, 26, 32, 0, 8)

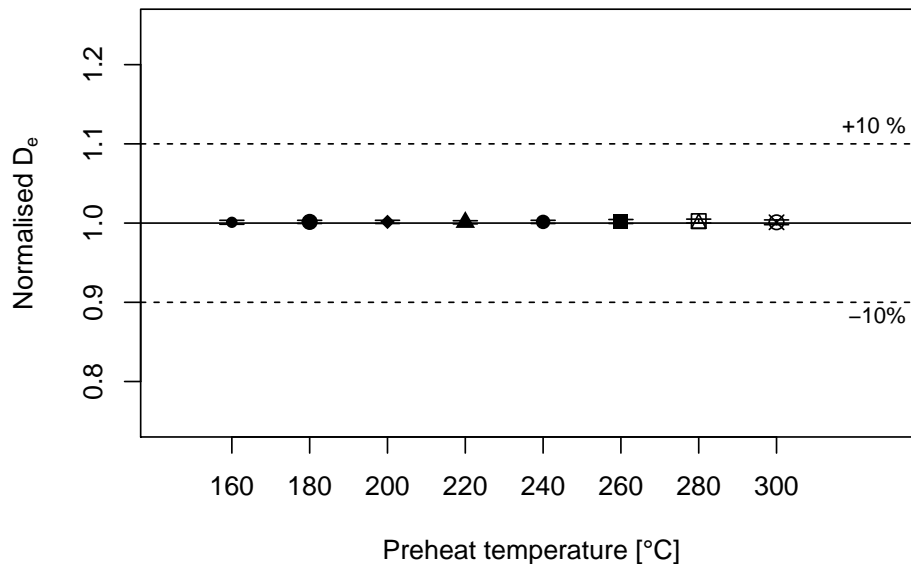
##loop over PH temperatures
DRT.output <- lapply(1:length(PH_temp), function(x){

  sequence <- list(
    RegDose = RegDose,
    TestDose = 2,
    PH = PH_temp[x],
    CH = PH_temp[x],
    OSL_temp = 125,
    Irr_2recover = 20
  )
})

```

```
model.output <- model_LuminescenceSignals(  
  sequence = sequence,  
  model = "Friedrich2018",  
  plot = FALSE,  
  verbose = FALSE  
)  
  
results <- analyse_SAR.CWOSL(object = model.output,  
  signal.integral.min = 1,  
  signal.integral.max = 7,  
  background.integral.min = 301,  
  background.integral.max = 401,  
  fit.method = "EXP",  
  dose.points = RegDose,  
  plot = FALSE)  
  
temp <- get_RLum(results)  
out <- data.frame(De = temp$De, De.error = temp$De.Error)  
return(out)  
})  
  
##output as data.frame for plot_DRTResults  
DRT.result <- as.data.frame(do.call(rbind, DRT.output))  
  
##plot DRT.results  
plot_DRTResults(DRT.result, preheat = PH_temp, given.dose = 20)
```

### Dose recovery test



**SAR protocol**

```
##set RegDose
RegDose = c(0, 8, 15, 26, 32, 0, 8)

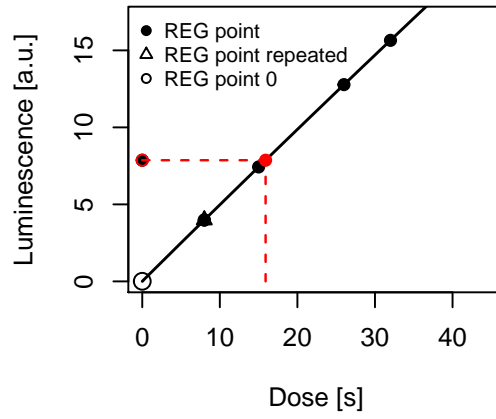
##set sequence
sequence <- list(
  RegDose = RegDose,
  TestDose = 2,
  PH = 220,
  CH = 200,
  OSL_temp = 125
)

##model
model.output <- model_LuminescenceSignals(
  sequence = sequence,
  model = "Friedrich2018",
  plot = FALSE,
  verbose = FALSE
)

##analyse SAR sequence and plot only the resulting growth curve
results <- analyse_SAR.CWOSL(
  model.output,
  signal.integral.min = 1,
  signal.integral.max = 7,
  background.integral.min = 301,
  background.integral.max = 401,
  fit.method = "EXP",
  dose.points = RegDose,
  verbose = FALSE,
  plot.single = c(6)
)
```

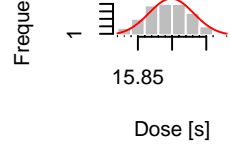
### Growth curve

$D_e = 15.9 \pm 0.03$  | fit: EXP



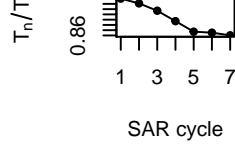
### $D_e$ from MC simulatio

$D_{eMC} = 15.9 \pm 0.03$  | quality = 100 %



n = 100 , valid fits = 100

### Test dose response





## B.2 Publication II - Chapter 3

### Quartz radiofluorescence: a modelling approach

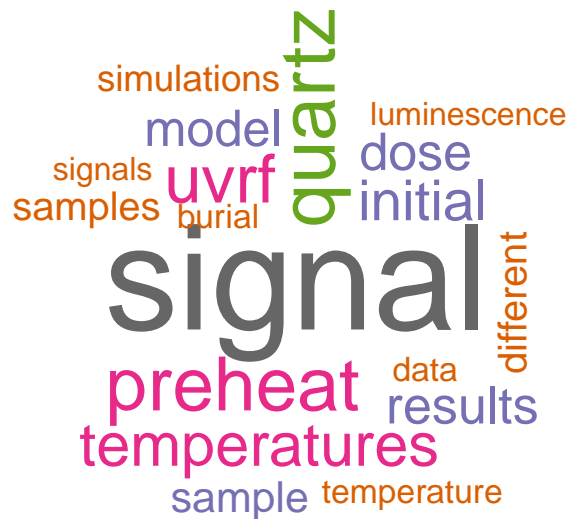
Johannes Friedrich, Vasilis Pagonis, Reuven Chen, Sebastian Kreutzer, Christoph Schmidt

*Journal of Luminescence* 186, 318 – 325, 2017

<https://doi.org/10.1016/j.jlumin.2017.02.039>

	JF	VP	RC	SK	CS
Measurements	100 %	-	-	-	-
Simulations	80 %	10 %	10 %	-	-
Manuscript preparation	80 %	-	-	5 %	15 %
Comments to improve the manuscript	-	20 %	20 %	30 %	30 %
Review handling	80 %	5 %	5 %	5 %	5 %

**Table B.2:** Individual contributions to Publication II - Chapter 3.





## B.4 Publication IV - Chapter 5

### On the dose rate dependence of radiofluorescence signals of natural quartz

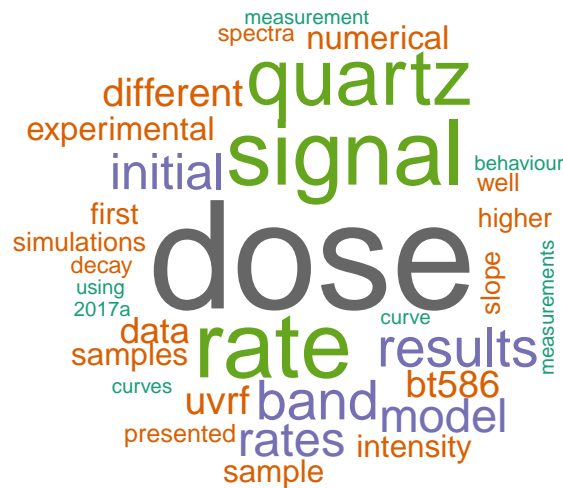
Johannes Friedrich, Mauro Fasoli, Sebastian Kreutzer, Christoph Schmidt

*Radiation Measurements 111, 19 – 26, 2018*

<https://doi.org/10.1016/j.radmeas.2018.02.006>

	JF	MF	SK	CS
Measurements	90 %	10 %	-	-
Simulations	100 %	-	-	-
Manuscript preparation	90 %	5 %	-	5 %
Comments to improve the manuscript	-	40 %	30 %	30 %
Review handling	80 %	5 %	5 %	10 %

**Table B.4:** Individual contributions to Publication IV - Chapter 5.



## B.5 Publication V - Chapter 6

### Radiofluorescence as a Detection Tool for Quartz Luminescence Quenching Processes

Johannes Friedrich, Sebastian Kreutzer, Christoph Schmidt

*Accepted for publication in Radiation Measurements*

<https://doi.org/10.1016/j.radmeas.2018.03.008>

	JF	SK	CS
Measurements	50 %	50 %	-
Simulations	100 %	-	-
Manuscript preparation	90 %	5 %	5 %
Comments to improve the manuscript	-	50 %	50 %
Review handling	80 %	10 %	10 %

**Table B.5:** Individual contributions to Publication V - Chapter 6.



## B.6 Publication VI - Chapter 7

### Making the Invisible Visible: Observing the UV-reversal Effect in Quartz using Radiofluorescence

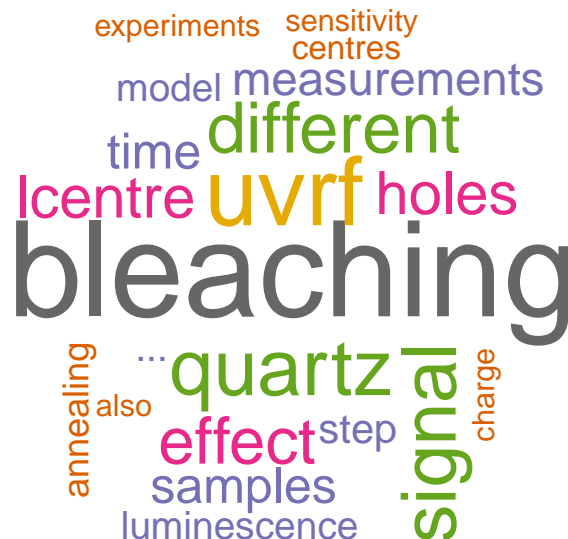
Johannes Friedrich, Sebastian Kreutzer, Christoph Schmidt

*Journal of Physics D: Applied Physics* 51, 335105

<http://iopscience.iop.org/article/10.1088/1361-6463/aacfd0>

	JF	SK	CS
Measurements	100 %	-	-
Simulations	100 %	-	-
Manuscript preparation	90 %	5 %	5 %
Comments to improve the manuscript	-	50 %	50 %
Review handling	90 %	5 %	5 %

**Table B.6:** Individual contributions to Publication VI - Chapter 7.



# C List of publications and presentations

## C.1 Peer reviewed journals

### C.1.1 accepted/published

Schmidt, C., **Friedrich, J.**, & Zöller, L. 2015. Thermochronometry using red TL of quartz? Numerical simulation and observations from in-situ drill-hole samples. *Radiation Measurements* 81, 98–103.

**Friedrich, J.**, Kreutzer, S., & Schmidt, C. 2016b. Solving ordinary differential equations to understand luminescence: 'RLumModel', an advanced research tool for simulating luminescence in quartz using R. *Quaternary Geochronology* 35, 88–100.

**Friedrich, J.**, Pagonis, V., Chen, R., Kreutzer, S., & Schmidt, C. 2017a. Quartz radiofluorescence: a modelling approach. *Journal of Luminescence* 186, 318–325.

**Friedrich, J.**, Fasoli, M., Kreutzer, S., & Schmidt, C. 2017e. The basic principles of quartz radiofluorescence dynamics in the UV-analytical, numerical and experimental results. *Journal of Luminescence* 192, 940–948.

Kreutzer, S., **Friedrich, J.**, Sanderson, D., Adamiec, G., Chruścińska, A., Fasoli, M., Martini, M., Polymeris, G. S., Burbidge, C. I., & Schmidt, C. 2017a. Les sables de Fontainebleau: A Natural Quartz Reference Sample and its Characterisation. *Ancient TL* 35(2), 21–31.

**Friedrich, J.**, Fasoli, M., Kreutzer, S., & Schmidt, C. 2018c. On the dose rate dependence of radiofluorescence signals of natural quartz. *Radiation Measurements* 111, 19–26.

**Friedrich, J.**, Kreutzer, S., & Schmidt, C. 2018d. Radiofluorescence as a detection tool for quartz luminescence quenching processes. *Radiation Measurements*.

Schmidt, C., **Friedrich, J.**, Adamiec, G., Chruścińska, A., Fasoli, M., Kreutzer, S., Martini, M., Panzeri, L., Polymeris, G. S., Przegiętka, K., Valla, P. G., King, G. E., & Sanderson, D. C. 2018. How reproducible are kinetic parameter constraints of quartz luminescence? An interlaboratory comparison for the 110 °C TL peak. *Radiation Measurements* 110, 14–24

**Friedrich, J.**, Kreutzer, S., & Schmidt, C. 2018b. Making the Invisible Visible: Observing the UV-reversal Effect in Quartz using Radiofluorescence. *Journal of Physics D: Applied Physics* 51(33), 335105

## **C.2 Conference posters and presentations**

**Friedrich, J.**, Kreutzer, S., & Schmidt, C. 2015. Simulating radiofluorescence of quartz: problems with current quartz luminescence models. German LED Conference 2015, Berlin, Germany

**Friedrich, J.**, Kreutzer, S., & Schmidt, C. 2016a. Finding appropriate model parameters for luminescence simulations: inverse modelling and model fitting with Markov-Chain Monte-Carlo methods in RLumModel. UK LED Conference 2016, Liverpool, UK

**Friedrich, J.**, Kreutzer, S., & Schmidt, C. 2016c. The basic principles of quartz radiofluorescence dynamics in the UV - analytical and numerical results. German LED Conference 2016, Emmendingen, Germany

**Friedrich, J.**, Kreutzer, S., & Schmidt, C. 2017f. The R package 'RLumModel': Simulating charge transfer in quartz. EGU General Assembly Conference Abstracts, vol. 19, 19318

Kreutzer, S., Burow, C., Dietze, M., Fuchs, M. C., **Friedrich, J.**, Fischer, M., & Schmidt, C. 2017b. The R package 'Luminescence': a history of unexpected complexity and concepts to deal with it. EGU General Assembly Conference Abstracts, vol. 19, 15461

Dietze, M., Fuchs, M. C., **Friedrich, J.**, & Kreutzer, S. 2017. Virtual sediment deposits - Exploring concepts and hypotheses in geomorphology. EGU 2017, Vienna, Austria

**Friedrich, J.**, Kreutzer, S., & Schmidt, C. 2017b. Radiofluorescence as a detection tool for quenching processes in quartz luminescence. International LED Conference 2017, Cape Town, South Africa

**Friedrich, J.**, Kreutzer, S., & Schmidt, C. 2018a. Finding appropriate model parameters for luminescence simulations: inverse modelling and model fitting with RLumModel. EGU General Assembly Conference Abstracts, vol. 20, 15579

### **C.3 Invited talks**

**Friedrich, J.**, Kreutzer, S., & Schmidt, C. 2017c. RLumModel – Eine kleine Einführung. Invited talk at the RLuminescence Developer Meeting, Kirchenbirkig

**Friedrich, J.**, Kreutzer, S., & Schmidt, C. 2017d. RLumModel – Simulating charge transfer in quartz. Invited talk at the workshop at the LED Meeting 2017, Cape Town



# Acknowledgements

Ohne die Zusammenarbeit Vieler wäre diese Arbeit nicht möglich gewesen und an dieser Stelle möchte ich meinen Dank aussprechen.

Zunächst danke ich meinen beiden Betreuern Dr. Christoph Schmidt und Dr. Sebastian Kreutzer. Sie haben im Vorfeld des Projekts viel Pionierarbeit zur Quarz-RF geleistet und das eingeworbene DFG Projekt machte diese Dissertation erst möglich. Ich konnte zu jeder Zeit Fragen, Ideen und Probleme erörtern. Danke für alle Freiheiten und jegliche nötige Unterstützung in den letzten Jahren.

Ebenso danke ich dem ganzen Team vom Lehrstuhl Geomorphologie für die zur Verfügung gestellte Infrastruktur, die täglichen Mensa-Gänge und den kollegialen Austausch über dies und das: Prof. Dr. Ludwig Zöller, Manfred Fischer, Eveline Löbl, Dr. Ulrich Hambach, PD Dr. Klaus-Martin Moldenhauer, Thomas Kolb und Prakrit Noppradit.

Viel Erfahrung und Wissen durfte ich bei internationalen Meetings und Konferenzen sammeln. Der Austausch mit den Kolleginnen und Kollegen aus Italien, Schottland, Polen und Frankreich war für mich immer sehr gewinnbringend. Vielen Dank hierfür!

Ebenso danke ich Prof. Dr. Vasilis Pagonis und Prof Dr. Reuven Chen für die inspirierende Zusammenarbeit und unser gemeinsames Treffen in München 2016.

Ohne die lebenslange Unterstützung meiner Familie wäre ich heute nicht da, wo ich bin. Ich danke meinen Eltern, dass ihr mir immer die Freiheit gegeben habt, die Wege zu gehen, die sich mir auftaten. Dass eure Unterstützung mir immer sicher war und ist, weiß ich sehr zu schätzen.

Ebenso unsagbar dankbar bin ich meiner Frau Clara. Du bist mein Fels in der Brandung und ich danke dir für deine Unterstützung in allen Lebenslagen! DANKE!

Zudem danke ich Gott dafür, dass er mein Leben so sehr segnet.



# (Eidesstattliche) Versicherungen und Erklärungen

(§ 8 Satz 2 Nr. 3 PromO Fakultät)

Hiermit versichere ich eidesstattlich, dass ich die Arbeit selbstständig verfasst und keine anderen als die von mir angegebenen Quellen und Hilfsmittel benutzt habe (vgl. Art. 64 Abs. 1 Satz 6 BayHSchG).

(§ 8 Satz 2 Nr. 3 PromO Fakultät)

Hiermit erkläre ich, dass ich die Dissertation nicht bereits zur Erlangung eines akademischen Grades eingereicht habe und dass ich nicht bereits diese oder eine gleichartige Doktorprüfung endgültig nicht bestanden habe.

(§ 8 Satz 2 Nr. 4 PromO Fakultät)

Hiermit erkläre ich, dass ich Hilfe von gewerblichen Promotionsberatern bzw. -vermittlern oder ähnlichen Dienstleistern weder bisher in Anspruch genommen habe noch künftig in Anspruch nehmen werde.

(§ 8 Satz 2 Nr. 7 PromO Fakultät)

Hiermit erkläre ich mein Einverständnis, dass die elektronische Fassung der Dissertation unter Wahrung meiner Urheberrechte und des Datenschutzes einer gesonderten Überprüfung unterzogen werden kann.

(§ 8 Satz 2 Nr. 8 PromO Fakultät)

Hiermit erkläre ich mein Einverständnis, dass bei Verdacht wissenschaftlichen Fehlverhaltens Ermittlungen durch universitätsinterne Organe der wissenschaftlichen Selbstkontrolle stattfinden können.

.....  
Ort, Datum, Unterschrift

